DOCTOR OF PHILOSOPHY

Mechanisms of laser shock peening residual stress and the influence on life enhancement

Leering, Mitchell

Award date:
2021

Awarding institution:
Coventry University

Mechanisms of laser shock peening residual stress and the influence on life enhancement

By

Mitchell P. Leering

Supervisor: Prof. M. E. Fitzpatrick

October 2021

Mechanisms of laser shock peening residual stress and the influence on life enhancement

By

Mitchell P. Leering

October 2021

A thesis submitted in partial fulfilment of the University's requirements for the Degree of Doctor of Philosophy

[redacted]

[redacted]

Certificate of Ethical Approval

Applicant:

Mitchell Leering

Project Title:

Mechanisms of life enhancement by laser shock peening surface treatment

This is to certify that the above named applicant has completed the Coventry University Ethical Approval process and their project has been confirmed and approved as Medium Risk

Date of approval:

29 July 2019

Project Reference Number:

P93284

Dedicated to Shannon, thank you for always being there.

Abstract

In recent decades, the manufacturing process of Laser Shock Peening (LSP) has been used to extend the service life of very particular aircraft components. This process introduces compressive residual stresses in the metallic components, effectively increasing its fatigue life and the resistance to stress corrosion cracking. Advancements in laser technology have now provided the ability to systematically study the influence of numerous LSP parameters on the formation of residual stresses and to develop novel uses of the induced stresses to increase the safety of aircraft structures.

This research aimed to determine the influence of laser temporal profiles on the LSP induced residual stress and explore the use of different LSP strategies to produce a redirection in the trajectory and extension in crack growth performance of aircraft fuselage structures. The experimental results of these studies were used to develop predictive methods to determine the outcome of the LSP processing and the behaviour of fatigue cracks in the presence of residual stresses.

The study of the mechanisms of LSP used 6 mm thick 2524-T351 clad aluminium samples with four different variations of the laser pulse temporal profiles (flat top, standard Gaussian, two variations of a double Gaussian). The maximum pulse power density, pulse duration, pulse size and spatial distribution were fixed so that the influence of the temporal profiles were isolated. Incremental hole drilling was used to measure the induced residual stress, whilst the surface deformation caused by the laser shot was characterised by interferometry techniques.

The results showed, no single tested temporal profile resulted in a significant increase in comparative performance of the LSP processing, as all deviations in the residual stress distributions were within the experimental scatter of the measurements. A physics-based finite element model was developed that accounted for the laser temporal profile and variations in the spatial distribution. The simulated and measured results indicated good agreement, with the proposed finite element model increasing the predictive accuracy of the post-LSP deformed surface.

The crack growth life extension and modification in the trajectory of the fatigue crack study focused on the application of LSP on 2 mm thick 2024-T3 clad aluminium. LSP patches were orientated at various angles and distances from the central crack notch, to evaluate the effectiveness of LSP residual stresses to force a modification of the crack trajectory.

Residual stress at multiple points on the sample was measured using incremental hole drilling and neutron diffraction techniques. Constant amplitude fatigue testing was conducted at two different stress ranges, to assess the influence of loading conditions on the crack growth rate and crack trajectory.

Results showed that the LSP increased the crack growth life by as much as 9.5 times compared to the unpeened samples. It was found that the LSP residual stress tended to deviate the crack towards the centre of the LSP patches as the crack propagated under mode I cyclic loading. The highest crack growth life extension was achieved by placing the LSP patch as close to the initial notch. The largest crack deviation was achieved by placing the LSP patches further along the crack trajectory. The largest crack deviation tended to occur as the crack approached the edge of the LSP patch, this was due to the adjacent balancing stresses which occurred due to the LSP compressive residual stress. Residual stress models were coupled with linear elastic fracture mechanics finite element simulations to characterise the complex loading condition which occurred due to the superposition of the applied load and residual stresses. The crack growth life and crack deviation potential were predicted.

Preface

This thesis is submitted for the degree of Doctor of Philosophy at Coventry University, United Kingdom. The data presented in this thesis was carried out at the Faculty of Engineering and Computing, between September 2017 and June 2021, under the supervision of Professor Michael E. Fitzpatrick. None of this work has been submitted for any other degree or similar qualification. Parts of this research was presented in various conferences as either posters or talks and submitted for peer-reviewed journals. A list has been provided:

M. Leering, M. Fitzpatrick, *"Conceptual study of the use of Laser Shock Peening for crack redirection"*. Poster at the 7th International Conference on Laser Shock Peening & Related Phenomena – June 2018, Singapore.

D. Furfari, M. Leering, M. E. Fitzpatrick, *"3D printed solid confinement for Laser Shock Peening"*. Oral presentation at the 2nd European Laser Shock Peening Workshop – September 2019, Hamburg, Germany.

M. Leering, M. E. Fitzpatrick, *"Laser Shock Peening surface treatment for fatigue crack life extension"*. Oral presentation at Engineering Integrity Society Peter Watson Prize – October 2019, Derby, United Kingdom.

Acknowledgements

I would like to sincerely thank my director of studies, Prof. Michael E. Fitzpatrick for all his guidance, support and patience during my PhD. His positivity and ability to always provide me with assistance, guidance or a kind word always made things easier. His generosity and supervision style allowed me to experience the most out of this experience and I am truly thankful.

I would like to express my gratitude to the rest of my supervisory team of Dr Niall Smyth and Prof Xiang Zhang, who both always made time to help me in the laboratory or guide me through the complexities of my research. I really could not have asked for a better support team.

I would like to acknowledge Dr Domenico Furfari from Airbus Operations for the financial support, material and wealth of knowledge during our review meetings. Thank you for providing me with this opportunity.

I would like to express my thanks to the whole Structural Integrity and Materials research group at Coventry University and especially Dr Abdul Khadar Syed, Dr Marco Pavan and Dr Jino Mathew for all your useful pointers, tips and discussions. I can not thank Barry Meek, Steve Allitt, Martyn Cockell, Geoffrey Booth, Steven Damms, Luke Trodden and Lawrence King enough for all their support no matter the issue, they were all always available to help.

I would like to thank Prof. Philippa Reed, Dr Julian Wharton and Dr Alvaro Sanchez from Southampton University for all their time, and constructive feedback during our Airbus reviews.

I am very thankful to Prof. Claudia Polese at the University of the Witwatersrand, Dr Daniel Glaser at the Council for Scientific and Industrial Research – National Laser Centre, Dr Jan Brajer and Jan Kaufman at HiLASE for all their assistance in providing vital access to their laser peening facilities, without it this research would have been impossible.

Lastly, I would like to thank my wife, Shannon who took the brunt of the difficult times and who was always there to pick me back up. Without her, I would have never been able to complete this. Thank you for your sacrifice, support, encouragement and the long discussion about what I tried to achieve each day.

Table of contents

Table of figures

Table of tables

Nomenclature

Symbol	Variable	Unit
I	Power density	GW/cm^2
E_{Beam}	Beam energy	mJ
τ_p	Pulse duration	ns
A_{Beam}	Beam area	mm^2 / cm^2
HEL	Hugoniot Elastic Limit	MPa
v	Poisson's ratio	-
$\sigma_y{}^{dyn}$	Dynamic yield strength	MPa
L_{pl}	Plastically affected depth	µm
P_{max}	Maximum plasma pressure	GPa
C_e,C_p	Velocity of elastic and plastic wave	m/s
P	Plasma pressure	GPa
P_o	Initial plasma pressure	GPa
L	Plasma thickness	m
L_o	Initial plasma thickness	m
α	Constant fraction of internal energy	-
γ	Constant of adiabatic cooling	-
Z	Total acoustic impedance	kg/m^2s
$Z_{confinement}$	Acoustic impedance of confinement media	kg/m^2s
Z_{target}	Acoustic impedance of target material	kg/m^2s
t	Time	s
$r,\ R_{pulse}$	Local radius and total radius of laser pulse	mm
x, y	Local position of laser pulse	mm
ρ	Density	kg/m^3
C	Speed of sound in the material	m/s
$L_{element}$	Shortest element length	m
E	Elastic modulus of the material	GPa
$\bar{\sigma}$	Flow stress	MPa
$\bar{\varepsilon}^p$	Effective plastic strain	µm/µm
$\dot{\bar{\varepsilon}}^p$	Effective plastic strain rate	-
$\dot{\varepsilon}_0$	Reference strain rate	-

a, b, c, n, m	Experimentally determined Johnson Cook constants	-
T, T_r, T_m	Temperature, room temperature, melting temperature	K
σ_{Tot}	Total measured residual stress	MPa
σ_{LSP}	Laser shock peening induced residual stress	MPa
σ_{Eq}	Balancing electric equilibrium residual stress	MPa
ε_{LSP}	Laser shock peening induced eigenstrains	-
σ	Nominal stress	MPa
F	Applied force	N
$A_{c.s.a}$	Cross-sectional area	mm^2
τ	Nominal shear stress	MPa
ε	Nominal strain	-
l_o, w_o	Original length and width of the sample	mm
$\Delta l, \Delta w$	Change in length and width of the sample	mm
Γ	Shear strain	-
G	Shear modulus	GPa
σ_m, σ_a	Mean stress and stress amplitude	MPa
$\sigma_{max}, \sigma_{min}$	Maximum and minimum stress	MPa
$\Delta\sigma$	Stress range	MPa
R, R_{Tot}	Stress ratio, Total stress ratio	-
ERR	Energy release rate	J/m^2
a	Crack length	mm
K, K_{min}, K_{max}	Stress intensity factor, minimum and maximum cyclic	$MPa.m^{0.5}$
K_I, K_{II}, K_{III}	Mode I, II, III stress intensity	$MPa.m^{0.5}$
u_x, u_y, u_z	Crack trip displacement field	m
Υ	Geometry factor	-
$SERR$	Strain energy release rate	J/m^2
r_p	Plastic zone	mm
a_{eff}	Effective crack length	mm
σ_{YS}	Yield strength	MPa
B	Sample thickness	mm
ΔK	Stress intensity range	$MPa.m^{0.5}$
da/dN	Fatigue crack growth rate	mm/cycle
C, m	Paris law coefficients	$mm/cycle.MPa.m^{0.5}$, -

C, γ, m	Walker Equation coefficients	mm/cycle.MPa.m$^{0.5}$, -, -
K_{Ic}	Fracture toughness	MPa.m$^{0.5}$
K_{res}	Residual stress intensity factor	MPa.m$^{0.5}$
K_{Tot}	Total stress intensity factor	MPa.m$^{0.5}$
K_{Op}	Crack opening stress intensity factor	MPa.m$^{0.5}$
K_{Eff}	Effective stress intensity factor	MPa.m$^{0.5}$
θ_p	Crack deviation angle	$^{\circ}$
D_{IHD}	Diameter of hole made during incremental hole drilling	mm
D	Gauge diameter	mm
σ_{res}	Incremental hole drilling residual stress	MPa
x_i	Relevant incremental hole drilling parameter	-
$p(x_i)$	Probability density function of the relevant parameter	-
$u(\sigma_{res})$	Standard uncertainty of Incremental hole drilling residual stress	MPa
$\hat{a}_{jk}, \hat{b}_{jk}$	Cumulative strain relaxation coefficients	-
λ	Wavelength	nm
d, d_o	Interplanar spacing, zero-stress interplanar spacing	Å
h	Planck's constant	J.s
C_n	Velocity of neutron	m/s
L	Flightpath of neutron	m
m_s	Mass of neutron	kg
a_o, a_x, a_y, a_z	Initial and deformed lattice parameters	nm
p_j, q_j, t_j	Combination strains	-
P_k, Q_k, T_k	Combination stress	MPa
$p_{std}, q_{std}, t_{std}$	Standard error in combination strains	-
$\bar{a}, \bar{b}$	Calibration matrices	-
$\alpha_P, \alpha_Q, \alpha_T$	Regularization factors	-

Acronyms

Acronym	Definition
LSP	Laser Shock Peening
OEM	Original Equipment Manufacturers
FEA	Finite Element Analysis
XRD	X-ray Diffraction
HEL	Hugoniot Elastic Limit
LSPwC	Laser Shock Peening without Coating
WLSP	Warm Laser Shock Peening
EPP	Elastic Perfectly Plastic
ZA	Zerillo-Armstrong
JC	Johnson-Cook
LEFM	Linear Elastic Fracture Mechanics
SIF	Stress Intensity Factor
FCGR	Fatigue Crack Growth Rate
SP	Superposition Principle
MSP	Modified Superposition Prinicple
SCP	Superposition Contact Prinicple
MTS	Maximum Tangential Stress
MERR	Maximum Energy Release Rate
L	Longitudinal direction
T	Transverse direction
S	Short transverse direction
CSIR-NLC	Council for Scientific and Industrial Research – National Laser Centre
FWHM	Full Width Half Maximum
Wits	University of the Witwatersrand
EDM	Electrical Dischage Machining
FT	Flat Top
G	Gaussian
DSG	Double Shallow Gaussian
DDG	Double Deep Gaussian
TOF	Time-Of-Flight
CMM	Coordinate Measurement Machine
XFEM	eXtended Finite Element Method

Chapter 1 Introduction

1.1. Background

Progress, by definition, is the movement to an improved or more developed state. The ongoing strive for engineering progress encapsulates the drive for higher performance and improved efficiency of innovative technologies. Since the ‘leap forward’ achieved by sustained powered flight in 1903, the aeronautical industry has been the primary driving force of numerous advancements in the field of propulsion, structures, materials and manufacturing technologies.

Modern large aircraft structures are designed so that “catastrophic failure due to fatigue, corrosion or accidental damage, will be avoided throughout the operational life of the aeroplane” [1]. This design evaluation is better known as the damage tolerance methodology. It dictates the load-carrying ability of a damaged structure and the interval between structural inspections [2]. However, over the last 75 years, there have been several unfortunate aircraft structural failures. Corrosion (16% of failures) and fatigue (55% of failures) are the two most frequent failure mechanisms associated with aircraft component failure [3]. Fatigue cracks typically initiate at stress concentrations, abnormalities in materials, or areas exposed to corrosive environments. In some cases, these cracks can propagate undetected between maintenance periods resulting in a structural weakness in the airframe.

The Chalk’s Ocean Airways Flight 101 accident which occurred in 2005, was an example of structural failure due to corrosion and fatigue. In this accident, several cracks were initiated at corrosion sites concealed within the airframe. Structural failure of a fatigued stringer within the wing structure caused abnormal loading of the lower wing skin panel. The accident investigation determined that fatigue cracks in the lower wing skins initiated at corrosion areas around the drain of a fuel sump and a fastener hole adjacent to the rear stringer. Once the lower skin fractured, fatigue cracks were initiated and propagated in various locations in the rear spar causing a substantial decrease in the structure’s residual strength. The cracks in the spar quickly reached their critical crack length upon which the right-wing separated from the aircraft [4].

Since the 1950s, the aeronautical industry and academia have attempted to address the concerns associated with fatigue issues in aerospace structures. Enhancements in predictive methods, fatigue testing techniques and aerospace materials have all been the primary areas of study relating to this field. Moreover, residual stress engineering has become a vital field in addressing fatigue-related issues.

Numerous factors, such as environmental, economic, and general aircraft fleet age, currently drive the need for innovative technologies that improve the critical aircraft components' fatigue resistance. The increased understanding of residual stresses and the development of the processes used to induce them has led to a significant increase in their incorporation at the design stage and as corrective tools to enhance high-value structures' service life. Residual stresses will be more influential in the future as the aviation industry heightens its environmental awareness and 'progress' to higher performing integrated aircraft structures. In so doing, the techniques and effects of introducing residual stress in structures have to be thoroughly and extensively studied to ensure the highest safety standards.

1.2. Motivation

Residual stresses are known to play a pivotal role in regards to the rate of propagation of fatigue cracks [5]. Several surface treatments are currently employed to induce beneficial residual stress that significantly enhances the performance of the metallic structure. Peening is a cold working process that induces compressive residual stresses in a component through plastic deformation imparted by an impulsive force. There are many variations of peening all with vastly varying levels of complexity and outcome, with Laser Shock Peening (LSP) being of particular interest in this research. As the most effective yet most advanced form of peening, LSP achieves deep compressive stresses with precise control and repeatability offered by laser-based technologies [6].

Laser technology has significantly advanced over the last 30 years, resulting in a steady growth of LSP academic and commercial providers. Most LSP systems incorporate large laser systems (laboratory sized apparatus) operating at a few joules in energy per laser pulse. These systems are typically coupled to a form of robotic sample manipulation. To achieve more robust operating opportunities, the industry trend at the time of this research was to move towards the development of small, low-cost, portable laser systems and laser beam manipulation attachments. This drive for cost-efficiency and compactness will limit the usable laser operational parameters (wavelength, peak power and repetition rate) and the beam quality (brilliance, spatial profile and beam propagation). However, effectiveness, repeatability and cost-effectiveness are the primary concern of any high-value engineering manufacturing process. Based on this trend, industry and academia are focused on determining the influence of LSP parameters, the effect of the imparted compressive residual stress on material behaviour and process predictive methods. Accurate predictions of the laser effects on residual stress and material behaviour will be instrumental in designing robust LSP systems and processing strategies.

Confinement of the rapidly expanding plasma has been a requirement of the LSP process since its inception. It is this medium that contains the LSP event which increases the effectiveness of the process. Multiple solid and fluid materials have been successfully used, with the current industry standard being a thin (1-2 mm) layer of water [7]. Figure 1.1 provides an example of an ejected water jet from the target surface due to the LSP event's impulse loading.

Figure 1.1: Ejection of a water jet from the target surface due to a laser shock peening event

The ubiquity of water as the confinement medium of choice is due to its cost-effectiveness, incompressible properties, and to some extent, its ability to flow over complex geometries. However, water as an LSP confinement medium poses restrictive factors that range from fundamental physics to operational restrictions set by Original Equipment Manufacturers (OEM). Examples of the limitations introduced from water and other solid confinement mediums in LSP are:

- Applications in which there are restrictions to flowing and splashing water in the vicinity of electrical systems and corrosion sensitive structures.
- Water contamination by the ablation of the target surface degrades the effectiveness of the process.
- The water layer must be strictly laminar in its flow characteristics to ensure no interference or inconsistencies in processing.
- Water vapour and droplets can accumulate on the optical setup of the system, which can negatively influence the focusing capabilities of the lenses leading to possible laser pulse inconsistencies. To over this, additional infrastructure and processes (air knives, fans and stagged processing) are required to mitigate these effects, adding to the cost and complexity of operating the LSP system.
- Solid media do not conform to the contours of the target surface easily, often resulting in delamination of the medium from the target, rendering the process ineffective.

Beyond these limitations in the stand alone LSP process, the water confinement excludes the in situ application of LSP with other manufacturing processes, like the additive processes of Selective Laser

Sintering and Melting. The combination of these technologies would provide a step-change in manufacturing technology. Hence, there is a drive for removing water and replacing it with a more suitable solid medium to overcome these concerns.

Part of this research is to investigate novel uses of LSP technology in fatigue and structural applications. All modern large commercial aircraft fuselage structures are designed as a skin structure supported by frames and stringers. These semi-monocoque structures are designed to carry the flight loads whilst adhering to the damage tolerance principles. The skin panels are designed as large as possible to reduce the number of splices, which are one of the most critical parts of the fuselage structure. Riveted longitudinal lap joints and circumferential butt joints are the two splicing techniques used on modern-day aircraft. Fatigue cracks have been found to occur in the upper row of rivet holes of the outer skin, and at the lower row of rivets in the inner skin of the lap joint, as illustrated in Figure 1.2 [8]. If fatigue cracks develop in one of these joints and are not easily identified because of the skin overlap positioning, they could rapidly propagate to failure [9].

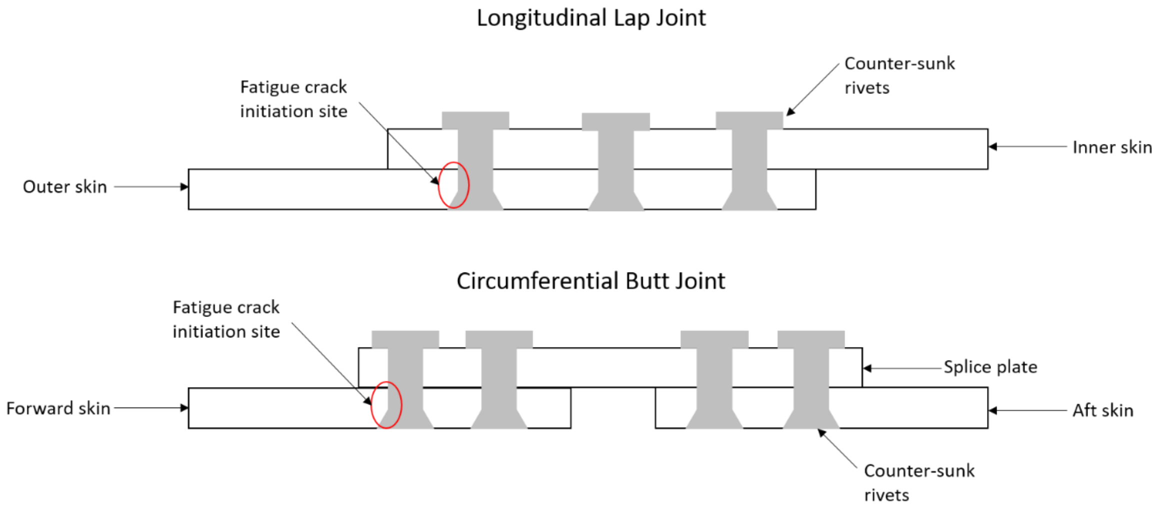

Figure 1.2: Schematic of aircraft longitudinal and circumferential joints demonstrating the location of fatigue cracks

To enhance the damage tolerance and reduced the crack growth rates, tear straps or crack arrestors are incorporated into the structure at and between fuselage frame stations. The purpose of these design features is to force longitudinal cracks in the skin panels (parallel with the fuselage's length) to turn circumferentially [10]. Crack kinking occurs due to complex crack-tip stress fields generated by the crack flap and the tear strap. This flapping and crack kinking provide a controlled failure of the fuselage's skin and decompression, enhancing the structure's residual strength. However, this additional structure does add to the weight of the aircraft. Residual stresses are known to alter the trajectory of cracks in metallic structures [11]. By coupling the versatile processing ability and unique anisotropic residual stress fields generated by LSP, structural crack kinking can potentially be achieved with LSP residual stress. This LSP application may result in a possible reduction in the size of the fuselage crack arrestors, increasing the performance of the structure.

1.3. Research objectives

The presented research has been conducted with the broad aims of contributing to the future developments of LSP infrastructure and innovative applications. This was achieved by contributing to the understanding of the influence of laser temporal profiles, power density and processing coverage on the formation of residual stresses during LSP. Simulation techniques are used to provide additional context to the influence of the processing parameters on the induced residual stresses. The research outcomes can validate the construction of future laser peening work cells, the selection of processing parameters and predictive methods of the induced residual stress. This work demonstrated the novel use of LSP residual stresses to modify the propagation rate and trajectory of fatigue cracks in aluminium samples which are representative of typical fuselage structures. Contributing to the industries understanding of the potential design implications that can be achieved by incorporating LSP residual stresses in the development and construction of future aircraft structures. In addition to the primary aims of this work, research was conducted to determine the feasibility of using a 3D printed solid confinement as a substitute for the generally used water overlay and proposed an adapted Monte Carlo simulation technique for determining the measurement uncertainty in incremental hole drilling residual stresses.

The following lists the expected objectives of this research:

- Investigation of the effects of LSP parameters on the formation of residual stress and material behaviour.
    - Investigate the effects of the laser temporal profiles on the introduction of residual stresses in aeronautical materials.
    - Study the effects of LSP parameters on the formation of residual stress and post-LSP material response.
- Development of LSP finite element modelling techniques to accurately predict introduced residual stress and material deformation.
    - Development of a physics-based finite element analysis capable of accurately predicting RS whilst incorporating the laser pulses spatial and temporal profiles.

  - Development of an optimisation-based Eigenstrain methodology to predict LSP residual stress in materials accurately.
- Investigation of the interaction of fatigue cracks and residual stress fields.
  - Determine the effects of LSP residual stress fields on extending the service life of fuselage representative structures.
  - Investigate the effects of LSP residual stress fields on the trajectory of fatigue cracks under mode I loading.
- Development of an innovative confinement medium that can be used in place of the current industry standard water confinement overlay - Appendix B.
  - Development of 3D printed polymer-based confinement medium.
  - Demonstrate the LSP operational window in which this medium can be implemented.
  - Determine the effectiveness of the medium compared to water.

1.4. Research approach

This research was separated into three individual studies relating to LSP processing, modelling, and application to achieve the research objects in section 1.3. The approach for each study is outlined accordingly.

The study of LSP processing and parameters (temporal profile and power density) effects are investigated to identify their influence on the introduction of residual stresses in AA2524-T351. The results of this study were used to create and validate dynamic pulse-by-pulse Finite Element Analysis (FEA) simulations of the LSP process. This work demonstrates the need to include the 2D laser spatial effects in simulations to increase the predicted residual stress and material deformation accuracy. The samples residual stress profiles were characterised using incremental hole drilling, and X-ray Diffraction (XRD) techniques were possible. Modelling the LSP process was completed using explicit-ABAQUS (dynamic) finite element simulation techniques and used analytical methods to estimate the plasma pulse pressure based on the LSP processing parameters. All simulations were validated according to the experimental results.

The study of the ability to force a crack trajectory modification was completed in thin AA2024-T351 material. LSP processing was applied as angled patches to establish a complex residual stress field that may modify the cracks' trajectory. Experimental fatigue crack growth testing was conducted on the samples to determine the experimental trajectory of the crack. The residual stress field was determined by incremental hole drilling and neutron diffraction methods. The experimental results have been coupled with detailed FEA simulations to provide a greater understanding of driving mechanisms associated with the cracks trajectory modifications.

The study of the investigation of an alternative LSP confinement media was carried out to determine a viable replacement for the LSP industry-standard of water confinement. Alternative media were identified based on a review of available literature and commercial product specifications. Clear 3D-printed solid polymer media met a viable replacement criterion as the material was reasonably transparent to the laser beam. The medium can be directly printed on the thin AA2024-T3 target surface and provided suitable stiffness to resist the expanding plasma. An overall assessment of the medium's suitability was provided by assessing the knock-down factor in expected LSP efficiency and ability to introduce compressive residual stress in the material. The introduced residual stress fields were characterised using X-ray diffraction techniques.

1.5. Structure of the thesis

This thesis has been organised into six chapters.

Chapter 1 presents an overview of the context of the use of LSP, the broader field of aircraft fatigue and the benefit of using LSP as a potential design tool to enhance aircraft structure. This chapter provides the research motivation and an overview of the structure and content of the thesis. Finally, the research objectives to be achieved from this work are presented.

Chapter 2 provides a literature review and summary of the relevant topics associated with this thesis. The presented literature encompassed the fundamentals of solid mechanics, residual stresses, fatigue, a background of LSP and relevant simulation techniques are presented.

Chapter 3 describes the applied experimental procedures used throughout this research.

Chapter 4 provides the research results generated by experimental and numerical efforts to investigate the LSP process parameters influence on the formation of residual stresses and quality of the processed surface. This chapter also details the advancements in the FEA prediction of LSP residual stress using numerical methods.

Chapter 5 provides the experimental and numerical efforts to investigate the use of LSP to drive a modification of a fatigue crack trajectory. This chapter details the finite element analysis of the combination of residual stresses and structural integrity.

Chapter 6 provides a summary of the research, contributions to the knowledge and suggestions of future work to continue on the achieved outcomes of this research.

Appendix A provides the fundamental background and methodology of the derived experimental uncertainty in the presented residual stress measurements determined by incremental hole drilling. This appendix details how Monte Carlo simulations have been used to determine the associated uncertainty in the experimental residual stress measurements.

Appendix B provides the research results generated by experimental efforts in developing an innovative solid confinement medium for the replacement of water in the LSP process.

Chapter 2 Literature Review

In this chapter, a detailed review of relevant literature on the fundamentals of solid mechanics, residual stresses, fatigue, a background of LSP and relevant simulation techniques are presented. Section 2.1 provided relevant background to solid mechanics principles and defines the relevance of residual stresses in engineering materials. Section 2.2 provided a comprehensive background to the relevant aspects of LSP, with a focus on processing parameters, influence on residual stress and simulation techniques of LSP. Finally, section 2.3 provided theoretical background on fatigue and fracture mechanics, with specific mention of the role of residual stress on fatigue behaviour of materials.

2.1. Solid mechanics

This branch of continuum mechanics is associated with the study of solid materials acted upon by internal and external forces, pressures and temperatures. These forces result in the deformation and motion of the solid material.

2.1.1. Stress

Mechanical stress is a physical measure of the internal forces or the intensity of the forces that neighbouring particles exert on each other. Dependent on the axis or direction in which the force is applied defines the type of stress state (axial, bending or torsion). Stress [σ], measured in pascals, in its simplest form is expressed by Equation 2-1, in which F and $A_{c.s.a}$ correspond to the applied force (internal force) and the cross-sectional area on which the force acts [12]. The directionality of the stresses defines how the body is deformed. A load that pushes against the body will establish compressive stresses whilst a pulling force will establish tensile stresses.

$$\sigma = \frac{F}{A_{c.s.a}} \qquad \textit{Equation 2-1}$$

The stress state in any generic three-dimensional body under load can be described by an infinitesimally small cubic element of that body. The faces will experience normal component or the principal stress (e.g. σ_x, σ_y, σ_z) and two shear stress components (e.g.τ_{xy},τ_{xz}) as shown in Figure 2.1 [13].

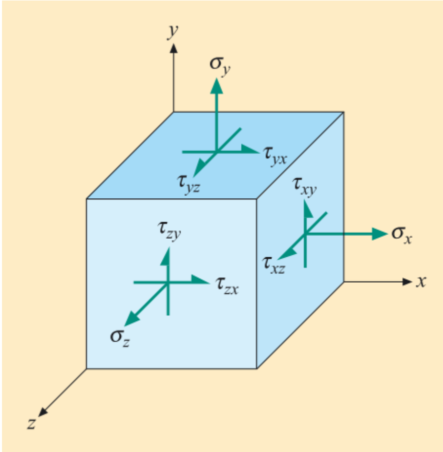

Figure 2.1: Infinitesimally small Stress element [13]

The nine components that fully define the stress state at any point is known as a stress tensor (also known as the Cauchy tensor) shown in Equation 2-2 [13]. To maintain equilibrium in the body, opposing shear stresses are required to be equal, hence $\tau_{xy} = \tau_{yx}$, $\tau_{yz} = \tau_{zy}$ and $\tau_{zx} = \tau_{xz}$.

$$\sigma = \begin{bmatrix} \sigma_x & \tau_{xy} & \tau_{xz} \\ \tau_{yx} & \sigma_y & \tau_{yz} \\ \tau_{zx} & \tau_{zy} & \sigma_z \end{bmatrix}$$ *Equation 2-2*

The stress tensor can be simplified by assuming that all stresses occur in a single plane. This results in a state of plane stress in which no shear or normal stresses are acting on the z-plane. This assumption can be extended to components that are relatively thin compared to the other two dimensions. In geometries of this nature, the stresses in the z-direction cannot be suitably generated through the small thickness, allowing the stress to be set to zero. The influence of the plane stress condition is reflected in the stress tensor in Equation 2-3.

$$\sigma = \begin{bmatrix} \sigma_x & \tau_{xy} & 0 \\ \tau_{yx} & \sigma_y & 0 \\ 0 & 0 & 0 \end{bmatrix}$$ *Equation 2-3*

2.1.2. Strain

When a body is exposed to external forces, the object undergoes a deformation or a change in dimension. It can be noted that the concept of stress and strain can be understood as the cause and effect, respectively. The deformation of length due to the presence of stress within the body is referred to as strain. Strain can be described by Equation 2-4 and Equation 2-5. Engineering is the most quoted manner in which strain is reported. True strain accounts for area reduction (necking) when the applied load causes stresses that exceed the yield strength of the material [12]. Figure 2.2 showed the change in geometry due to the applied load [13].

$$\varepsilon = \ln \frac{l}{l_o}\ (True\ Strain) \qquad \text{Equation 2-4}$$

$$\varepsilon = \frac{\Delta l}{l_o} = \frac{\Delta w}{w_o}\ (Engineering\ Strain) \qquad \text{Equation 2-5}$$

Engineering or Normal Strain will be used throughout this research. The change in the bar's width accounts for the reduction in size due to the applied load. As with the stress tensor (Equation 2-2), there will be a strain in the z-direction. Strains in the y- and z- directions are produced even though there was no direct load in that plane. This occurs due to Poisson effects. Poisson's ratio can be referred to as the ratio between the proportional decrease and the increase in the various components of a body's geometry.

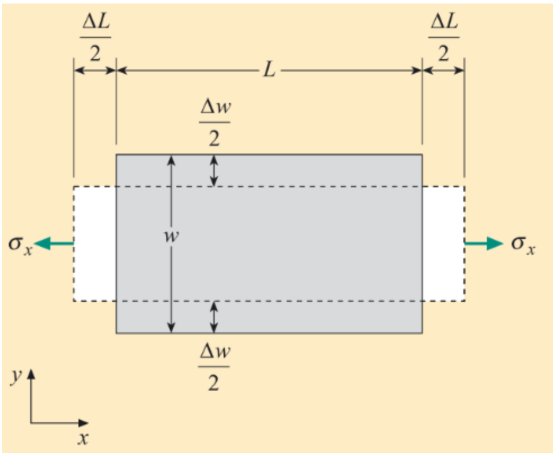

Figure 2.2: Two dimensional representation of strain in a bar [13]

Unlike normal strain, shear strain gives rise to an angular deformation of the body as shown by Figure 2.3. The applied pure shear strain causes a change in the rectangle's internal angles.

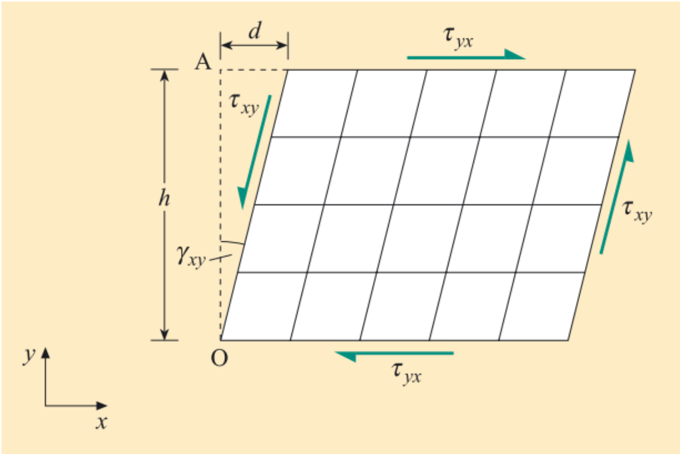

Figure 2.3: Angular deformation of a body due to shear strains [13]

Equation 2-6 provided the shear strain (Γ) according to Figure 2.3, because of the very small angles associated with this component of strain, the ratio of the change in geometry provides an accurate representation of the strain.

$$\Gamma = \frac{d}{h}$$ *Equation 2-6*

The strain analysis can be extended to any generic three-dimensional body by similarly using an infinitesimal cube-like in Figure 2.1. The stress can be defined by three normal and six shear strains, as provided in Equation 2-7. The same symmetry between the shear components hold in this relationship in that $\Gamma_{xy} = \Gamma_{yx}, \Gamma_{xz} = \Gamma_{zx}$ and $\Gamma_{yz} = \Gamma_{zy}$.

$$\varepsilon = \begin{bmatrix} \varepsilon_x & \Gamma_{xy} & \Gamma_{xz} \\ \Gamma_{yx} & \varepsilon_y & \Gamma_{yz} \\ \Gamma_{zx} & \Gamma_{zy} & \varepsilon_z \end{bmatrix}$$ *Equation 2-7*

2.1.3. Linear elastic relationship

As previously mentioned, stress and strain are directly related to each other as the cause and effect. These two properties are related to one another through the modulus of elasticity or Young's modulus (E). Equation 2-8 gives the relationship for elastic modules and is defined as Hooke's Law. This relationship is only valid whilst the load causes elastic material behaviour (no plastic or permanent deformations), and the material is isotropic (it has the same properties in all directions).

$$E = \frac{\sigma}{\varepsilon}$$ *Equation 2-8*

By accounting for Poisson's ratio and Hooke's Law, Equation 2-9 can be written in the form of Equation 2-10.

$$\begin{Bmatrix} \varepsilon_x \\ \varepsilon_y \\ \varepsilon_z \end{Bmatrix} = \frac{1}{E} \begin{bmatrix} 1 & -v & -v \\ -v & 1 & -v \\ -v & -v & 1 \end{bmatrix} \begin{Bmatrix} \sigma_x \\ \sigma_y \\ \sigma_z \end{Bmatrix}$$ *Equation 2-9*

The Shear Modulus (G), is a similar relationship between the shear components of stress and strain. It was defined by Equation 2-10.

$$G = \frac{\tau}{\Gamma} = \frac{E}{2(1+v)}$$ *Equation 2-10*

Plane strain assumptions can be applied if significant strains are prevented from occurring in a particular direction due to physical constraints. This state can also be assumed when the strains in one direction are considerably smaller (by order of magnitude) than the strains in the remaining two directions. In these cases, Equation 2-11 can be applied to simplify any analysis.

$$\varepsilon_z = \Gamma_{xz} = \Gamma_{yz} = 0$$ *Equation 2-11*

2.1.4. Residual stress

Residual stresses are internal stresses within a material at a steady-state condition or when all external loads have been removed [14]. Residual stresses are introduced through permanent deformation of the component, thermal loading or during the manufacturing process (machining). These internal stresses can be of an order of magnitude similar to the yield strength of the material. Residual stresses maintain the same directional nature (tensile and compressive) as applied stresses. The consideration of residual stress is vital as these internal stresses can act in a manner of superposition with any external loading. This could lead to unforeseen loading conditions which exceed the operational or design boundaries of a component.

The primary use of intentional residual stress is to extend the fatigue life of engineering components. This is done through the controlled introduction of compressive residual stress. Beneficial compressive residual stress reduces the overall loading on the component and can extend the operational period before cracks initiate and propagate.

Residual stresses can be classified into three categories based on their length scale, Type I, Type II and Type III [15]. Figure 2.4 provided a schematic of the length scale of the classification of residual stress.

Type I (σ^{I}): Occur within the body of the component. They are known as the macro-stresses, as they are over a large portion (multiple crystal grains) of the component.

Type II (σ^{II}): These stress occur over a length scale of a single crystal grain. Type I residual stress is caused by the superposition of type II residual stress from multiple grains. Type II and III are both known as micro-stresses.

Type III (σ^{III}): This is the stress which occurs at an atomic level. The residual stress occurs due to dislocations and other lattice imperfections.

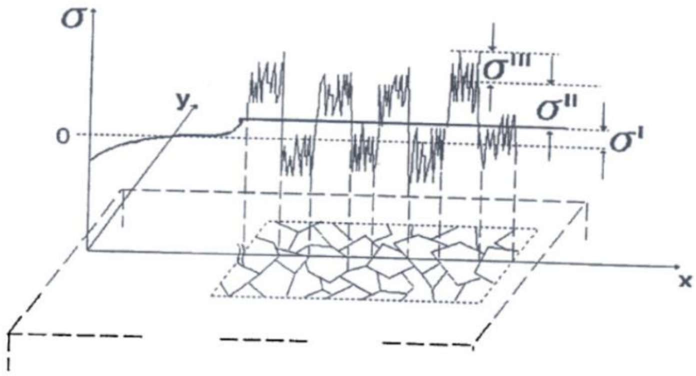

Figure 2.4: Length scale classification of residual stress types [15]

Many manufacturing processes can induce inherent by-product residual stress in components. Table 2.1 listed some of the most common origins of residual stresses [16]. A more in-depth investigation of each method falls out of the scope of this research.

Table 2.1: Common origins of residual stresses [16]

Origin	Mechanical	Thermal	Structural
Smelting Casting	No	Temperature gradient during cooling	Change in phase
Shot-peening Hammer-peening Roller burnishing Laser shock peening Bending Rolling	Plastic deformation	No	No
Grinding Turning Drilling Milling	Plastic deformation	Temperature gradient	Change of phase if the temperature is sufficiently high
Welding	Flanging	Temperature gradient	Microstructural change

2.1.4.1. Introduction of residual stress by Laser Shock Peening

During LSP, the induced shock wave acts on the target surface. Each shot acts as a high-intensity hammer that creates a dimple on the component's surface, plastically deforming the near-surface layer by stretching, as illustrated in Figure 2.5 [6]. The residual stress is essentially formed in a component through the plastic deformation of the material under the LSP treated area. The magnitude of the deformation decreases with depth to an unaffected area. The unaffected depth is defined as the position in which the generated shock wave's peak pressure no longer exceeds the HEL. This is the transition point of the material from an elastic-plastic state to a purely elastic state [17].

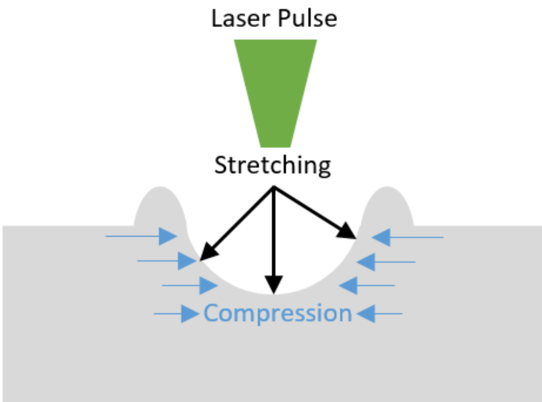

Figure 2.5: Schematic of surface deformation of the material during laser shock peening

The adjacent material to the peened area forms a stress state which attempts to return the plastically deformed material towards its original state resulting in a reasonably compressive residual stress state in the peened area, up to a millimetre or more in-depth. To maintain equilibrium, tensile residual stress occurs in the surrounding material of the peened region [18]. Figure 2.6 provided an example of the in-plane strain map from the laser shock peened sample, showing compressive residual strain directly under the peened surface and tension to the sides [19].

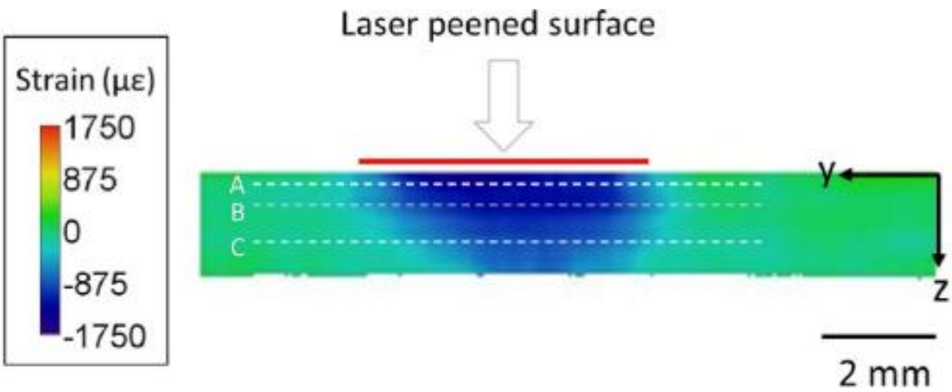

Figure 2.6: In-plane strain map from laser shock peened sample [19]

2.2. Laser Shock Peening

Laser Shock Peening is an advanced manufacturing technique used to impart compressive residual stress to millimetres in-depth in metallic components. The interaction between a short-pulsed (ns scale) laser set to a pulse density of a few GW/cm^2 (laser pulse area of a few mm^2) and a confined target surface interact to form a high-temperature plasma. An alternative peening strategy uses a laser energy range of below 1 J per pulse (a few GW/cm^2), but with significantly more smaller laser spot interactions with a higher spot overlapping area. A residual stress-inducing shock wave occurs and propagates into the material upon the expansion of the plasma [20]. A transparent overlay acts to confine the plasma's expansion, prolonging its growth and intensifying the shockwave [21]. A 2 to 5 mm thick layer of water is the industry standard confinement medium, but various glass overlays were used in the process's initial development [22]. Figure 2.7.a provided a basic schematic of the typical LSP process without a sacrificial coating. Figure 2.7.b showed an example of the plasma and ejection of the ablated surface.

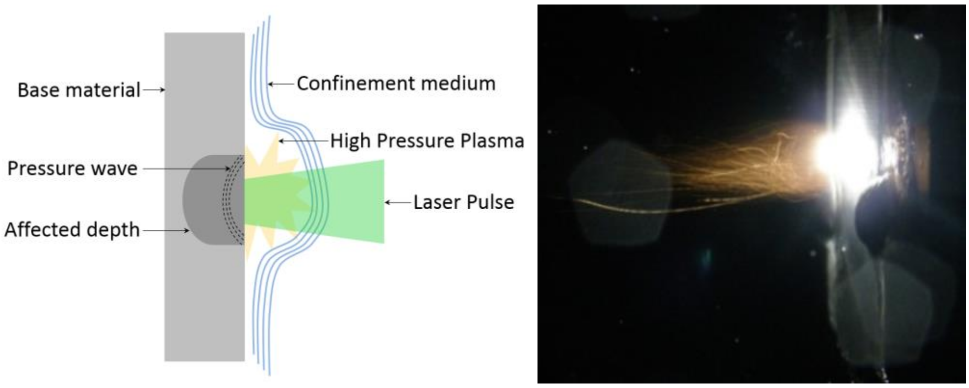

Figure 2.7: (a) Schematic of the laser shock peening process (b) application of laser shock peening

The propagation of the shock wave plastically deforms the material introducing a state of compressive residual stress. The dynamic compressive stress is typically highest near the processed surface and reduces through the depth. However, an associated tensile component of residual stress is induced in the processed patch's surrounding area to maintain equilibrium. The peak compressive stress and transitional depth are dependent on the laser shock peening parameters and material properties and geometry. Figure 2.8 illustrated the typical in-depth residual stress profile created by LSP in various engineering materials. A region of large compressive stress is present near the surface and reduces to a transition depth where the stresses become tensile. The superiority of LSP over that of conventional shot peening is evident, as a substantial increase in the magnitude of the peak stress and affected depth is achieved [23,24].

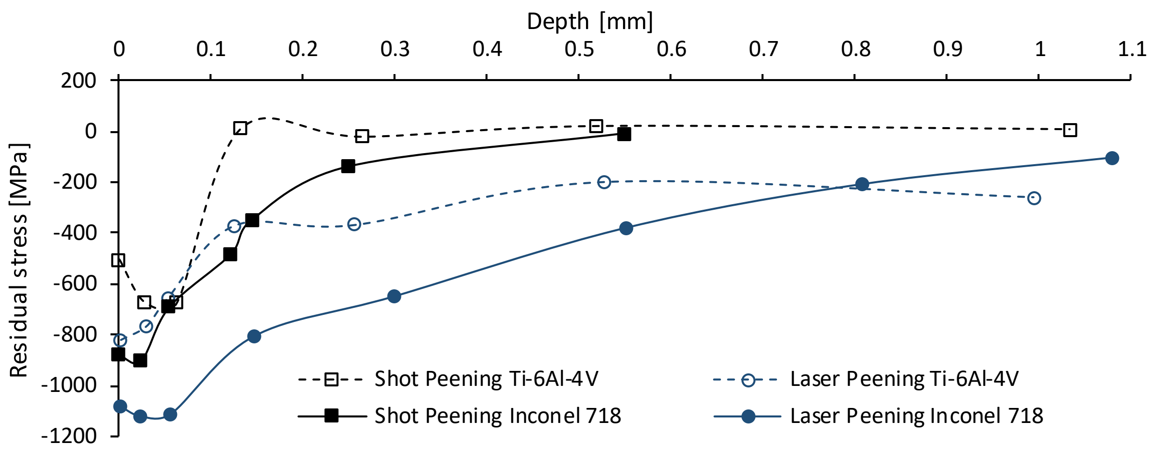

Figure 2.8: Typical laser shock peening residual stress profile in various materials [23,24]

2.2.1. Laser Shock Peening processing parameters

There are several fundamental parameters associated with LSP processing, each requiring to be adequately controlled for achieving an effective result. Power density (I), coverage, traversing speed, percentage overlap, pulse rate of repetition, wavelength and pulse duration are the core parameters associated with LSP. These parameters define the peening intensity and the number of pulse interactions.

2.2.1.1. Laser power density

Laser intensity or power density is the crucial parameter in the delivery of LSP. Typically, LSP applications' power densities range between 1 and 10 GW/cm^2 and are selected based on the processed material's properties. Power density is defined by Equation 2-12, where beam energy (E_{Beam}), pulse duration (τ_p) and beam area (A_{Beam}) are the defining variables in the equation [25].

$$I = \frac{E_{Beam}}{\tau_p \cdot A_{Beam}}$$ *Equation 2-12*

Figure 2.9 indicated that shock pressure or peening intensity is directly related to the power density. This result was specific to a 1064 nm laser pulse with a 25 ns pulse duration [26]. The combination of these parameters, the confinement and sacrificial coating will affect the achievable peak pressure and saturation point or breakdown threshold. Laser-induced dielectric breakdown often occurs at power intensities larger than 10 GW/cm^2. Past this point either the confining medium or air in which the beam propagates becomes opaque to the laser pulse creating a plasma that is not on the target surface. The breakdown plasma will reduce the pulse energy through absorption and can lead to inconsistent LSP processing.

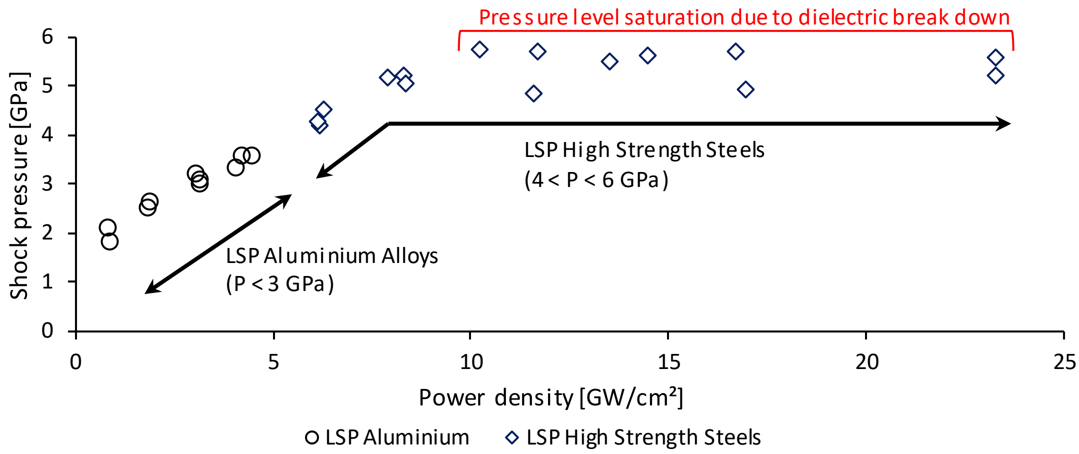

Figure 2.9: Peak shock pressure variation with laser power density with water confinement [26]

During processing, the pressure generated has to overcome the material's dynamic yield strength to cause the deformation required to establish the residual stress [17]. Figure 2.9 indicated that lower strength materials such as aluminium should be processed with power intensities lower than 5 GW/cm^2. Operating within similar parameter ranges is vital for successful peening and preventing adverse effects such as reverse yielding of the material. Stress attenuation and reverse yielding effect will reduce the magnitude and depth of achievable compressive stress. Over-peening can lead to irreversible damage of the target material by exceeding the material's fracture strength or degrading the processed surface, leading to pits and fatigue crack initiation sites [27]. This saturation point is the plastic deformation limit point where the magnitude of the shock pressure becomes greater than twice the Hugoniot Elastic Limit (HEL) of the material. This value is defined by Equation 2-13, where v is the Poisson's ratio and σ_y^{dyn} is the dynamic yield strength of the material.

$$HEL = \frac{1 - v}{1 - 2v}\sigma_y^{dyn} \qquad \textit{Equation 2-13}$$

Figure 2.10 demonstrated the influence of escalating power density on the magnitude and depth of compressive stress induced within aluminium A356-T6 (15 mm thick plate) and A2024-T62 [7,28]. The higher power intensities tended to drive larger magnitude and deeper depths of compressive residual stress. Each of these data sets was achieved with a single impact and at beam diameters greater than 5 mm.

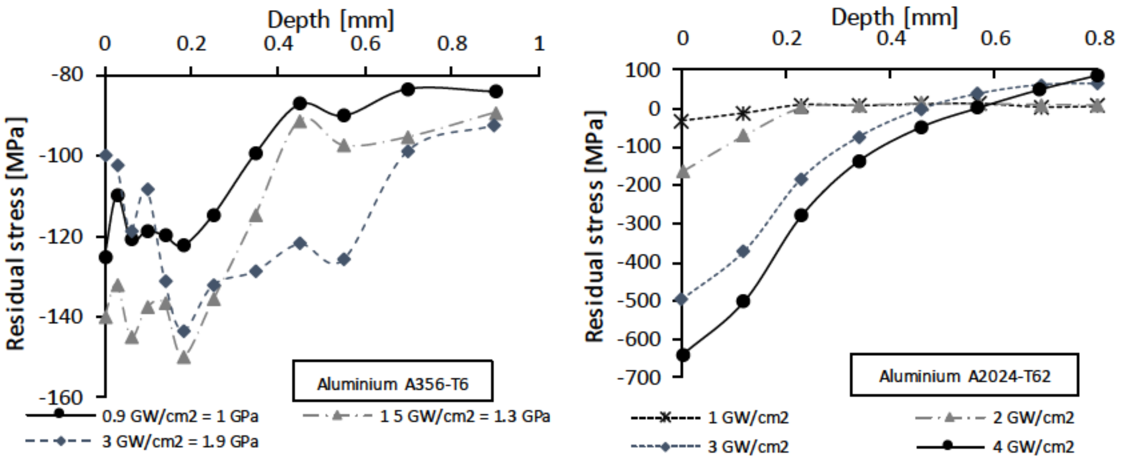

Figure 2.10: Laser shock peening induced residual stress for increasing power density (a) Aluminium A356-T6 [7], *(b) Aluminium A2024-T62* [7,28]

2.2.1.2. Laser beam temporal profile and pulse duration

Nanosecond scale laser pulses form a fundamental element in the rapid formation of the plasma. The pulsed laser's temporal profile defines the time distribution of laser energy over the pulse duration. A characteristic feature of the laser system, the temporal profile effectively defines the plasma's growth during the 'laser on' stage of the LSP process. Figure 2.11 showed this dependency as the measured pulse pressure closely coincides with the laser temporal profile [29]. The majority of the initial laser energy goes towards heating the plasma and increasing the pressure acting on the target surface. Upon completing the pulse, the pressure decays at a much slower rate than the initial heating phase. The mechanics of this event has been discussed further in section 2.2.1.3.

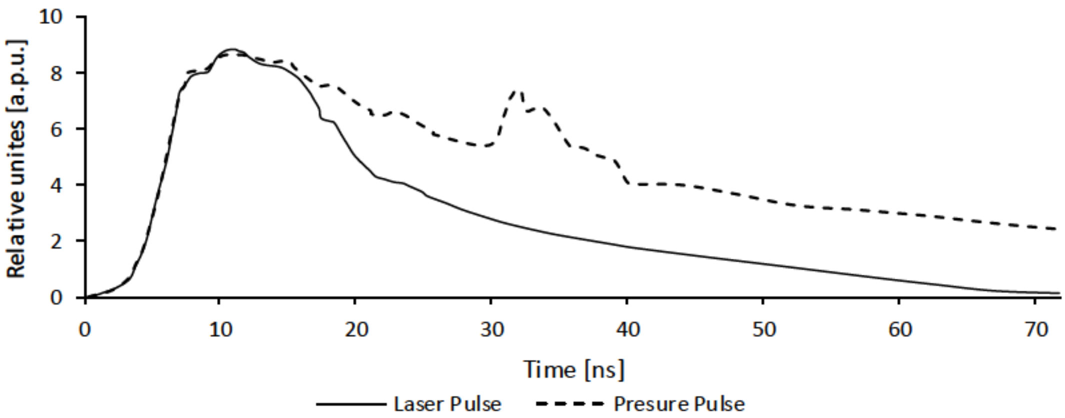

Figure 2.11: Comparison of laser temporal and pressure pulse profiles [29]

Most laser sources used for LSP applications operate with a near-perfect Gaussian or flat top temporal profile shape. Typical LSP laser pulse durations range between 0.1 to 50 ns for shock processing [30]. Figure 2.12 showed the variation in the generated peak pressure with regard to pulse duration [31]. It was shown that shorter pulses generate higher impulse pressures. However, dielectric breakdown (point of ionisation) is dependent on the pulse width as shown by the higher saturation point th at can be achieved with a shorter pulse (approximately 100 GW/cm^2 for 0.6 ns and 10 GW/cm^2 for 10 and 25 ns). This fact should be considered when selecting parameters based on the laser processing duration (femto, pico or nanosecond time scales) [32].

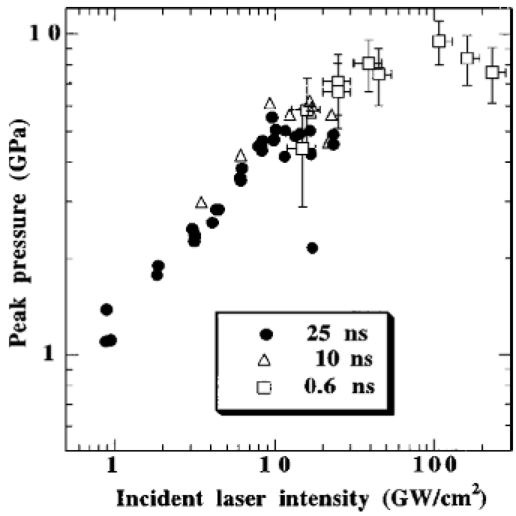

Figure 2.12: Peak pressure variation with power density for pulse durations of 0.6, 10 and 25 ns [31]

Although a shorter pulse produced higher peak pressures, Peyre et al. showed that laser pulse duration (τ_p) has a quasi-linear effect on the affected depth (L_{pl}) [33]. Equation 2-14 provided this relationship in which longer pulses will plastify the material to greater depths due to the extended pressure on the target, causing larger surface displacements. Where C_e,C_p are the velocity of the elastic and plastic waves and P_{max} is the peak pressure caused by the laser pulse and is defined by Equation 2-16.

$$L_{pl} = \frac{C_e C_p \tau_p}{(C_e - C_p)} \left(\frac{P_{max} - HEL}{2HEL} \right) \qquad \textit{Equation 2-14}$$

Figure 2.13 showed that the shorter pulse produced high magnitude compressive residual stresses, but the effects were considerably shallower than the longer pulse, as predicted by Equation 2-12 [34].

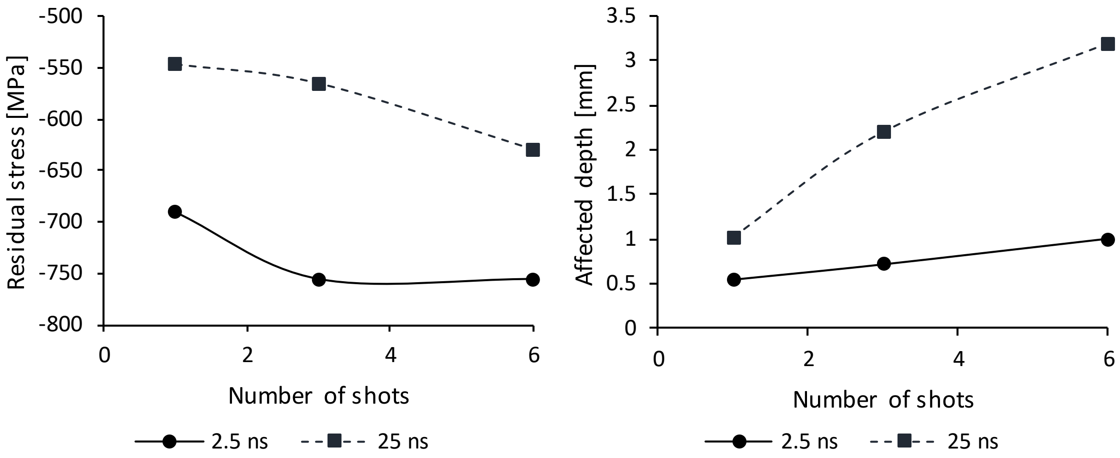

Figure 2.13: Residual stress and effected depth dependence on pulse duration measured in 35CF4 steel specimens [34]

2.2.1.3. Plasma pressure created during Laser Shock Peening

The irradiation and ablation of a solid surface with a focused high-power laser typically creates a high-temperature plasma. The explosion of the plasma generates a mechanical impulse in the solid. In most LSP activities, the laser-material interaction is confined with a transparent medium, which confines the plasma's expansion into the target. The influence of confinement mediums is discussed further in section 2.2.2. The behaviour of the generated plasma can be defined in three stages, as described by Fabbro et al. [35]:

1) During the laser pulse duration (laser on), the energy heats the plasma and creates a shockwave that propagates into the target and confinement medium.
2) After the laser pulse duration (laser off), the plasma still maintains the pressure but will decay due to adiabatic cooling and losses determined by the plasma's work against the confinement material by continued expansion.
3) After the plasma's complete recombination, the heated gas inside the interface expands and adds to the target's momentum.

2.2.1.3.1. Plasma heating phase

Energy from the laser pulse is absorbed to increase the plasma's internal energy and expands the interface between the target material and the confinement medium. The plasma thickness during this phase is defined as $L(t)$. The plasma pressure can be determined through an energy balance of the system that accounts for energy per unit surface deposited by the laser, the internal energy of the plasma, and the work of the pressure force. The final relationship of the plasma pressure $P(t)$, the inclusion of the assumption that the plasma is an ideal gas resulted in Equation 2-15. This equation validates the coincidence of the rise time of the laser intensity and pressure pulse and defines the rate of decay upon surpassing the peak power density of the laser pulse as seen in Figure 2.11.

$$I(t) = P(t)\frac{dL(t)}{dt} + \frac{3}{2\alpha}\frac{d}{dt}[P(t)L(t)] \qquad \text{Equation 2-15}$$

Where $I(t)$ is the power density and α is a constant fraction of internal energy being used to increase the thermal energy of the plasma. Equation 2-15 can be simplified by considering a constant laser intensity (maximum peak value) and is defined by Equation 2-16. The growth of the thickness of the plasma is defined by Equation 2-17.

$$P_{max}(GPa) = 0.01\sqrt{\left(\frac{\alpha}{2\alpha+3}\right)}\sqrt{Z\, I_o} \qquad \text{Equation 2-16}$$

$$L(t) = L_o + \frac{2P_o t}{Z} \qquad \text{Equation 2-17}$$

Where L_o and P_o are the initial thickness and pressure and Z is the shock impedance of the interface between confinement medium and target material, as defined by Equation 2-18 [36].

$$\frac{2}{Z} = \frac{1}{Z_{confinement}} + \frac{1}{Z_{target}} \qquad \text{Equation 2-18}$$

2.2.1.3.2. Adiabatic cooling of the plasma

The laser pulse ends (laser off) at the pulse duration, τ_p. As no additional energy is added to the system, the plasma loses energy through adiabatic cooling to the surroundings. The plasma thickness and pressure at the end of the laser on stage is defined as $L(\tau_p)$ and $P(\tau_p)$. The pressure during the cooling stage is characterised by Equation 2-19.

$$P(t) = P(\tau_p)\left(\frac{L(\tau_p)}{L(t)}\right)^{\gamma} \qquad \text{Equation 2-19}$$

Where γ is the adiabatic cooling rate, the plasma thickness is defined by Equation 2-20.

$$L(t) = L(\tau_p)\left(1 + \frac{(\gamma+1)}{\tau}(t-\tau_p)\right)^{1/(\gamma+1)} \qquad \text{Equation 2-20}$$

Fabbro et al. estimated from Equation 2-19 that the pressure at the end of the heating stage decreased to half its value at time 1.8 τ_p. The prolonged decay of the pressure is an incident of the presence of the confinement medium. Without the confinement, the pressure would quickly dissipate.

The final stage defining the plasma behaviour does not affect the plastic deformation as the pressure has decayed to a level below the elastic limit of the material. The target and confinement material will increase the momentum, but this will not affect the introduced residual stress.

Figure 2.14 provided an example of the analytically determined pressure distribution based on Fabbro confinement model. A ramped flat top temporal profile characterised the energy delivery to the target. The HEL for AA2024-T351 has been indicated in the figure to indicate the magnitude of the generated pressures. The slightly larger fixed pressure estimation was determined based on Equation 2-16. It should be noted that the plasma pressure is many times longer than the incident laser pulse duration.

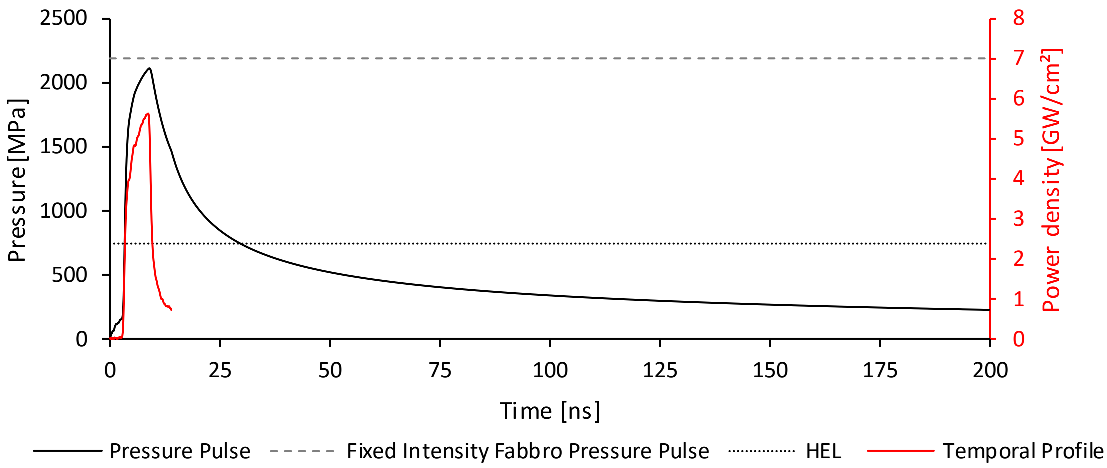

Figure 2.14: Confined ablative plasma pressure distribution, α – 0.1 and γ – 1.2

2.2.1.4. Laser spot size

The beam size is a crucial LSP parameter and is often dependent on the laser system's operating capability and the optical setup of the system. With reference to Equation 2-12, the beam incident size directly influences the power density. Typically, the spot dimension is selected to achieve the desired power density within the laser's available energy output.

The spot size directly influences the shock wave propagation, the attenuation rate, magnitude and depth of compressive stress introduced during LSP [17]. In a study by Fabbro et al., the effect of the spot diameter (1.5 mm and 5 mm diameter) was investigated on shockwave propagation behaviour in 55C1 steel. With a smaller diameter, the shock wave expanded like a sphere, with an attenuation rate of $1/r^2$. The larger diameter shock wave behaved more as a planar wave that attenuated at the rate of 1/r. This result indicated that energy attenuation rates were less for larger spot diameters, allowing the wave to propagate deeper into the material [30]. Implying that larger spot sizes can plastically affect the material to greater depths due to the larger shock front. Figure 2.15 showed the LSP parametric study results conducted on 1.9 mm thick AA2024-T351, whilst maintaining the power density and varying spot sizes. Figure 2.15.a showed that the various spot sizes resulted in similar magnitudes of compressive stress. However, the zero-depth (the depth at which the stress transitions from compression to tensile) was increased and higher balancing tensile stresses were associated with the larger spot geometry [37]. Figure 2.15.b showed that this trend holds for different coverages.

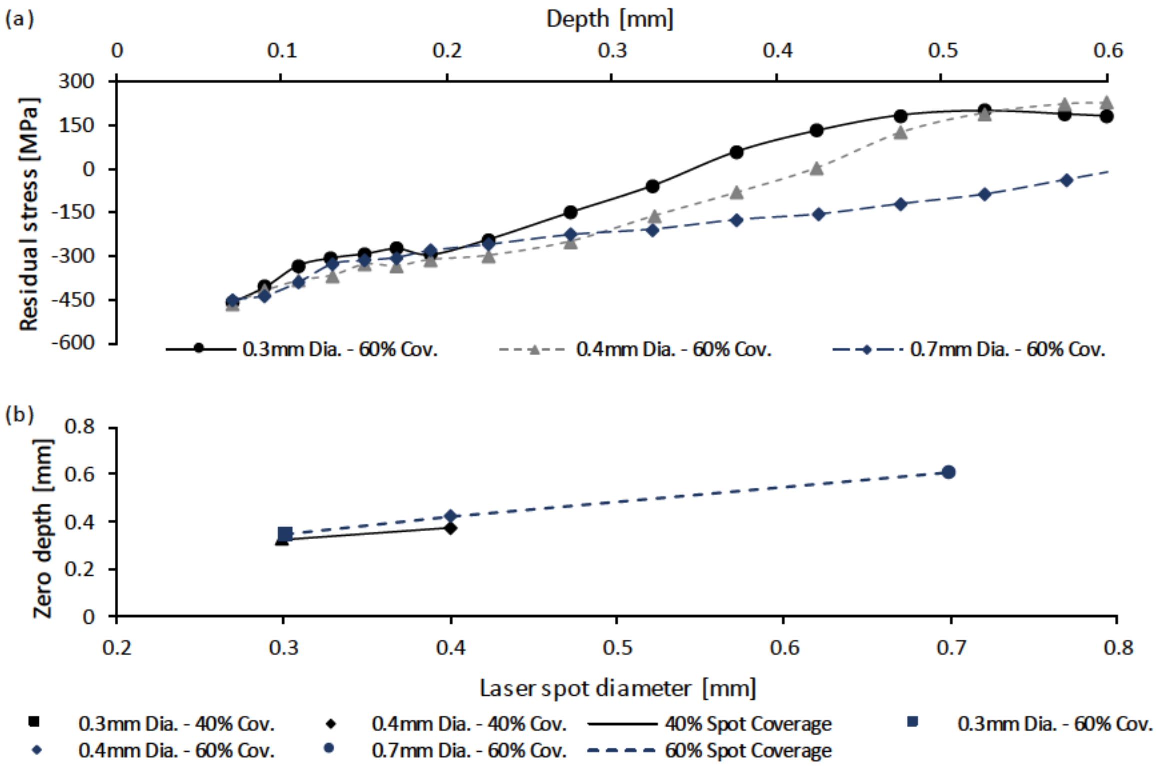

Figure 2.15: Effect of spot size on the formation of residual stress (a) constant coverage with varying spot size (b) variation of zero-depth residual stress in aluminium alloys [37]

Across all shot diameters (from 100 μm to 10 mm) surface modifications are similar. However, the affected depth tends to drastically decrease with impact sizes of less than 1 mm [30]. The decrease was due to the 2D shock wave attenuation in-depth [7]. It should be noted that even with spot sizes of a few hundred microns, LSP had a higher plastified penetration depth than that of shot peening.

2.2.1.5. Beam geometric shape and spatial profile

Circular and square laser pulse geometries are the most commonly used in applications of LSP. The geometry of the spot is a general feature of the construction of the laser system. The spot geometry can influence the formation of the residual stress in the component during LSP. This is because the response of the target material is very complex due to the interaction of numerous propagating stress waves created during peening. A particular shortcoming of shock-induced residual stress fields is that they are not uniform over the spot. For example, lower residual stress occurs at the centre of the spot compared to the interaction area's extremities, as indicated in Figure 2.16 [38]. This result was determined in 1045 steel of an unknown sample thickness.

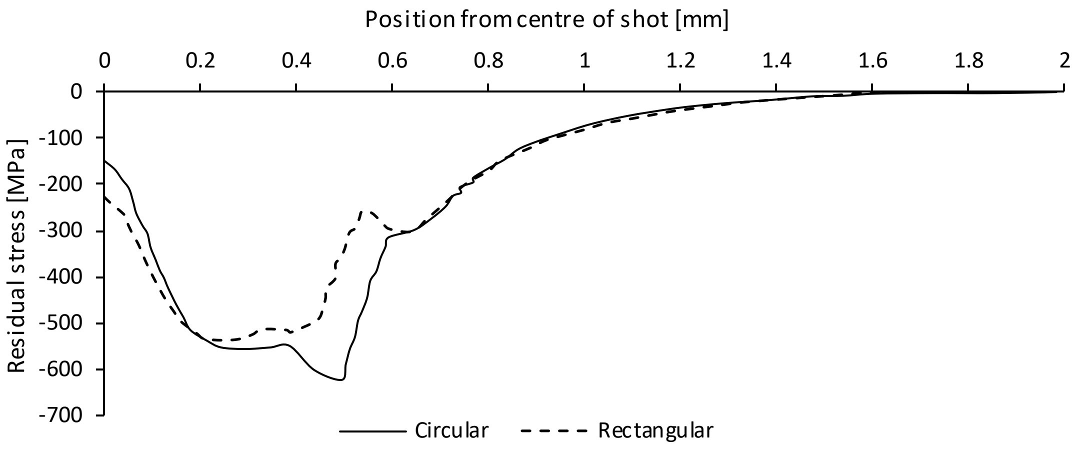

Figure 2.16: Distribution of residual stress across a uniform laser shock peening impact [38]

A possible cause of this non-uniformity is attributed to a surface release wave induced by the impact [7]. Peyre et al. described the generated shock wave system as having two components: an elastic component (peak stresses below the HEL of the material) and an elastic-plastic component (peak stresses above the HEL limit). The elastic wave has a higher velocity than the plastic wave and was known as the elastic precursor. Due to the mismatch in velocities, the shock pressure was reduced by a high-velocity elastic recoil wave from the back free surface. This interaction of the elastic surface release wave causes a drop in stress at the spot's centre. Additionally, Figure 2.17 illustrated the lateral release wave generated at the LSP spot parameter that focuses towards the shock centre, exacerbating the residual stress drop. However, as there was no focusing point for the square laser geometry this reduced the residual stress drop caused by the propagating shock's interactions [38].

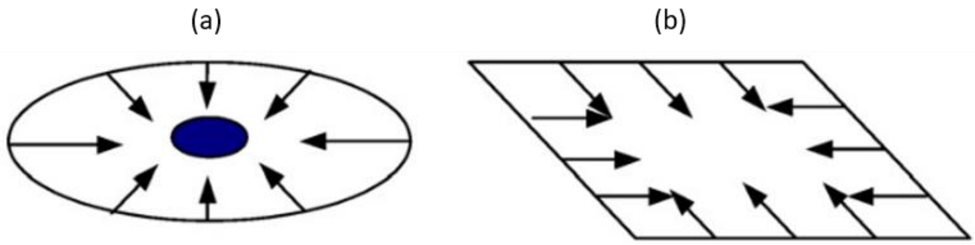

Figure 2.17: Propagation direction of stress wave from the edge of the laser peening spot geometry (a) circular spot geometry and (b) square laser pulse geometry [38]

The laser pulse cross section's spatial energy distribution provides a two-dimensional variation of the laser intensity. The characterisation of the laser pulse's spatial features is necessary as it can significantly affect the LSP residual stress field uniformity. Figure 2.18 showed the experimentally determined local peak pressure of the plasma and the laser intensity along the laser spot radius [30]. The magnitude of the local plasma pressure is directly related to the pulse's spatial distribution. Most commercial LSP providers attempt to provide a uniform spatial distribution to prevent local variations in intensity, but this requires close control of the laser parameters and a high-quality laser and optical system.

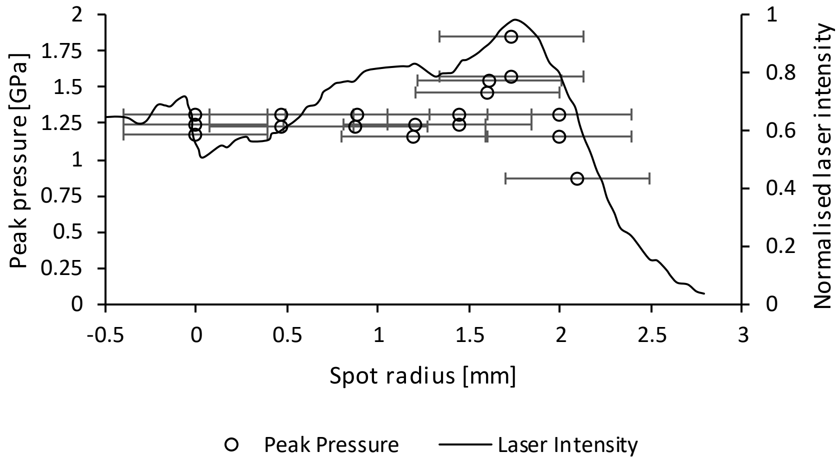

Figure 2.18: Comparison of the spatial profile of laser intensity and local peak plasma pressure [30]

Figure 2.19 provided examples of the measured spatial energy variation of a Gaussian beam and Flat Top beam, the pulse energy was varied from 3 to 5 J per pulse [39]. Li et al. determined that a Gaussian spatial distribution induced a higher and deeper compressive residual stress field than the Flat-Top distribution. The Gaussian pulse produced a peak pressure 1.5 times greater than the flat-top distribution, increasing the laser-induced shockwave strength and plastic deformation. This was due to the Gaussian pulse distribution temperatures are higher and have the tendency to create less colder interaction compared to a flat-top beam.

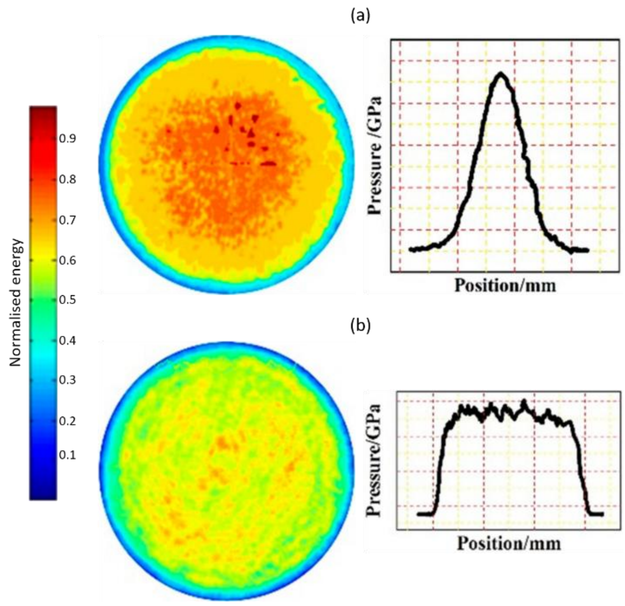

Figure 2.19: Spatial variation of laser energy of different laser shock peening pulse (a) Gaussian distribution and (b) flat-top distribution [39]

Several researchers have attempted to estimate the spatial variations of the plasma pressure in FEA analyses of LSP with different spatial shapes by tailoring the applied pressure according to the equations listed in Table 2.2. In all equations, R_{pulse} is the total spot radius and x, y, r are the local positions where the pressure is being determined.

Table 2.2: Spatial variations of simulated plasma pressure

Laser Spatial Shape	Pressure Variation	Reference	Equation
Gaussian	$P(r) = P(t)\exp\left(\frac{-r^2}{2{R_{pulse}}^2}\right)$	[39]	*Equation 2-21*
Gaussian	$P(r) = P(t)\sqrt{1 - \frac{1}{2}\left(\frac{x^2 + y^2}{r^2}\right)}$	[40]	*Equation 2-22*
Quasi- Gaussian	$P(r) = P(t)exp\lfloor -2.5(x^2 + y^2)/{R_{pulse}}^2 \rfloor$	[41]	*Equation 2-23*

Le Bras et al. characterised the LSP pulse's spatial distribution using a diffractive optical element, which allowed for the extraction of the intensity profile across the 3-mm laser spot, as shown in Figure 2.20 [42]. The laser intensity distribution is represented by the magnitude of the image pixel intensity. A spatial scaling factor representative of the laser distribution can be achieved by normalising the local pixel intensity by the peak image intensity.

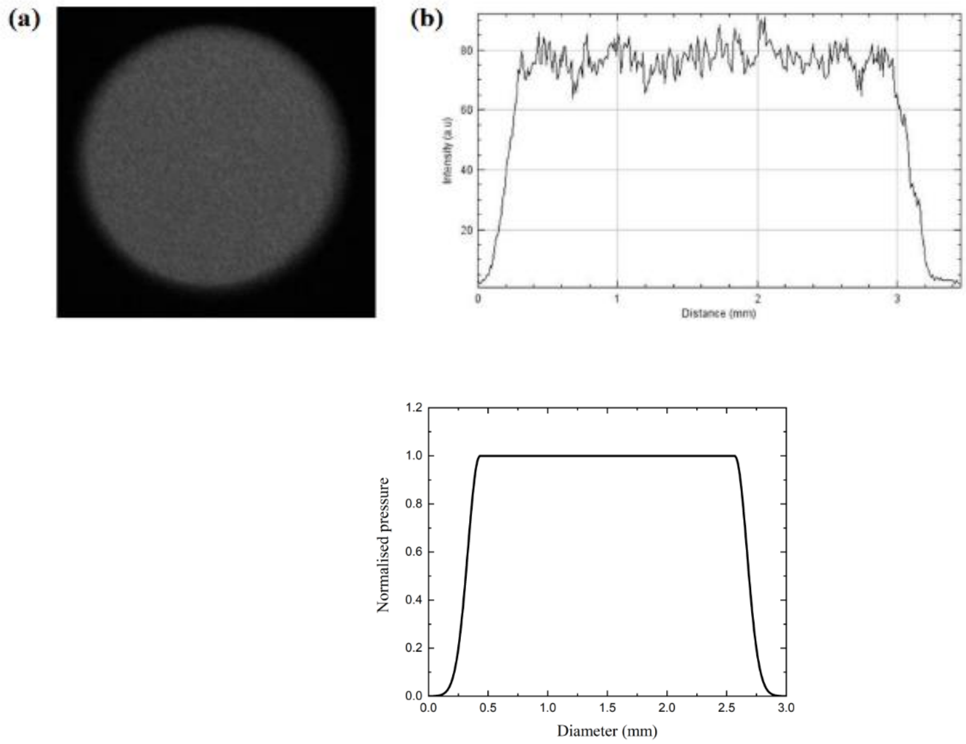

Figure 2.20: Spatial measurement of laser intensity across a circular laser shock peening pulse [42]

2.2.1.6. Processing coverage and overlap

Most engineering applications of LSP are on components that are orders of magnitude larger than a single laser spot. Several sequentially overlapping laser shots are used to cover the desired area of a component. The accurate synchronisation of the laser pulses allows for precise placement of the sequential shots on the target medium. A general X-Y raster pattern is the most common processing pattern for LSP applications, and an example of this pattern is provided in Figure 2.21.

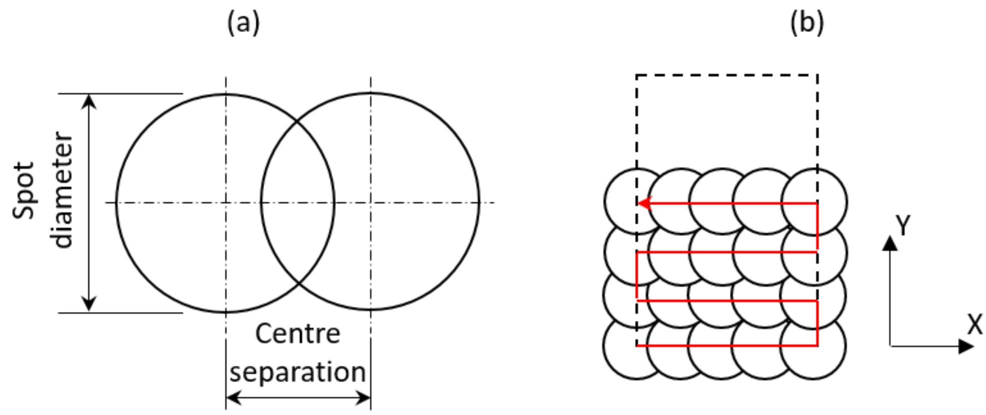

Figure 2.21: (a) Schematic representation of percentage overlapping of the laser spots, (b) typical x-y raster laser beam path used for laser shock peening

The response of a material to process overlap and coverage is highly dependent on its mechanical properties, but there are clear benefits to increasing the coverage. An increase in the number of impacts tends to drive the compressive residual stress field deeper into the material's thickness. Figure 2.22 demonstrated an increase in the compressive residual stress depth in 0.5% carbon steel with an increase in LSP shots [43].

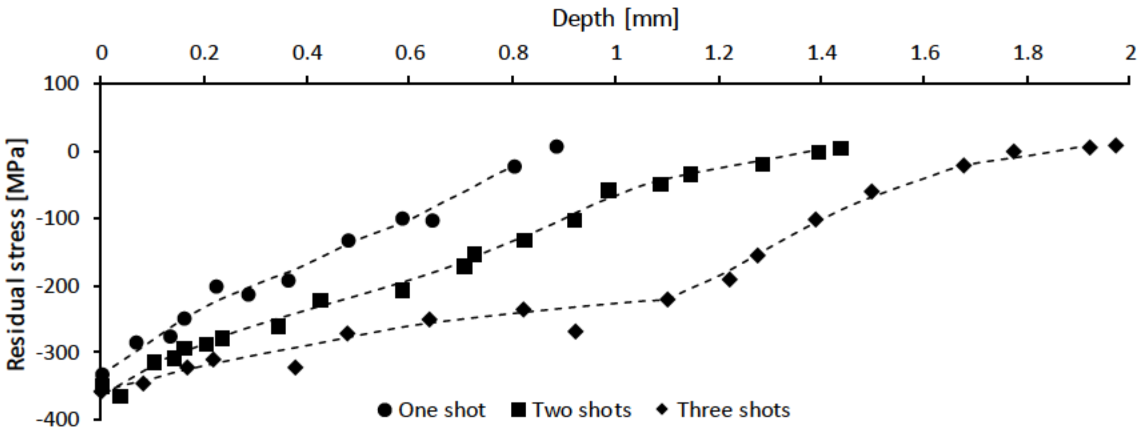

Figure 2.22: The effect of an increased number of laser shock peening shots on 0.55% carbon steel [43]

The application of multiple laser spots or layers tends to increase the uniformity of the introduced residual stress field as the tensile stress in the peened spot's centre was alleviated. Figure 2.23 showed that the first layer's tensile residual stress at the surface was entirely removed by the second offset layer of LSP [44]. Caution should be applied when selecting appropriate coverage as over-peening can quickly occur, and although surface tension may be alleviated, the detrimental tensile residual stress will form elsewhere, as seen in the depth of layer two which had the highest predicted tensile residual stress in the core of the material.

An additional limiting factor for selecting the laser spot separation or coverage in a single layer was the damage threshold of the thermal protective coating. Ablative coatings are used to maintain the surface integrity of the peened surface. These coatings are typically some form of thin laser-opaque tape that is applied to the target surface. High overlapping coverage of sequential shots will tend to degrade the integrity of the various tapes which can fail, leading to flow disruptions in the confinement medium and thermal tensile residual stresses in the near-surface of the peened samples.

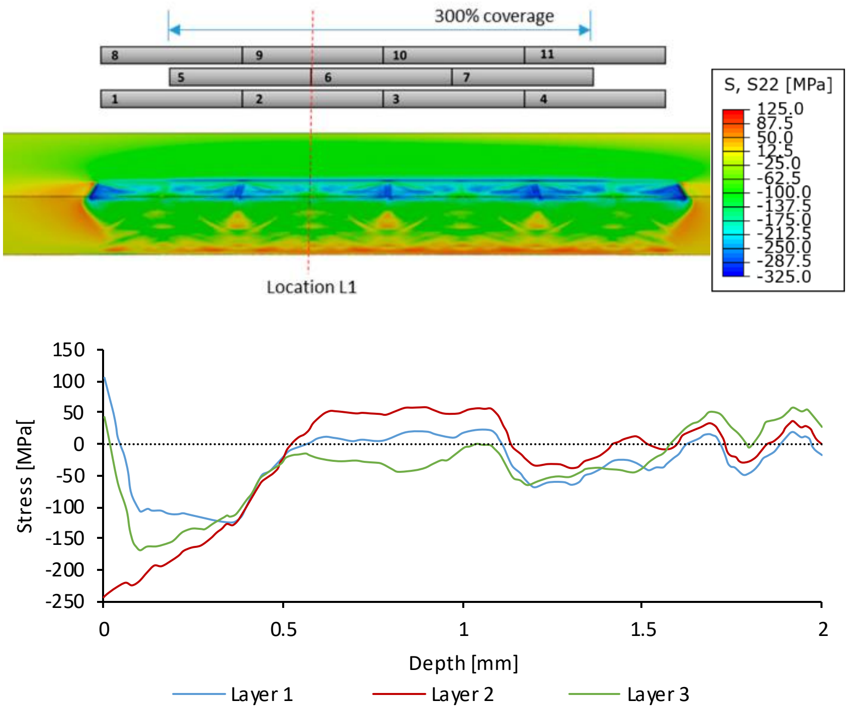

Figure 2.23: Effect of peen layering on predicted in-plane residual stress in thin sections [44]

2.2.1.7. Effect of protective coatings

To preserve the component surface's integrity, a sacrificial coating formed part of the initial conception of the LSP process. This removable thermal ablative coating protected the target surface resulting in a pure cold working process or mechanical process [45]. The plasma is generated upon the ionisation of the opaque coating. The shockwave propagates through the coating and into the target material whilst maintaining the general surface quality.

In certain instances, applying thermal coatings is not feasible as in the LSP processing of in-service nuclear reactors or applications of very low energy LSP [46]. This form of peening is known as Laser Shock Peening without Coating (LSPwC). In this case, the plasma is formed through the ionisation of the target surface. Thermal heat is conducted into the material as the shockwave develops causing a combined thermomechanical process. The thermally affected zone is typically a few microns thick near the processed surface. Figure 2.24 indicated the main effects and differences between these types of LSP processes [47]. During irradiance of the target surface without insulation from the thermal effects, peak temperatures can reach as high as 20,000 K over a few microseconds. The resulting thermal effects are typically within the first 50 µm, with an additional tensile residual stress affected the depth of 50 µm caused by the process's mechanical component [47,48].

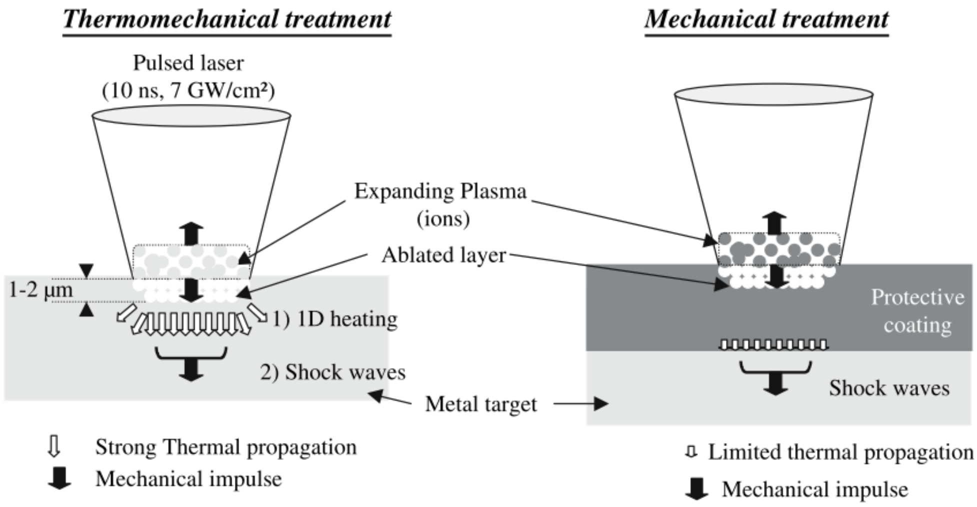

Figure 2.24: Schematic comparison between thermomechanical and mechanical laser shock peening [47]

Figure 2.25 (a-b) Ti 6Al-4V [49,50] and (c) Aluminium alloy 2524-T351 [51] showed to post-LPS surfaces in various materials when an ablative coating was used. Clear indentations can be seen where the laser shots have been applied. The clarity of the spot is dependent on the laser parameters and material properties. There are no indications of surface modifications associated with ablation, reiterating that LSP with a coating was a purely mechanical cold-working process.

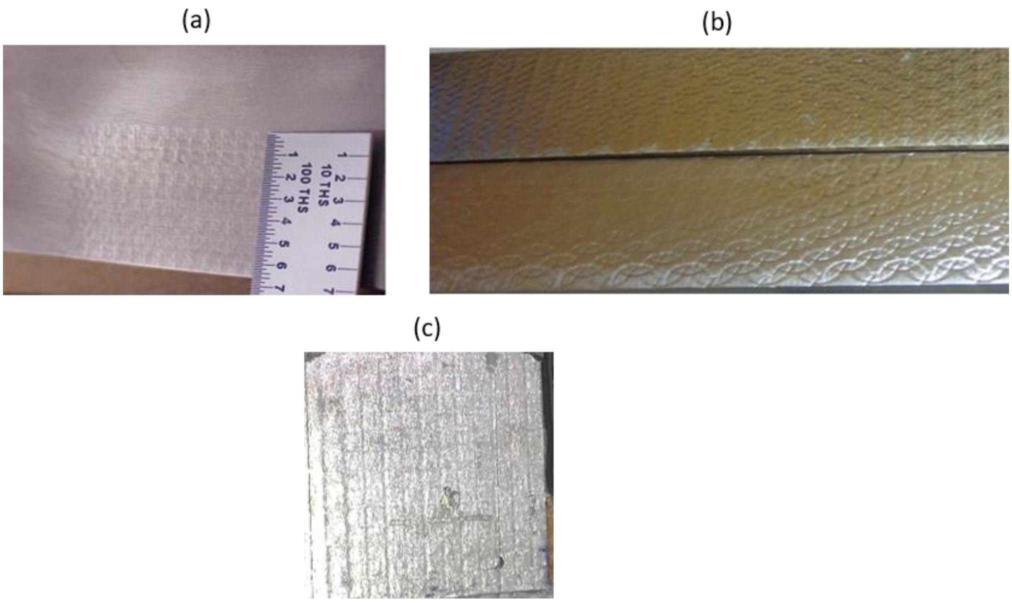

Figure 2.25: Examples of laser peening surfaces with a protective coating (a-b) Titanium 6Al-4V, (c) Aluminium alloy 2524-T351 [49–51]

Direct irradiance of the target surface results in a visible modification of the surface due to the surface's direct ablation. Figure 2.26 provided examples of the surface modification caused by the direct ablation during LSPwC. The darkened surface in Figure 2.26.a was attributed to the formation of an oxide layer caused by a reaction between the surface and the nascent-state oxygen supplied from the decomposition of the water during plasma formation [52]. Figure 2.26.d showed the 2-3 µm thick oxide surface that formed as a combination of ablation and melting of the original surface [47].

Many shots or high overlap are often required with LSPwC to obtain an even residual stress profile. A higher number of impacts leads to increased surface ablation and subsurface (>5 µm from the processed surface) damage of the material structure. Figure 2.26.c. provided an example of the cross-section of AA6082-T651 with higher coverage, an apparent increase in crater depth (peak to peak height) was observed [48]. In all cases of LSPwC, a suitable depth of compressive stress can be achieved. However, surface modifications should be accounted for in any fatigue dependent application.

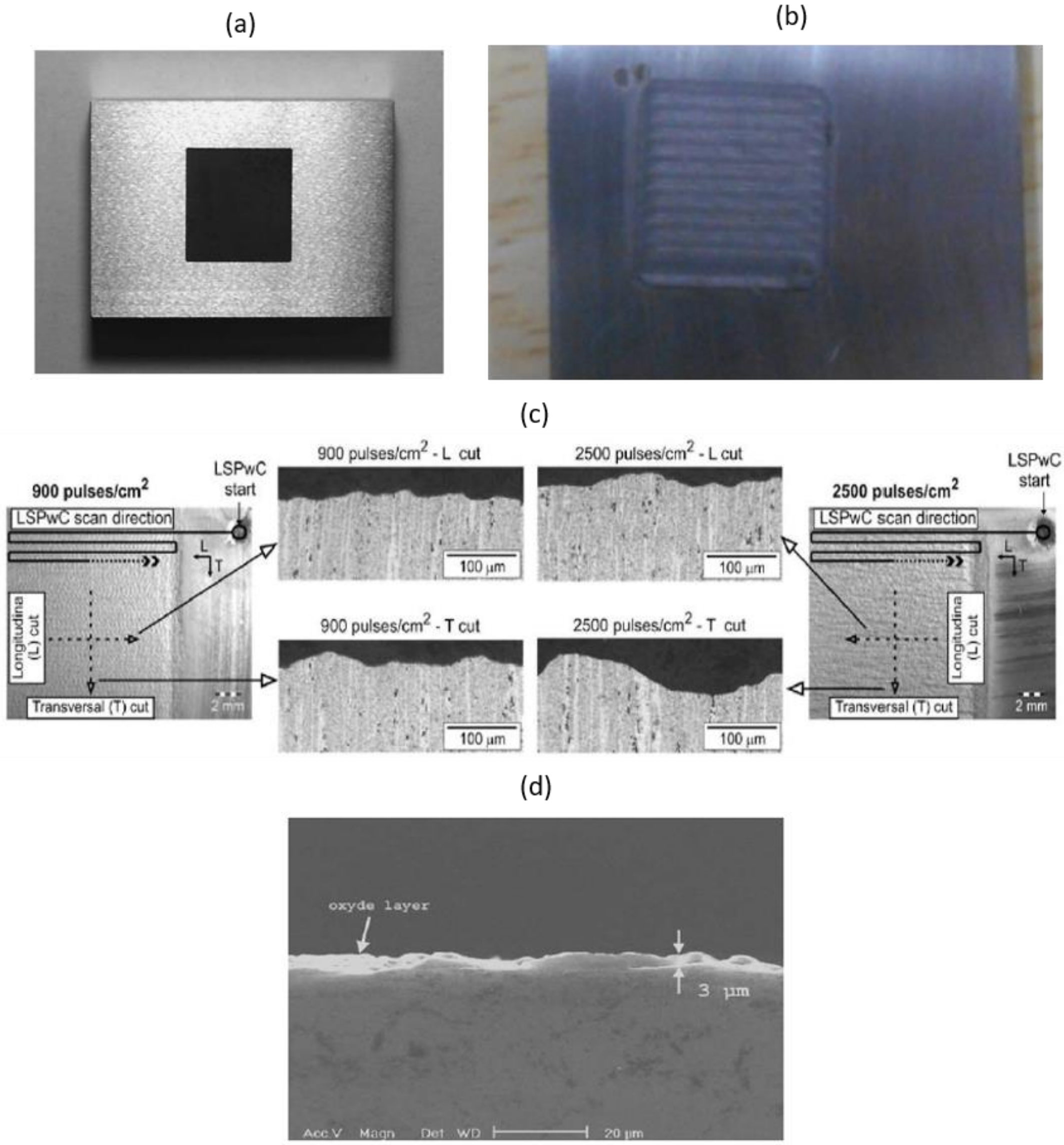

Figure 2.26: Examples of laser peening without coating (a) SUS304 stainless steel [52], *(b) 17-4 PH stainless steel* [53], *(c) cross-section of ablated surfaces with varying coverage on aluminium alloy 6082-T651* [48], *(d) example of a thin oxide layer that is formed during direct laser shock peening irradiance of 316L stainless steel [47]*

2.2.1.8. Influence of component thickness on induced laser peening residual stress

Component thickness can greatly influence the induced residual stress magnitude and affected depth caused by LSP processing. This is largely due to how the shockwave propagates through the thickness of the sample and interacts with the reflected waves from the opposite surface. With the consistent LSP processing parameters and varying the sample thickness from 1.6 mm to 10 mm, Nobre et al showed that a significant reduction in the magnitude of the LSP compressive residual stress occurs when the thickness of the treated specimen is decreased. The LSP affected depth was approximately 1 mm and increased with sample thickness, as seen in Figure 2.27 [54]. The residual stress profiles shown in Figure 2.27 were measured along the stepping direction of the LSP processing.

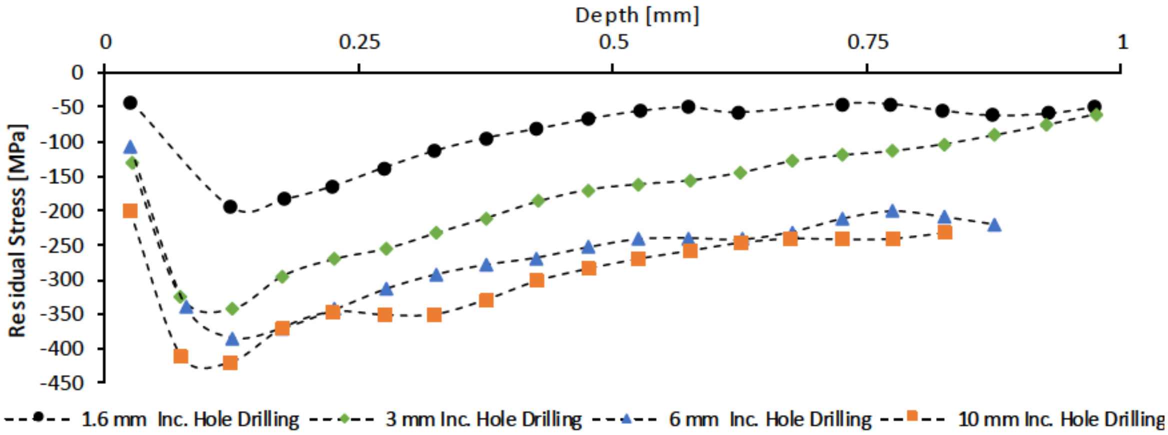

Figure 2.27: Influence of sample thickness on induced residual stress by laser shock peening with consistent processing parameters (a) comparison of residual stress indicating an increase in the magnitude of compressive stress [54]

Fitzpatrick et al. validated the above findings in the simulation of the response of LSP induced residual stress in a 2 and 10 mm thick plate. For a constant LSP pressure of 2.5 times the HEL (single square LSP spot of 5x5 mm^2), the common tensile residual stress near the centre of the LSP spot was present in the thin section and initially removed in the thicker section. Additionally, the maximum compressive residual stress in the thicker section was almost a factor of two times more compressive than that of the thinner sample, as shown in Figure 2.28. The cause of this behaviour was due to the thicker sample not experiencing stress reversal from the reflected wave [44].

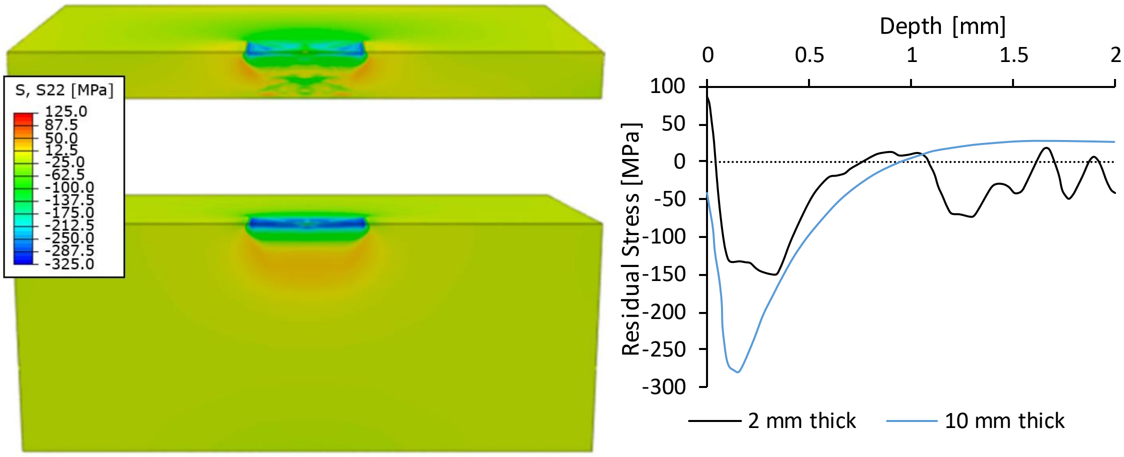

Figure 2.28: Influence of sample thickness on the predicted in-plane residual stress [44]

2.2.2. Laser Shock Peening confinement media

The transparent confinement layer shown in Figure 2.7 is fundamental in the success of LSP over all other cold working processes. Ideally, this layer is entirely transparent to laser irradiation and works to increase the magnitude of the plasma pressure pulse on the target. Figure 2.29.a illustrated the need for the containment of the rapid expansion of the plasma. Under an air confinement regime, the plasma quickly expands away from the target surface, resulting in little pressure loading [55]. In Figure 2.29.b the water layer's incompressible nature resists the expansion, intensifying the pressure pulse and extending the effective duration by a factor of 2-3. This implied that higher peak pressures were achieved by prolonging the plasma with the water confinement [35]. As stated in section 2.2.1.2, the longer pulse duration adds additional energy to the plasma, significantly increasing the peak pressure. The dielectric breakdown limit of water confinement was shown in Figure 2.29.b., as the peak pressure tended to plateau for power densities larger than 10 GW/cm^2. Figure 2.29.b. showed that it was possible to achieve peening pressures of a few hundred MPa, however, this was achieved with a very small spot area. This is relatively ineffective as an industrial process as it would negatively influence the time required to process a standard engineering component which is typical of a few mm in size.

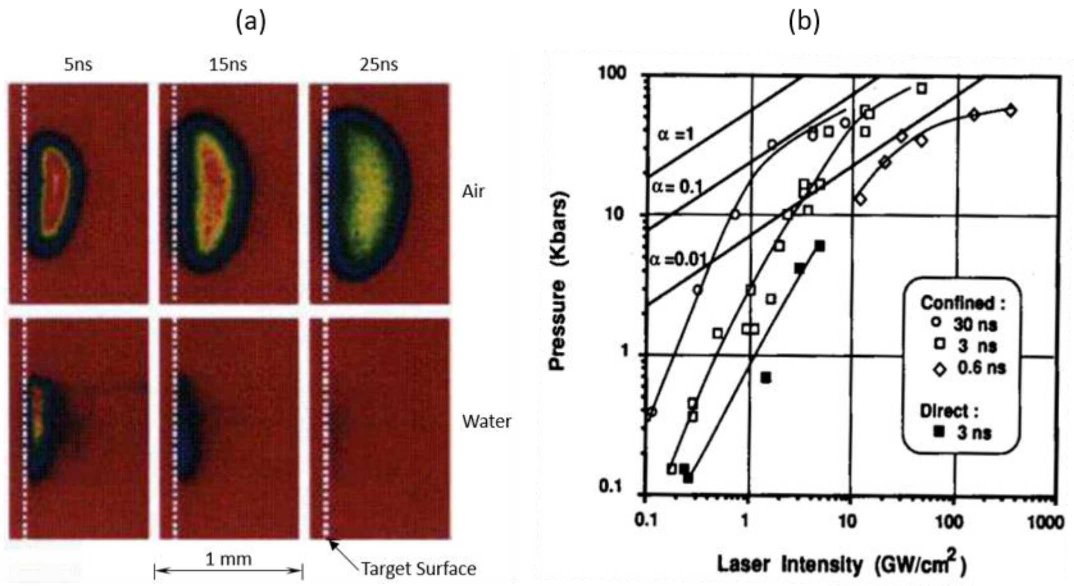

Figure 2.29: (a) Plasma expansion with water and air confinement regimes [55]*, (b) effect of confinement on peak pressure* [35]

During the initial conception of the process, solid media such as silicon rubber, acrylic plastics and various grades of glass were used as confinement media [22]. Deionised water has been used extensively in the LSP industry as it is exceptionally cheap, generally conforms to the contour of the target surface and is easily accessible. However, numerous drawbacks such as water contamination, splashing (as seen in Figure 1.1), and difficulties maintaining desired layer thickness have been identified as hindrances for the process. Flowing water in the vicinity of electrical systems and corrosion sensitive components is a significant restriction to the total uptake of onsite applications and assembly lines.

The preceding sections of this chapter have made clear the need to confine the LSP event. Equation 2-15 relates the strength of the pressure pulse to the combined interface acoustic impedance (Z). The acoustic impedance describes the amount of resistance the material provides to a propagating wave, as stated in Equation 2-24.

$$Z = \rho \times C \qquad \text{Equation 2-24}$$

Where ρ is the density of the material and c is the speed at which sound travels in that material.

Table 2.3 listed examples of alternative solid confinement media used for LSP activities. It must be noted that these media were used in single LSP shot events only. The higher impedance tends to increase the shock pressure thus the magnitude of the material deformations. The target surface's absorption ability of the laser light was increased by applying a layer of black paint to the target surface, increasing the absorbance of the surface. The overlaying paint addition increased the shock amplitude for Perspex by approximately 192%, K9 glass 24%, quartz glass 20% and Pb glass by 40% [36].

Table 2.3: Summary of measured shock pressures for various confinement media [36]

Confining Medium	Density [g/cm^3]	Acoustic impedance [$10^6\ g/cm^2s$]	Black paint overlay		No paint overlay	
			Power density [GW/cm^2]	Peak pressure [GPa]	Power density [GW/cm^2]	Peak pressure [GPa]
Perspex	1.18	0.32	0.74	1.11	0.84	0.38
Silicon rubber	1.10	0.47	0.74	1.35	0.8	0.61
K9 glass	2.51	1.14	0.68	1.66	0.72	1.59
Quartz glass	2.20	1.31	0.76	1.66	0.72	1.39
PB glass	3.10	1.54	0.9	1.93	0.75	1.38

2.2.2.1. Comparison of confinement media on mechanical properties

In the results produced by Ye et al., BK7 glass was used as the confinement medium for the LSP of AISI 4140 steel. The beam diameter was set at 1 mm, with an overlap ratio of 75%. The power density was varied from 0.5 to 4 GW/cm^2 [56]. Ye et al. attempted Warm Laser Shock Peening (WLSP): this was a variation of the standard LSP process by pre-warming the target surface to temperatures above the boiling point of water. Figure 2.30 and Figure 2.31 provides a comparison between the BK7 and water confinement media. Figure 2.30 showed that the peak residual stress for both materials is similar for all tested power intensities. This fact was in opposition to the idea that higher peak pressures are achieved with more dense materials. A possible explanation for the equivalent peak pressures was that the material may incur damage from sequential laser shots. This will degrade the energy throughput and the efficiency of the LSP process. The BK7 glass was reported to have fractured at intensities above 4 GW/cm^2, limiting the useable process parameters.

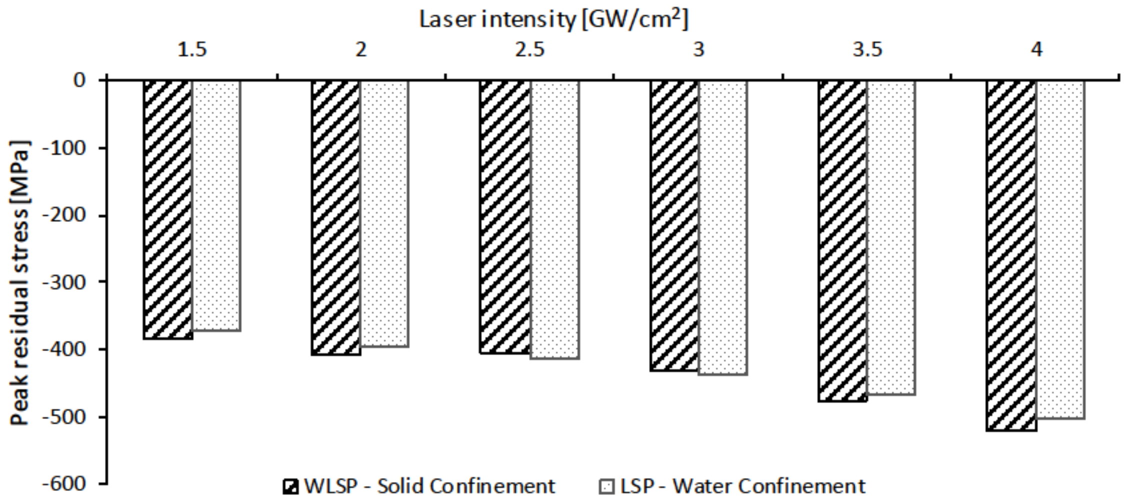

Figure 2.30: Comparison of peak residual stress achieved with various confinement regimes [56]

Figure 2.31 showed that the measured residual stress profile in the depth of the material for both confinements are similar. This would be expected based on the comparative peak pressures displayed in Figure 2.30. The maximum variation in compressive stress was approximately 4% at a power density of 4 GW/cm^2, which could have been considered to be within the experimental scatter of the measurement. Ye et al. noted that the maximum compressive stress increased with power density for both mediums, a trend confirmed by Peyre et al. with only water confinement [57].

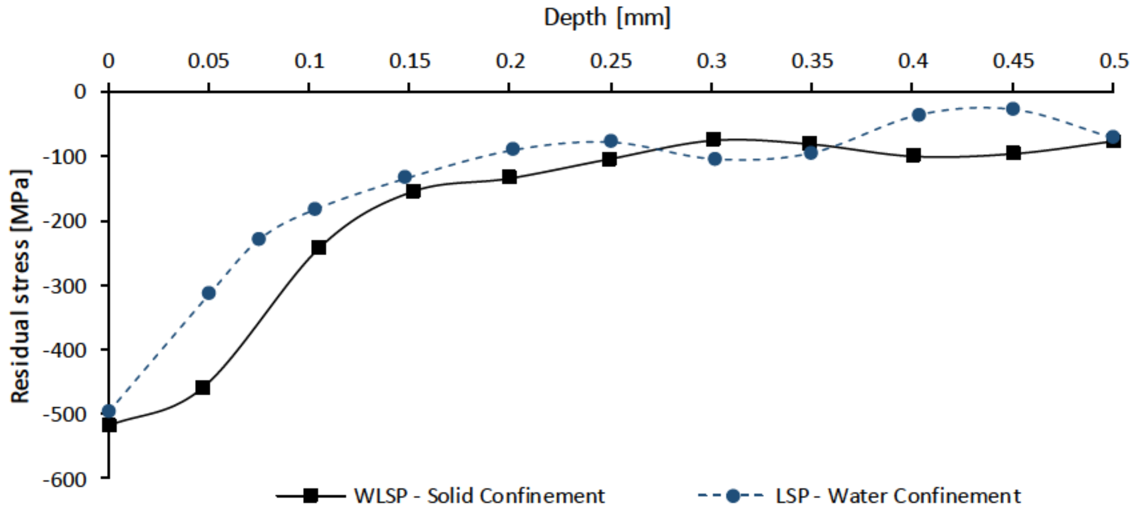

Figure 2.31: Through thickness residual stress profile with various confinements at 4 GW/cm² [56]

Ye et al. showed that the residual stress results achieved with the two confinement strategies were fairly similar, with the deviation in results likely influenced by the experimental uncertainties. To date, the shift away from solid confinement overlays to deionised water was due to the higher associated costs of LSP processing with solid media. In addition, solid overlays do not adhere to the contour of complex three-dimensional components.

2.2.3. Laser Shock Peening finite element modelling

Researchers have made numerous attempts to develop accurate FEA models capable of predicting the LSP process's effects (residual stress, deformation). Complications from accurately representing laser-target interaction, plasma formation, shockwave dynamics and material response make it extremely difficult to achieve a full FEA simulation of the process in its entirety. Due to these factors, two main simulation strategies are currently implemented to predict the induced LSP residual stress.

2.2.3.1. Pulse-by-pulse Laser Shock Peening simulation

Modelling the laser shock peening process by simulating each laser spot or a representative number of spots has significantly evolved from the initial 3D LSP simulations completed by Braisted and Brockman [58]. A significant amount of research has been undertaken to develop accurate prediction methods that provide a clearer understanding of the dynamics of the LSP residual stress field and how they can be used. The remainder of this section will review notable published studies whilst addressing the significant aspects of simulating an LSP event [44,58–65]. These published works were all based on different laser peening parameters and materials restricting a direct results comparison. However, the particular methods of the simulation techniques have been described in greater detail in the following sections. In all reported cases, the models are typically validated based on experimental residual stress measurements of the induced LSP. In some cases, the model validation was achieved by matching the residual stress and surface deformation of a single LSP event.

2.2.3.1.1. Computational model

The current FEA trend in all cited works represents the single LSP event by two distinct computational steps. Braisted and Brockman pioneered this as they used an explicit-implicit (dynamic-static) modelling procedure to solve the resulting residual stresses. Figure 2.32 provided an example of the two-step (explicit-implicit) LSP analysis procedure [58]. Explicit analyses should be adopted for the LSP event's pulse phase as this code can accurately account for the shock wave propagation and the dynamic response of the material. Once the model's dynamic stress state becomes approximately stable, an implicit solver can compute the transient stress state determining the residual stress field and the spring-back deformation in achieving static equilibrium. Several authors have successfully implemented this method in recently published research [40,58–60,62].

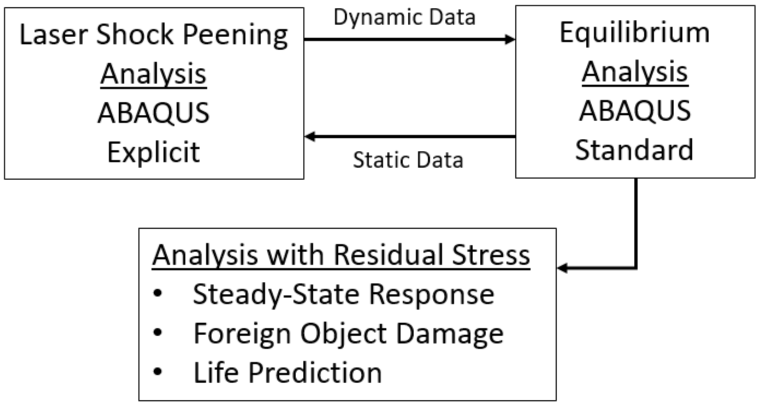

Figure 2.32: Explicit-implicit analysis procedure for a single laser shock peening event [58]

This computational strategy attempts to take advantage of the best aspects of commercial FEA codes. Explicit methods are the most suitable solver for fast nonlinear dynamic systems but are plagued by convergence issues. Nonlinear explicit solvers are based on explicit time integration FE codes which are designed for short duration transient analysis. Implicit methods are more reliable but are computationally expensive in solving dynamic problems. Nonlinear implicit solvers are based on implicit time integration and are used primarily for static computations.

In the remainder of the cited studies, the second explicit computational step was used to determine the model's residual stress and deformation [44,61,63,65]. The use of explicit solvers for both steps returns a solution quicker, it is more scalable and is less computationally expensive. Additionally, artificial damping properties can be introduced in the model to speed the system's return to a near-state of equilibrium [64].

The total length of time of the first solution step was defined based on the time required to stabilise the system's plastic deformation. The model is considered to have undergone all induced deformation once the plastic dissipation energy had stabilised. The solution time must be much longer than the LSP loading pulse duration to achieve a fully saturated plastic deformation, owing to the reflection and interaction of the multiple shock waves propagating in the material. The second step's length was dependent on the computational strategy and if additional system damping was used. However, system equilibrium was judged based on the return to a state of near-zero kinetic energy. This was based on the model's dissipated kinetic energy. Table 2.4 listed the computational strategies of some of the most recent published studies relating to LSP simulations.

Table 2.4: Summary of laser shock peening simulation computational strategies

Study	Computational Strategy	Pulse phase time duration	Equilibrium phase time duration
Braisted & Brockman [58]	Explicit / Implicit	± 0.2 µs (x2 LSP pulse length)	Not stated
Ding & Ye [59]	Explicit / Implicit	2.5 µs (x25 LSP pulse length)	±4 µs
Ocaña et al. [60]	Explicit / Implicit	-	-
Keller et al. [62]	Explicit / Implicit	±0.2 µs (x1 LSP pulse length)	±5.8 µs
Hfaiedh et al. [40]	Explicit / Implicit	Not stated	±100 µs
Brockman et al. [61]	Explicit / Explicit	2.5 µs (x8.33 LSP pulse length)	100 µs (Rayleigh damping applied)
Langer et al. [44]	Explicit / Explicit	2.5 µs (x12.5 LSP pulse length)	100 µs (Rayleigh damping applied)

It must be noted that the incremental step duration and subsequently, the total integration time of the solver must be set in strict relation to the mesh size. ABAQUS/Explicit implements a central differencing scheme that is conditionally stable [66]. If the time increment is larger than a critical time, a numerical instability may lead to an unbounded solution. The stability limit can be determined by Equation 2-25 which relates the shortest element length ($L_{element}$) to the wave speed of the material (C) which is defined by Equation 2-26.

$$\Delta t = \frac{L_{element}}{C} \quad \text{Equation 2-25}$$

$$C = \sqrt{\frac{E}{\rho}} \quad \text{Equation 2-26}$$

2.2.3.1.2. Laser Shock Peening confined pressure loading

In all reported cases, the laser-matter interaction and subsequent plasma formation are not modelled directly. Instead, the LSP event was described by a particular time-dependent pressure pulse, which can easily be applied to the FEA model's corresponding LSP spot area. In most cases, the applied pressure pulse was determined according to the Fabbro et al. confined plasma model, discussed in section 2.2.1.3. The coefficients in this model are typically optimised to produce a pressure loading that gives the best alignment of the predicted and experimental results. Other researchers use simplified triangular estimations of the pressure pulse duration which was based on experimental measurements of the pressure pulse. Table 2.5 summarises the method of plasma pressure distribution used in several publications.

Table 2.5: Summary of confined plasma pressure distributions

Study	Pressure pulse modelling	Time of peak pressure [ns]	Total time of pressure pulse [ns]
Braisted & Brockman [58]	Offset peak triangular	±25	±100
Ding & Ye [59]	Triangular	50	100
Ocaña et al. [60]	LSPSIM based Fabbro confined model	±22	100
Brockman et al. [61]	Staggered triangular based on Clauer et al. [67]	20	300
Keller et al. [62]	Triangular based on experimental optimisation	2	200
Zhu et al. [63]	Fabbro confined model (α 0.35)	±18	200
Hfaiedh et al. [40]	Fabbro confined model	±20	±225
Fabbro et al. [30]	Fabbro confined model (α 0.3)	±30	300
Zhou et al. [68]	Fabbro confined model (α 0.25)	25	130
Langer et al. [44]	Fabbro confined model (α 0.09 / γ 1.3)	25	200

As stated in section 2.2.1.3, this pressure variation is a purely one-dimensional representation of the plasma pressure. Although small transitions in pressure likely exist along the spot perimeters, many authors have assumed a uniform pressure distribution across the spot area [44,58–61,68]. Other researchers have attempted to incorporate the spatial effects of the laser pressure by scaling the applied pressure in the FEA models according to the discussed methods in section 2.2.1.5 [7,30,35,36,42,57].

2.2.3.1.3. Material response due to high strain rates

A single pulse event subjects the material to an extremely high strain rate (10^6 s^{-1}) over the few hundred nanoseconds in which the plasma pressure is sustained [69]. At these rates, accurate predictions of material properties become increasingly more important as the material no longer behaves as it would in quasi-static conditions (strain rate of 10^{-3} s^{-1}). Materials typically exhibit little change in elastic modulus but increase in yield strength as the strain rate increases. A brief overview of the three most popular nonlinear material models for describing the elastic-plastic behaviour of materials at elevated strain rates is provided:

Elastic Perfectly Plastic (EPP) model - No strain hardening or strain rate dependence is considered in this model. The stress remains constant once the plastic regime is reached. The yield stress is derived based on the HEL because of the LSP process's shock wave phenomenon. This can be calculated based on Equation 2-13. Although only a small amount of experimentally determined factors are required for this model, it is heavily disadvantaged by not accounting for the strain hardening and strain rate [70,71].

Zerillo-Armstrong (ZA) model – Is based on dislocation mechanics and the materials' respective crystal structure [72]. The ZA model considers the interaction effects between strain rate and temperature but is disadvantaged by the need for a large number of experimentally determined constants to define the flow stress for the various crystal structures, as seen in Equation 2-27 for FCC structures and Equation 2-28 BCC structures [70,71].

$$\bar{\sigma} = C_1 + C_5\varepsilon^n e^{(-C_3T + C_4T\ln\dot{\varepsilon})} \ [FCC] \qquad \text{Equation 2-27}$$

$$\bar{\sigma} = C_1 + C_2 e^{(-C_3T + C_4T\ln\dot{\varepsilon})} + C_5\varepsilon^n \ [BCC] \qquad \text{Equation 2-28}$$

Johnson-Cook (JC) model – This is one of the most frequently used material models for dynamic impact studies. It is based on a curve-fit representation of the post-yield stress-strain curve, which accounts for the strain hardening, strain rate and thermal effects on the flow stress, as described in Equation 2-9.

$$\bar{\sigma} = [a + b(\bar{\varepsilon}^p)^n]\left[1 + c\ln\left(\frac{\dot{\bar{\varepsilon}}^p}{\dot{\varepsilon}_o}\right)\right]\left[1 - \left(\frac{T - T_r}{T_m - T_r}\right)^m\right] \qquad \text{Equation 2-29}$$

Where $\bar{\sigma}$ is the flow stress based on the effective plastic strain $\bar{\varepsilon}^p$, the effective plastic strain rate $\dot{\bar{\varepsilon}}^p$ the reference strain rate $\dot{\varepsilon}_o$ and experimentally determined constants a, b, c, n and m. The JC model incorporates a thermal factor as well, T represents the temperature in Kelvin, T_r and T_m are the room and melting temperatures. The temperature-dependent term is often omitted in standard LSP processing due to the sacrificial overlays that thermally protect the material. The water overlay prevents a significant thermal build up in the material [73]. The empirical constants used in the above formulation are most often determined at significantly lower strain rates ($\sim 10^3$ s^{-1}) than those experienced during LSP [74]. Due to the difficulty in measuring the exact values of the constants for the JC model at strain rates associated with LSP, Brockman et al. conducted a study to determine the suitability of using factors determined at low strain rates in the formulation. It was shown that the JC model was capable of predicting the stress within AA2024 samples at high strain rates to within a 10% accuracy using the lower parameters determined from Lesurer [69]. This provides some confidence in the continued use of these experimental factors while simulating the residual stresses created during LSP. The popularity of this model is increased by the fact that it is built into the ABAQUS software.

Figure 2.33 compared the accuracy of the three material models in predicting the residual stress induced by LSP. Amarchinta et al. determined that all three models could predict an increase in plastic strains due to higher peak pressure loading [70].

The EPP model could not predict residual stress trends through the full depth like the other two models. This is attributed to how the model predicts a steep decline in the compressive stress wave's magnitude during the initial propagation through the material, significantly affecting the EPP model's ability to predict the near-surface residual stresses correctly.

In addition, by not accounting for strain rate dependences, the EPP model overestimates the predicted residual stress. Although the other methods conformed to the general trends, the JC model was found to over predict the magnitude of residual stress throughout, whilst the ZA model over predicts the magnitudes near the surface and then under predicts the stress in the remaining depth. The standard ZA model's undulating response is accredited to the lack of dependence on plastic responses and shear modulus [73]. Overall, the JC model showed the best agreement with experimental trends and results.

It should be noted that all conventional modelling approaches do not account for the possibility of cyclic straining due to multiple LSP events. Angulo et al. estimate that cyclic loading occurs in the material because of reverse yielding after the initial plastic deformation. Better agreement between experimental and simulation results was seen by including the cyclic plasticity [75].

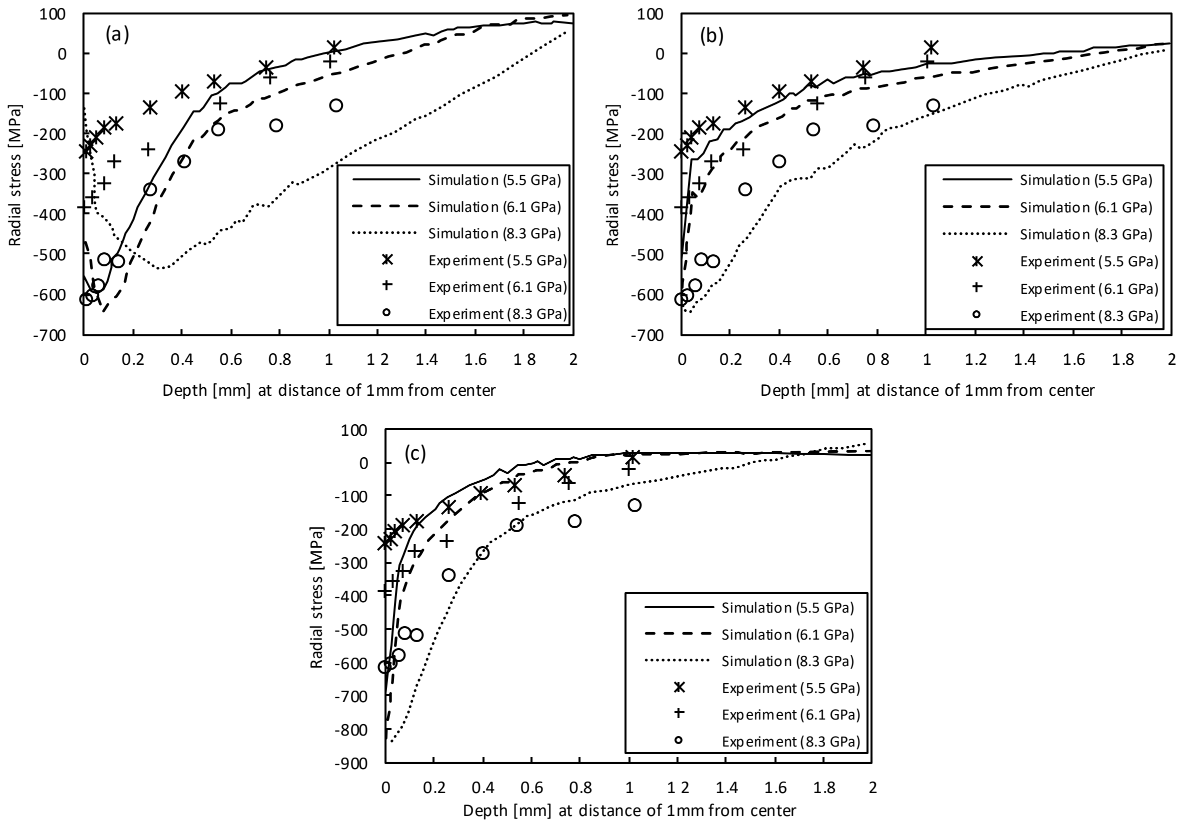

Figure 2.33: Residual stress comparison between experimentally measured and (a) Elastic-Plastic model (b) Johnson-Cook model (c) Zerilli-Armstrong model [70]

2.2.3.2. Eigenstrain approach to simulation of Laser Shock Peening

The Eigenstrain approach, proposed by DeWald and Hill, has gained considerable popularity in predicting residual stresses introduced by LSP [76]. This modelling strategy allows for the accurate estimation of the LSP residual stress field in a coupon with minimal experimental results and without extensive computation. The Eigenstrain approach consists of three steps: firstly, an ideally stress-free simple geometry sample is peened over its entire surface, as shown in Figure 2.34.

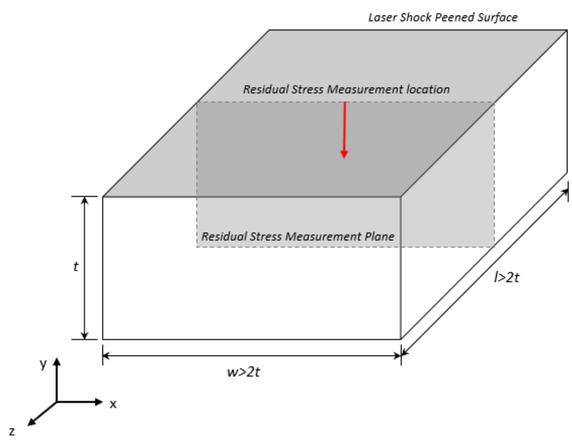

Figure 2.34: Sample Geometry for Eigenstrain Stress Measurements

Secondly, the measured residual stress (σ_{Tot}) can be determined through the depth using contour or diffraction methods. This measured residual stress can be considered as the superposition of the LSP residual stress (σ_{LSP}) and the balancing elastic stress field (σ_{Eq}) that occurs to ensure equilibrium in the sample, as defined by Equation 2-30 [77].

$$\sigma_{Tot} = \sigma_{LSP} + \sigma_{Eq} \qquad \textit{Equation 2-30}$$

The LSP component's contribution to the total residual stress is purely dependent on the LSP parameters (power density, coverage and number of layers) and the material properties. The second contribution in Equation 2-30 is dependent on the sample geometry through standard material mechanics. Figure 2.35 provided an example of the two components' superposition towards the total measurable residual stress (study conducted in 28 mm thick AA 7050-T7451) [77]. The equilibrium stress can be determined as the elastic balancing stress and can be extrapolated throughout the laser peening affected depth.

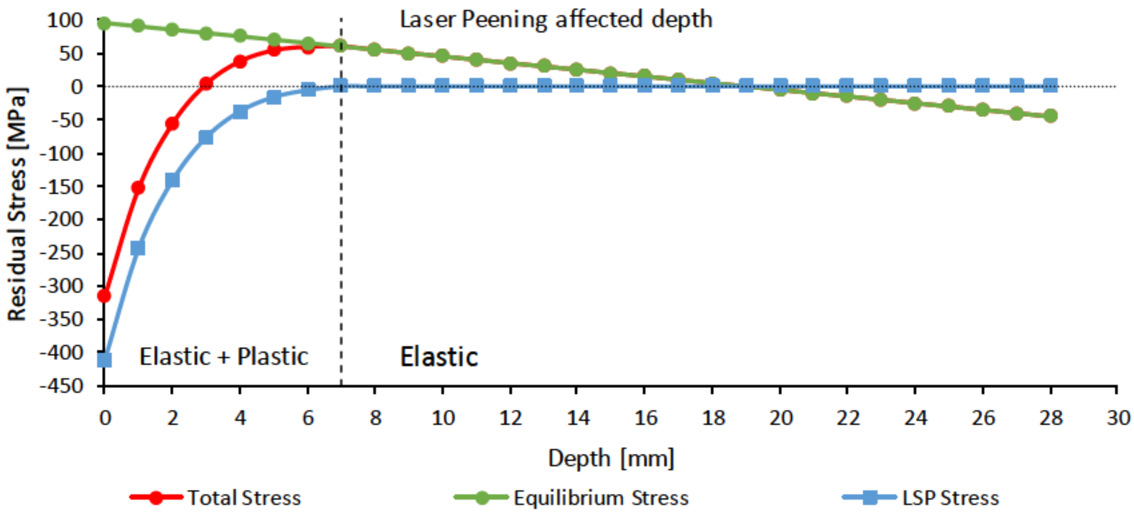

Figure 2.35: Representation of the superposition of laser peening induced and equilibrium residual stress [77]

Thirdly, the LSP induced eigenstrains can be obtained by assuming a biaxial stress state in the irradiated surface plane and rearranging Equation 2-30, resulting in Equation 2-31.

$$\varepsilon^*_{LSP} = \begin{bmatrix} \varepsilon^*_{LSP,xx}(z) \\ \varepsilon^*_{LSP,yy}(z) \\ \varepsilon^*_{LSP,zz}(z) \end{bmatrix} = -\frac{1}{E}\begin{bmatrix} 1 & -v & -v \\ -v & 1 & -v \\ -v & -v & 1 \end{bmatrix}\begin{bmatrix} \sigma_{LSP,xx}(z) \\ \sigma_{LSP,yy}(z) \\ 0 \end{bmatrix} \qquad \textit{Equation 2-31}$$

Once the induced eigenstrains are obtained, an elastic simulation can be completed to determine the total residual stresses produced by LSP. These strains are introduced into the FEA model as anisotropic thermal expansion coefficients [41].

2.3. Fatigue and fracture mechanics

2.3.1. Fatigue

Fatigue is the structural weakening of a component through cyclic varying of an applied load. This form of loading causes the progressive formation and growth of localised growth of flaws in a component. The tensile stresses and plastic strain per cycle (no matter how small) will contribute to crack initiation. Once initiated, these cracks will grow a finite length per cycle. The core stages of fatigue are defined as:

Stage I - Crack nucleation, continuous cyclic stresses cause sliding and shearing of atomic planes within the crystals resulting in slip bands on the surface grains. These slip bands grow in size and eventually separate, leading to the formation of cracks. Internal defects such as dislocations, voids and pits can cause the initiation of a crack. The majority of total fatigue life is associated with this stage.

Stage II – Crack propagation, cyclic stresses cause the crack's incremental growth along the grain's slip plane. A transition will occur when the crack tip's plastic zone is large enough to activate multiple slip systems. This causes the crack's propagation to depend on the loading condition rather than on the crystallographic orientation. The crack propagation direction tends to be normal to the loading direction.

Stage III – Ultimate failure, occurs when the crack length becomes long enough that the remaining undamaged material can no longer sustain the applied loading. The crack will then propagate in a rapid and unstable manner.

Crack growth is driven by the range of applied loading and material properties. Additional factors such as stress concentrations, environmental effects and mean stress can affect the growth. Most material fatigue data is represented in an S-N curve (Wöhler curve), representing an estimation of the cycles to failure due to constant amplitude cyclic loading. Fatigue life is heavily dependent on the type of bulk material dependency as clearly shown in Figure 2.36 [78]. Additionally, a lower stress amplitude will lead to more cycles to failure. In strain ageing materials such as carbon steels, a fatigue limit (endurance limit) occurs where the stress amplitude below a certain value will not cause fatigue failure. However, this does not occur in materials such as aluminium.

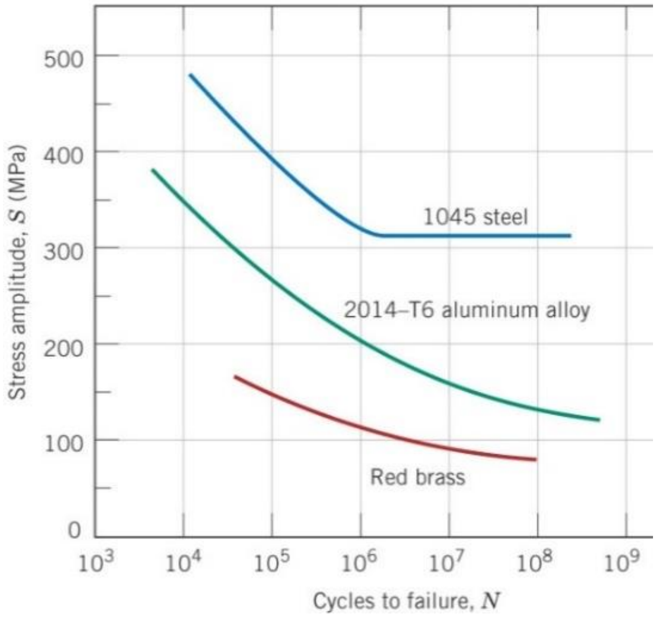

Figure 2.36: Applied stress to the number of cycles to failure curves for various common engineering materials [78]

A component is subjected to various cyclic stress with varying upper and lower bounds over its service life. For simplicity, most fatigue studies are undertaken with constant amplitude loading, which takes the form of a sinusoidal waveform, as illustrated in Figure 2.37.

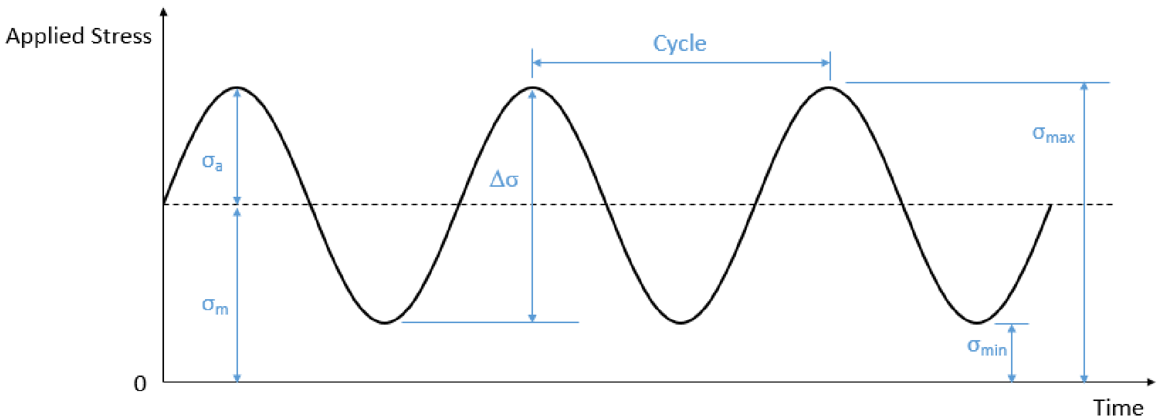

Figure 2.37: Typical nomenclature of a constant amplitude fatigue test

The mean stress and stress amplitude are described by Equation 2-32 and Equation 2-33.

$$\sigma_m = \frac{\sigma_{max} + \sigma_{min}}{2} \qquad \textit{Equation 2-32}$$

$$\sigma_a = \frac{\sigma_{max} - \sigma_{min}}{2} \qquad \textit{Equation 2-33}$$

The stress range and ratio are described by Equation 2-34 and Equation 2-35.

$$\Delta\sigma = \sigma_{max} - \sigma_{min} \qquad \text{Equation 2-34}$$

$$R = \frac{\sigma_{min}}{\sigma_{max}} \qquad \text{Equation 2-35}$$

2.3.2. Linear elastic fracture mechanics

Linear Elastic Fracture Mechanics (LEFM) is a solid mechanics field associated with the origin and propagation of cracks. It provides capabilities to characterise the driving forces of crack growth and eventual fracture of materials. Fracture mechanics assumes that all materials have internal flaws or cracks, which will cause applied stress to concentrate around the crack tip, as shown in Figure 2.38 [79]. If remote tensile stresses are applied (σ_∞), in the crack opening direction (y directions for Figure 2.38), the stress tends to infinity at the local crack tip (σ_{loc}). This effect can lead to local stresses exceeding the material yield strength and design limitations, even when the remote stresses are within safe limits.

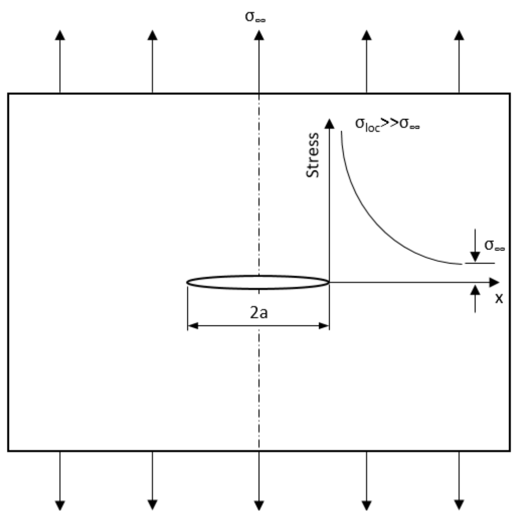

Figure 2.38: Stress concentration around a crack tip [79]

There are three different modes of fracture in LEFM, shown in Figure 2.39 [79].

Mode I: Opening mode - The crack is loaded in its plane, causing the two surfaces to open relative to one another. It is the most common form of loading and causes the crack to grow perpendicular to the maximum tensile stress.

Mode II: Sliding mode – Occurs when a crack is subjected to shear stresses. It causes the surfaces of the crack to slide on one another. The crack tends to grow in the same direction as the applied load.

Mode III: Tearing mode – Occurs when a crack is subjected to an out of plane load. The crack tends to propagate perpendicular to the direction of the shear stress.

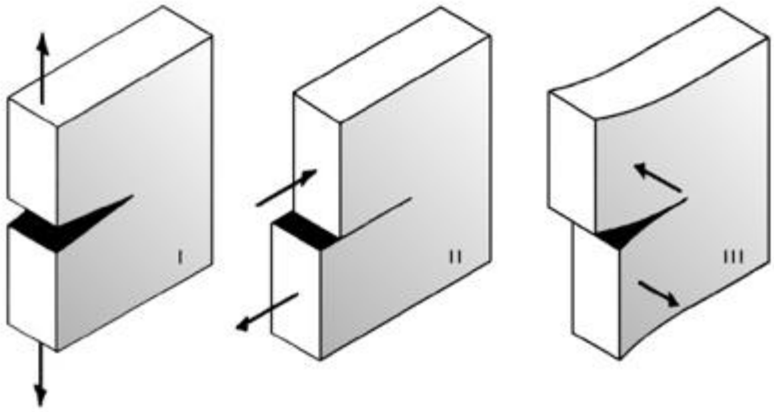

Figure 2.39: Three modes of loading in Linear Elastic Fracture Mechanics [79]

In 1920, Griffith introduced the concept that a crack will form or propagate if a process causes a change in the strain energy larger than the energy required to create new crack surfaces [80]. Griffiths thermodynamic-like approach defined the energy balance for an incremental increase in the crack area, dA, provided by Equation 2-36:

$$\frac{dE}{dA} = \frac{dU}{dA} + \frac{dW}{dA} = 0 \qquad \text{Equation 2-36}$$

Where dE is the total energy, dU is the potential energy of the internal strain energy, and dW is the required energy to create a new surface [2]. Irwin designated the term, -dU/dA is as the energy release rate (ERR), which defines the rate of energy conversion as a material fractures and was described by Equation 2-37 and Equation 2-38 [81]:

$$ERR = \frac{\pi a \sigma^2}{E} \ (Plane\ stress) \qquad \text{Equation 2-37}$$

$$ERR = (1 - v^2)\frac{\pi a \sigma^2}{E} \ (Plane\ strain) \qquad \text{Equation 2-38}$$

Where a is the crack length. Irwin later developed the stress intensity approach, which provided a method to determine the stresses near a crack tip, defined by Equation 2-39.

$$\lim_{r\to 0} \sigma_{ij} = \frac{K}{\sqrt{2\pi r}} f_{ij} \qquad \text{Equation 2-39}$$

Where σ_{ij} is the stress tensor for a homogenous, isotropic linear elastic material acting on an infinite element whose location relative to the crack tip is defined by polar coordinates, as illustrated in Figure 2.40. The Stress Intensity Factor (SIF), K, gives the magnitude of the elastic stress field at the crack.

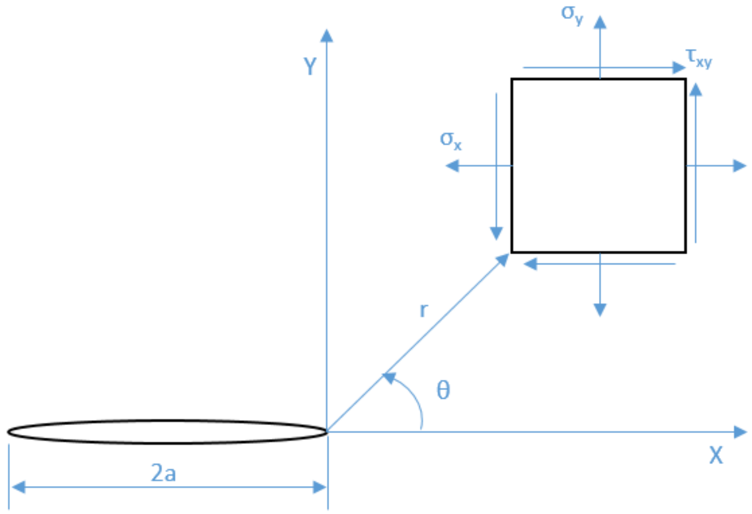

Figure 2.40: Polar coordinate system for determining stresses relative to a crack tip [81]

Equation 2-40 to Equation 2-43 define the stresses at the crack tip for the most general loading case of pure mode I loading, as seen in Figure 2.39. Full derivations of the stress at the crack tip are provided by Wang [2].

$$\sigma_{xx} = \frac{K_I}{\sqrt{2\pi r}}\cos\frac{\theta}{2}\left[1 - \sin\frac{\theta}{2}\sin\frac{3\theta}{2}\right] \qquad \text{Equation 2-40}$$

$$\sigma_{yy} = \frac{K_I}{\sqrt{2\pi r}}\cos\frac{\theta}{2}\left[1 + \sin\frac{\theta}{2}\sin\frac{3\theta}{2}\right] \qquad \text{Equation 2-41}$$

$$\tau_{xy} = \frac{K_I}{\sqrt{2\pi r}}\cos\frac{\theta}{2}\sin\frac{\theta}{2}\cos\frac{3\theta}{2} \qquad \text{Equation 2-42}$$

$$\sigma_{zz} = \begin{cases} 0 & \textit{Plane stress} \\ v(\sigma_{xx} + \sigma_{yy}) & \textit{Plane strain} \end{cases} \qquad \text{Equation 2-43}$$

Equation 2-44 to Equation 2-46 define the displacement field (G is the shear modulus, κ=3-4v for plane strain and κ=(3-v)/(1+v) for plane stress) :

$$u_x = \frac{K_I}{2\mu}\sqrt{\frac{r}{2\pi}}\cos\frac{\theta}{2}\left[\kappa + 1 - 2\sin^2\frac{\theta}{2}\right] \qquad \text{Equation 2-44}$$

$$u_y = \frac{K_I}{2\mu}\sqrt{\frac{r}{2\pi}}\sin\frac{\theta}{2}\left[\kappa + 1 - 2\cos^2\frac{\theta}{2}\right] \qquad \text{Equation 2-45}$$

$$u_z = \begin{cases} -\frac{vz}{E}(\sigma_{xx} + \sigma_{yy}) & \textit{Plane stress} \\ 0 & \textit{Plane strain} \end{cases} \qquad \text{Equation 2-46}$$

Dimensional analysis indicates that the stress intensity factor is linearly related to the applied stress and directly related to the square root of the crack length [81]. A general solution for the stress intensity was provided by , where Υ is the geometry factor that relates the geometry of the crack system to the applied load, σ is the applied loading and a is the cracks length. Table 2.6 listed the stress intensity factors for the sample configurations used in this work [82].

$$K = \Upsilon\sigma\sqrt{\pi a}$$

Equation 2-47

Table 2.6: Stress intensity factors for various sample configurations

Geometry	Stress Intensity Factor
1. Crack in an infinite body 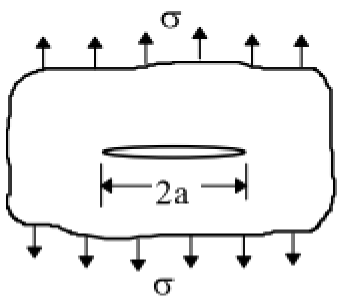	$K_I = \sigma\sqrt{\pi a}$ *Equation 2-48*
2. Centre crack in a finite width body 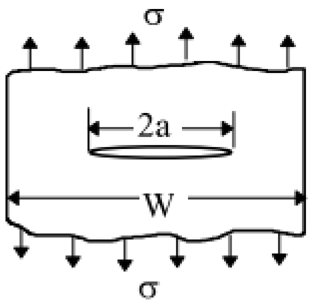	$K_I = \sqrt{\sec\frac{\pi a}{W}}\,\sigma\sqrt{\pi a}$ *Equation 2-49*

Stress intensity is a critical factor in LEFM, as it describes the local stress field. The factors listed in Table 2.6 are only valid near the crack tip, higher-order functions are required for the stress further away. Combining the strain energy release rate (Equation 2-50 and Equation 2-51) and SIF, we can determine a relationship between the two factors:

Mode I	Mode II	Mode III		
$SERR = \frac{{K_I}^2}{E}$	$SERR = \frac{{K_{II}}^2}{E}$	$SERR = \frac{{K_{III}}^2}{E}(1+\nu)$	*Plane stress*	*Equation 2-50*
$SERR = (1-\nu^2)\frac{{K_I}^2}{E}$	$SERR = (1-\nu^2)\frac{{K_{II}}^2}{E}$	$SERR = \frac{{K_{III}}^2}{E}(1+\nu)$	*Plane strain*	*Equation 2-51*

Although the stress intensity factor is beneficial, the stresses in the crack tip's vicinity tend to infinity (singularity at the crack tip) as r in Equation 2-40 - Equation 2-42 tends to zero. This implies that the increased stress will cause the material to deform plastically above the yield stress. The occurrence of plasticity causes the crack to behave as if it was longer than its physical size. The effects of plasticity are accounted for by adding the size of the plastic zone (r_p) to the actual crack length to form the effective crack length, as shown in Equation 2-52.

$$a_{eff} = a + r_p \qquad \text{Equation 2-52}$$

Additionally, the stress is not uniform along the crack front for a full through crack. Plane stress occurs near the surface due to the free boundary. Plane strain develops in the middle of the crack front as the surrounding material constrains the deformation. The plastic region's typical is shape based on mode I loading is shown in Figure 2.41 [81].

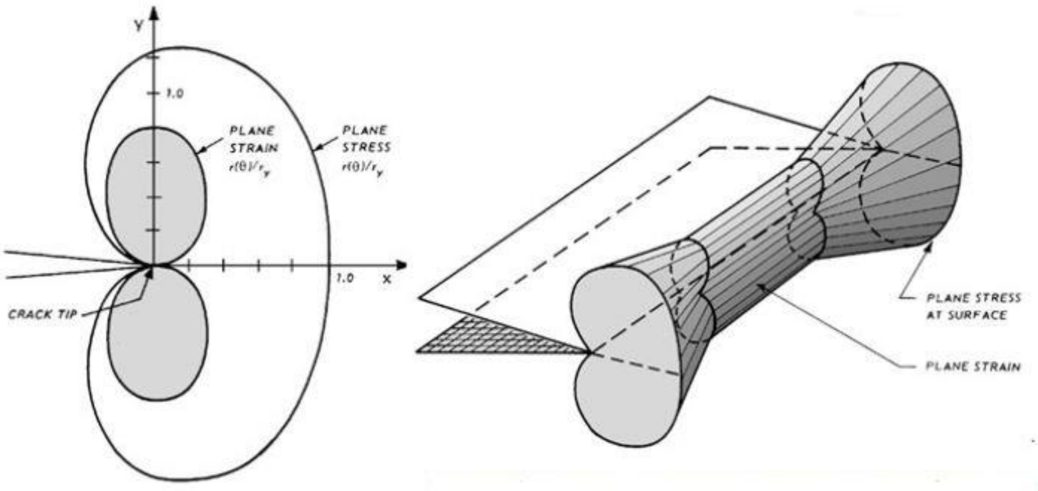

Figure 2.41: Schematic of the plastic zone ahead of a crack tip [81]

The plane stress/strain plastic zone size can be estimated by Equation 2-53 and Equation 2-54. Anderson related the plastic zone size relative to the applied loading and the specimen thickness (B). Plane strain occurs if the plastic zone is small compared to the thickness $(r_p << B)$ or empirically estimated as $r_p > \left(B/_{50}\right)$. However, if the plastic zone is of a similar magnitude as the thickness then plane stress prevails and can be empirically estimated by $r_p > \left(B/_{2}\right)$ [83].

$$r_p = \frac{1}{3\pi}\left(\frac{K}{\sigma_{YS}}\right)^2 \ (Plane\ strain) \qquad \text{Equation 2-53}$$

$$r_p = \frac{1}{\pi}\left(\frac{K}{\sigma_{YS}}\right)^2 \; (Plane\ stress) \qquad \text{Equation 2-54}$$

2.3.3. Fatigue crack growth rate prediction methods

Fatigue cracks can grow and propagate when a range of cyclic stresses, such as that expressed by Equation 2-34, are applied to a cracked structure. This can occur at a range of magnitudes of applied stress levels and even at stresses well below the yield strength of the material. This occurs as the material near the crack tip is exposed to server plastic deformation. As previously shown, the stress intensity defines the stress-strain field near the crack tip thus the Fatigue Crack Growth Rate (FCGR) can be correlated to the variation in applied stress intensity, as shown in Figure 2.42. The variation in the stress intensity was defined by Equation 2-55 and the stress ratio by Equation 2-56.

$$\Delta K = K_{max} - K_{min} \qquad \text{Equation 2-55}$$

$$R = \frac{K_{min}}{K_{max}} \qquad \text{Equation 2-56}$$

Paris was the first to determine a direct relationship between the FCGR (da/dN) and the stress intensity factor range (ΔK). This indicates how quickly or slowly a crack propagates per cycle when plotted against the stress intensity range: an example of this is provided in Figure 2.42. A logarithmic scale is typically used on these plots.

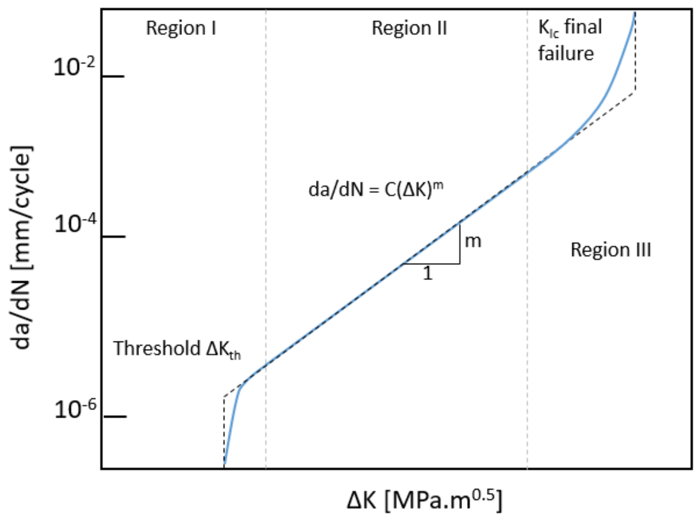

Figure 2.42: Relationship between crack growth rate and stress intensity factor

Three distinct regions can be identified in Figure 2.42, which link to the various stages of crack growth previously discussed in section 2.3.1. A threshold stress intensity factor range defines the first region

(ΔK_{th}), below which long cracks do not grow. This threshold limit separates crack nucleation from crack propagation. Region II, or the linear portion of the curve, is better known as the Paris law. This linear section is defined by Equation 2-57, where C and m are material, environmental, temperature and stress ratio dependent. They can be determined as the intercept and slope of the curve.

$$\frac{da}{dN} = C(\Delta K)^m \quad \textit{Equation 2-57}$$

When the crack reaches a critical length, the crack becomes unstable and rapidly accelerates since K_{max} is close to the fracture toughness of the material (K_{Ic}). The major limitation of the Paris equation is that the material constants must be determined for various loading conditions. This effect was highlighted in Figure 2.43 [84]. Each curve is determined with a specific set of C and m values. It can be concluded that higher stress ratios cause faster crack growth rates due to the higher mean stress.

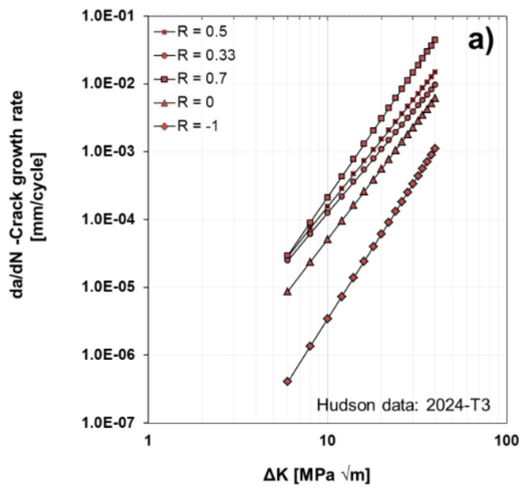

Figure 2.43: Effect of stress ratio (R) on aluminium alloy 2024-T3 [84]

Walker was one of the first to attempt to include the effect of stress ratio through the development of the Walker Equation [85], provided in Equation 2-58.

$$\frac{da}{dN} = \frac{C \cdot \Delta K^m}{(1-R)^{m(1-\gamma)}} \quad \textit{Equation 2-58}$$

Where γ is a material constant that indicates the shift in the crack growth data. AA 2024-T3 has a γ value of approximately 0.68 [14].

Forman et al. [86] improved on the Walker Equation by improving the accuracy of prediction of crack growth rates near the upper region of the da/dN versus ΔK curve (region III in Figure 2.42). The Forman Equation, provided in Equation 2-59, includes the fracture toughness of the material K_{Ic}. As

ΔK approaches K_{Ic} the equation tends to infinity and therefore predicts the rapid and unstable mechanical failure.

$$\frac{da}{dN} = \frac{C\Delta K^m}{(1-R)K_{Ic} - \Delta K} \qquad \text{Equation 2-59}$$

The NASGRO equation [87] accounts for the full crack growth curve (all three regions), stress ratio and crack closure. The crack closure is accounted for through the addition of f which is the Newman crack closure function. The NASGRO equation is provided in Equation 2-60, where $C$and m are the material constants and p and q describe the slope of the threshold and failure regions.

$$\frac{da}{dN} = C\left[\left(\frac{1-f}{1-R}\right)\Delta K\right]^m \frac{\left[1-\frac{\Delta K_{th}}{\Delta K}\right]^p}{\left[1-\frac{\Delta K_{max}}{\Delta K_{Ic}}\right]^q} \qquad \text{Equation 2-60}$$

2.3.4. Influence of residual stress on fatigue performance

Residual stress fields in engineering components can impact a components mechanical properties and service capabilities. These are self-balancing stresses that can occur in engineering parts. Residual stresses must be accounted for as they can combine with the externally applied load. The combination of the various stresses can result in an unexpected loading condition that may exceed the mechanical strength of the material. Additionally, residual stresses can influence the cyclic loading and stress ratio at the crack tip which leads to possible variations in the behaviour of the FCGR of the sample.

Two widely used methods, developed by Parker [88] and Nelson [5], are used to determine the effect of both the applied and residual stress acting at a crack tip. The former employs the use of superposition methods whilst the latter is based on crack closure. The Superposition Principle (SP) assumes the fact the stress intensity factors are derived from a linear elastic analysis. Thus a stress system due to multiple loads acting together is equivalent to the stresses' sum due to each loading acting separately. The stress intensity factor due to the residual stress (K_{res}) can be superimposed on the stress intensity caused by a cyclic loading. These values are summed to determine the total stress intensity acting at the crack tip, as defined by Equation 2-61:

$$K_{Tot,max} = K_{max} + K_{Res}$$
$$K_{Tot,min} = K_{min} + K_{Res}$$

Equation 2-61

The stress intensity range can be determined as normal, by taking the difference of the two factors in Equation 2-61. It can be noted that there is no effect of the residual stress on the stress intensity factor range as K_{res} contributions are cancelled out, as shown in Equation 2-62.

$$\Delta K_{Tot} = K_{Tot,max} - K_{Tot,min} = K_{max} - K_{min} = \Delta K \qquad \textit{Equation 2-62}$$

The stress ratio is affected by the presence of residual stress as the K_{Res} components cannot be cancelled out. This is shown in Equation 2-63. A new effective stress ratio can be determined, which will affect the rate of crack growth, as demonstrated in Figure 2.43.

$$R_{Tot} = \frac{K_{Tot,min}}{K_{Tot,max}} = \frac{K_{min} + K_{Res}}{K_{max} + K_{Res}} \qquad \textit{Equation 2-63}$$

Weight functions and elastic-plastic finite element modelling are commonly used to calculate K_{res} and have a good correlation between the methods when applied to the same problem. Elastic-plastic finite element modelling of the advancing crack is the generally preferred method of determining K_{res} as the redistribution of the initial residual stress field can be easily determined as the crack propagates.

Crack closure, the cyclic loading spectrum region that causes the two surfaces of the crack to make contact, can significantly affect the FCGR prediction. Elber noted that a fatigue crack was only open for a portion of the loading cycle, even when the cycle was fully tensile [89]. It was argued that the compressive residual stress that developed due to the plastic deformation that occurred in the wake of the advancing crack caused the closure phenomenon. The compressive residual stress caused the crack to close prematurely before the minimum load was reached, as shown in Figure 2.44. An effective stress intensity range (ΔK_{Eff}) can be determined by replacing the minimum stress intensity factor with the stress intensity factor which causes the crack to start to be fully open (K_{Op}), as given in Equation 2-64.

$$\Delta K_{Eff} = K_{Tot,max} - K_{Op} \qquad \textit{Equation 2-64}$$

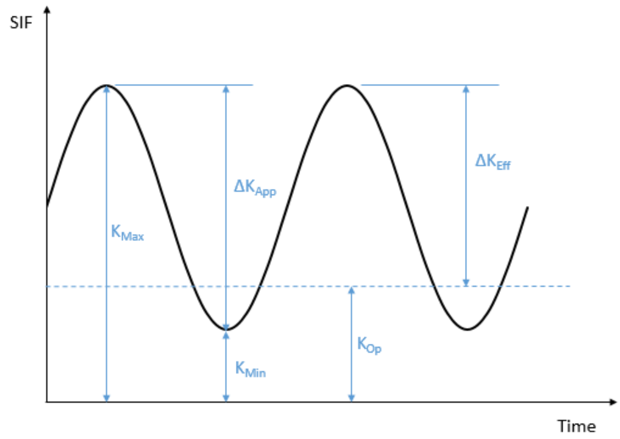

Figure 2.44: Effective loading cycle due to crack closure

The superposition principle should only be used when the crack is fully open. A compressive residual stress field will cause a negative K_{res} and the superposition method is still valid assuming no crack face closure occurs ($K_{Tot,min} \geq 0$). The Modified Superposition Principle (MSP) accounts for the closure by setting $K_{Tot,min}$ to zero when a negative stress intensity is predicted. The stress intensity range and stress ratio can be determined by Equation 2-65 and Equation 2-66.

$$\Delta K_{Tot} = K_{Tot,max} - K_{Tot,min} \qquad \mathrm{K_{Tot,min}} > 0$$

$$\Delta K_{Tot} = K_{Tot,max} \qquad \mathrm{K_{Tot,min}} \leq 0$$

Equation 2-65

$$R_{Tot} = \frac{K_{Tot,min}}{K_{Tot,max}} \qquad \mathrm{K_{Tot,min}} > 0$$

$$R_{Tot} = 0 \qquad K_{Tot,min} \leq 0$$

Equation 2-66

LaRue et al. [90] and Jones et al. [91] used the Superposition, Modified Superposition and a plasticity induced crack closure approach which is known as a Superposition Contact Principle (SCP) to determine the FCGR in AA2024-T351 central pre-yielded hole and 11 mm thick beams. The Modified Superposition technique overestimated the life in both investigations. In comparison, the Superposition Contact principle showed a better correlation to the experimental results. Equation 2-67 and Equation 2-68 provided the stress intensity range and stress ratio according to the Superposition Contact method.

$$\Delta K_{Tot} = K_{max} + K_{res} - K_{Tot,min} \qquad K_{Tot,min} > 0$$

$$\Delta K_{Tot} = K_{Tot,max} - K_{Tot,min} = K_{max} - K_{min} \qquad K_{Tot,min} \leq 0$$

Equation 2-67

$$R_{Tot} = \frac{K_{Tot,min}}{K_{Tot,max}} = \frac{K_{Tot,min}}{K_{max+}K_{res}} \qquad K_{Tot,min} > 0$$

Equation 2-68

$$R_{Tot} = \frac{K_{Tot,min}}{K_{Tot,max}} = \frac{K_{min+}K_{res}}{K_{max+}K_{res}} \qquad K_{Tot,min} \leq 0$$

2.3.4.1. Experimental effects of residual stress on fatigue and crack growth performance

The influence of residual stress on fatigue and crack growth has been widely researched in various engineering materials. Residual stresses can be introduced in the samples through numerous means. However, only LSP cases will be covered in this section.

It has been shown that LSP residual stress fields have a significant influence on the fatigue resistance and location of the crack initiation. Peyre et al. showed the increase in fatigue life was primarily related to the significant extension of the crack initiation period, as shown in Figure 2.45.a. Additionally, Figure 2.45.b showed that LSP was a far superior process to that of shot peening [7]. Several authors have observed this fact in many engineering materials [92–95].

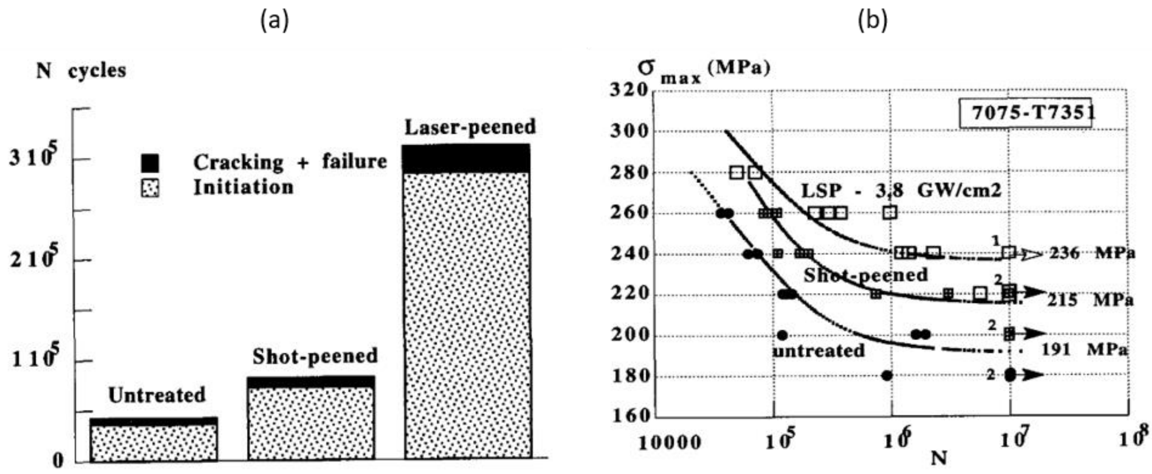

Figure 2.45: Influence of laser shock peening induced residual stress fields (a) comparison of initiation and cracking stages of total fatigue (b) S-n curves showing the life extension due to laser peening in AA7075-T735 [7]

Several authors have confirmed that LSP's near-surface compressive residual stresses introduced by LSP cause a sub-surface shift of the crack initiation site. The shift in failure location typically correlates with the regions of significant balancing tensile residual stresses. The balancing tensile stress is a by-product of the LSP process to equilibrate the compressive stress [96–99]. Sanchez et al. showed that LSP caused a change in the micro-mechanisms of the crack initiation. The compressive residual stress deactivates crack initiation at coarse intermetallic particles (of size 1-10 µm) found at the surface and initiation is driven to occur subsurface, as indicated by Figure 2.46 [100]. A finite element analysis conducted by Sanchez et al. indicated that the compressive residual stresses can institute negative mean stresses in the surface region that resists surface crack initiation.

LSP residual stress fields' beneficial effects are not always realised, as in the study of the effect of LSP on fretting fatigue conducted by Liu and Hill [99]. The failure occurred outside the fretting area and provided no enhancement in fatigue life. Chaharddehi et al. observed no considerable retardation of fatigue cracks by the surface compressive residual stress in steel samples. It was believed that a tensile core of approximately 150 MPa could overwhelm all benefits of the compressive residual stress field of -550 MPa [101]. These results imply that LSP should not be indiscriminately applied without consideration for the balancing tensile stress. This shows the need for accurate LSP residual stress predictive models in furthering the uses of LSP.

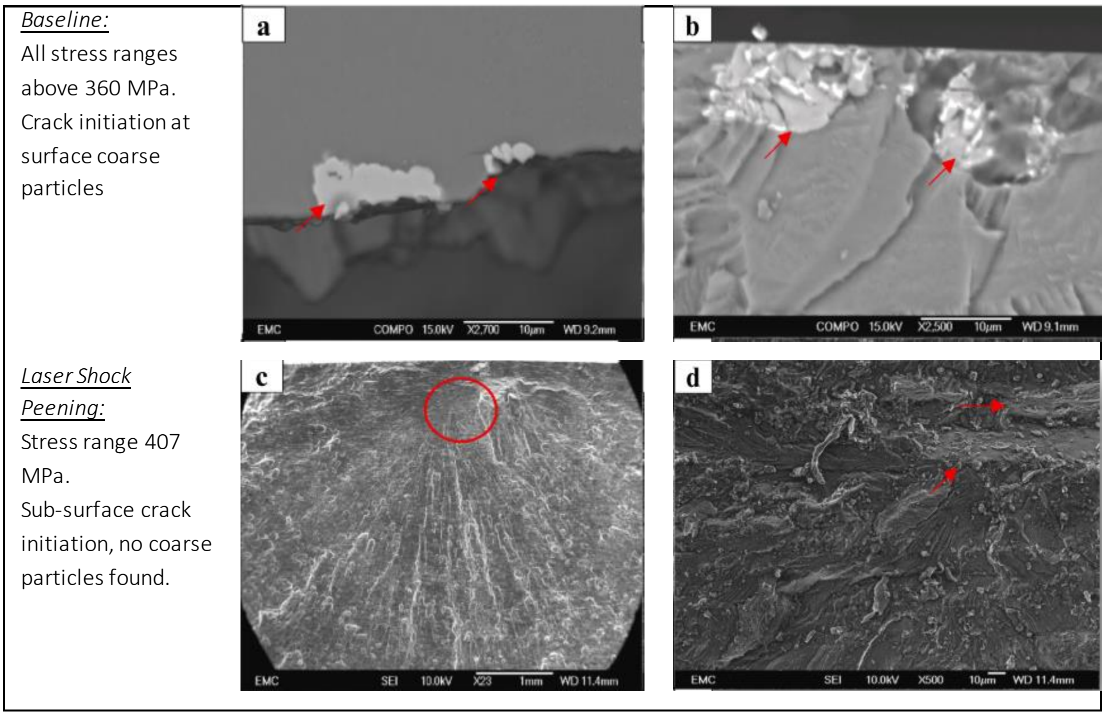

Figure 2.46: Variation in crack initiation site of AA7075-T651 due to laser shock peening residual stress field [100]

Several authors have observed reductions in FCGR by placing an LSP residual stress field along the crack trajectory [102–105]. Pavan et al. showed a significant deceleration in growth due to the crack entering the LSP compressive residual stress field, as indicated in Figure 2.47 [106]. The LSP patches extended the fatigue life by as much as four times the unpeend specimens. However, an acceleration in crack growth was observed just before the crack entering the LSP patch due to the balancing tensile residual stress and this occurred in multiple cases [102,104,106].

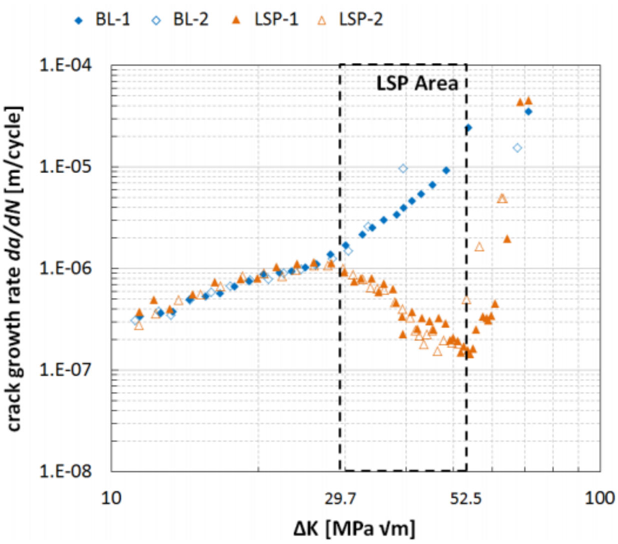

Figure 2.47: Reduction in fatigue crack growth rate due to laser shock peening induced residual stresses, BL – baseline AA2524, LSP – laser peened samples with the same parameters [106]

These studies' overall outcome showed that the LSP patches should be elongated in the loading direction and placed as near the crack tip as possible to achieve the maximum outcome of life enhancement. The fundamental crack retardation mechanism is that the compressive residual stress lowers the effective stress intensity factor and potentially causes full crack closure for parts of the loading cycle.

2.3.5. Fatigue crack trajectory

It has been reasonably well established that a crack will propagate in the orthogonal direction to a mode I loading. This is because cracks seek the path of least resistance or maximum driving force (the path where the maximum amount of energy can be released). Additionally, multiple loading systems contributions can be summed together in their respective modes using the Superposition principle. In reality, structures are subjected to complex loading systems that give rise to multiple modes occurring concurrently. The combination of these modes is known as mixed-mode loading. The superposition of modes I and II are generally called 2D Mixed Mode, while 3D Mixed Mode characterises mode III's inclusion. Mixed-mode loading can be established either through the orientation of the crack or through the external load/s. Figure 2.48 provided a schematic of the loading system of a crack with an infinitesimal kink. The stress field at the crack tip can be defined (using polar coordinates as in Figure 2.40) by Equation 2-69 and Equation 2-70 [2].

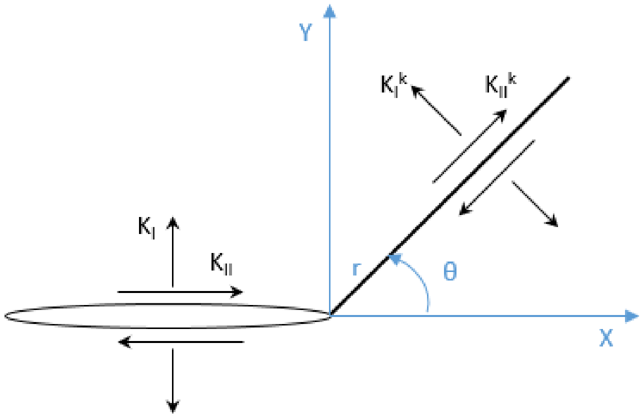

Figure 2.48: Schematic of a kinked crack

$$\sigma_{\theta\theta} = \frac{1}{\sqrt{2\pi r}} \cos^2\left(\frac{\theta}{2}\right)\left[K_I \cos\frac{\theta}{2} - 3K_{II} \sin\frac{\theta}{2}\right] \qquad \textit{Equation 2-69}$$

$$\tau_{r\theta} = \frac{1}{\sqrt{2\pi r}} \cos\frac{\theta}{2}\left[K_I \sin\frac{\theta}{2}\cos\frac{\theta}{2} + K_{II}\left(1 - 3\sin^2\frac{\theta}{2}\right)\right] \qquad \textit{Equation 2-70}$$

Multiple criteria have been suggested to predict the crack path due to the influence of complex mixed loading.

The Maximum Tangential Stress (MTS) criterion [107] proposes that crack growth occurs when the maximum tangential stress reaches a critical value, and the crack extends in the radial direction corresponding to the maximum tangential stress. The crack deviation angle (θ_p) can be determined based on the MTS criteria which specifies $\partial\sigma_{\theta\theta}/\partial x = 0$ or $\tau_{r\theta} = 0$, which can be expressed by Equation 2-71 [11]:

$$\theta_p = \cos^{-1}\left(\frac{3{K_{II}}^2 + \sqrt{{K_I}^4 + 8{K_I}^2{K_{II}}^2}}{{K_I}^2 + 9{K_{II}}^2}\right) \qquad \textit{Equation 2-71}$$

The crack deviation angle is measured counterclockwise with respect to the initial crack plane. The crack deviation angle ($\theta_p = 0$) will continue to propagate straight ahead when $K_{II} = 0$, whereas if $K_{II} > 0$ the deviation angle will be negative ($\theta_p < 0$) and if $K_{II} < 0$ the deviation angle will be positive ($\theta_p > 0$) and this was shown in Figure 2.49.

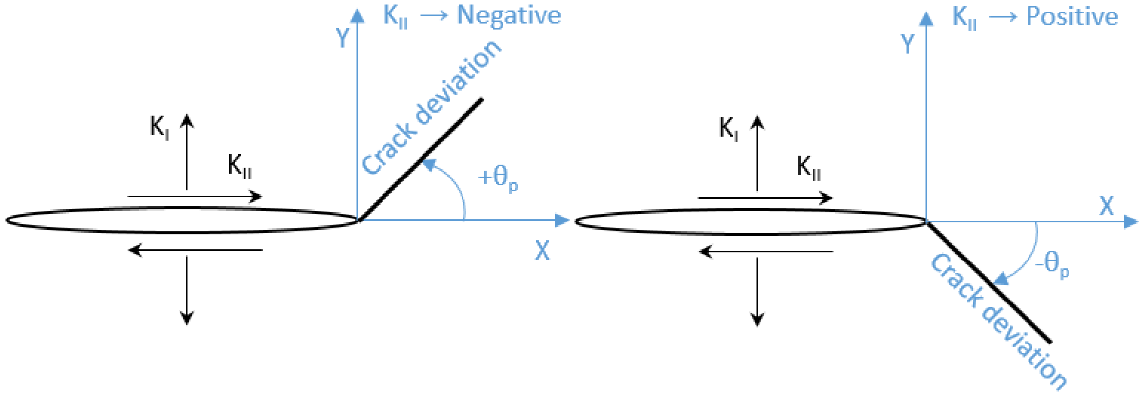

Figure 2.49: Crack deviation angle under mixed-mode loading

The Maximum Energy Release Rate (MERR) criterion [108] stipulates that the crack will grow in the direction along which the maximum potential energy is released. The energy release under mixed-mode conditions of a small kinked crack from the original main tip, as shown in Figure 2.48, can be determined by considering the kinked crack's stress intensity factors, as in Equation 2-72.

$$G^k = \frac{1}{E}\left[\left(K_I{}^k\right)^2 + \left(K_{II}{}^k\right)^2\right] \qquad \textit{Equation 2-72}$$

By considering a kinked crack which is significantly smaller than the main crack, the stress intensity factors of the kinked crack can be expressed in terms of the main crack stress intensity factors, as provided by Equation 2-73:

$$K_I{}^k = C_{11}K_I + C_{12}K_{II}$$

Equation 2-73

$$K_{II}{}^k = C_{21}K_I + C_{22}K_{II}$$

Solutions to determining the coefficients in Equation 2-73 have been provided by multiple sources such as Hussain et al. [109], Nuismer [110], and later by Cotterell and Rice [111]. Cotterell and Rice used the small kink angle assumption to expressed C_{ij}, which are defined by Equation 2-74.

$$C_{11} = \frac{1}{4}\left(3\cos\frac{\theta}{2} + \cos\frac{3\theta}{2}\right) \qquad C_{12} = -\frac{3}{4}\left(\sin\frac{\theta}{2} + \sin\frac{3\theta}{2}\right)$$

Equation 2-74

$$C_{21} = \frac{1}{4}\left(\sin\frac{\theta}{2} + \sin\frac{3\theta}{2}\right) \qquad C_{22} = \frac{1}{4}\left(\cos\frac{\theta}{2} + 3\cos\frac{3\theta}{2}\right)$$

If a crack extension follows a path that continuously changes direction, a local Mode I condition $(K_{II} = 0)$ prevails near the tip of the kinked crack. This leads to the $K_{II} = 0$ criterion which stipulates that a crack will initially propagate in the direction that makes ${K_{II}}^{k}$ equal to zero. This leads to Equation 2-75, also known as the local symmetry criterion [112].

$$ {K_{II}}^{k} = \frac{1}{4}\left[\sin\frac{\theta}{2} + \sin\frac{3\theta}{2}\right]K_I + \frac{1}{4}\left[\cos\frac{\theta}{2} + 3\cos\frac{3\theta}{2}\right]K_{II} \qquad \textit{Equation 2-75} $$

2.3.5.1. Experimental effects of residual stress on the crack trajectory

The establishment of a mix mode stress field is the fundamental key in obtaining crack kinking or trajectory modifications. In most cases, the mixed-mode loading was established through a secondary perpendicular loading or by creating a stress concentration, like a hole in the sample [107,113–115]. Irving et al. studied the influence of welding residual stresses on crack trajectories by combining them with a stress concentration factor. Figure 2.50 showed that the welding residual stress caused a crack deviation to occur at a smaller crack length than the case without the weld [11]. Finite element analysis confirmed the trajectory modification which occurred at shorter crack lengths. This gives rise to the fact that residual stress could be used to induce a modification of the crack trajectory.

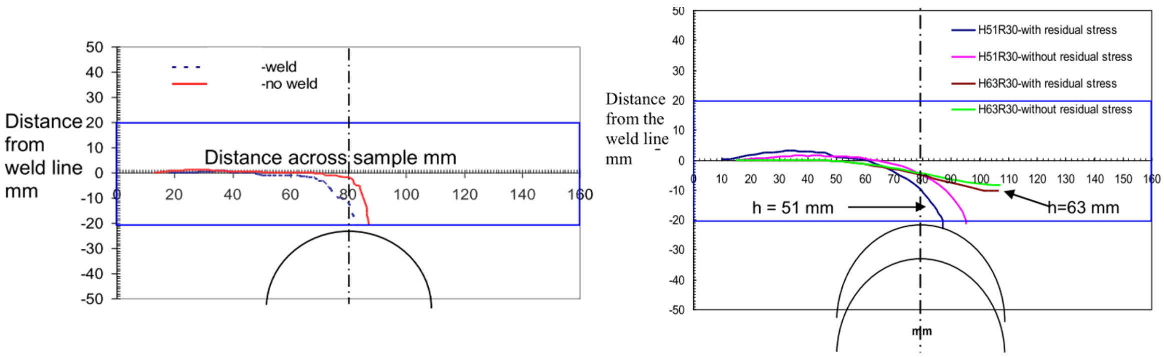

Figure 2.50: Influence of welding residual stresses on crack trajectory (a) experimental determined crack trajectory, (b) finite element analysis of crack trajectory in the presence of welding residual stresses [11]

2.4. Conclusions

This chapter has provided an overview of the general concepts of stress, strain, residual stress and linear elastic fracture mechanics. With a particular focus on LSP, the influence of the fundamental process parameters on the induced residual stress distribution and fatigue performance have been provided. Application of LSP requires substantial consideration of all factors to ensure an optimum outcome. A review of the most relevant LSP simulation techniques showed the associated complexities of accurately predicting the LSP process outcomes and that further developments are required to improve this dynamic process's predictive methods.

Residual stress effects on fatigue crack propagation were also analysed, and the most relevant techniques to determine the stress intensity in complex loading systems were introduced. These methods provided an adequate understanding of predicting the growth and trajectory of cracks in residual stress fields' vicinity. Experimental results from published works in this field show that LSP is a powerful tool in influencing fatigue cracks in engineering structures.

2.5. References

[1] European Aviation Safety Agency. Certification Specifications for Large Aeroplanes CS-25 2007:1-C–22.

[2] Wang CH. Introduction To Fracture Mechanics. DSTO Aeronautical and Maritime Research Laboratory; 1996. https://doi.org/10.13140/RG.2.1.1444.2408.

[3] Findlay SJ, Harrison ND. Why aircraft fail. Mater Today 2002;5:18–25. https://doi.org/10.1016/S1369-7021(02)01138-0.

[4] National Transportation Safety Board. AAR-07-04: In-flight Separation of Right Wing Flying Boat, Inc. (doing business as Chalk's Ocean Airways) light 101 Grumman Turbo Mallard (G-73T). CreateSpace Independent Publishing Platform; 2005.

[5] Nelson DV. Effect of residual stress on fatigue crack propagation. In: Throop J, Reemsnyder H, editors. ASTM STP 776, Am. Soc. Test. Mater., 1982, p. 172–94. https://doi.org/https://doi.org/10.1520/STP30104S.

[6] Clauer AH. Laser Shock Peening for Fatigue Resistance. In: Gregory JK, Rack HJ, Eylon D, editors. Surf. Perform. Titan., 1996, p. 217–30.

[7] Peyre P, Fabbro R, Merrien P, Lieurade HP. Laser shock processing of aluminium alloys. Application to high cycle fatigue behaviour. Mater Sci Eng A 1996;210:102–13. https://doi.org/10.1016/0921-5093(95)10084-9.

[8] National Transportation Safety Board Aircraft Accident Report. Aviation Accident Report AAR-89/03 - Aloha Airlines Flight 243, Boeing 737-200, N73711. Near Maui, Hawaii: 1989.

[9] Kosai M, Kobayashi AS. DOT/FAA/AR-95/43 Axial Crack Propagation and Arrest in Pressurized Fuselage. In: Atluri SN, Sampath SG, Tong P, editors. Struct. Integr. Ageing Airplanes, Springer Series in Computational Mechanics. Springer,; 1991, p. 1–187. https://doi.org/https://doi.org/10.1007/978-3-642-84364-8_16.

[10] Skorupa A, Skorupa M. Riveted Lap Joints in a Pressurized Aircraft Fuselage. In: Gladwell GML, editor. Solid Mech. its Appl., Springer; 2012, p. 1–9. https://doi.org/10.1007/978-94-007-4282-6_1.

[11] Irving P, Ma YE, Zhang X, Servetti G, Williams S, dos Santos J, et al. Control of crack growth rates and crack trajectories for enhanced fail safety and damage tolerance in welded aircraft strucutres. 25th Symp. Int. Comm. Aeronaut. Fatigue (ICAF 2009), Rotterdam: 2009. https://doi.org/10.1007/978-90-481-2746-7_23.

[12] Askeland DR, Fulay PP. Essentials of Material science and engineering. Second edi. Cengage Learning; 2010.

[13] Fitzpatrick ME, Demaid A, Earl C, Edwards L, Gungor S, Hush M, et al. Structural integrity: designing against failure Stress Analysis. The Open University; 2007.

[14] Dowling NE. Mechanical behavior of materials: Engineering methods for deformation, fracture and fatigue. 4th ed. Pearson; 2012.

[15] Soul F, Hamdy N. Numerical Simulation of Residual Stress and Strain Behavior After Temperature Modification. Weld Process 2012:217–46. https://doi.org/978-953-51-0854-2.

[16] Withers PJ, Bhadeshia HKDH. Residual stress. Part 1–measurement techniques. Mater Sci Technol 2001;17:355–65. https://doi.org/10.1179/026708301101509980.

[17] Montross CS, Wei T, Ye L, Clark G, Mai YW. Laser shock processing and its effects on microstructure and properties of metal alloys: A review. Int J Fatigue 2002;24:1021–36. https://doi.org/10.1016/S0142-1123(02)00022-1.

[18] Ding K, Ye L. Laser shock peening performance and process simulation. Cambridge England: Woodhead Publishing Limited; 2006. https://doi.org/10.1016/B978-1-85573-929-1.50009-3.

[19] Ramadhan RS, Syed AK, Tremsin AS, Kockelmann W, Dalgliesh R, Chen B, et al. Mapping residual strain induced by cold working and by laser shock peening using neutron transmission spectroscopy. Mater Des 2018;143:56–64. https://doi.org/10.1016/j.matdes.2018.01.054.

[20] Clauer AH, Fairand BP, Wilcox BA. Pulsed laser induced deformation in an Fe-3 Wt Pct Si alloy. Metall Trans A 1977;8:119–25. https://doi.org/10.1007/BF02677273.

[21] Polese C, Glaser D, Bedekar R. Water Confinement Influences on the Laser Shock Peening process Water Confinement Influences on the Laser Shock Peening process. 30th Int. Congr. High-Speed Imaging Photonics, 2016. https://doi.org/978-0-620-56214-0.

[22] Gujba A, Medraj M. Laser Peening Process and Its Impact on Materials Properties in Comparison with Shot Peening and Ultrasonic Impact Peening. Materials (Basel) 2014;7:7925–74. https://doi.org/10.3390/ma7127925.

[23] Dane C, Hackel L, Daly J. Shot Peening with Laser. Adv Mater Process 1998;153:37–48.

[24] Champagne V, Grendahl S, Tenaglia R, Lahrman D. Laser Peening for U.S. Army Helicopters. 27th Replace. Hard Chrome Cadmium Plat. Progr. Rev. Meet., Army Research Laboratory, LSP Technologies, Aberdeen Proving Ground; 2007.

[25] Guo YB, Caslaru R. Fabrication and characterization of micro dent arrays produced by laser shock peening on titanium Ti-6Al-4V surfaces. J Mater Process Technol 2011;211:729–36. https://doi.org/10.1016/j.jmatprotec.2010.12.007.

[26] Peyre P, Fabbro R, Berthe L. Laser shock processing to improve mechanical properties of metallic materials 1997;17:589–98. https://doi.org/10.2495/SURF970261.

[27] Clauer A, Walters C, Ford S. The effects of laser shock processing on the fatigue properties of 2024-T3 aluminium. Lasers Mater. Process., ASM International; 1983, p. 7.

[28] Zhang YK, Ren XD, Zhou JZ, Lu JZ, Zhou LC. Investigation of the stress intensity factor changing on the hole crack subject to laser shock processing. Mater Des 2009;30:2769–73. https://doi.org/10.1016/j.matdes.2008.09.033.

[29] Fairand BP, Clauer AH. Effect of water and paint coatings on the magnitude of laser-generated shocks. Opt Commun 1976;18:588–91. https://doi.org/https://doi.org/10.1016/0030-4018(76)90327-8.

[30] Fabbro R, Peyre P, Berthe L, Scherpereel X. Physics and applications of laser-shock processing. J Laser Appl 1998;10:265–79. https://doi.org/10.2351/1.521861.

[31] Berthe L. Laser-breakdown phenomena in transparent materials: Application to shock wave generation from a water-confined laser-generated plasma. Orsay University, 1998.

[32] Kennedy PK, Hammer DX, Rockwell BA. Laser-induced breakdown in aqueous media. Prog Quantum Electron 1997;21:155–248. https://doi.org/10.1016/S0079-6727(97)00002-5.

[33] Peyre P, Fabbro R. Laser shock processing: a review of the physics and applications. Opt Quantum Electron 1995;27:1213–29. https://doi.org/10.1007/BF00326477.

[34] Fournier J, Ballard P, Merrien P, Barralis J, Castex L, Fabbro R. Mechanical effects induced by shock waves generated by high energy laser pulses. J Phys III 1991;9:1467–80. https://doi.org/10.1051/jp3:1991204.

[35] Fabbro R, Fournier J, Ballard P, Devaux D, Virmont J. Physical study of laser-produced plasma in confined geometry. J Appl Phys 1990;68:775–84. https://doi.org/10.1063/1.346783.

[36] Hong X, Wang S, Guo D, Wu H, Wang J, Dai Y, et al. Confining medium and absorptive overlay: Their effects on a laser-induced shock wave. Opt Lasers Eng 1998;29:447–55. https://doi.org/10.1016/S0143-8166(98)80012-2.

[37] Sticchi M, Staron P, Sano Y, Meixer M, Klaus M, Rebelo-Kornmeier J, et al. A parametric study of laser spot size and coverage on the laser shock peening induced residual stress in thin aluminium samples. J Eng 2015;2015:97–105. https://doi.org/10.1049/joe.2015.0106.

[38] Hu Y, Gong C, Yao Z, Hu J. Investigation on the non-homogeneity of residual stress field induced by laser shock peening. Surf Coatings Technol 2009;203:3503–8. https://doi.org/10.1016/j.surfcoat.2009.04.029.

[39] Li X, He W, Luo S, Nie X, Tian L, Feng X, et al. Simulation and experimental study on residual stress distribution in titanium alloy treated by laser shock peening with flat-top and Gaussian laser beams. Materials (Basel) 2019;12:1–12. https://doi.org/10.3390/ma12081343.

[40] Hfaiedh N, Peyre P, Song H, Popa I, Ji V, Vignal V. Finite element analysis of laser shock peening of 2050-T8 aluminum alloy. Int J Fatigue 2015;70:480–9. https://doi.org/10.1016/j.ijfatigue.2014.05.015.

[41] Correa C, Gil-Santos A, Porro JA, Díaz M, Ocaña JL. Eigenstrain simulation of residual stresses induced by laser shock processing in a Ti6Al4V hip replacement. Mater Des 2015;79:106–14. https://doi.org/10.1016/j.matdes.2015.04.048.

[42] Le Bras C, Rondepierre A, Seddik R, Scius-Bertrand M, Rouchausse Y, Videau L, et al. Laser shock peening: toward the use of pliable solid polymers for confinement. Metals (Basel) 2019;9:1–13. https://doi.org/10.3390/met9070793.

[43] Masse JE, Barreau G. Surface Modification by Laser Induced Shock Waves. Surf Eng 1995;11:131–2. https://doi.org/10.1179/sur.1995.11.2.131.

[44] Langer K, Spradlin TJ, Fitzpatrick ME. Finite element analysis of laser peening of thin aluminum structures. Metals (Basel) 2020;10. https://doi.org/10.3390/met10010093.

[45] Clauer A. Laser Shock Peening for Fatigue Resistance. Surf Perform Titan 1996:217–30.

[46] Sano Y, Kimura M, Yoda M, Mukai N, Sato K, Uehara T, et al. Development of Fiber-Delivered Laser Peening System to Prevent Stress Corrosion Cracking of Reactor Components. 9th Int. Conf. Nucl. Eng., Nice Acropolis France: 2001.

[47] Peyre P, Carboni C, Forget P, Beranger G, Lemaitre C, Stuart D. Influence of thermal and mechanical surface modifications induced by laser shock processing on the initiation of corrosion pits in 316L stainless steel. J Mater Sci 2007;42:6866–77. https://doi.org/10.1007/s10853-007-1502-4.

[48] Porro JA, Ocaña JL, Grum J. Laser shock peening without absorbent coating (LSPwC) effect on 3D surface topography and mechanical properties of 6082-T651 Al alloy. Surf Coat Technol

2012;208:109–16. https://doi.org//10.1016/j.surfcoat.2012.08.048.

[49] Davis B, Mannava S, Rockstroh T, Hahn J. Performance of Gen IV LSP for Thick Section Airfoil Damage Tolerance. 45th AIAA/ASCE/AHS/ASC Struct. Struct. Dyn. Mater. Conf., Palm Springs, California: 2012, p. 1–10. https://doi.org/10.2514/6.2004-2062.

[50] LSP Technologies Inc. Application Review 2014.

[51] Pavan M. Laser Shock Peening for Fatigue Life enhancement of Aerospace Components. Coventry University, 2018.

[52] Sano Y, Obata M, Kubo T, Mukai N, Yoda M, Masaki K, et al. Retardation of crack initiation and growth in austenitic stainless steels by laser peening without protective coating 2006;417:334–40. https://doi.org/10.1016/j.msea.2005.11.017.

[53] Karthik D, Kalainathan S, Swaroop S. Surface & Coatings Technology Surface modi fi cation of 17-4 PH stainless steel by laser peening without protective coating process. Surf Coat Technol 2015;278:138–45. https://doi.org/10.1016/j.surfcoat.2015.08.012.

[54] Nobre JP, Polese C, van Staden SN. Incremental Hole Drilling Residual Stress Measurement in Thin Aluminum Alloy Plates Subjected to Laser Shock Peening. Exp Mech 2020;60:553–64. https://doi.org/10.1007/s11340-020-00586-5.

[55] Crooker P, Lian T. Materials Reliability Program: Technical Basis for Primary Water Stress Corrosion Cracking Mitigation by Surface Stress Improvement (MRP-267, Revision 2). 2016.

[56] Ye C, Suslov S, Kim BJ, Stach EA, Cheng GJ. Fatigue performance improvement in AISI 4140 steel by dynamic strain ageing and dynamic precipitation during warm laser shock peening. Acta Mater 2011;59:1014–25. https://doi.org/10.1016/j.actamat.2010.10.032.

[57] Peyre P, Fabbro R, Merrien P, Lieurade H. Laser shock processing of aluminium alloys. Application to high cycle fatigue behaviour. Mater Sci Eng 1996;210:102–13. https://doi.org/10.1016/0921-5093(95)10084-9.

[58] Braisted W, Brockman R. Finite element simulation of laser shock peening. Int J Fatigue 1999;21:719–24. https://doi.org/10.1016/S0142-1123(99)00035-3.

[59] Ding K, Ye L. Three-dimensional dynamic finite element analysis of multiple laser shock peening processes. Surf Eng 2003;19:351–8. https://doi.org/10.1179/026708403225007563.

[60] Ocaña JL, Morales M, Molpeceres C, Torres J. Numerical simulation of surface deformation and residual stresses fields in laser shock processing experiments. Appl Surf Sci 2004;238:242–8. https://doi.org/10.1016/j.apsusc.2004.05.232.

[61] Brockman RA, Braisted WR, Olson SE, Tenaglia RD, Clauer AH, Langer K, et al. Prediction and characterization of residual stresses from laser shock peening. Int J Fatigue 2012;36:96–108. https://doi.org/10.1016/j.ijfatigue.2011.08.011.

[62] Keller S, Chupakhin S, Staron P, Maawad E, Kashaev N, Klusemann B. Experimental and numerical investigation of residual stresses in laser shock peened AA2198. J Mater Process Technol 2018;255:294–307. https://doi.org/10.1016/j.jmatprotec.2017.11.023.

[63] Zhu R, Zhang YK, Sun GF, Zhang SB, Li P, Ni ZH. Finite Element Analysis of Residual Stress Induced by Multiple Laser Shock Peening with Square Spots. Int J Peen Sci Technol 2018;1:99–118. https://doi.org/10.1051/epjap:2003037.

[64] Hatamleh MI, Shankar Mahadevan J, Malik AS, Qian D. Variable Damping Profiles for Laser Shock Peening Simulation Using Modal Analysis and the SEATD Method 2017. https://doi.org/10.1115/msec2017-2891.

[65] Warren AW, Guo YB, Chen SC. Massive parallel laser shock peening: Simulation, analysis, and validation. Int J Fatigue 2008;30:188–97. https://doi.org/10.1016/j.ijfatigue.2007.01.033.

[66] Dassault Systemes. ABAQUS User's Manual, version 6.14 2014.

[67] Clauer AH, Holbrook JH, Fairand BP. Effects of Laser Induced Shock Waves on Metals. Shock Waves High-Strain-Rate Phenom. Met., Boston, MA: Springer; 1981. https://doi.org/10.1007/978-1-4613-3219-0_38.

[68] Zhou W, Ren X, Yang Y, Tong Z, Asuako Larson E. Finite element analysis of laser shock peening induced near-surface deformation in engineering metals. Opt Laser Technol 2019;119:105608. https://doi.org/10.1016/j.optlastec.2019.105608.

[69] Brockman R, Braisted W, Spradlin T, Langer K, Olson S, Fitzpatrick ME. High Strain-Rate Material Model Validation for Laser Peening Simulation. J Eng 2015:1–8. https://doi.org/10.1049/joe.2015.0118.

[70] Amarchinta HK, Grandhi R V, Langer K, Stargel DS. Material model validation for laser shock peening process simulation. Model Simul Mater Sci Eng 2009;17:015010. https://doi.org/10.1088/0965-0393/17/1/015010.

[71] Crudo C, Troiani E. Investigation on Laser Shock Peening Capability by FE Simulation. University of Bologna, 2013.

[72] Zerilli FJ, Armstrong RW, Frank J, Armstrong RW. Dislocation mechanics based constitutive relations for material dynamics calculations dislocation mechanics based constit utive relations for material dynamics calculations 1987;1816. https://doi.org/10.1063/1.338024.

[73] Bhamare S, Ramakrishnan G, Mannava SR, Langer K, Vasudevan VK, Qian D. Simulation-based optimization of Laser Shock Peening process for improved bending fatigue life of Ti-6Al-2Sn-4Zr-2MoAlloy. Surf Coat Technol 2013;232:464–74. https://doi.org/10.1016/j.surfcoat.2013.06.003.

[74] Lesuer DR. Experimental Investigations of Material Models for Ti6Al4V Titanium and 2024-T3 Aluminum. vol. DOT/FAA/AR. 1999. https://doi.org//10.2172/11977.

[75] Angulo I, Cordovilla F, García-Beltrán A, Smyth NS, Langer K, Fitzpatrick ME, et al. The effect of material cyclic deformation properties on residual stress generation by laser shock processing. Int J Mech Sci 2019;156:370–81. https://doi.org/10.1016/j.ijmecsci.2019.03.029.

[76] Dewald AT, Hill MR. Eigenstrain based model for prediction of laser peening residual stresses in arbitrary 3D bodies : Part 1 model description. J Strain Anal Eng Des 2009;44:1–11. https://doi.org/10.1243/03093247JSA417.

[77] Coratella S, Sticchi M, Toparli MB, Fitzpatrick ME, Kashaev N. Surface & Coatings Technology Application of the eigenstrain approach to predict the residual stress distribution in laser shock peened AA7050-T7451 samples. Surf Coat Technol 2015;273:39–49. https://doi.org/10.1016/j.surfcoat.2015.03.026.

[78] Callister Jr. WD, Rethwisch DG. Materials Science and Engineering. 7th ed. Wiley, 2007; 2010. https://doi.org/10.1007/BF01184995.

[79] Janssen M, Zuidema J, Wanhill RJH. Fracture mechanics. 2nd ed. 2003. https://doi.org/10.1016/B978-012654640-8/50019-5.

[80] Griffith AA. The phenomena of rupture and flow in solids. Philos Trans Ser A 1920;221:163–98. https://doi.org/10.1098/rsta.1921.0006.

[81] Janssen M, Zuidema J, Wanhill R. Fracture Mechanics. 2nd ed. Springer; 2004. https://doi.org/10.1007/978-3-319-24999-5.

[82] ASTM International. ASTM E647 - Standard Test Method for Measurement of Fatigue Crack Growth Rates. ASTM B Stand 2016;03:1–49. https://doi.org/10.1520/E0647-15E01.2.

[83] Anderson TL. Fracture mechanics: fundamentals and application. 3rd ed. CRC Press; 2005.

[84] Michael Hudson C. Effect of stress ratio on fatigue-crack growth in 7075-T6 and 2024-T3 aluminium alloy specimens. Eng Fract Mech 1969;1:429–46. https://doi.org/10.1016/0013-7944(69)90003-4.

[85] Walker K. The Effect of Stress Ratio During Crack Propagation and Fatigue for 2024-T3 and 7075-T6 Aluminum, Effects of Environment and Complex Load History on Fatigue Life, ASTM STP 462. Am Soc Test Mater 1970:1–14. https://doi.org/10.1520/stp32032s.

[86] Forman RG, Hearney VE, Engle RM. Numerical analysis of crack propagation in cyclic-loaded structures. J Basic Eng 1967;89:459–64. https://doi.org/10.1115/1.3609637.

[87] Forman RG, Mettu SR. Behavior of surface and corner cracks subjected to tensile and bending loads in a Ti-6Al-4V alloy. NASA Tech Memo 102165 1990;I:1–54.

[88] Parker AP. Stress Intensity Factors, Crack Profiles, and Fatigue Crack Growth Rates in Residual Stress Fields. ASTM STP 776, Am Soc Test Mater 1982:13–31. https://doi.org/10.1520/stp30095s.

[89] Wolf E. Fatigue crack closure under cyclic tension. Eng Fract Mech 1970;2:37–45. https://doi.org/10.1017/CBO9781107415324.004.

[90] LaRue JE, Daniewicz SR. Predicting the effect of residual stress on fatigue crack growth. Int J Fatigue 2007;29:508–15. https://doi.org/10.1016/j.ijfatigue.2006.05.008.

[91] Jones KW, Dunn ML. Fatigue crack growth through a residual stress field introduced by plastic beam bending. Fatigue Fract Eng Mater Struct 2008;31:863–75. https://doi.org/10.1111/j.1460-2695.2008.01274.x.

[92] Sikhamov R, Fomin F, Klusemann B, Kashaev N. The influence of laser shock peening on fatigue properties of AA2024-T3 alloy with a fastener hole. Metals (Basel) 2020;10:1–13. https://doi.org/10.3390/met10040495.

[93] Rubio-González C, Felix-Martinez C, Gomez-Rosas G, Ocaña JL, Morales M, Porro JA. Effect of laser shock processing on fatigue crack growth of duplex stainless steel. Mater Sci Eng A 2011;528:914–9. https://doi.org/10.1016/j.msea.2010.10.020.

[94] Rubio-González C, Ocaña JL, Gomez-Rosas G, Molpeceres C, Paredes M, Banderas A, et al. Effect of laser shock processing on fatigue crack growth and fracture toughness of 6061-T6 aluminum alloy. Mater Sci Eng A 2004;386:291–5. https://doi.org/10.1016/j.msea.2004.07.025.

[95] Hong Z, Chengye Y. Laser shock processing of 2024-T62 aluminum alloy. Mater Sci Eng A 1998;257:322–7. https://doi.org/10.1016/S0921-5093(98)00793-X.

[96] Ivetic G, Meneghin I, Troiani E, Molinari G, Ocaña J, Morales M, et al. Fatigue in laser shock peened open-hole thin aluminium specimens. Mater Sci Eng A 2012;534:573–9. https://doi.org/10.1016/j.msea.2011.12.010.

[97] Zhang XQ, Li H, Yu XL, Zhou Y, Duan SW, Li SZ, et al. Investigation on effect of laser shock processing on fatigue crack initiation and its growth in aluminum alloy plate. Mater Des 2015;65:425–31. https://doi.org/10.1016/j.matdes.2014.09.001.

[98] Zhang L, Lu JZ, Zhang YK, Luo KY, Zhong JW, Cui CY, et al. Effects of different shocked paths on fatigue property of 7050-T7451 aluminum alloy during two-sided laser shock processing. Mater Des 2011;32:480–6. https://doi.org/10.1016/j.matdes.2010.08.039.

[99] Liu KK, Hill MR. The effects of laser peening and shot peening on fretting fatigue in Ti-6Al-4V coupons. Tribol Int 2009;42:1250–62. https://doi.org/10.1016/j.triboint.2009.04.005.

[100] Sanchez AG, You C, Leering M, Glaser D, Furfari D, Fitzpatrick ME, et al. Effects of laser shock peening on the mechanisms of fatigue short crack initiation and propagation of AA7075-T651. Int J Fatigue 2021;143:106025. https://doi.org/10.1016/j.ijfatigue.2020.106025.

[101] Chahardehi A, Brennan FP, Steuwer A. The effect of residual stresses arising from laser shock peening on fatigue crack growth. Eng Fract Mech 2010;77:2033–9. https://doi.org/10.1016/j.engfracmech.2010.03.033.

[102] Taddia S, Troiani E. Effect of Laser Shock Peening on the Fatigue Behavior of Thin Aluminum Panels. Mater Today Proc 2015;2:5006–14. https://doi.org/10.1016/j.matpr.2015.10.090.

[103] Busse DO. Extending fatigue life of aircraft fuselage structures using laser peening. Cranfield University, 2017.

[104] Keller S, Horstmann M, Kashaev N, Klusemann B. Crack closure mechanisms in residual stress fields generated by laser shock peening: A combined experimental-numerical approach. Eng Fract Mech 2019;221:106630. https://doi.org/10.1016/j.engfracmech.2019.106630.

[105] van Aswegen DC, Polese C. Experimental and analytical investigation of the effects of laser shock peening processing strategy on fatigue crack growth in thin 2024 aluminium alloy panels. Int J Fatigue 2021;142:105969. https://doi.org/10.1016/j.ijfatigue.2020.105969.

[106] Pavan M, Furfari D, Ahmad B, Gharghouri MA, Fitzpatrick ME. Fatigue crack growth in a laser shock peened residual stress field. Int J Fatigue 2019;123:157–67. https://doi.org/10.1016/j.ijfatigue.2019.01.020.

[107] Erdogan F, Sih GC. On the crack extension in plates under plane loading and transverse shear. J Fluids Eng Trans ASME 1963;85:519–25. https://doi.org/10.1115/1.3656897.

[108] Palaniswamy K, Knauss WG. On the Problem of Crack Extension in Brittle Solids Under General Loading. vol. 4. Pergamon Press Inc; 1978. https://doi.org/10.1016/B978-0-08-021792-5.50010-0.

[109] Hussain MA, Pu SL, Underwood J. Strain Energy Release Rate for a Crack Under Combined Mode I and Mode II. Am Soc Test Mater 1974:2–28. https://doi.org/10.1520/stp33130s.

[110] Nuismer RJ. An energy release rate criterion for mixed mode fracture. Int J Fract 1975;11:245–50. https://doi.org/10.1007/BF00038891.

[111] Cotterell B, Rice JR. Slightly curved or kinked cracks. Int J Fract 1980;16:155–69. https://doi.org/10.1007/BF00012619.

[112] Goldstein RV, Salganik RL. Brittle fracture of solids with arbitrary cracks. Int J Fract 1974;10:507–23. https://doi.org/10.1007/BF00155254.

[113] Blažić M, Maksimović S, Petrović Z, Vasović I, Turnić D. Determination of fatigue crack growth trajectory and residual life under mixed modes. Stroj Vestnik/Journal Mech Eng 2014;60:250–4. https://doi.org/10.5545/sv-jme.2013.1354.

[114] Tilbrook M, Hoffman M. Approximation of curved cracks under mixed-mode loading. Eng Fract Mech 2007;74:1026–40. https://doi.org/10.1016/j.engfracmech.2006.12.008.

[115] Dirik H, Yalçinkaya T. Crack path and life prediction under mixed mode cyclic variable amplitude loading through XFEM. Mech Today 1978;4:87–148. https://doi.org/10.1016/j.ijfatigue.2018.04.026.

Chapter 3 Experimental procedures

This chapter introduces and describes the various materials, sample specifications, LSP treatments, and test procedures used to complete this work. A general overview of the materials used and their relation to the respective studies has been provided below:

(1) *LSP temporal profile samples* (6 mm thick AA2524-T351) were used to study the laser beam temporal profile's effect on residual stress formation. This alloy and temper were selected for this study as it is a representative material used in the underwing skin sections of commercial aircraft and was readily available. Additionally, the thickness of the sample resisted excessive distortion during LSP processing. This material was provided by Airbus (project sponsor).

(2) *Innovative confinement samples* (2 mm thick AA2024-T351) were used to study the effects of LSP whilst utilising an innovative confinement medium. This alloy and temper were selected for this study as it is a representative material that is widely used in the construction of commercial aircraft fuselage structures. The material was supplied by Airbus and had been chemically milled to remove the clad layer.

(3) *Crack trajectory modification samples* (2.032 mm thick AA2024-T3) were used to investigate the feasibility of using LSP residual stresses as a crack trajectory modification technique. This alloy, temper and thickness were selected for this study due to its similarity to the materials used in the construction of modern commercial aircraft fuselage structures. AA2024-T3 is extensively used in aircraft construction but has recently been replaced by AA2524-T3 as the primary fuselage material [1]. AA2524-T3 in suitable gauge thickness could not be sourced for this research thus appropriate AA2024-T3 material has been used. These alloys were found to have similar material properties.

Descriptions of the residual stress measurements using the incremental hole drilling and diffraction techniques are discussed and provide details about the techniques instrumentation and methodologies. Lastly, this chapter outlines the test procedures and test matrices used in the mechanical crack growth testing campaign.

3.1. Material characterisation

Three different aluminium alloys and tempers were used in the completion of this research. The nominal chemical composition of the materials is listed in Table 3.1 [1].

Table 3.1: Alloying composition of all research materials [1]

Alloy	Weight percentage of alloying elements (remainder aluminium)								
	Cu	Zn	Mg	Mn	Fe	Si	Cr	Zr	Ti
AA2024	4.4	-	1.5	0.6	≤0.5	≤0.5	0.1	-	0.15
AA2524	4.0-4.5	0.15	1.2-1.6	0.45–0.7	0.12	0.06	0.05	-	0.1

The T3 treatment of the material consisted of solution heat treatment, cold working and natural ageing to a stable condition. The T351 treatment of the material consisted of solution heat treatment and stress relief by stretching [2].

3.1.1. Metallographic analysis of materials

A metallographic analysis was carried out on the various materials to estimate the grain size along the Longitudinal (L), Transverse (T) and Short transverse (S) directions. Small samples along L-S and T-S directions were extracted, mounted and polished with mechanical grinding (600, 800, 1200 grit and 3 μm diamond compound). Figure 3.1 indicated the grain orientation reference used throughout this research. The prepared surface was etched with a chemical solution of 92% distilled water, 6% nitric acid, and 2% hydrofluoric acid to expose the grain boundaries [3].

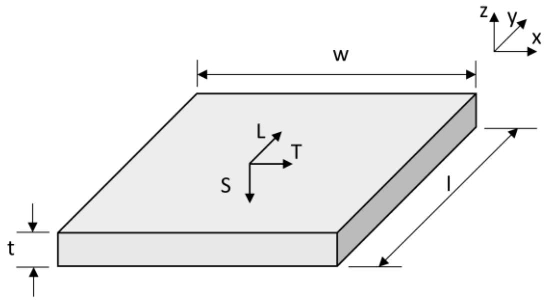

Figure 3.1: Grain orientation reference, L – Longitudinal direction, T - Transverse direction, S – Short direction

The grain size was estimated using the linear intercept method described in the ASTM standard E112-13 [4]. All materials exhibited a typical 'pancake' grain structure with elongated grains along the longitudinal direction, as shown in Figure 3.2 to Figure 3.4. Table 3.2 listed the grain size estimations for the various alloys.

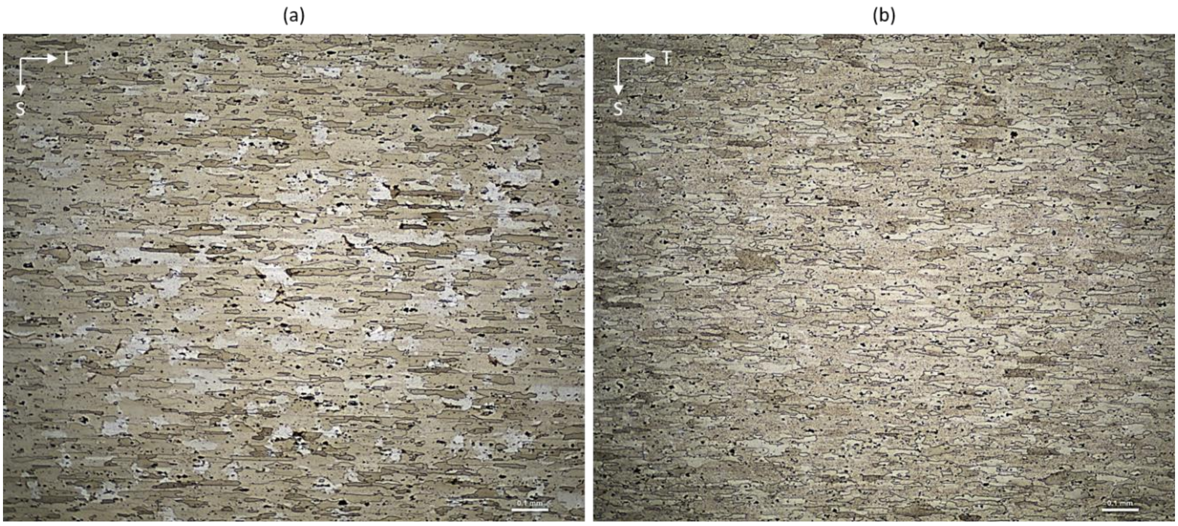

Figure 3.2: Optical micrograph of AA2024-T3 grain structure, (a) L-S orientation, (b) T-S orientation

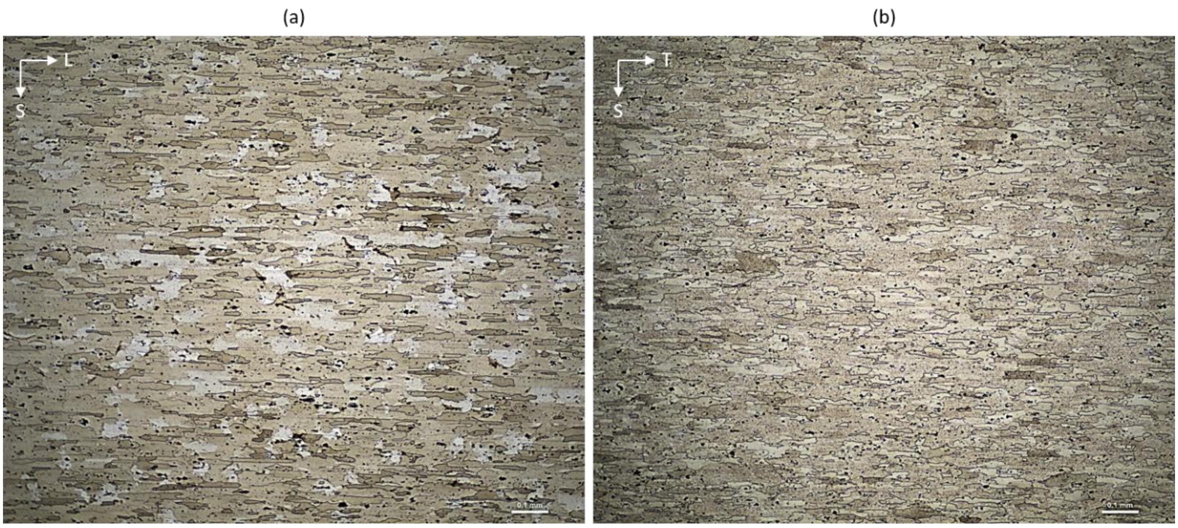

Figure 3.3: Optical micrograph of AA2024-T351 grain structure, (a) L-S orientation, (b) T-S orientation

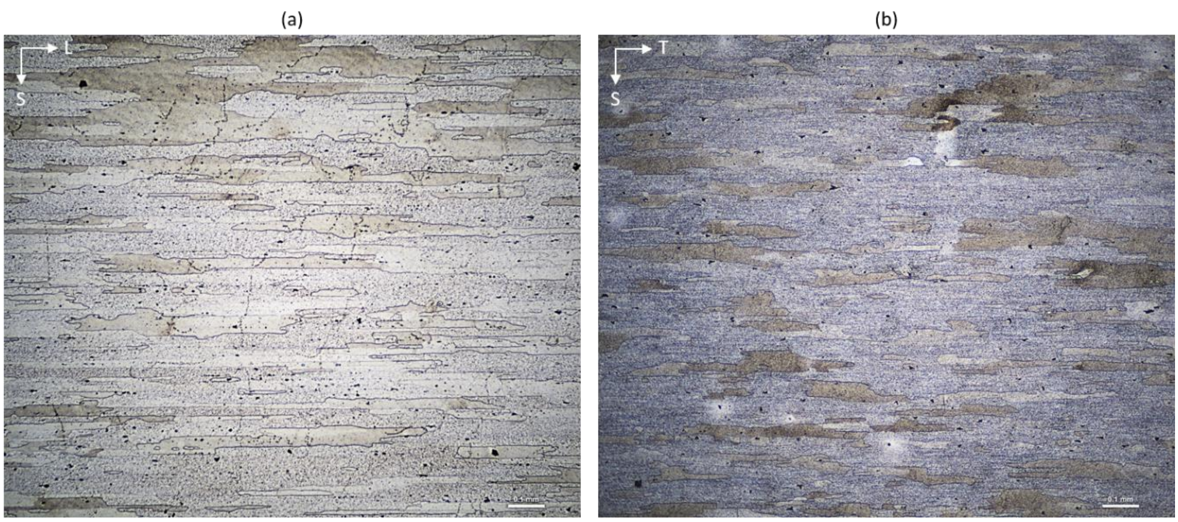

Figure 3.4: Optical micrograph of AA2524-T351 grain structure, (a) L-S orientation, (b) T-S orientation

Table 3.2: Grain size measurements of the research materials along the principle axis

Material	L - Longitudinal direction [µm]	T - Transverse direction [µm]
AA2024-T3	176	84
AA2024-T351	76	71
AA2524-T351	264	141

The clad layer of the AA2024-T3 and AA2524-T351 were measured with an optical microscope. The AA2024-T3 manufacturing specification sheet indicated a clad thickness range of 3-4% of the total thickness and was applied to both sides of the material. The AA2524-T351 nominal clad thickness was estimated as 2.5% of the total thickness and applied to both sides of the material. The clad layers in Figure 3.5 are identifiable by the difference in brightness from the underlying material. An averaged thickness from ten measurements on each side determined the clad layer thickness of the AA2024-T3 as 71±10 µm and AA2524-T351 as 185±10 µm.

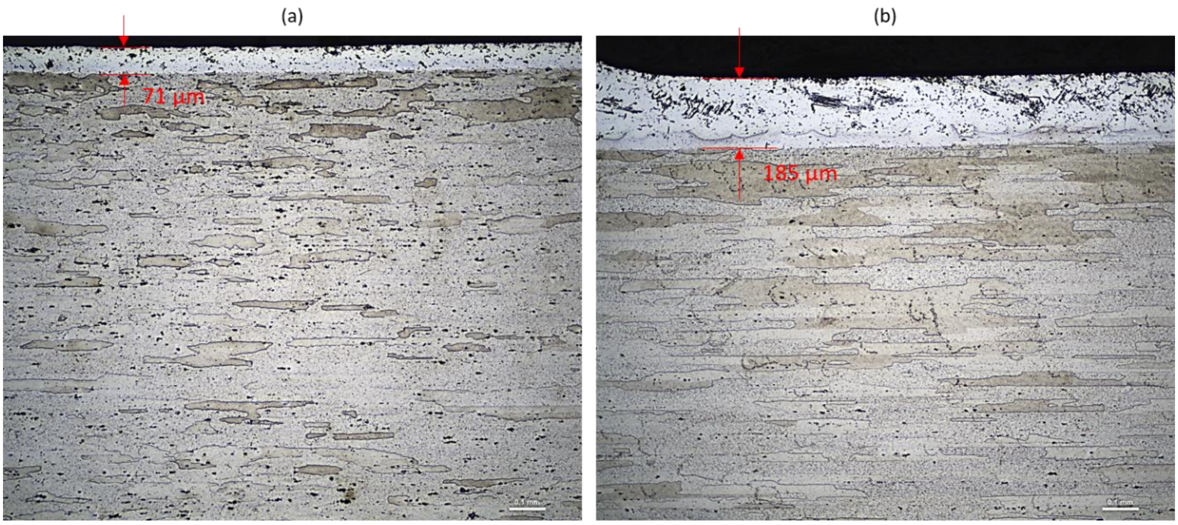

Figure 3.5: Estimated clad layer thickness (a) 2.032 mm thick AA2024-T3, (b) 6 mm thick AA2524-T351

3.1.2. Mechanical properties of research materials

Where possible, the mechanical properties of the research materials were experimentally validated. The dynamic elastic modulus was determined by impulse excitation of vibration according to ASTM standard E1876-15 [5]. An IMCE RFDA Basic impulse excitation apparatus was used with the measurement made in the flexural mode of vibration.

The static strength of the materials was measured parallel (L-S orientation) and perpendicular (T-S orientation) to the longitudinal rolling direction and in accordance with the ASTM standard E8/ E8m [6]. An INSTRON universal testing system with a maximum load capacity of 50 kN and a loading accuracy of 0.5% was used to test the samples to failure. The tests were completed in load controlled mode with the displacements measured with an INSTRON extensometer of a gauge length of 25 mm ± 10%. Table 3.3 listed the properties which are the arithmetic average of three test samples. The listed range in the averaged value in the table indicated the largest variation of any of the three tested samples from the nominal mean value.

Table 3.3: Mechanical properties of research materials

Material	Elastic Modulus [GPa]	Yield Tensile Stress (0.2% offset) [MPa]	Ultimate Tensile Stress [MPa]	Elongation at fracture [%]	Grain direction
AA2024-T3	73.1	313±5	443±5	18±3	T-L
	73.1	338±5	457±9	17±4	L-T
AA2024-T351	73.1	376±2	490±2	17±3	T-L
	73.1	290±3	472±3	19±3	L-T
AA2524-T351	73.1	291±3	430±4	24±5	T-L
	73.1	308±3	440±10	22±6	L-T

3.2. Laser shock peening providers

Two LSP providers were used to process the various samples for this research, namely the HiLASE Laser Shock Peening facility, and the Council for Scientific and Industrial Research – National Laser Centre (CSIR-NLC).

3.2.1. HiLASE laser shock peening facility

Test samples from the LSP temporal profile (Chapter 4) and innovative confinement study (Appendix A) were LSP processed at HiLASE in the Czech Republic. A successful open-access application for LSP processing provided access to this facility and its specialised equipment.

The HiLASE LSP set-up consists of the BIVOJ laser system, a 100 J diode-pumped solid-state laser that was limited to operate with a peak energy of 5 J. The emitted laser light wavelength was 1030 nm (near infra-red region of the spectrum) at a 10 Hz repetition rate. The beam quality (m^2) was found to be 1.7 and 2.3 in the x and y directions [7,8]. Black vinyl tape protected the target surface from direct ablation. The confinement medium was standard tap water in the temporal study, whilst a 3D printed solid polymer confinement was used in the innovative confinement study. The confinement was delivered as a water jet that dispersed into a thin water layer over the processing area. A Fanuc M-20iA/20M robot (load limited to 20 kg with 0.08 mm positioning repeatability) provided the sample manipulation whilst the laser was fixed in position. Figure 3.6 provided an example of the LSP setup used at HiLASE.

A square laser geometry was used throughout and the size was set according to the requirements of the individual samples' LSP parameter requirements. The dimension of the spot size was measured directly on the target surface with a Vernier calliper. The spatial beam profile was measured with a diffractive optical element and is discussed further in Chapter 4. The BIVOJ laser system allowed for user-defined laser temporal profiles and was monitored continuously using a fast measuring oscilloscope. A ramped temporal profile with a measured 7.2 ns representative pulse width at Full Width Half Maximum (FWHM) was used in the confinement study. The various peak power intensities were dependent on the fixed parameters and the variable energy per pulse and adjusted within the operational capabilities of the laser. The peak laser pulse energy (unfocused beam) was measured with a Gentec fast photo-diode and was averaged over at least ten consecutive pulses, the energy was determined with a repetition rate of 10 Hz. The power density was set according to the desired value in each study.

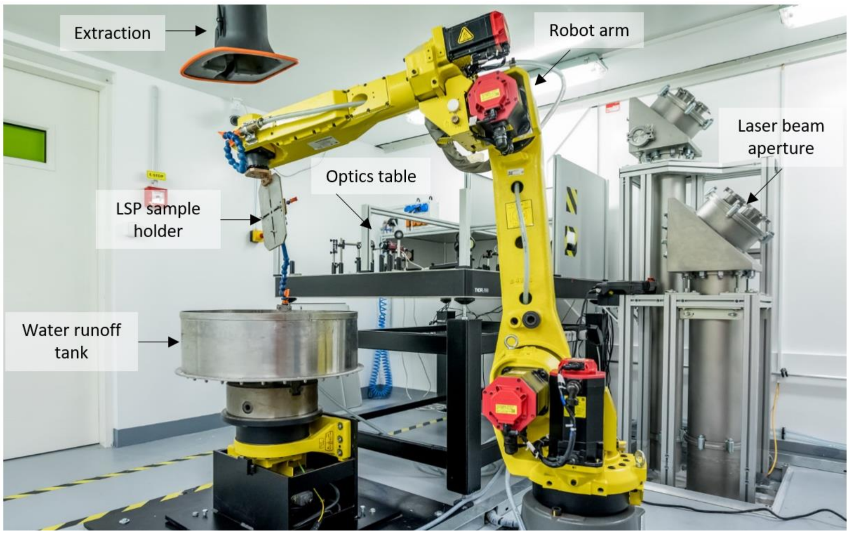

Figure 3.6: Laser shock peening setup at Hilase [9]

3.2.2. Council for Scientific and Industrial Research – National Laser Centre

Test samples from the crack trajectory modification study (Chapter 5) were LSP processed at the Council for Scientific and Industrial Research - National Laser Centre in Johannesburg, South Africa, in collaboration with the University of the Witwatersrand (Wits).

The CSIR-NLC LSP setup consists of a solid-state Thales Nd: Yag laser, capable of operating at a peak energy of 1.8 J per pulse. The emitted laser light wavelength was 532 nm (green region of the spectrum) at a repetition rate of 10 Hz. Black vinyl tape protected the target surface from direct ablation. Standard tap water was used throughout as the confinement medium. The confinement was delivered as a water jet that dispersed into a thin water layer over the processing area. A programmable XYZ Aerotech Pro165 high precision positioning system (accuracy of ±8 µm, bi-directional repeatability of 1 µm and encoder feedback of 0.1 µm) provided the sample manipulation whilst the laser fixed in position. Figure 3.7 provided an example of the LSP processing conducted at the CSIR-NLC.

A circular laser geometry of approximately 1.5 mm in diameter was maintained throughout the peening. A charge-coupled device beam profiler verified the spot size and estimated a near-uniform top-hat spatial intensity. The laser pulses temporal profile was estimated as a Gaussian profile with a 5.15 ns representative pulse width at the FWHM. The various peak power intensities were dependent on the fixed parameters and the variable energy per pulse and adjusted within the operational capabilities of the laser. The peak laser pulse energy (unfocused beam) was measured with a Coherent fast photo-diode and was averaged over at least ten consecutive pulses, the energy was measured with a repetition rate of 20 Hz. Figure 3.7 provided an example of the LSP processing at the CSIR-NLC facility.

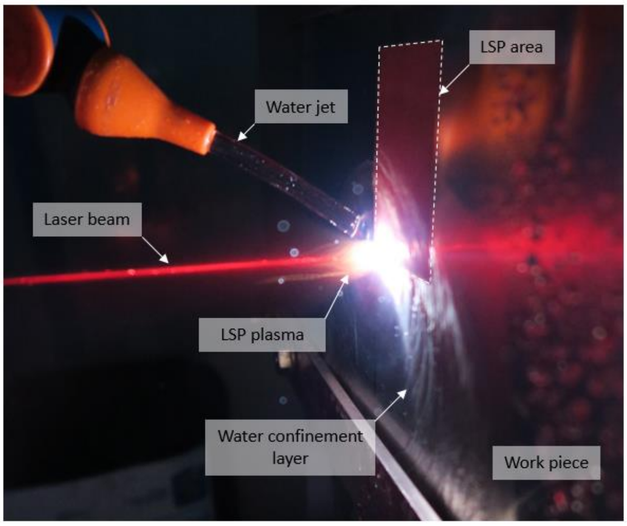

Figure 3.7: Laser shock peening setup at the CSIR-NLC

3.3. Specimen configuration and laser shock peening processing

This section outlines the sample geometry, test matrix and LSP processing of the various sample configurations.

3.3.1. Effect of laser shock peening parameters sample configuration and processing

Individual AA2524-T351 samples of 6 mm in thickness were extracted using wire Electrical Discharge Machining (EDM) from a larger plate after LSP processing to a size of 45x45 mm^2. A single LSP patch of 20x20 mm^2 was applied to the surface of the samples. A single laser shot was placed on the sample for the characterisation of a single LSP event. Figure 3.8 provided a schematic of the LSP temporal profile samples.

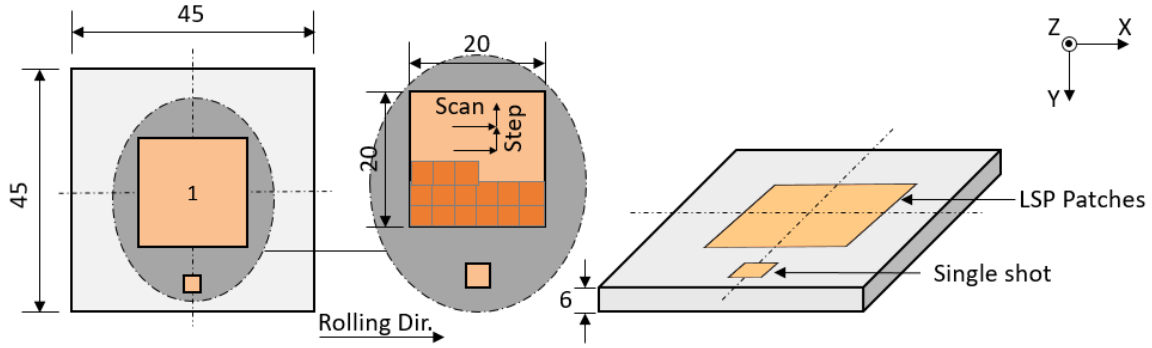

Figure 3.8: Schematic of laser shock peening temporal profile samples

Peening was completed at HiLASE in the Czech Republic with the fixed laser parameters described in section 3.2.1. The samples were processed with four different temporal profiles, Flat Top (FT), Gaussian (G), Double Shallow Gaussian (DSG) and Double Deep Gaussian (DDG). Additional details of the temporal profiles are provided in Chapter 4. Table 3.4 listed the sample matrix and variable LSP parameters used for the processing of these samples. The peening was applied to the sample in the as-received surface condition.

Single and double layer (50% layer offset) samples were produced to investigate the effect of additional LSP layers. Two power intensities of approximately 1.85 and 5.56 GW/cm^2 were used to investigate the link between the temporal profile and power density. An ablative coating of black vinyl tape was used throughout and was replaced between sequential layers. A square laser geometry of approximately 3x3 mm^2 in dimension was maintained throughout the peening. All samples were processed with a laser spot overlap of 10% and a layer offset of half the laser spot size (50% layer offset). The peening was completed in a bottom-up raster pattern starting at the bottom left of the patches and scanned left to the right. A thin sheet of tap water was used as the confinement medium for all LSP processing.

Table 3.4: Laser shock peening temporal profile sample matrix and peening parameters

Sample ID	Temporal profile	Power density [GW/cm^2]	Energy per pulse [J]	No. of layers
TP-FT-1.85-1-1	Flat Top	1.85	1	1
TP-FT-1.85-1-2		1.85	1	2
TP-FT-5.56-3-1		5.56	3	1
TP-FT-5.56-3-2		5.56	3	2
TP-G-1.85-1-1	Gaussian	1.85	1	1
TP-G-1.85-1-2		1.85	1	2
TP-G-5.56-3-1		5.56	3	1
TP-G-5.56-3-2		5.56	3	2
TP-DSG-1.85-1-1	Double Shallow Gaussian	1.85	1	1
TP-DSG-1.85-1-2		1.85	1	2
TP-DSG-5.56-3-1		5.56	3	1
TP-DSG-5.56-3-2		5.56	3	2
TP-DDG-1.85-1-1	Double Deep Gaussian	1.85	1	1
TP-DDG-1.85-1-2		1.85	1	2
TP-DDG-5.56-3-1		5.56	3	1
TP-DDG-5.56-3-2		5.56	3	2

3.3.2. Innovative laser shock peening confinement medium

AA2024-T351 samples of 2 mm in thickness were extracted by guillotine from a larger sheet of material to a size of 25x25 mm^2. Four equally spaced LSP patches of 5x5 mm^2 were applied to the surface of the samples. Figure 3.9 provided a schematic of the samples and the order in which the LSP patches were applied. Table 3.5 listed the various LSP parameter combinations that were investigated in this study.

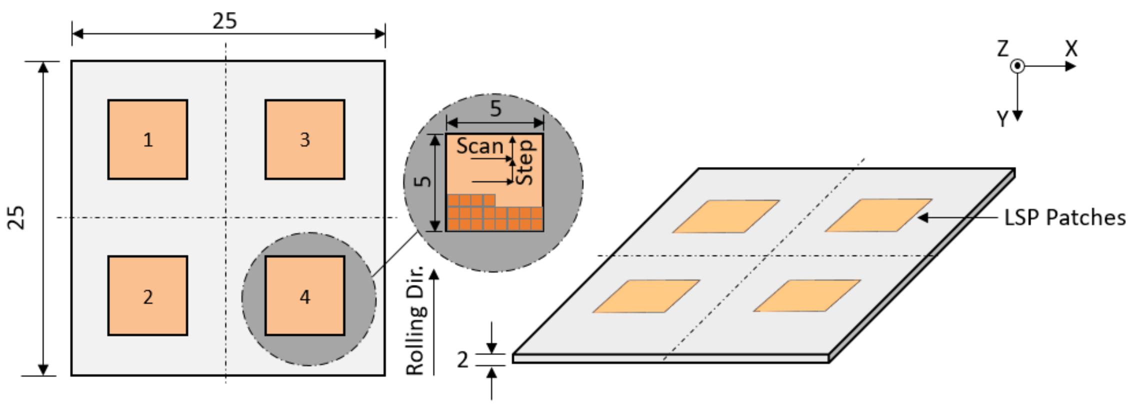

Figure 3.9: Schematic of laser shock peening solid confinement samples

Peening was completed at HiLASE with the fixed laser parameters described in section 3.2.1. The samples were processed with a flat top temporal profile. The samples were processed with three dimensional printed solid confinements of various thicknesses and are described further in Chapter 5. No ablative coating was used in this study as the higher surface roughness of the base material improved the surface adhesion of the confinement material. The peening was applied directly to the surface which had undergone chemical milling to remove the clad layer. This chemical milling process would like to have had little to no influence on the pre-existing residual stress in the material. Three samples were printed without an AA2024 substrate to characterise the energy reduction due to the solid confinement medium.

Table 3.5: 3D printed solid confinement laser shock peening test matrix and processing parameters

Sample ID	Confinement thickness [mm]	Power density [GW/cm^2]	Energy [mJ]	Spot size [mm^2]	Spot overlap [%]
SC-1-Energy	1	-	-	-	-
SC-2-Energy	2	-	-	-	-
SC-3.5-Energy	3.5	-	-	-	-
SC-1-LSP-1	1	1	16	0.4x0.4	0
SC-1-LSP-2	1	1	16	0.4x0.4	0
SC-1-LSP-3	1	1	16	0.4x0.4	0
SC-1-LSP-4	1	1	16	0.4x0.4	30
SC-1-LSP-5	1	2	32	0.4x0.4	0
SC-2-LSP-1	2	3	200	1.5x1.5	0
SC-2-LSP-2	2	1	16	0.4x0.4	0
SC-2-LSP-3	2	1	16	0.4x0.4	30
SC-2-LSP-4	2	1	16	0.4x0.4	0
SC-3.5-LSP-2	3.5	1	16	0.4x0.4	0
WC-LSP-1	-	1	16	0.4x0.4	0
WC-LSP-2	-	1	16	0.4x0.4	30

3.3.3.Crack Trajectory Modification by Laser Shock Peening Residual Stress

AA2024-T3 samples of 2.032 mm (0.008'') in thickness were extracted by guillotine from a larger sheet of material to 360x160 mm^2. A set of samples was later reduced to 140 mm in width to increase the length-to-width ratio of the samples. This improved the formation of a uniform stress field during FCGR testing. Additional detail has been provided in Chapter 6. Two angled LSP patches of 80x15 mm^2 were sequentially applied to both surfaces of the sample (apply two patches, then flip the sample and repeat on the reverse surface). A wire EDM fatigue crack notch was machined at the centre of the sample after LSP processing to complete the manufacture of the Middle Tension (MT) FCGR samples. Figure 3.10 provided a schematic of the samples.

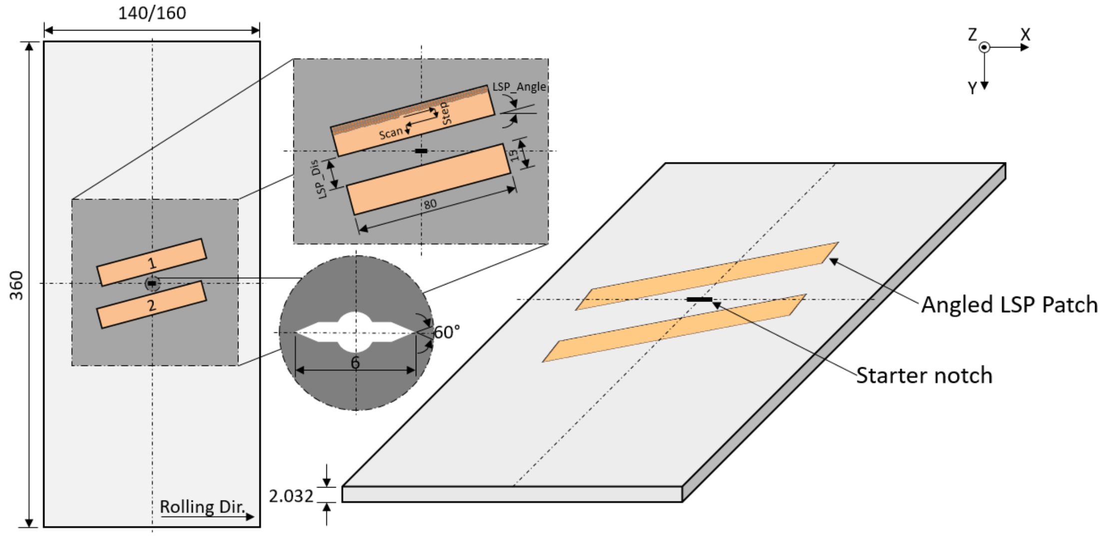

Figure 3.10: Schematic of crack trajectory modification by laser shock peening samples

Peening was completed at the CSIR-NLC facility with the fixed laser parameters described in section 3.2.2. Two sequential layers of LSP were applied with a spot overlap of 24% or layer coverage of 166.7 spots/cm^2. This peening strategy resulted in an effective total LSP coverage of 333.4 spots/cm^2 per side. This strategy ensured that the black vinyl ablative coating tape did not fail due to excessive peening between sequential spots. The ablative coating was replaced between layers. The peening was applied directly to the as-received clad surface of the material. The peening was completed with a rotated top-down raster pattern, starting at the top left of the patch. A fixed power density of 4 GW/cm^2 (energy 0.364 J per pulse) was used throughout. Three LSP processing angles of 15°, 30° and 45° were used in combination with two LSP patch spacing distances of 7.5 and 15 mm. Table 3.6 listed the test matrix and variable LSP parameters. Additional details regarding the samples used in this study are listed inTable 3.10 in section 3.5.

Table 3.6: Crack trajectory modification by laser shock peening sample matrix and parameters

Sample ID	Patch Angle [°]	Patch Spacing [mm]
MT-15-7.5	15	7.5
MT-15-15	15	15
MT-30-7.5	30	7.5
MT-30-15	30	15
MT-45-15	45	15

The two LSP patches have been set at these specific angles and spacing to ideally create a channel in which the crack will propagate along the un-peened region. Alternatively, if the tensile residual which will occur in the adjacent area is not capable of sustaining the crack within the unpeened area, the crack will likely alter its trajectory by turning away from its preferential fracture direction due to the compressive residual stress, as seen by Irving et al [10].

3.4. Residual stress characterisation and testing

Multiple residual stress characterisation techniques have been used to determine the effects of the LSP processing. These techniques were incremental hole drilling, X-ray diffraction and neutron diffraction. Incremental hole drilling is a semi-destructive technique that was applied in strategic positions. The remaining techniques were all non-destructive methods, which allowed for the characterisation of the residual stress field prior to further experimentation.

3.4.1. Incremental hole drilling

Incremental hole drilling is a mechanical strain release technique used to determine the residual stress in a specific area of a component. This is achieved by measuring relaxed strains during the incremental removal of the material [11]. A three-element strain gauge rosette is mounted directly to the drilling surface and can accurately capture the deformation of the hole due to the relaxed strains. The complete process of measuring residual stresses by incremental hole drilling has been outlined in ASTM E837 [12] and the National Physical Laboratory Measurement Good Practice Guide No. 53 [13]. The core steps of the process are listed below:

1) Installation of three-element strain gauge rosette – The standard of the installation directly influences the quality of the strain readings. The measurement surface should be as clean as possible and should be an appropriate surface roughness to ensure good adhesion of the gauge. Caution must be taken when roughing the surface as this can alter the near-surface stresses. Recommended steps to be taken for adequate surface preparation have been outlined by the Measurements Group Bulletin B-129-8 [14]. ASTM E837 stipulates that the instrumentation resolution on the measured strains be within ±2 µm [12]. The adhesion layer must be made as thin as possible whilst maintaining high bond quality between the surface and the gauge.
2) Alignment and setup of the drilling fixture – Eccentricity and misalignment between the centre of the drill and rosette will introduce measurement errors. Previous investigation has shown that a 10% off-centre misalignment of the hole radius can lead to a 5% measurement error [15]. ASTM E837 limits the misalignment of the drill and the centre of the rosette to be within $\pm 0.004 D_{IHD}$ or $\pm 0.025\ mm$, whichever is greater [12]. ASTM E837 recommends a minimum hole diameter of 60%

of the maximum allowable diameter of the rosette [12]. It is good practice to replace the drill bits between measurements to ensure the quality (shape and depth) of the drilled hole. When multiple measurements are required on the same sample, measurement points must be located at least three-hole diameters away from each other. Additionally, the gauge elements must be placed away from adjacent holes [13].

3) Establishment of the sample surface or zero-depth position – Accurate detection of the sample surface (zero/datum depth) is vitally important for the correct characterisation of shallow residual stress and the variations within the depth. Ideally, the zero-depth must be set when the gauge backing and adhesive have been completely removed, and the drill is first in direct contact with the surface. Figure 3.11 indicated how the zero-depth surface should be determined by successively removing incremental layers of the gauge backing and adhesive [13].

Figure 3.11: Multi-stage drilling to determine the zero-depth surface [13]

4) Drilling in a series of depth increments – The measurement increments are often set by the processing software. However, a larger number of small depth increments should be implemented to determine the residual stress near the surface.
5) Recording of the separate strain gauge readings at each depth increment – Once the interval depth has been achieved, the drill must be shut off and sufficient time must be allowed for the strain readings to stabilise before recording the values.
6) Calculation of the initial residual stress state from recorded data – The details of the calculation associated with this technique are outlined in the ASTM E837 (this method was provided in Appendix A) and National Physics Laboratory Measurement Good Practice Guide No. 53 [12,13].

3.4.1.1. Incremental centre hole drilling experimental procedure

The exact position of each measurement location was specific to the individual samples and has been defined at the presentation of the results. All incremental hole drilling measurements were completed using a Stresscraft Ltd orbital milling incremental hole drilling apparatus shown in Figure 3.12. All holes were drilled to a nominal hole depth of 1408 µm. Drilling increments were defined as six steps of 16 µm each (0 to 96 µm in-depth), five steps of 32 µm each (96 to 256 µm in-depth), six steps of 64 µm each (256 to 640 µm in-depth) and six steps of 128 µm each (640 to 1408 µm in-depth). Calculation of the residual stress was completed using the Stresscraft RS INT software which is based on the ASTM E837 integral method with a moving average smoothing technique applied to the strains.

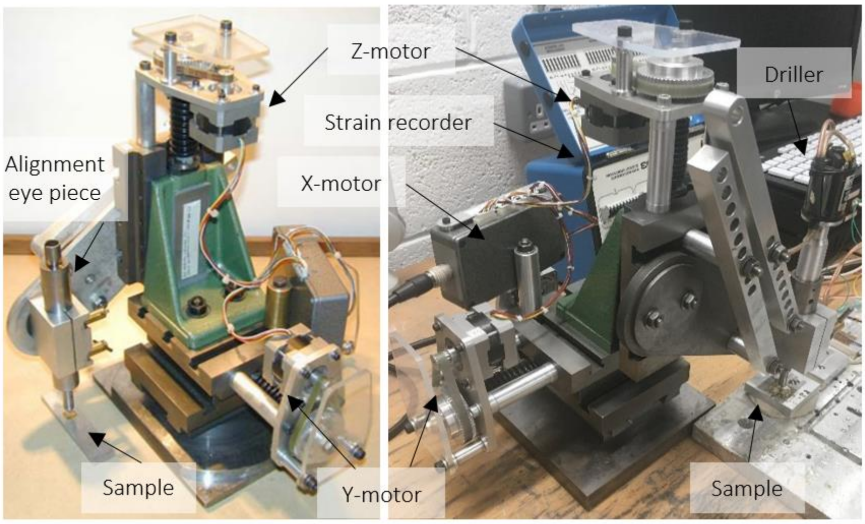

Figure 3.12: Incremental Centre Hole Drilling apparatus used for all measurements, (a) alignment eyepiece and (b) with drill attachment

All measurements were conducted using Vishay Micro Measurement three-element gauge rosettes. Figure 3.13 provides an example of the CEA-13-062-UL-120/SE and EA-13-062RE-120/SE rosettes used in this research [13].

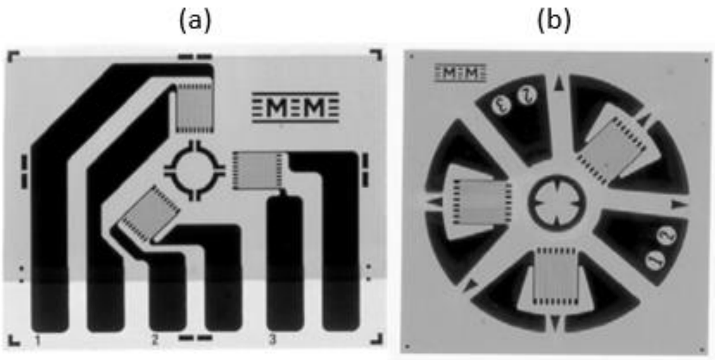

Figure 3.13: Three gauge rosette used for incremental hole drilling (a) CEA-13-062-UL-120/SE (b) EA-13-062RE-120 [11]

3.4.1.2. Residual stress uncertainty in incremental hole drilling measurements

Classification of the associated uncertainty in any incremental hole drilling residual stress measurement can be fairly complex due to the numerous possible sources of experimental and analytical errors. The law of propagation of uncertainty cannot easily determine the uncertainty in the incremental hole drilling measurement due to the indirect relationship between the measured strains and the stress. Oettel suggested that the incremental hole drilling measurement uncertainty is a function of the individual test procedure, apparatus, and operator skill [16]. These general uncertainties can be defined explicitly into three primary sources of uncertainty. The most notable uncertainties are the material properties (elastic modulus and Poisson's ratio), measurements uncertainties (instrument noise, hole diameter, zero-depth and strain variations) and computation of the calibration matrices. As the residual stress determination is based on the cumulative release of strains in the material, a small error at the beginning of the measurement can result in a reasonably large error in the subsequent stages of the measurements. The easiest way to validate a residual stress result is by carrying out a repeat measurement in the same sample area, which is at least three-hole diameters away from the first measurement location. However, this may not always be practical or feasible and it was considered good practice to report a residual stress result within a specified level of confidence.

Several researchers have attempted to develop methods to determine the associated uncertainty in an incremental hole drilling measurement. Otettel summarised and classified the various uncertainty sources [16]. Scafidi et al. provided an uncertainty evaluation based on strain corrections caused by thermal effects, hole-rosette eccentricity, hole-bottom fillet radius, and plasticity in determining the uncertainty in a uniform stress field [17]. Smit et al. and Peral et al. independently developed incremental hole drilling residual stress uncertainty evaluations based on the ASTM E837 integral method coupled with Monte Carlo simulations [18,19]. The Monte Carlo method determined the residual stress based on random variations in the input data.

The Monte Carlo numerical method is a numerical technique used to solve analytical problems by simulating random variables [20]. The Monte Carlo simulation of the propagation of uncertainty was simpler and more manageable than the root mean square method, which requires partial differentials of the governing equations, and the methods outlined in the previously mentioned published works [21]. All uncertainty associated with incremental hole drilling measurements in this work has been determined by coupling the ASTM E837 integral method and Monte Carlo methods outlined in Smit et al. [18] and JCGM 101:2008 [20]. A summary of this method was provided below, with a full outline presented in Appendix A:

1. Establish the residual stress model equations based on the ASTM E837 integral method. This relates the analytical residual stress results (σ_{res}) to the parameters (x_i) according to $\sigma_{res} = \sigma_{res}(x_i, \ldots, x_n)$.
2. Select the number of Monte Carlo simulations and identify the probability density functions $p(x_i)$ of the uncertainty sources.
3. Simulate the samples $\{x_{i1}, \ldots, x_{iMC}\}$ of each source of uncertainty. These are based on random variables within the bounds of the probability density functions.
4. Compute the results of the residual stress $\{\sigma_{res_{i1}}, \ldots, \sigma_{res_{ICM}}\}$ based on the established equations and random variables.

5. Calculate the combined standard uncertainty $u(\sigma_{res})$ as the standard deviation of σ_{res}.

Table 3.7 listed the considered sources of uncertainty and associated uncertainty ranges (probability density functions) used in the 50 000 Monte Carlo trials (number of trials was defined based on results presented in Appendix A). The uncertainty of each parameter has been selected based on the recommendations of Oettel and the estimated experimental variations of the incremental hole drilling apparatus, discussed in section 3.4.1.1 [16]. The uncertainty in the elastic modulus has been increased from the prescribed value by Oettel to account for the higher variation of the thin clad overlay material. Appendix A provides a full outline of this method and sample calculation.

Table 3.7: Uncertainty limitations for measurements and mechanical properties

Category of uncertainty	Source of uncertainty	Uncertainty range
Material property	Elastic modulus	±4%
	Poisson's ratio	±3%
Measurement	Instrumentation noise (encompassing thermal effects)	±2 με
	Strain variation	±2 με
	Final hole diameter	±50 μm
	Zero depth position	±2 μm
	Depth increments	±2 μm
Computational	Cumulative strain relaxation polynomial coefficients (ASTM E837)	±2% $\hat{a}_{jk}$ & $\hat{b}_{jk}$

The ASTM standard E837-20 defines three ranges of material workpiece thickness as 'thin', 'intermediate' and 'thick' [12]. This classification is based on the sample's nominal thickness and the type of strain gauge rosette used in the measurement. In this work, no samples were classified as thin. Samples that had a thickness between 1.28 and 3.08 mm were considered intermediate, and samples with thicknesses greater than 3.08 mm were considered thick. The thickness of the sample needs to be accurately represented in the calculations as it affected the cumulative strain relaxation calibration matrices used to determine the residual stress at each nominal depth.

Although the uncertainty bounds cannot be generalised across a set of similar samples (uncertainty is dependent on the residual stress state of each specimen) Table 3.8 listed an example of the averaged uncertainty over several depth increments from each thickness category. This allowed for the evaluation of the uncertainty trends across the stress profiles. The uncertainty was larger near the surface because of the low associated strain relaxations, the uncertainty in detecting the zero-depth position and the higher uncertainty in mechanical properties of the clad material. The large uncertainty at the surface would naturally reduce with a reduction in the associated uncertainty of the material properties and lower measured stress.

Table 3.8: Averaged uncertainty bound across multiple hole depth increments for intermediate and thick samples

Depth Increment [mm]	Intermediate sample uncertainty [MPa]	Thick sample uncertainty [MPa]
0 – 0.04	±30	±58
0.04 – 0.088	±20	±28
0.088 – 0.176	±23	±23
0.176 – 0.288	±21	±22
0.288 – 0.512	±14	±15
0.512 – 0.768	±8	±13
0.768 – 1.024	±10	±18

The uncertainty bounds decrease towards with middle of the measurements before increasing again at the full depth. The uncertainty was found to worsen at the full depth due to the strain sensor's lower sensitivity and compounded depth position uncertainty. The higher near-surface uncertainty in the thicker samples was due to the effects of the larger clad layer and the low associated strain relaxations which occurred in the lower-stiffness material. The clad layer was 2-3% of the total material thickness (approximately 185 μm thick) but accounted for 15-20% of the total measurement depth. The lower strain response and variations in the material property in this region naturally increased the overall uncertainty of the measurement.

3.4.1.3. Incremental hole drilling of intermediate thickness aluminium sheets

The AA2024-T3 2.032 mm thick crack trajectory modification samples exhibited significant distortion after LSP. The final equilibrium shape of the samples resembled that of a bowed beam where the concave surface (LSP face 1) and convex surface (LSP face 2) occurred due to the LSP processing. Incremental hole drilling measurements were taken on both surfaces of the sample, as shown in Chapter 6. To avoid pseudo residual stress effects from the drilling process on the intermediate thickness and deformed sheets, the back surface to the measurement face was secured with a non-expanding polyester filler which cold cured to a thickness of at least a few millimetres in thickness. This allowed for the perpendicular alignment of the measurement surface and the drill, increased the stiffness at the measurement location and prevented any deflection of the sample during the removal of the material. The method of reinforcing the back surface was developed by Toparli [22]. In Toparli's work, reinforcing the thin sample eliminated the need for analysis corrections for thin structures in the computation of the residual stresses.

3.4.2. X-ray Diffraction Techniques

X-ray and neutron diffraction are non-destructive stress characterisation techniques used on crystalline materials. These techniques are based on Bragg's Law which defines the condition necessary to determine the inter-planar spacing of a crystal structure and the scattering angle of electromagnetic radiation [23]. Constructively interfering scattered waves remain in phase with one another only when the path difference is equal to many wavelengths. Figure 3.14 shows a schematic of Bragg's Law in which, for two rays scattered from atoms *K* and *L* to be in phase and parallel, the second ray must travel the extra distance as stated in Equation 3–1 [24].

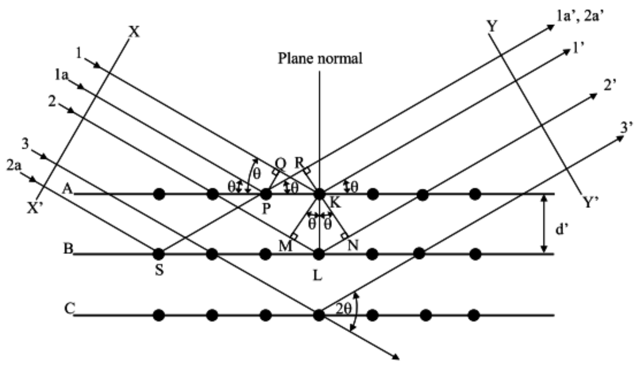

Figure 3.14: Scattering of electromagnetic radiation by a crystal lattice [24]

$$ML + LN = d' \sin\theta + d' \sin\theta \qquad \text{Equation 3–1}$$

For the rays to be in phase, the extra distance must be integer multiples of the wavelength, as set out by Equation 3–2.

$$n\lambda = 2d \sin\theta \qquad \text{Equation 3–2}$$

3.4.2.1. Sin^{2}ψ diffraction stress analysis

X-ray diffraction techniques are used for measurements in the near subsurface (less than 50 μm). This allows for the assumption of plane stress conditions. This simplification leads to a stress distribution which is described by the principal stresses (σ_1 and σ_2) existing in the plane of the surface and no out of plane (perpendicular) stress ($\sigma_3 = 0$). However, there will be a strain component perpendicular to the surface caused by Poisson's ratio contractions caused by the two principal in-plane stresses. Figure 3.15 provided a schematic of all reference planes and orientations [24].

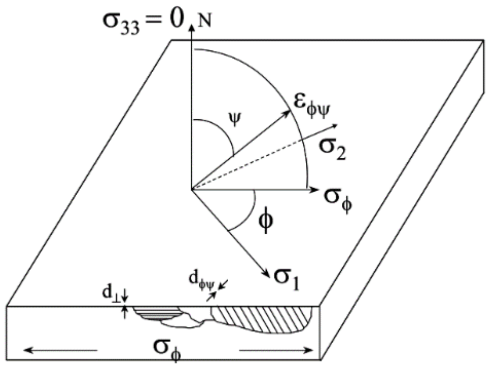

Figure 3.15: Schematic of the diffraction planes and relevant angles associated with the measurement of the strain using the X-ray diffraction technique [24]

The perpendicular strain component can be determined by Equation 3–3. The strain acting in any direction defined by angles ϕ and ψ can be determined by Equation 3–4.

$$\varepsilon_{33} = \frac{d_\perp - d_o}{d_o} \qquad \textit{Equation 3–3}$$

$$\varepsilon_{\phi\psi} = \frac{d_{\phi\psi} - d_o}{d_o} = \frac{1+v}{E}(\sigma_1 \cos^2\phi + \sigma_2 \sin^2\phi)\sin^2\psi - \frac{v}{E}(\sigma_1 + \sigma_2) \qquad \textit{Equation 3–4}$$

If the angle ψ is set to 90° and combing Equation 3–4 with Hooke's Law, the surface stress component can be written as Equation 3–5. Combining these equations, the lattice spacing in any orientation can be determined by Equation 3–7.

$$\sigma_\phi = (\sigma_1 \cos^2\phi) + (\sigma_2 \sin^2\phi) \qquad \textit{Equation 3–5}$$

$$d_{\phi\psi} = \left(\frac{1+v}{E} d_o\right) \qquad \textit{Equation 3–6}$$

$$d_{\phi\psi} = \left[\left(\frac{1+v}{E}\right)\sigma_\phi d_o \sin^2\psi\right] - \left[\left(\frac{v}{E}\right) d_o(\sigma_1 + \sigma_2) + d_o\right] \qquad \textit{Equation 3–7}$$

Figure 3.16 provided an example of the relationship between lattice spacing on the (311) plane and ψ, ranging from 0 to 45° for shot peened aluminium alloy 5056-O [25]. A straight line can be fitted using several regressions and the gradient of the line can be used with the elastic properties of the material to determine the stress. The inter-planar spacing at the intercept of the plot at $\sin^2\psi=0$ can be described by Equation 3–8.

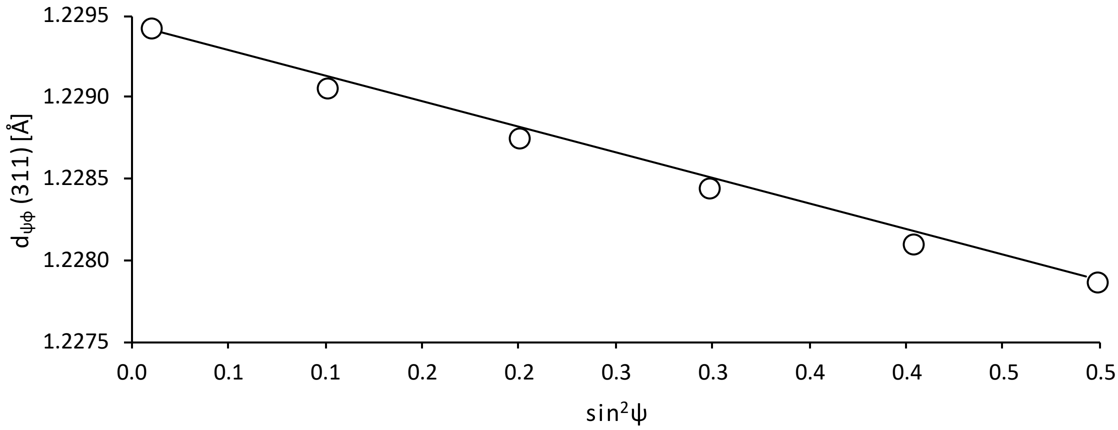

Figure 3.16: Example of inter-planar spacing and sin²ψ for shot peened aluminium alloy 5056-O [24][25]

$$d_{\phi 0} = d_o\left[1 - \left(\frac{v}{E}\right)(\sigma_1 + \sigma_2)\right] \qquad \textit{Equation 3–8}$$

This equates to the difference in the unstressed lattice spacing d_o and Poisson's ratio contraction. Equation 3–9 can be used to determine the stress.

$$\sigma_\phi = \left(\frac{E}{1+v}\right)m = \left(\frac{E}{1+v}\right)\sin^2\psi\frac{d - d_o}{d_o} \qquad \textit{Equation 3–9}$$

3.4.2.2. X-ray diffraction sources

Special laboratory X-ray sources are the most common techniques used to probe in the very near thin surface (tens of micrometre scale) [26]. These small scale machines use X-ray tubes in which a focused beam of accelerated electrons strike a metal anode target at high energy which produces the required X-rays [24]. This type of equipment is often incorporated into some form of articulating system, allowing for detailed surface mapping of a sample. Sequential depth XRD measurements can be made by incrementally removing layers of material and probing the newly exposed surface. Material removal is most commonly done by electropolishing [27].

In this research, a Stresstech XStress Robot was used for all laboratory XRD measurements, as shown in Figure 3.17. A copper X-ray tube was used as the X-ray source and operated at 5-30 kV/0-10mA/270W. The robot's six-axis rotation provided the ability to measure stress in any direction, with various sized collimators. The measurement height from the surface of the sample was determined based on the provided stress-free aluminium powder sample.

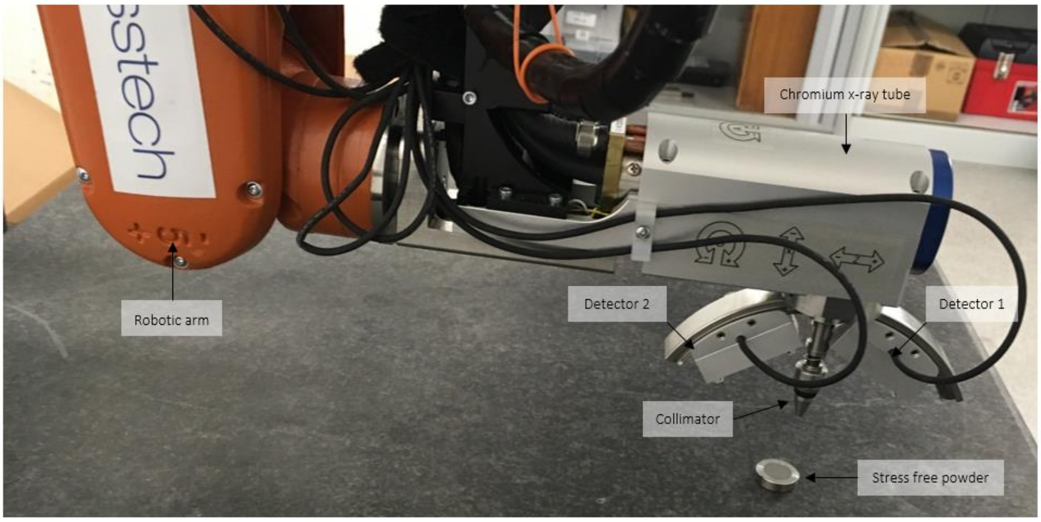

Figure 3.17: Stresstech XStress X-ray diffraction apparatus and stress-free calibration sample

3.4.3. Neutron diffraction techniques

Unlike X-rays, neutrons are not as easily absorbed by engineering materials, allowing deeper probing depths of up to tens of millimetres depending on the material. There are two primary sources of neutrons, spallation and reactor sources. Each source has a unique methodology in measuring and computing residual stress.

3.4.3.1. Spallation neutron sources

A spallation source is an accelerator-based facility that creates pulsed neutron beams by bombarding a target with intense proton beams [28]. The disadvantage of this beam is that it is of a relatively low flux (defined as the number of neutrons travelling through a small area in a given time) compared to typical reactor sources. The pulse rates vary between 20 to 60 Hz depending on the facility [29].

A Time-Of-Flight (TOF) analysis approach is used with spallation sources because of the non-continuous beam. In this method, the neutron's speed is measured by timing its flight from the source to the detector [30]. Strain measurements are made by maintaining the scattering angle and measuring the difference in the TOF of unstressed and stressed samples. Figure 3.18 provided an example of how TOF can be used to determine the change in inter-planar distance due to applied stress. Measurements were taken from the ISIS ENGIN-X beamline [31].

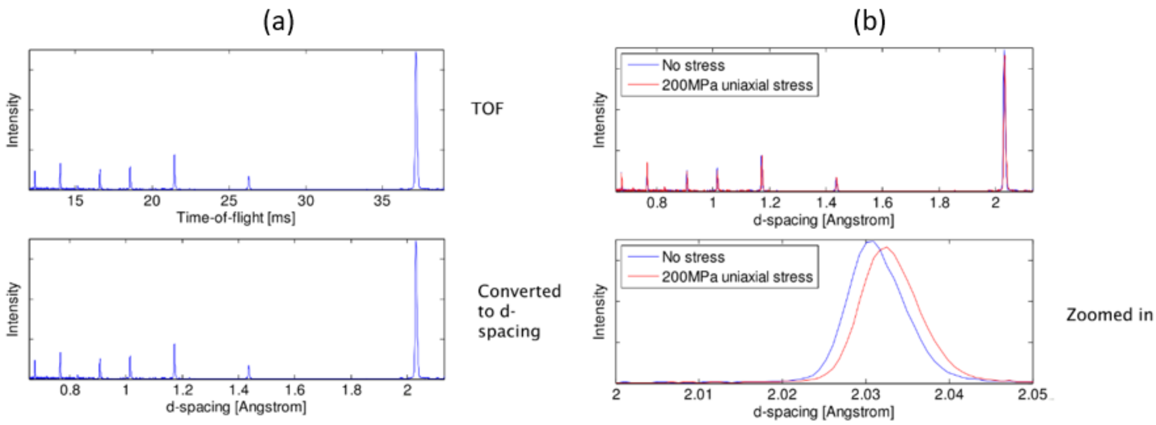

Figure 3.18: Example of Time-Of-Flight measurement from ISIS ENGIN-X (a) full Time-Of-Flight data and conversion between Time-Of-Flight and inter-planar spacing, (b) Comparison in peak shifts due to applied stress [31]

The neutrons are created over a wide range of wavelengths but can be easily determined using the TOF method. The speed of the neutrons (C_n) can be determined based on De Broglie's relation, given by Equation 3–10 [32]. The speed of the neutron can be determined based on the length of the flight path (L) and the TOF (t). Where, h is Planck's constant, t is the time-of-flight and m_n is the mass of the neutron.

$$\lambda = \frac{h}{m_n C_n} = \frac{h}{m_n} \frac{t}{L}$$ *Equation 3–10*

The neutrons are counted as a function of time by placing the detector at a specific scattering angle 2 θ, most commonly ±90° [33]. When Bragg's Law applies, Equation 2-25 can be combined with Equation 3–10 to determine the lattice spacing based on TOF, as set out in Equation 3–11.

$$d_{hkl} = \frac{h}{2 \sin \theta \, m_n} \frac{t_{hkl}}{L}$$ *Equation 3–11*

The peak spectrum in Figure 3.18 showed the diffraction peaks which correspond to different (hkl) lattice planes. The measured inter-planar spacing can be used to determine the residual stress according to Hooke's Law as discussed in Chapter 2.

The assumption of plane stress conditions was applied to the crack redirection samples due to the thin nature of AA2024-T3 sheets. This condition can be exploited to calculate the value of the lattice parameter by the application of the condition $\sigma_z = 0$ to the tri-axial formula (Equation 3–12), this methodology was outlined by Albertini et al. [34].

$$\sigma_{zz} = \frac{(1-v)E}{(1+v)(1-2v)} \cdot \varepsilon_{zz} + \frac{vE}{(1+v)(1-2v)} \cdot (\varepsilon_{xx} + \varepsilon_{yy}) \qquad \textit{Equation 3–12}$$

In Equation 3–12, E refers to the macroscopic elastic modulus of the material and v is the Poisson's ratio. Equation 3–12 can be combined with Equation 3–3 to define a relationship between the unstrained lattice parameter and the two orthogonally measured deformed lattice parameters. Additionally, it is assumed that the material is homogeneous in composition and structure in the area in which the measurements were taken.

$$a_0 = \frac{1-v}{1+v} a_z + \frac{v}{1+v} (a_{xx} + a_{yy}) \qquad \textit{Equation 3–13}$$

Bi-axial stresses could be calculated according to Equation 3–14.

$$\sigma_{xx} = \frac{E}{1-v^2} \left(\varepsilon_{xx} + v\varepsilon_{yy}\right) \text{ and } \sigma_{yy} = \frac{E}{1-v^2} \left(\varepsilon_{yy} + v\varepsilon_{xx}\right) \qquad \textit{Equation 3–14}$$

3.4.3.2. ISIS ENGIN-X Neutron Beamline

The ENGIN-X is a time of flight thermal neutron diffractometer beamline at ISIS, United Kingdom. The beamline is optimised to measure strain within crystalline materials, using the principle of deformed atomic lattice planes. ENGIN-X is a 50 m flight path instrument, operating with a wavelength range of 0.5-6 Å. The detectors are two ±90° diffraction banks of ZnS scintillators. Samples are placed in a high precision large capacity positioning system [35]. Figure 3.19 provided an example of the ENGIN-X instrument layout.

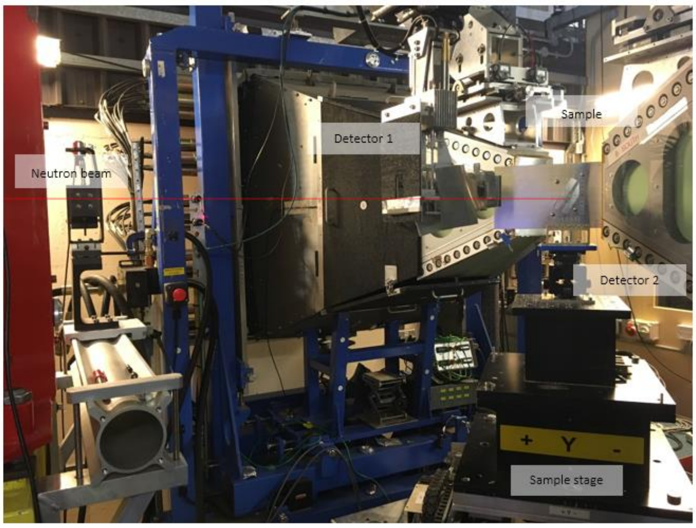

Figure 3.19: ENGIN-X instrument layout

Figure 3.20 provided a schematic representation of the ENGIN-X experiments with a representation of the incident neutron beam cross-section and elongated gauge volume. The incoming neutron beam was shaped to form a scattering gauge volume of 1x1x5 mm^3. The measurements were carried out along the approximate centre line of the thickness of the sample to achieve an averaged near through-thickness residual stress measurement. Approximately 70% of the AA2024-T3 2.032 mm thickness was averaged over the gauge volume in the measurements. Every effort was made to fully immerse the gauge volume within the material to avoiding pseudo-strain effects. The measurement parameters were maintained throughout the measurements and were listed in

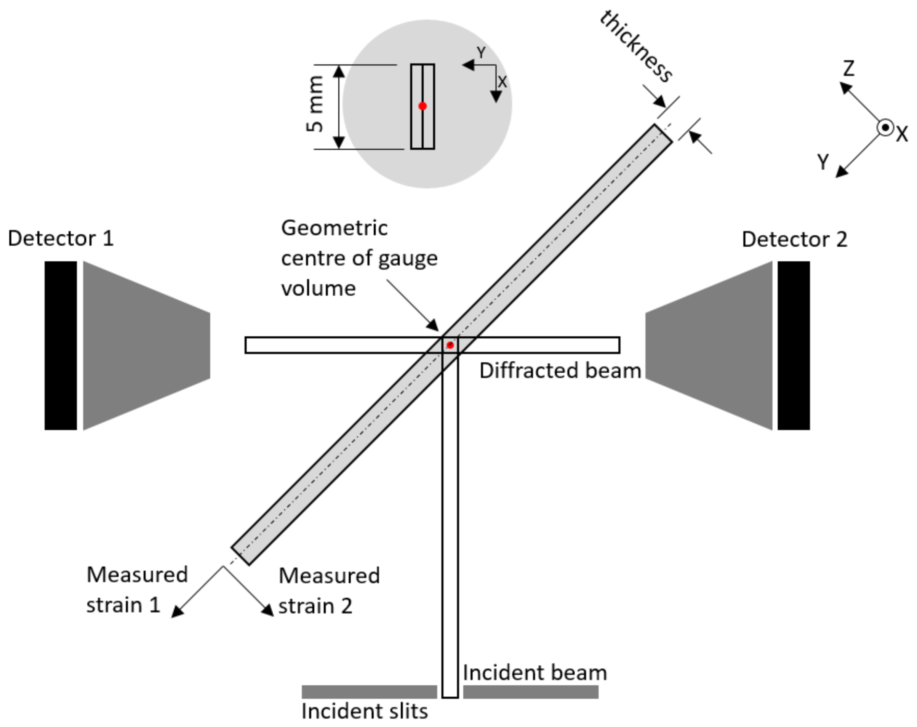

Figure 3.20: Schematic of ENGIN-X measurement with incident neutron beam cross-section and resulting gauge volume

Table 3.9: EnginX measurement parameters

Parameter	Setting
Reflection used	Multiple diffraction spectra
Time of flight range	20 000 – 44 595 μsec
Fitting function	Pawley refinement of entire diffraction spectra utilising GSAS
2θ	90º
Gauge volume	1x1x5 mm^3 (longitudinal and normal direction)
Measurement directions	LD (loading direction) & SD (thickness direction)
Reference material	Base material in unpeened sample
Measurement time	22.5 minutes per point

3.5. Fatigue crack growth rate experimentation

Mechanical tension-tension fatigue crack growth tests were performed to analyse the effects of LSP on the fatigue crack performance and its influence on the crack trajectory in middle tension samples.

Fatigue crack growth testing of the MT samples was performed using a load controlled INSTRON 8501 servo-hydraulic dynamic fatigue testing system with a maximum load capacity of ±100 kN. Figure 3.21 provided the configuration of the fatigue apparatus used in this research. The system was operated by the standard INSTRON Waveform software which generated the sine wave loading and displacements. All tests were performed at room temperature. The tests were all performed by applying a constant amplitude load cycle frequency range of 7.5 Hz (used in testing samples at higher maximum loads – larger than 100 MPa) to 15 Hz (standard fuselage testing loads – less than 100 MPa). The samples were aligned along its vertical centre line and clamped in fatigue grips which had flat faced serrated jaw faces and were secured by four evenly spaced bolts that were torqued to 150 N.m. Figure 3.21 provided an example of the experimental setup.

Crack lengths were measured with a digital optical travelling microscope and assisted with surface scribe marks which were equidistance spaced at 1 mm apart, shown in Figure 3.21.b-c. The travelling microscope had a 3-megapixel camera which could be interchanged with the standard viewing optic. Crack length measurements were taken on the front surface only as there was no apparent deviation of the crack lengths on the two surfaces.

At the time of the experimentation, the crack growth rates were calculated according to the ASTM E647-00 secant method [36]. This was completed to validate the experimental test procedure during the baseline testing. As a large amount of experimental data was achieved from the crack growth testing, the incremental polynomial data reduction method, outlined in the ASTM E647-00 standard [36], was used to compute crack growth rates of the various tested samples. This method involved fitting a second-order polynomial to seven (where n was set to 3 in *(2n+1)*) successive data points. The fitted crack size ($\hat{a}_i$) at the number of cycles (N_i) is determined by Equation 3–15.

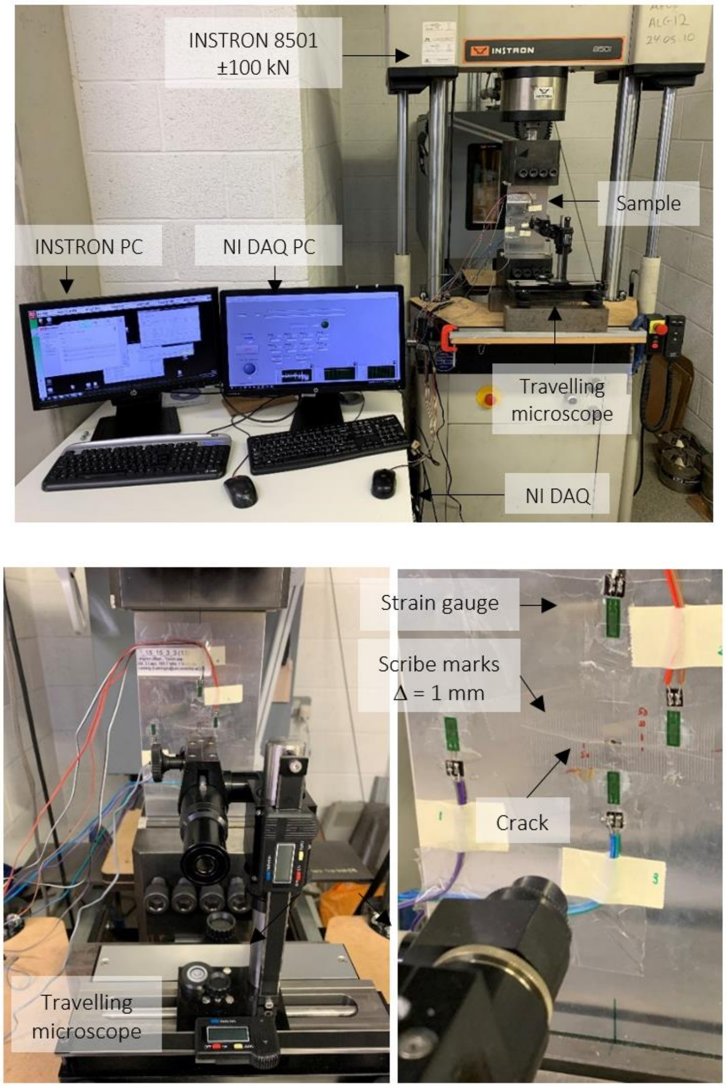

Figure 3.21: Fatigue crack growth rate experimental set up (a) overview of the test setup, (b) digital travelling microscope, (c) crack growth measurement surface with equidistance scribe marks

$$\hat{a}_i = b_0 + b_1\left(\frac{N_i - C_1}{C_2}\right) + b_2\left(\frac{N_i - C_1}{C_2}\right)^2 \qquad \text{Equation 3–15}$$

$$-1 \leq \left(\frac{N_i - C_1}{C_2}\right) \leq 1 \qquad \text{Equation 3–16}$$

Where b_0, b_1, and b_2 are the regression parameters that are determined by the least-squares method (which minimises the square of the deviations between the observed and fitted values of the crack size) over the range $a_{i-n} \leq a \leq a_{i+n}$. The parameters $C_1 = 0.5(N_{i-n} + N_{i+n})$ and $C_2 = 0.5(N_{i+n} - N_{i-n})$ are used to scale the input data to avoid numerical issues in determining the regression parameters. The crack growth rate at N_i is obtained from the derivative of the parabola, which is given by Equation 3–17. The value of ΔK associated with the da/dN value is determined with the fitted crack size [36]. This data processing was completed in Matlab and the programme was benchmarked against the provided example in the ASTM standards.

$$(da/dN)_{\hat{a}_i} = \frac{b_1}{C_2} + \frac{2b_2(N_i - C_1)}{{C_2}^2}$$ *Equation 3–17*

A series of baseline samples were tested under constant amplitude loading at three R-ratios of R = 0.1, R = 0.3 and R = 0.5. This was done to derive the Walker's crack growth model constants for AA2024-T3 2.032 mm thick sheets. All other samples were tested at R = 0.1. All sample details and testing parameters are outlined in Table 3.10.

LSP application to thin aluminium sheets typically results in an out of plane bending of the sample as the equilibrium of the residual stresses is achieved. The sample curvature can lead to out of plane or secondary bending occurring on the application of the cyclic tensile loads. This loading component was quantified using uniaxial strain gauges located on the sample surfaces, as shown in Figure 3.21 and Figure 3.22. A National Instruments data acquisition system was used with a NI4880 8-channel strain recorder and a NI4880 current recorder to acquire the strains which occurred on the surfaces and the load and position output of the Instron. Consequent stresses were calculated using the uniaxial Hooke's law. Figure 3.22 provided a schematic of the two strain gauge layouts that were implemented throughout the MT sample testing. The second configuration provided greater detail of the combined loading (residual and applied stresses) during FCGR tests. The gauges were placed at the half-width position and along the angled centre line between the LSP patches.

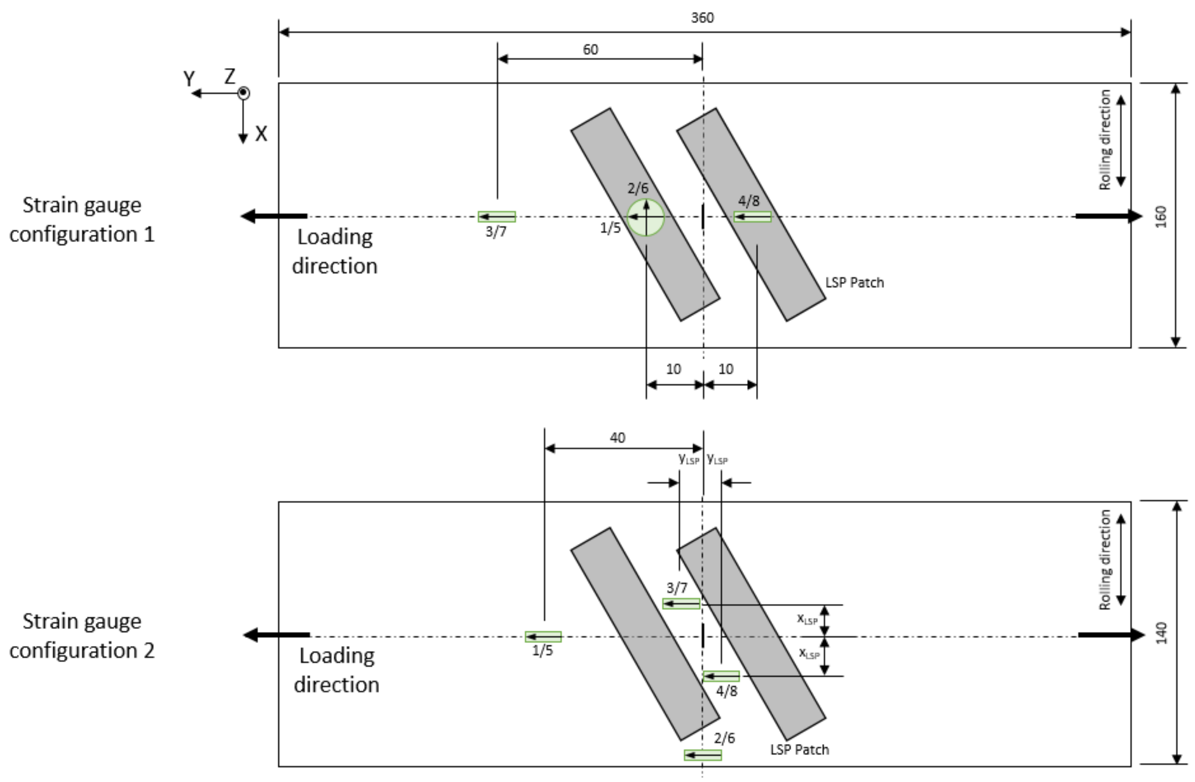

Figure 3.22: Schematic of strain gauge layout on the crack trajectory modification samples

Table 3.10: Test matrix of middle tension crack growth samples

Sample ID	LSP configuration (Angle-Spacing)	Cross-sectional area [mm^2]	Loading frequency [Hz]	R - ratio	Nominal max applied stress [MPa]
MT-BL-1	-	325	10	0.1	80
MT-BL-2	-	325	10	0.1	80
MT-BL-3	-	285	15	0.1	90
MT-BL-4	-	285	10	0.1	140
MT-BL-5	-	285	7.5	0.1	200
MT-BL-6	-	285	15	0.3	90
MT-BL-7	-	285	15	0.5	90
MT-15-7.5-1	15° - 7.5 mm	325	10	0.1	80
MT-15-7.5-2	15° - 7.5 mm	285	15	0.1	90
MT-15-7.5-3	15° - 7.5 mm	285	10	0.1	140
MT-15-7.5-4	15° - 7.5 mm	285	10	0.1	200
MT-15-15-1	15° - 15 mm	325	10	0.1	80
MT-15-15-2	15° - 15 mm	285	15	0.1	90
MT-15-15-3	15° - 15 mm	285	10	0.1	140
MT-30-7.5-1	30° - 7.5 mm	325	10	0.1	80
MT-30-7.5-2	30° - 7.5 mm	285	15	0.1	90
MT-30-7.5-3	30° - 7.5 mm	285	10	0.1	140
MT-30-15-1	30° - 15 mm	325	10	0.1	80
MT-30-15-2	30° - 15 mm	285	15	0.1	90
MT-30-15-3	30° - 15 mm	285	10	0.1	140
MT-45-15-1	45° - 15 mm	325	10	0.1	80
MT-45-15-2	45° - 15 mm	285	15	0.1	90
MT-45-15-3	45° - 15 mm	285	10	0.1	140

3.6. Conclusion

This chapter provided an overview of the aluminium alloys used in the study, the LSP processing facilities and used parameters. Additional, the employed residual stress and mechanical testing characterisation techniques were detailed in this chapter. This chapter aimed to show the importance of applying best practices when undertaking detailed characterisation of the metallic samples that had been exposed to various forms of LSP processing. The suggested approaches and techniques described in this chapter were systematically applied throughout the experimental work which is described in the forthcoming chapters.

3.7. References

[1] Dursun T, Soutis C. Recent developments in advanced aircraft aluminium alloys. Mater Des 2014;56:862–71. https://doi.org/10.1016/j.matdes.2013.12.002.

[2] Aalco. Aluminum Alloy Temper Designations 2017:1–3. https://www.aalco.co.uk/datasheets/Aluminium-Alloy-Temper-Designations_93.ashx.

[3] American Society for Testing and Materials. ASTM E407-07: Standard practice for microetching metals and alloys. Annu B ASTM Stand 2007:22. https://doi.org/10.1520/E0407-07.2.

[4] American Society for Testing and Materials. ASTM E112-13: Standard Test Methods for Determining Average Grain Size. Astm E112-10 2010:1–27. https://doi.org/10.1520/E0112-13.1.4.

[5] Materials AS for T and. ASTM E1876-15: Standard Test Method for Dynamic Young's Modulus, Shear Modulus, and Poisson's Ratio by Impulse Excitation of Vibration 2013;i:1–9. https://doi.org/10.1520/E1875-08.2.

[6] American Society for Testing and Materials. ASTM E8/E8M: Standard test methods for tension testing of metallic materials. Annu B ASTM Stand 4 2010:1–27. https://doi.org/10.1520/E0008.

[7] Mason P, Divoký M, Ertel K, Pilař J, Butcher T, Hanuš M, et al. Kilowatt average power 100 J-level diode pumped solid state laser. Optica 2017;4:438. https://doi.org/10.1364/optica.4.000438.

[8] Mason P, Banerjee S, Smith J, Butcher T, Phillips J, Höppner H, et al. Development of a 100 J, 10 Hz laser for compression experiments at the High Energy Density instrument at the European XFEL. High Power Laser Sci Eng 2018;6:1–10. https://doi.org/10.1017/hpl.2018.56.

[9] Hilase – Laser Shock Peening 2021. https://www.hilase.cz/en/we- offer/services/laser-shock-peening/ (accessed March 14, 2021).

[10] Irving P, Ma YE, Zhang X, Servetti G, Williams S, dos Santos J, et al. Control of crack growth rates and crack trajectories for enhanced fail safety and damage tolerance in welded aircraft strucutres. 25th Symp. Int. Comm. Aeronaut. Fatigue (ICAF 2009), Rotterdam: 2009. https://doi.org/10.1007/978-90-481-2746-7_23.

[11] Vishay Precision Group. Tech Note TN-503: Measurement of Residual Stresses by the Hole-Drilling Strain Gage Method 2010. http://www.vishaypg.com/docs/11053/tn503.pdf.

[12] ASTM International. ASTM E837-20 Determining Residual Stresses by the Hole-Drilling Strain-Gage Method. vol. i. 2020. https://doi.org/10.1520/E0837-13A.2.

[13] Grant P V, Lord JD, Whitehead P. The Measurement of Residual Stresses by the Incremental Hole Drilling Technique. Meas Good Pract Guid No 53 - Issue 2 2006:63. https://eprintspublications.npl.co.uk/2517/.

[14] Vishay Precision Group. Instruction Bullettin B-129-8: Surface Preparation for Strain Gage Bonding 2014:7. http://www.vishaypg.com/docs/11129/11129_b1.pdf.

[15] Wang H. The alignment error of the hole-drilling method. Exp Mech 1979;19:23–7. https://doi.org/https://doi.org/10.1007/BF02327766.

[16] Oettel R. The Determination of Uncertainties in Residual Stress Measurement (Using the hole drilling technique) 2000:18. https://doi.org/10.1007/bf02327502.

[17] Scafidi M, Valentini E, Zuccarello B. Error and uncertainty analysis of the residual stresses computed by using the hole drilling method. Strain 2011;47:301–12. https://doi.org/10.1111/j.1475-1305.2009.00688.x.

[18] Smit TC, Reid RG. Residual Stress Measurement in Composite Laminates Using Incremental Hole-Drilling with Power Series. Exp Mech 2018;58:1221–35. https://doi.org/10.1007/s11340-018-0403-6.

[19] Peral D, de Vicente J, Porro JA, Ocaña JL. Uncertainty analysis for non-uniform residual stresses determined by the hole drilling strain gauge method. Meas J Int Meas Confed 2017;97:51–63. https://doi.org/10.1016/j.measurement.2016.11.010.

[20] Joint Committee For Guides In Metrology 101. JCGM 101: Evaluation of measurement data - Supplement 1 to the “Guide to the expression of uncertainty in measurement” -Propagation of distributions using a Monte Carlo method 2008. https://www.bipm.org/en/publications/guides/gum.html.

[21] Joint Committee For Guides In Metrology. JCGM 100: Evaluation of measurement data — Guide to the expression of uncertainty in measurement. Int Organ Stand Geneva ISBN 2008;50:134. http://www.bipm.org/en/publications/guides/gum.html.

[22] Toparli MB. Analysis of Residual Stress Fields in Aerospace Materials After Laser Peening. The Open University, PhD thesis, 2012.

[23] Bragg WH, Bragg WL. The reflection of X-rays by crystals. Proc R Soc A 1913;88:428–38. https://doi.org/https://doi.org/10.1098/rspa.1913.0040.

[24] Fitzpatrick ME, Fry AT, Holdway P, Kandil FA, Suominen L. Determination of Residual Stresses by X-ray Diffraction - Issue 2. Natl Phys Lab - Meas Good Pract Guid No 52 2005. https://doi.org/10.1007/s00028-005-0194-y.

[25] Prevéy PS. X-ray diffraction residual stress techniques. Met Handbook 10 Met Park Soc Met 1986:380–92. https://doi.org/10.1361/asmhba0001761.

[26] Withers PJ, Bhadeshia HKDH. Residual stress. Part 1–measurement techniques. Mater Sci Technol 2001;17:355–65. https://doi.org/10.1179/026708301101509980.

[27] Gazzara CP. The Measurement of Residual Stress With X-Ray Diffraction. Army Mater Mech Res Cent 1983. https://pdfs.semanticscholar.org/9b5a/87d526495d271bbef14b61c36243291c8161.pdf.

[28] Chou W. Spallation Neutron Source and Other High Intensity Proton Sources. Accel Physics, Technol Appl 2004:231–55. https://doi.org/https://doi.org/10.1142/9789812702807_0010.

[29] Comsan MNH. Spallation Neutron Sources for Science and Technology. Proc Eighth Nucl Part Phys Conf 2011:20–4. https://inis.iaea.org/collection/NCLCollectionStore/_Public/43/099/43099436.pdf?r=1.

[30] Arai M, Crawford K, Anderson IS, McGreevy RL, Bilheux HZ. Neutron Imaging and Applications - A reference for the imaging community 2009:13–31. https://doi.org/10.1007/978-0-387-78693-3.

[31] Oliver E. Time of Flight Neutron Diffraction for Residual Stress Measurement. Mater Eng Program STFC 2008. https://www.isis.stfc.ac.uk/Pages/engin-x-training-presentation6510.pdf.

[32] Feldmann K. Texture Investigations by Neutron Time-of-Flight Diffraction. Textures Microstruct 1989;10:309–23. https://doi.org/10.1155/TSM.10.309.

[33] Santisteban J, Staron P, Schreyer A, Clemens H, Mayer S. Neutrons and Synchrotron Radiation in Engineering Materials Science. Wiley-VCH Verlag GmbH & Co. KGaA; 2008.

https://doi.org/10.1002/9783527621927.

[34] Albertini G, Bruno G, Dunn BD, Fiori F, Reimers W, Wright JS. Comparative neutron and X-ray residual stress measurements on Al-2219 welded plate. Mater Sci Eng A 1997;224:157–65. https://doi.org/10.1016/s0921-5093(96)10546-3.

[35] Oliver E, Santisteban J, James J, Daymond M, Dann J. ENGIN-X user manual 2004. http://www.isis.stfc.ac.uk/instruments/engin-x/documents/engin-x-manual6488.pdf.

[36] ASTM International. ASTM E647 - Standard Test Method for Measurement of Fatigue Crack Growth Rates. ASTM B Stand 2016;03:1–49. https://doi.org/10.1520/E0647-15E01.2.

Chapter 4 Experimental and analytical investigation of the effects of different laser shock peening parameters

This chapter presents the experimental and analytical investigation of the effects of LSP parameters on the formation of residual stresses and surface deformation. The primary investigated parameters were laser temporal profile, power density and extent of LSP processing applied to the target surface. The temporal profile of the laser pulse defines the time dependency of the energy delivery to the target surface. The temporal profile is typically a fixed characteristic of the laser source. The pulses' temporal effects on the LSP outcomes has not previously been extensively or systematically investigated. The BIVOJ laser at the Hilase facility in the Czech Republic has the unique capability of allowing the laser operator to define the shape of the laser temporal profile within a total duration of 14 ns, whilst maintaining other parameters such as pulse peak energy, duration and spatial distribution. This unique feature allows for the effects of the temporal profiles on residual stress and material deformation to be studied by isolating its influence from other laser and LSP processing-related parameters.

A dynamic pulse-by-pulse or what is commonly referred to as a 'physics based' LSP finite element model was developed to analytically study the effects of the temporal profiles on the LSP process. Two of the four studied temporal profiles were incorporated into the analytical confined plasma model defined by Fabbro et al., which provided an estimation of the time-varying pressure exerted on the target surface by the plasma [1]. Additionally, the analytical modelling section of this chapter presents several innovative advancements to the current LSP simulation techniques. These developments are aimed to increase the accuracy of predicting the biaxial residual stress and surface material deformation induced by each LSP shot.

4.1. Experimental characterisation of the effects of laser shock peening parameters

Laser pulse durations in the nanosecond time scale are most commonly used in LSP applications. This time scale is the ideal period to generate strong shock pressures capable of introducing residual stress whilst minimising target surface damage and melting [2]. The rise time and overall shape of the profiles can influence the formation of the plasma and the magnitude of the resulting shock wave that propagates within the material [3]. The BIVOJ laser system at Hilase has the unique functionality for the variation of the laser's temporal profile whilst maintaining the various other laser-related parameters. This unique feature allowed for the systematic study of the influence of temporal profile on the formation of LSP induced residual stresses and surface deformation.

4.1.1. Characterisation of the laser temporal profiles

Four profiles were studied to identify the effects of the laser pulse energy distribution on the formation of residual stresses and surface deformation over a short pulse duration. The profiles were characterised as Flat Top (FT), Gaussian (G), Double Shallow Gaussian (DSG) and Double Deep Gaussian (DDG). Figure 4.1 showed the normalised measured temporal profiles at 1 and 3 J energy settings. These profiles were normalised to directly compare the distributions at the different energy settings. As the profiles were so similar, the higher energy distributions were time-shifted by -2 ns in the figures for ease of comparison.

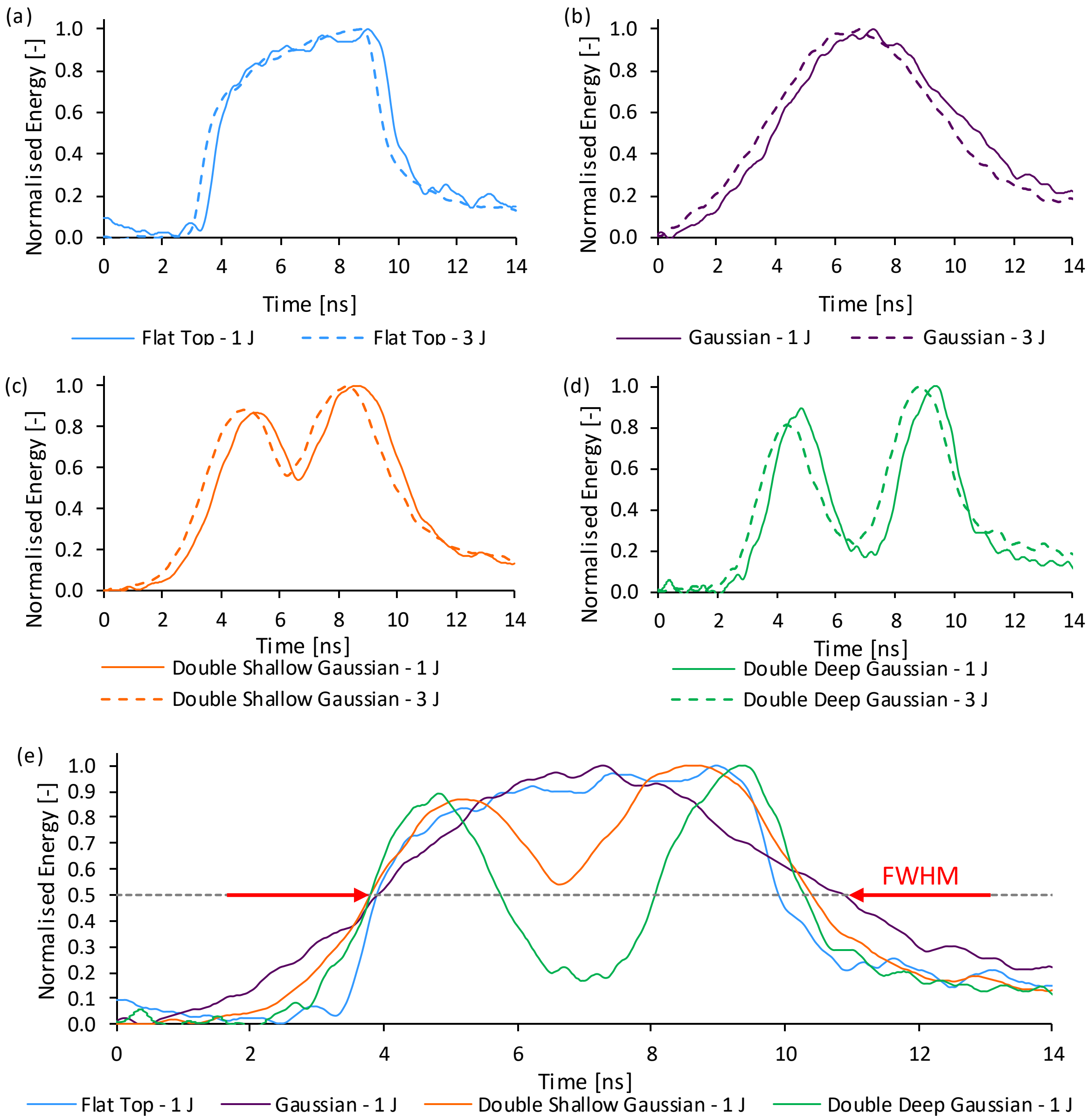

Figure 4.1: Normalised laser temporal profiles measured at two energy levels, with the larger energy profile time-shifted by -2 ns (a) flat top, (b) Gaussian, (c) double shallow Gaussian, (d) double deep Gaussian and (e) overlaid 1 J profiles with the full width half maximum indicated

The Flat Top and standard Gaussian profiles were selected as they are the most widely used temporal profile in most academic and commercial LSP systems. Double peaked Gaussian profiles were defined to attempt to emulate the effects of two laser pulses. The pulses were limited to a total duration of 14 ns. For consistency purposes, the FWHM time was specified to be within 6–7 ns and this has been indicated in Figure 4.1.e. The pulse duration of each profile could not be set to an exact value as the process of tuning and programming of each temporal profile was a complex and variable process. Table 4.1 listed the measured pulse widths at the FWHM of the four temporal profile shapes. The pulse widths were averaged over the two measured profiles and were used in the calculation of the pulse power intensities. The energy per pulse was measured with a fast photodiode and was found to be extremely stable during LSP processing. The spot size was determined at the time of peening by measuring the extremities of the surface dimple on the target material with a digital Vernier calliper and later accurately determined using a 3D surface profiler. An approximate square spot geometry of 3x3 mm^2 was used throughout. The variations in pulse width inevitably resulted in calculated differences in the power density of each temporal profile, as shown in Table 4.1. The frequency of the laser pulses was 10 Hz for all temporal profiles. However, this was determined to be the most consistent means of comparing the effects of the temporal profiles. The power density was calculated using equation 2-1. The largest power density range between temporal profiles were 0.2 and 0.7 GW/cm^2 per energy setting. These variations were considered within the general power density variations and tolerance for LSP processing.

Table 4.1: Measured temporal pulse width at full-width half maximum of each profile

Temporal profile	1 J pulse width [ns]	3 J pulse width [ns]	Avg. pulse width [ns]	1 J pulse measured spot size [mm^2]	3 J pulse measured spot size [mm^2]	1 J power density [GW/cm^2]	3 J power density [GW/cm^2]
Flat Top	6.01	5.97	5.99	2.9x2.6	3.2x3	1.85	5.62
Gaussian	6.98	6.58	6.78	2.9x2.6	3.0x2.9	1.65	4.95
Double Shallow Gaussian	6.60	6.60	6.60	2.8x2.7	3.1x2.9	1.70	5.08
Double Deep Gaussian	6.49	6.68	6.59	3.0x2.7	3.0x2.8	1.70	5.09

4.1.2. Experimental characterisation of laser shock peening parameter effects on residual stress

Incremental hole drilling measurements were used to characterise the induced residual stresses from the four temporal profiles. Figure 4.2 provided a schematic of the measurement locations on the LSP samples. The direction of the residual stresses was shown in Figure 4.2, with the x-direction along the laser scanning direction (transverse) and y-direction in the laser stepping direction (longitudinal).

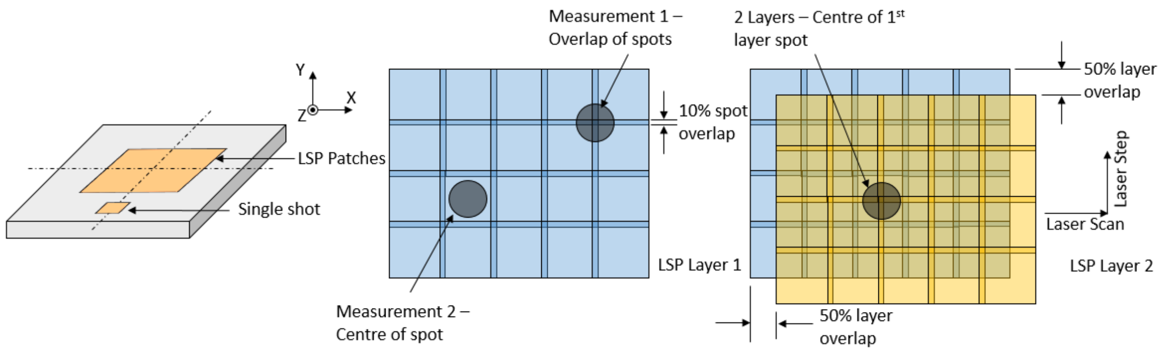

Figure 4.2: Laser shock peening processing strategy and incremental hole drilling measurement locations

The incremental hole drilling measurements at the centre of a single 3x3 mm^2 laser spot were carried out to characterise the induced residual stress from a single LSP event. Due to sample complications, measurements could only be made on the FT and DSG sample sets. Figure 4.3 indicated the measured residual stress from a single LSP pulse for the two temporal profiles at the two pulse energy settings. The variations in the residual stress profiles within the first 0.2 mm were attributed to the clad layer. It was assumed that the softer clad layer had an equivalent elastic modulus to that of the bulk material in the calculation of the residual stress. This was assumed due to restrictions in the computation software used to determine the residual stress from the measured relaxed strains (it was expected that the clad layer would have variations in the mechanical properties compared to the bulk material but are considered extremely difficult to determine as described by Khan et al. [4]). It is evident from the figures that the measured residual stress for both temporal profiles and pulse energies was fairly similar to one another in magnitude, trend and depth of compression.

Figure 4.3.a showed that the residual stress profiles of the two temporal profiles were fairly similar in peak compressive stress, approximately 125 MPa with a range between profiles of 25 MPa, and depth of compression of approximately 0.6 mm, with a range of 0.1 mm. At the higher energy setting shown in Figure 4.3.b, the DSG profile was found to have a higher peak compressive stress at approximately 170-225 MPa than that of the FT profile, which was within 50 MPa. The higher power density did increase the depth of compression per pulse to above 1 mm in depth. Overall, the DSG temporal profile did result in a slightly higher peak compressive residual stress at both energy settings but it did not

indicate any significant advantage in the depth of compression. This indicates that any potential observed benefit at this stage may have been simply due to measurement variations.

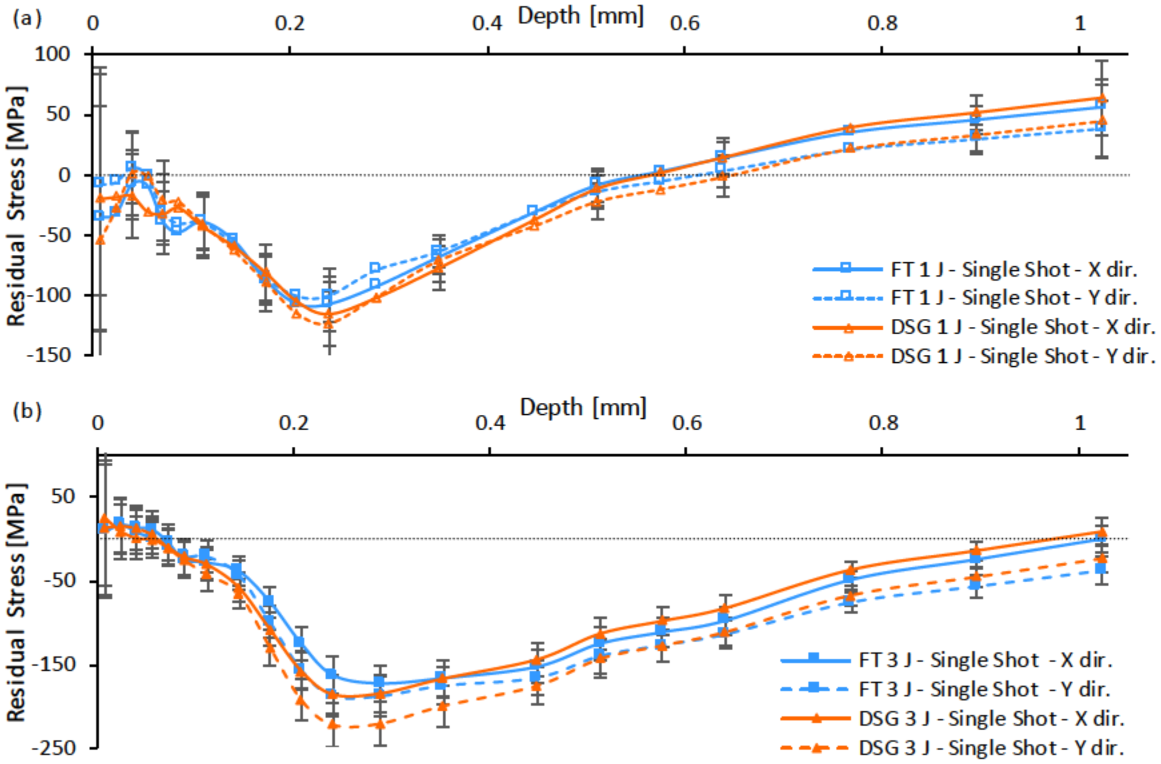

Figure 4.3: Residual stress measurement at the centre of a single laser shock peening pulse (a) 1 J – 1.85 GW/cm², (b) 3 J – 5.62 GW/cm²

An LSP processing strategy of a 10% spot overlap in the scanning and stepping directions was used to manufacture LSP patched samples (an array of multiple adjacent LSP pulses). An additional set of samples were manufactured with a second applied LSP layer which was offset by 50% of the spot size from the original layer. The specified spot overlap was maintained per layer. The LSP processing strategies and the incremental hole drilling measurement locations are schematically shown in Figure 4.2. The two measurements of the single-layer samples were centred about the LSP spot overlaps (measurement 1) and the centre of an individual LSP spot (measurement 2) respectively. Figure 4.4.a-d (a. Flat Top, b. Gaussian, c. Double Shallow Gaussian and d. Double Deep Gaussian) provided the residual stress results of the two single layer and the double LSP layer measurements at 1 J for each temporal profile. The results from each of the orthogonal gauge directions were plotted individually to allow for direct comparison. Figure 4.5.a-d showed the same set of data but at the higher energy setting. The error bounds in the present data were determined using the Monte Carlo method outline in chapter 3 and with only half the data points presented for clarity of the figures.

Figure 4.4 showed larger variations in the residual stress at the two measurement locations. The measurement at the spot overlap was found to have a reduction in peak compression of a percentage difference as large as 73% in the DDG profile to that at the centre of the spot. The reduction in compressive stress was attributed to the presence of balancing tensile stresses that occur in the surrounding area of the LSP spot to ensure equilibrium thus lowering the compressive stress. These variations were observed in both measurement directions but were most prevalent in the x-direction or the laser scanning direction. In all temporal cases, the overlap measurement did have a larger depth of compression than that of the measurement at the spot centre. This was expected as the spot overlap effectively increases the amount of peening or shot interactions occurring in that area which drives deeper stresses within the thickness of the material. This increase in depth of compression was predominantly observed in the y-direction or the laser stepping direction.

Figure 4.5 showed no notable variation in residual stress between measurement locations at the higher power setting for a single layer. The increased uniformity of the stress field was due to the higher power density inducing larger surface deformations that resulted in the near saturation of the material. This power density setting was at the extreme useable limit for aluminium before over peening and saturation may occur (no significant increase in compressive residual stress with an increasing amount of peening, as shown to occur by Hu et al. [5,6]). This increased uniformity did come at the cost of increased surface deformation which in some fatigue applications could be detrimental to the performance of the component, this will be discussed further in section 4.1.3 [7].

The addition of the second LSP layer was shown in Figure 4.4 and Figure 4.5 to have the effect of increasing the depth of compression by driving the stresses deeper into the material. In all cases, the second layer increased the depth of compressive residual stress to more than 1 mm in depth. At the lower power density, the influence of the second layer on the peak compressive stress was inconclusive as an increase in magnitude was observed only in half the samples whilst the reminder was either unaffected or saw a slight reduction. Figure 4.4 showed that the main increase in the peak values was associated with the stress in the longitudinal direction (laser stepping direction). The tendency of a marginal increase in peak compression was observed by Clauer in that additional peening had little effect on the surface and peak stresses but approximately doubled the depth of compression [8]. The cause of this can be attributed to it becoming increasingly harder to significantly increase the magnitude of the residual stress as the material tends to cyclically harden under repeated applications of the laser shots. This plateau-like point is dependent on the cyclic hardening behaviour of the material. Figure 4.5 reiterated this point as the second layer of LSP had hardly any effect on the residual stress profile at the higher power density.

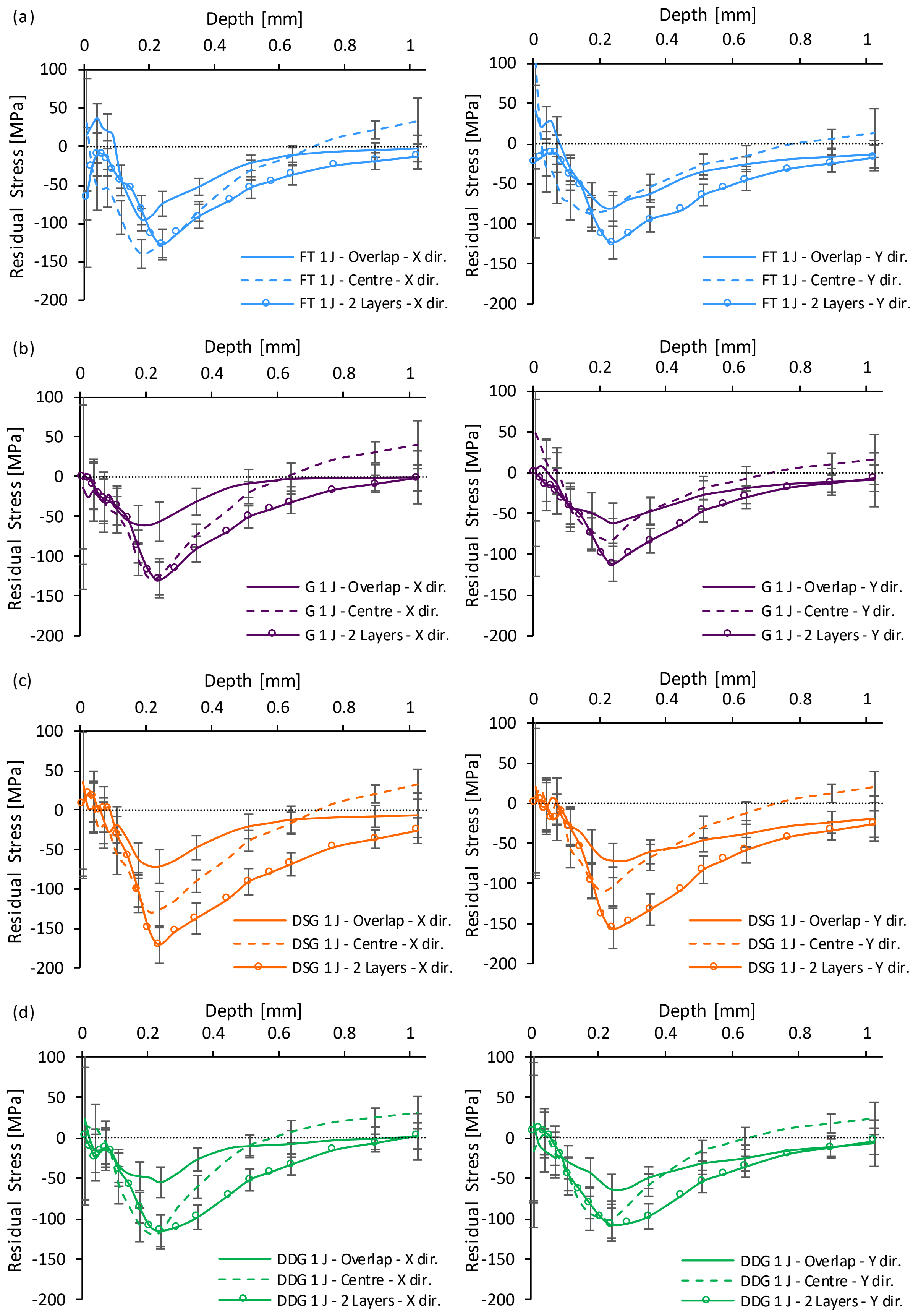

Figure 4.4: Residual stress of temporal profile samples at a peak power density of 1 J - 1.85 GW/cm² and a single / multi-layer peening strategy (a) Flat Top, (b) Gaussian, (c) Double Shallow Gaussian, (d) Double Deep Gaussian

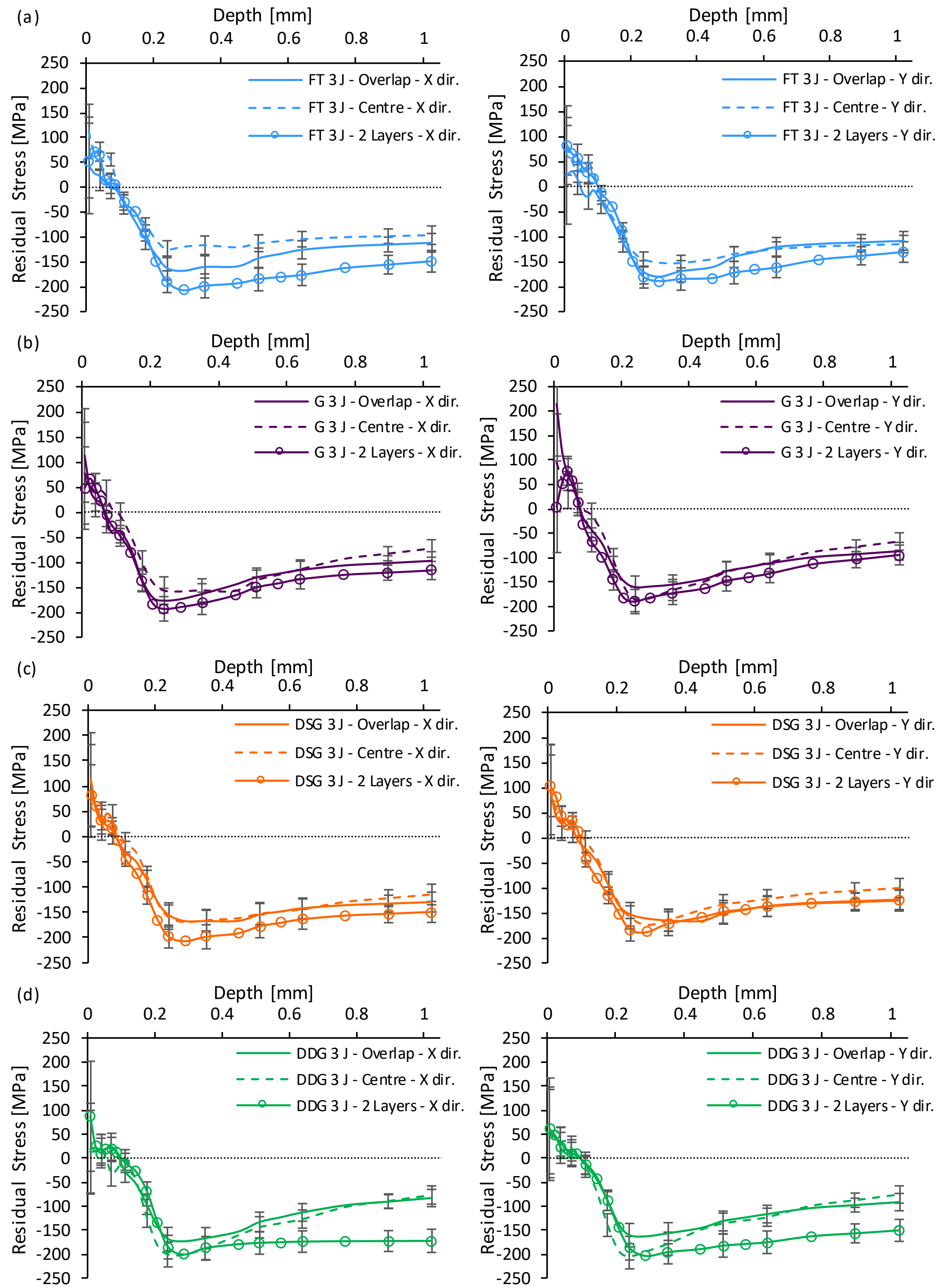

Figure 4.5: Residual stress of temporal profile samples at a peak power density of 3 J - 5.56 GW/cm² and a single / multi-layer peening strategy (a) Flat Top, (b) Gaussian, (c) Double Shallow Gaussian, (d) Double Deep Gaussian

Figure 4.6.a-b provided a comparison of the residual stress at the centre of the LSP spot at both power intensities. This comparison showed that no one temporal profile exhibited a significant advantage over another concerning inducing residual stresses. Closer analysis of the data indicated the two double peak profiles (DSG and DDG) did result in the lowest peak compressive stress. The range in peak compression between the DDG (worst) and FT (best) at 1 J energy was approximately 21 MPa and DSG (worst) and G (best) at 3 J energy was approximately 10 MPa. These ranges are all well within possible experimental variations of incremental hole drilling measurement. However, it may be suggested that the cause of the double peak profiles having the lowest peak compression was due to the reduction in total energy deposition per pulse, as indicated in Figure 4.1. The lower deposited energy would result in a slightly weaker plasma strength forming on the target surface, resulting in lower compressive stress. The experimental data showed no significant variation in the depth of compression between the four tested temporal profiles. Any discrepancies may be attributed to measurement uncertainties at the surface and in the depth.

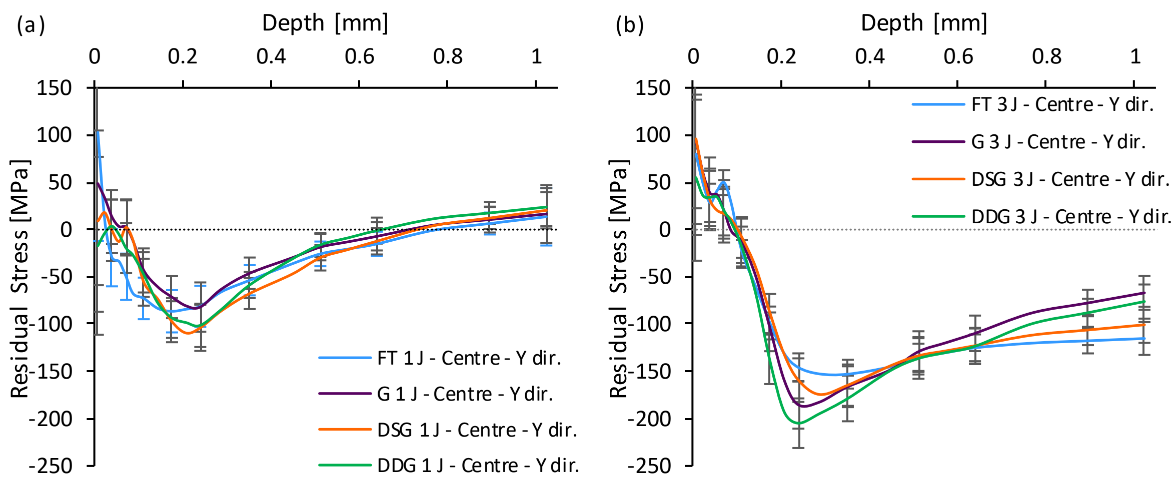

Figure 4.6: Residual stress of a single layer processing in all temporal profiles (a) 1 J – 1.85 GW/cm², (b) 3 J - 5.56 GW/cm²

Figure 4.7.a-b showed the effects of power density, in which a near doubling in peak compressive residual stress was observed for all temporal profiles (Figure 4.7 compared the FT and DSG data set). The higher laser intensities reduced the anisotropic variations in the two measured orthogonal directions of the residual stress across the temporal profiles. The higher laser pulse energy increased the depth of compression from approximately 0.8 mm to well above 1 mm. Similar results were observed in the remaining two temporal profiles.

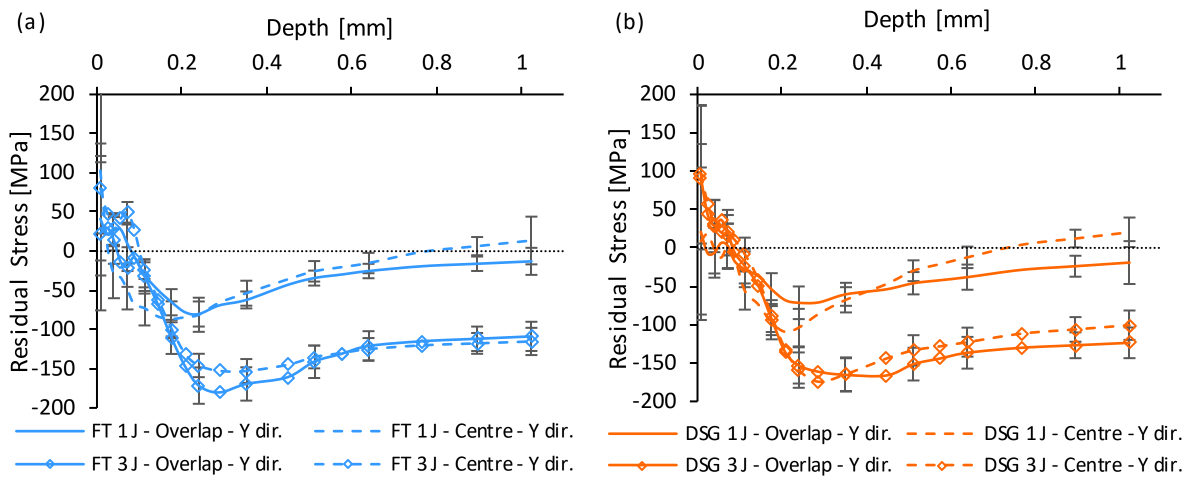

Figure 4.7: Effect of power density on the formation of residual stress (a) Flat Top, (b) Double Shallow Gaussian

Figure 4.8 showed the effects of the peening strategy as it compares the residual stress profiles of a single LSP shot, fully processed patch and multiple LSP layers at both laser energy settings. The adjacent LSP shots were found to reduce the peak compressive stress at the centre of the LSP shot by as much as 15% and 20% at the two power intensities. This indicated that the sequential LSP shots drive the compressive residual stress to a deeper extent but push balancing tensile stresses towards the extremity of the current spot effectively lowering the average compressive stress of the surrounding LSP spots. Another possible explanation for the reduction in peak compressive stress was that the residual stress introduced by the first LSP shot undergoes relaxation due to the propagation of the stress wave that was caused by the next sequential LSP shot. This occurrence of stress relaxation was observed by Cao et al. [9].

The additional LSP layer had little effect on the peak compressive stress but did tend to increase the stress throughout the depth. This was caused by an increased amount of plastic deformation on the material. As previously mentioned, a clear saturation limit was observed as there was no notable increase in peak compressive stress achieved between the LSP processing strategies at the higher power density. These trends were apparent across all of the tested temporal profiles.

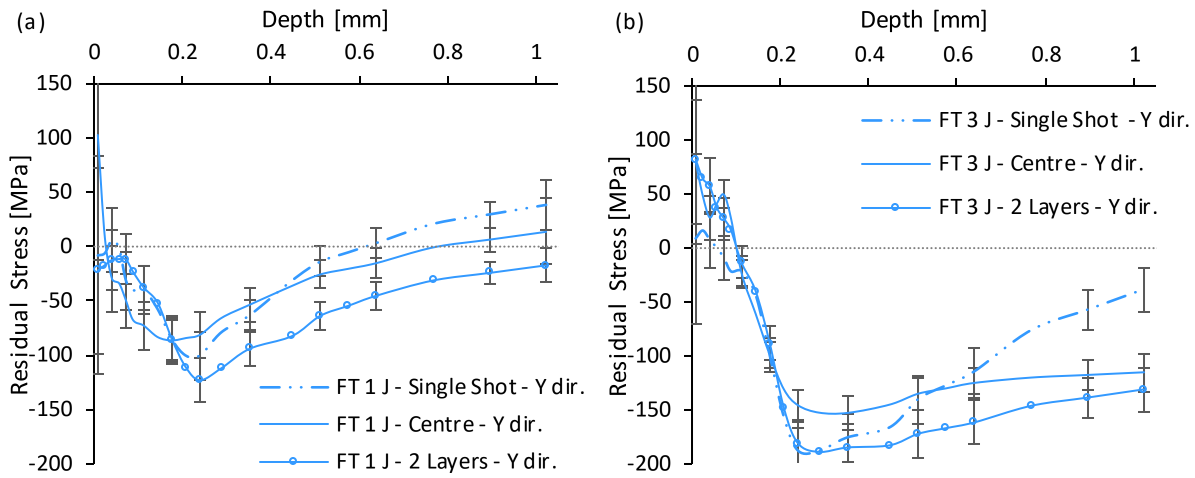

Figure 4.8: Influence of multiple laser shock peening shots on the formation of residual stress (a) 1 J – 1.85 GW/cm^2, (b) 3 J - 5.56 GW/cm^2

4.1.3. Experimental characterisation of laser shock peening parameter effects on surface deformation

Deformation of the target material was the fundamental mechanism associated with the formation of LSP residual stress. It was vital to characterise the effects of LSP surface deformation as this factor can greatly influence the mechanical performance of engineering components. In this study, the surface deformation of LSP processed samples with the various temporal profile, power density and peening strategies (single shot, single layer and multiple layers) was characterised with a Bruker Contour X-100 3D optical surface profilometer. Figure 4.9 and Figure 4.10 provided the measured surface deformations for all temporal profiles, peening strategies and pulse energy settings.

The deformation scale limits for each sample type in Figure 4.9 and Figure 4.10 was specified according to the maximum and minimum values of each data set. This was done to increase the clarity of the figures at the lowest deformation level. Any variation in the relative rotation of the samples was purely due to the alignment of the sample during the imaging of the surface and was not due to misalignment during LSP processing.

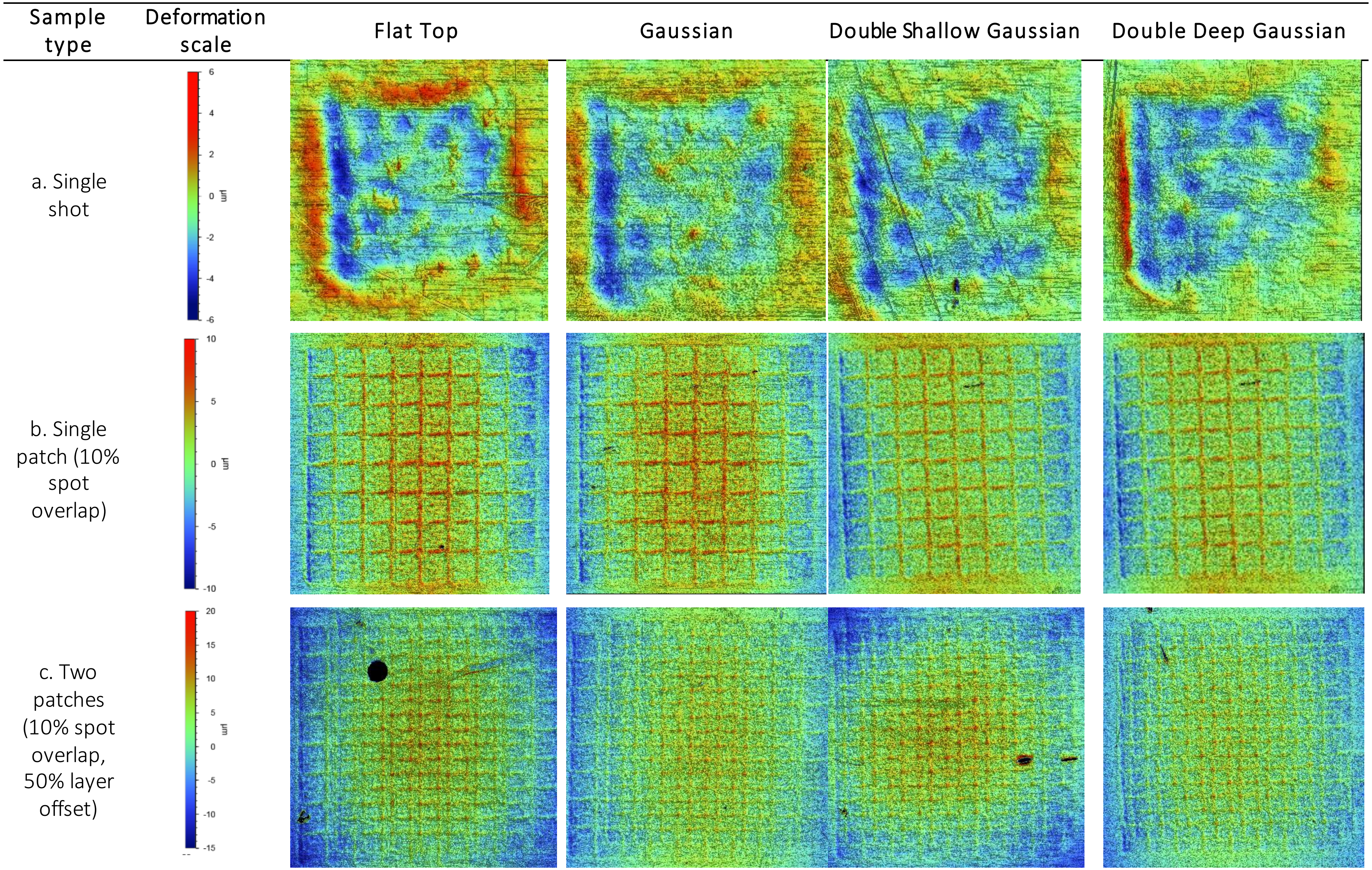

Figure 4.9: Surface deformation due to laser shock peening temporal profiles and peening strategy at 1 J – 1.85 GW/cm²

<table>
<tr><th>Sample type</th><th>Deformation scale</th><th>Flat Top</th><th>Gaussian</th><th>Double Shallow Gaussian</th><th>Double Deep Gaussian</th></tr>
<tr><td>a. Single shot</td><td>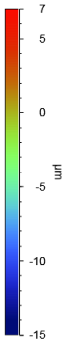</td><td>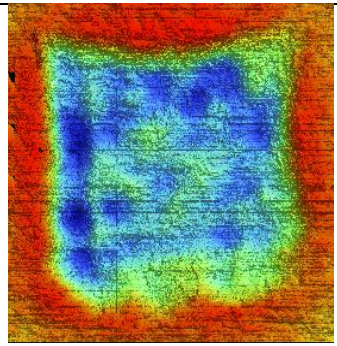</td><td>No sample</td><td>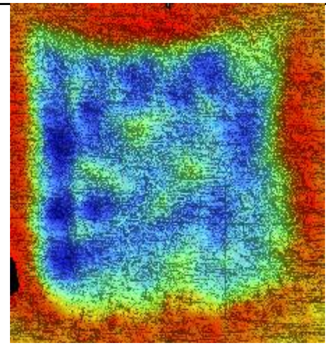</td><td>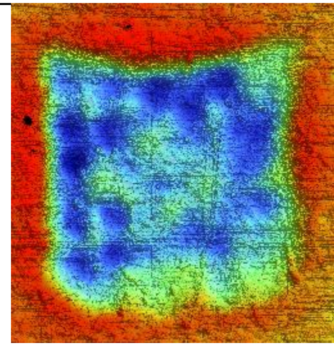</td></tr>
<tr><td>b. Single patch (30% spot overlap)</td><td>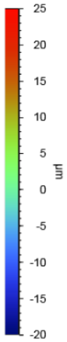</td><td>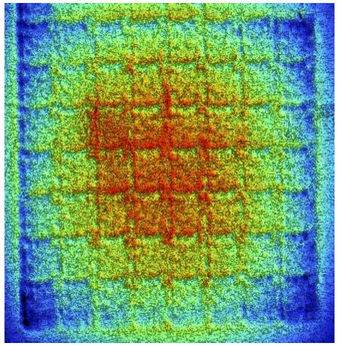</td><td>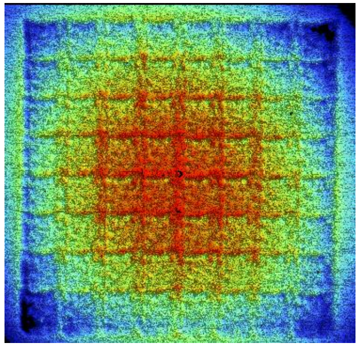</td><td>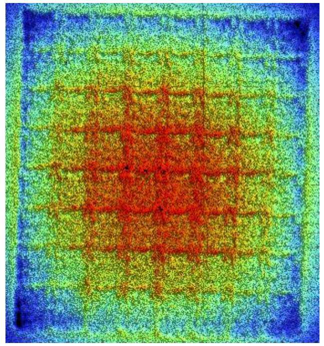</td><td>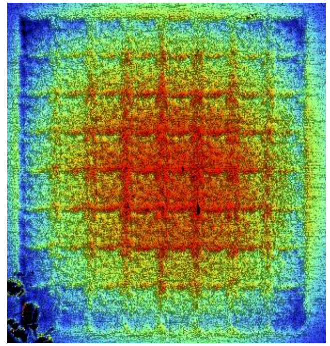</td></tr>
<tr><td>c. Two patches (30% spot overlap, 50% layer offset)</td><td>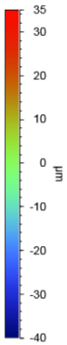</td><td>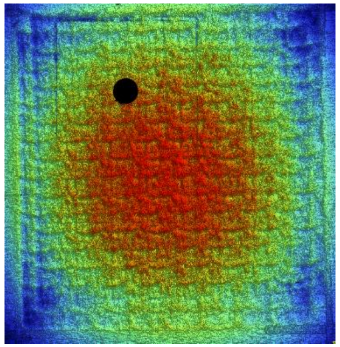</td><td>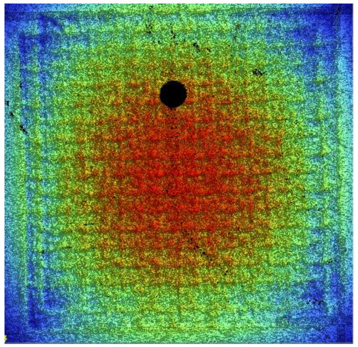</td><td>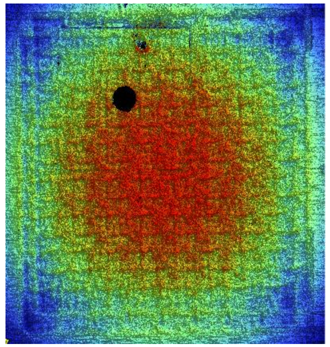</td><td>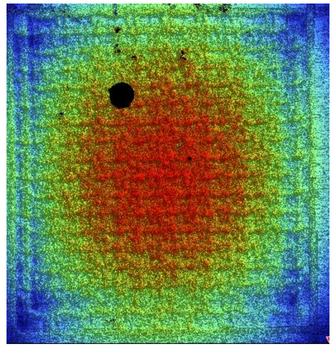</td></tr>
</table>

Figure 4.10: Surface deformation due to laser shock peening temporal profiles and peening strategy at 3 J – 5.56 GW/cm²

Figure 4.9.a and Figure 4.10.a provided the surface deformation caused by a single LSP shot at the two laser energy settings. The higher power density approximately doubled the maximum deformation that occurred in the lower power density shot. The increase in surface deformation was expected as it would be required to induce the previously shown compressive residual stress distributions. These figures show that the surface deformation is not uniform in magnitude and size, with no planes of symmetry across the dimple of laser spot geometry. This non-uniformity of the deformation can be considered as one of the contributing factors to the anisotropic nature of the residual stress in the two orthogonal measurement directions (x and y directions) for a single LSP shot, as was shown in Figure 4.3. A uniformly distributed deformation would naturally result in a equal stress distribution in the two orthogonal directions (with the condition that there are no differences in the geometric constraints in the two orthogonal directions).

Figure 4.11 provided an averaged deformation across the centre of the single-shot for every available temporal profile. The presented values were determined as the athematic mean of every deformation value across the spot within ±0.15 mm of the horizontal centre line. Due to sample complications, there was no measurement of the Gaussian single shot at 3 J. The averaged surface deformation for the presented samples indicated that the laser temporal profile had little effect on the surface deformation as the measured deformations were extremely similar and with no discernible standout features when compared to each other.

Figure 4.11 showed that the highest deformation occurred toward the edge of the left side of the spot and can be seen in Figure 4.9.a and Figure 4.10.a. The non-uniformity of the spot deformation would indicate that the laser spatial distribution (two-dimensional energy variations across the laser cross-section) was not initially uniform. This conclusion was based on the Fabbro et al. findings that showed the local laser intensity varied according to the spatial distribution of the laser pulse [10], this was shown in Figure 2.5. This implied that an increase in local power density would result in a higher localised surface deformation producing the non-uniformity in the measured deformations. The full effects of the laser spatial variations will be explored in section 4.2.1 where an LSP FEA model was used to analytically investigate these effects.

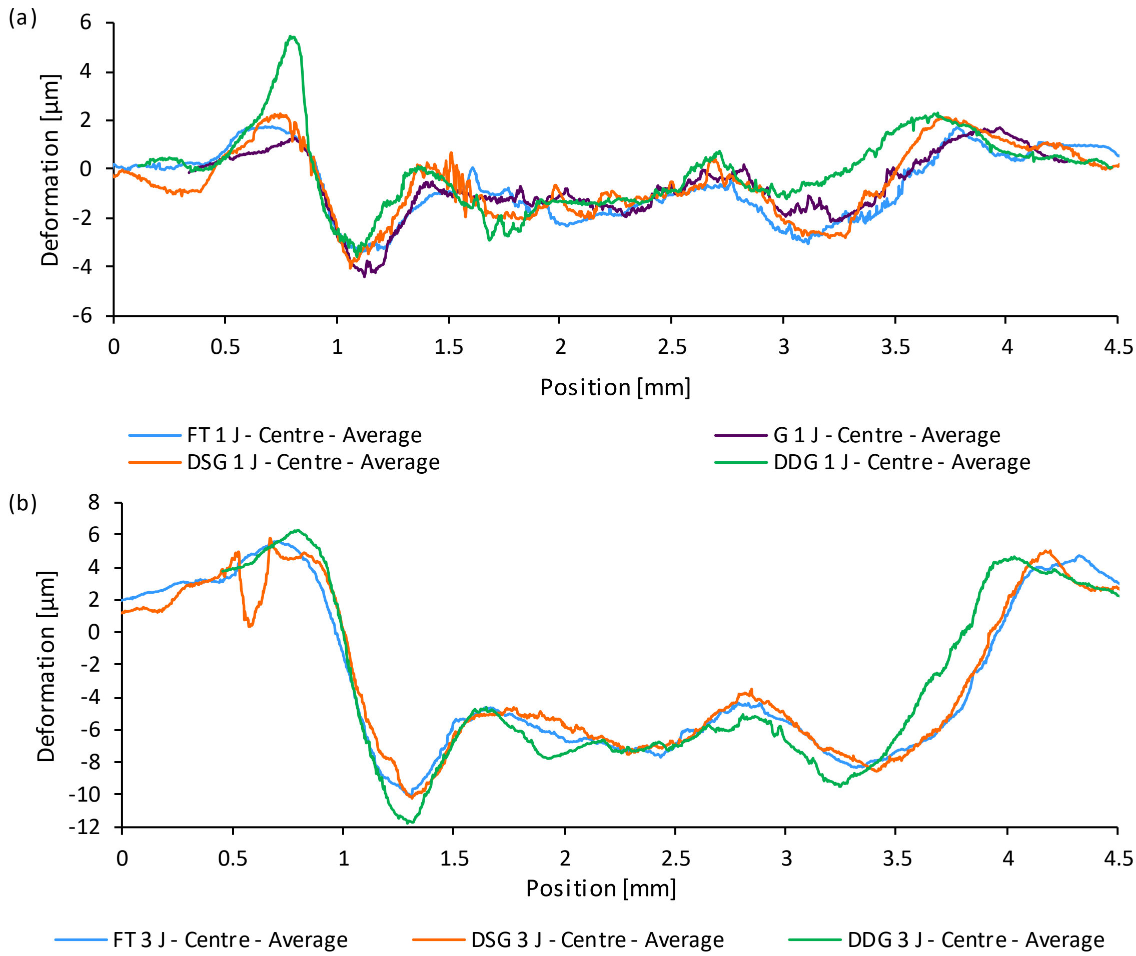

Figure 4.11: Combined centre averages of single shot deformations (a) 1 J – 1.85 GW/cm² (b) 3 J – 5.56 GW/cm²

Figure 4.9.b-c and Figure 4.10.b-c provided the measured surface deformation that occurred due to the processing of single and multiple offset LSP layers. The circular black artefact in a number of the images was caused by the incremental hole drilling of the samples. From these figures, it was clear that the temporal profiles had no distinguishable influence on the deformation of the target surface. No inconsistencies in the application of the sequential LSP spots were observed. This would indicate a fairly uniform residual stress field over the processed area, barring any local variations within each LSP shots. The application of multiple LSP spots did cause the sample to bend out of plane slightly. This is distinguishable by the fact that the peening was consistent yet the overall sample deformation tended to increase toward the centre of the sample. This is a common factor associated with LSP processing of larger areas and occurs most noticeably in thinner samples. This bending occurs as the surrounding material achieves equilibrium with the newly introduced LSP residual stress. The maximum out of plane bending was measured to be approximately 25 µm which was of a similar order of magnitude as the spot indent and was considered to not severely influence the measurement of the residual stress by incremental hole drilling.

4.2. Finite element analysis of laser shock peening

The primary focus of this chapter has been concentrated on detailing the experimentally determined effects of various LSP parameters (temporal profile, power density and processing strategies) on residual stress and surface morphology. The remainder of this chapter was dedicated to the development of LSP FEA modelling techniques which used these experimental results to validate the output of the LSP simulations. These simulations provided additional insight and context to fundamental mechanisms behind the experimental results.

As indicated in Chapter 2, the benefits of an accurate LSP model capable of predicting the total residual stresses in an arbitrary three-dimensional body treated with arbitrary LSP parameters sets are extremely valuable. Accurate models will provide the ability to inexpensively develop the LSP process (new lasers, confinement mediums and processing procedures) and enable the optimisation of the treatment parameters and strategies (temporal profiles, power density, pulse duration, overlaps and coverages).

All presented LSP models were developed using the commercial finite element ABAQUS software. The key factor in the development of a dynamic 'pulse-by-pulse' LSP model was the appropriate selection and refinement of the computational strategy, the material model, the pressure model and analysis parameters. By correctly representing these items the optimised single-shot simulation can be expanded to provide an accurate and efficient solution to any LSP configuration. Figure 4.12 illustrates the undertaken steps to simulate the induced residual stresses. examiners

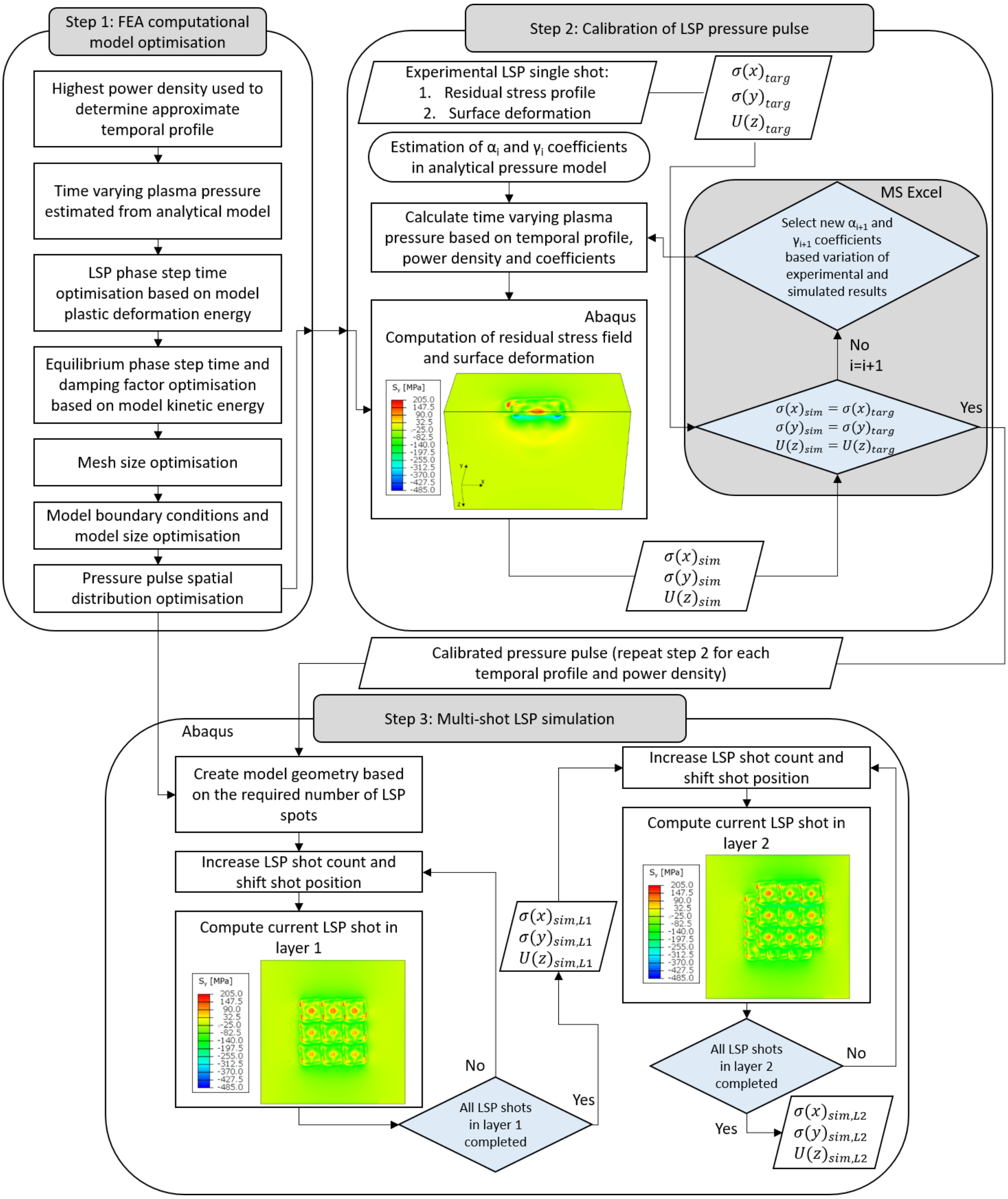

Figure 4.12: Illustration of the laser shock peening modelling process to compute residual stresses

4.2.1. Laser shock peening process modelling

This section provided a detailed description of all aspects required to perform an accurate simulation of a single LSP event. The results of the single-shot simulation were used for additional multi-shot simulations.

4.2.1.1. Laser shock peening material model

The explosion of the LSP-formed plasma induces a shock wave that propagates within the material causing deformations at extremely high strain rates (10^6 s^{-1}) [11]. To capture these effects in the LSP simulations, the Johnson-Cook constitutive material model was used throughout this analytical assessment of the LSP process. The Von Mises yield criterion was defined by equation 2-29 in chapter 2, with the used empirical constants being determined at lower strain rates (10^3 s^{-1}). Brockman et al. showed LSP simulation results were accurate to within 10% when using lower strain rate JC factors [12].

The Johnson-Cook material constants of aluminium 2024-T351 have been used to represent the behaviour of the experimentally used aluminium 2524-T351 [13]. This was done due to a lack of published empirical factors for this specific alloy and it was considered that the two materials were sufficiently similar. In an attempt to accurately predict the spatial effects of the LSP shot and the variations in residual stress near the surface, the high purity aluminium clad material has been included in the simulation. The Johnson-Cook material constants of very high purity (99.00%) aluminium were used to approximate the material behaviour of the clad layer [14]. This was done due to the lack of published data for this specific material. It was assumed that the closest matching alloy for which published data was available would result in a suitable level of accuracy to represent the experimental material. Additionally, it can be assumed that a larger error is attributed to the inability in determining the JC factors at the appropriate LSP strain rate than that of the slight mismatch in aluminium alloy. The Johnson-Cook material constants that were used to represent the AA2524-T351 and clad in the simulations are listed in Table 4.2 [13,14]. The constitutive model did not account for the LSP induced cyclic deformation effects which occur due to successive laser impacts [15].

Table 4.2: Johnson-Cook material constants for AA2524-T351 and high purity aluminium clad [13,14]

Material	$\boldsymbol{a}$ [MPa]	$\boldsymbol{b}$ [MPa]	$\boldsymbol{c}$	$\boldsymbol{n}$	$\dot{\varepsilon}_0$
AA2524-T351	369	684	0.0083	0.73	1
Aluminium clad	129	200	0.03	0.45	0.01

The material assigned to the respective areas in the three-dimensional model is shown in Figure 4.13. The dimensions of the material layers (clad 0.185 mm on each side and the remaining thickness as AA2524) were set according to the material characterisation in chapter 3. The model was portioned so that the single LSP shot occurred in the centre of the model domain, as indicated by the red dashed lines in Figure 4.13. A second partition in the thickness (z-direction) of the AA2524 material near the impact surface was made to allow for mesh refinement in a critical region of the model. The thickness of this section was specified as half the LSP spot dimension. Refinement in this region of the model was vital as the majority of the LSP induced residual stress would occur in this region.

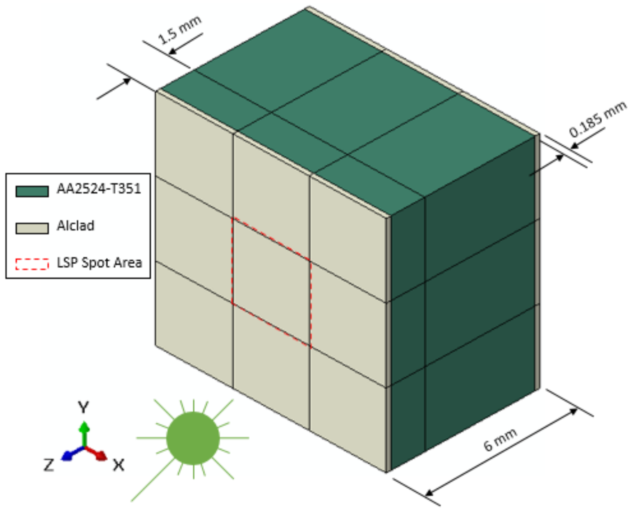

Figure 4.13: Single-shot laser shock peening model material assignment

4.2.1.2. Laser shock peening computational model

All LSP events were simulated using only explicit time integration (ABAQUS/Explicit) to solve the dynamic system. As described by Brockman et al. [16], the use of the explicit solver in the simulation of the laser shot and return to equilibrium was quicker, more scalable and improves the practicality in the analysis of multiple series of pulses. Each impact pulse was simulated using two distinct solution steps, the LSP impact step and the equilibrium step. This was done to include additional material parameters to improve convergence and accelerate the return of the system to equilibrium. All computational model optimisation was completed with a pressure profile generated with a 3 J flat-top laser beam energy profile as this was the highest loading condition.

4.2.1.2.1. Step definition

Each LSP impact was modelled by two distinct solution steps, designated as 'LSP phase' and 'Equilibrium phase'. The LSP phase is defined with the start of the application of the pressure pulse and ends when no further plastic deformation occurred. The plastic deformation was defined based on the energy dissipated by the model plastic deformation. Figure 4.14 provided an example of the energy dissipation history from the application of the LSP pressure pulse. It was considered that no further plastic deformation occurred in the model after a time when the percentage change in plastic deformation energy was less than 0.001%, as indicated by the dotted line in the figure. A total step time of 2.5 µs was found to be appropriate to ensure enough time for the dissipation of plastic deformation energy for all LSP plasma pressure conditions investigated in this work.

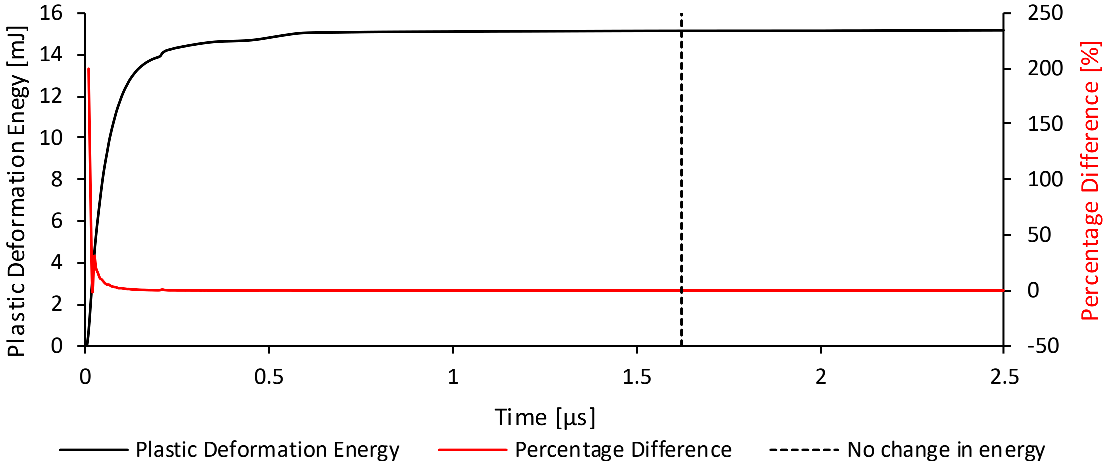

Figure 4.14: Plastic deformation energy history for a single laser shock peening event in the first phase of the simulation

The second solution step which was defined as the 'Equilibrium phase', introduces artificial damping or Rayleigh damping into the model to accelerate the return of the system to a state of near-zero kinetic energy. Mass proportional damping was the only form of artificial damping applied to these models. The length of the first computational step was set when no further plastic deformation occurred. However, the model had not yet fully reached equilibrium by the end of the first solution phase as the model's kinetic energy had not dissipated to an acceptable limit. Equilibrium was judged at the point where the kinetic energy of the model was less than 10^{-6} J. The magnitude of the damping factor did greatly affect the rate of return to equilibrium. The results from an unsteady model can result in large errors in the predicted stress and deformation as the solution had not fully converged. Figure 4.15.a-c showed the effects of the magnitude of the damping factor on the models kinetic energy, predicated residual stress and surface deformation across the horizontal centre of the LSP spot. The FE residual stress results were the averaged principal stresses over a 1.9 mm circular area which was equivalent to the volume of material removed at each incremental hole drilling measurement step. All FE residual stress and equivalent plastic strain were determined in this manner. The results in the figures indicated that for a fixed solution time step, a damping factor of at least $1\text{x}10^5$ was required to achieve equilibrium of the model and convergence of the model outputs. This initial total solution time was set based on the available computational resources required to accommodate the thousands of solution integration steps.

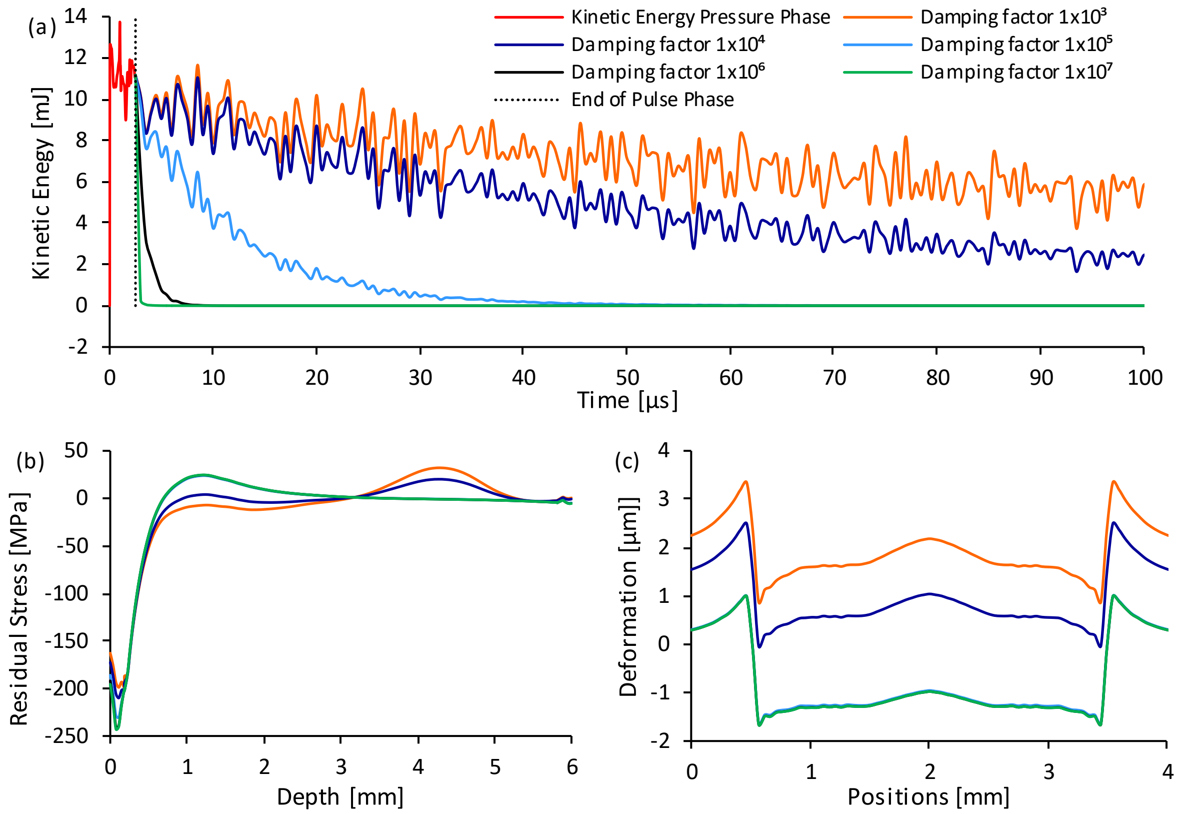

Figure 4.15: Effect of Rayleigh damping factor on (a) rate of return to near equilibrium, (b) predicted average residual stress determined in a 1.9 mm area at the centre of the laser shot, (c) surface deformation across the centre of the laser shot

The simulations with lower damping factors predicted large variations in the residual stress in the thickness of the material and under predicted the peak compressive stress near the surface. Figure 4.15.c showed the sensitivity of the surface deformation to the damping factors in that if the solution was taken before the model reached equilibrium an unrealistic and overestimated deformation was achieved. A damping factor of $1x10^6$ was selected as an appropriate damping factor as $1x10^5$ was judged to be possibly insufficient to fully damp a model which had multiple LSP shots thus larger amounts of kinetic energy in the system. A total step time of 100 µs was found to be an appropriate length of time to ensure sufficient return to equilibrium between LSP events and full convergence of the model outcomes. Additionally, this was in line with previously published work, shown in chapter 2.

Figure 4.16 showed the influence of the lack of convergence and return to equilibrium on the predicted residual stress in the entirety of the model domain. Residual stress variations were observed in the surroundings of the LSP spot at lower damping factors. These regions of instability were identified as the dark orange and red regions in damping factors less than $1x10^5$. Although the residual stress in the spot area had been predicted with some small inaccuracy, there should be little to no residual stress in the surrounding material of the model and these should be considered as inaccuracies that must be avoided.

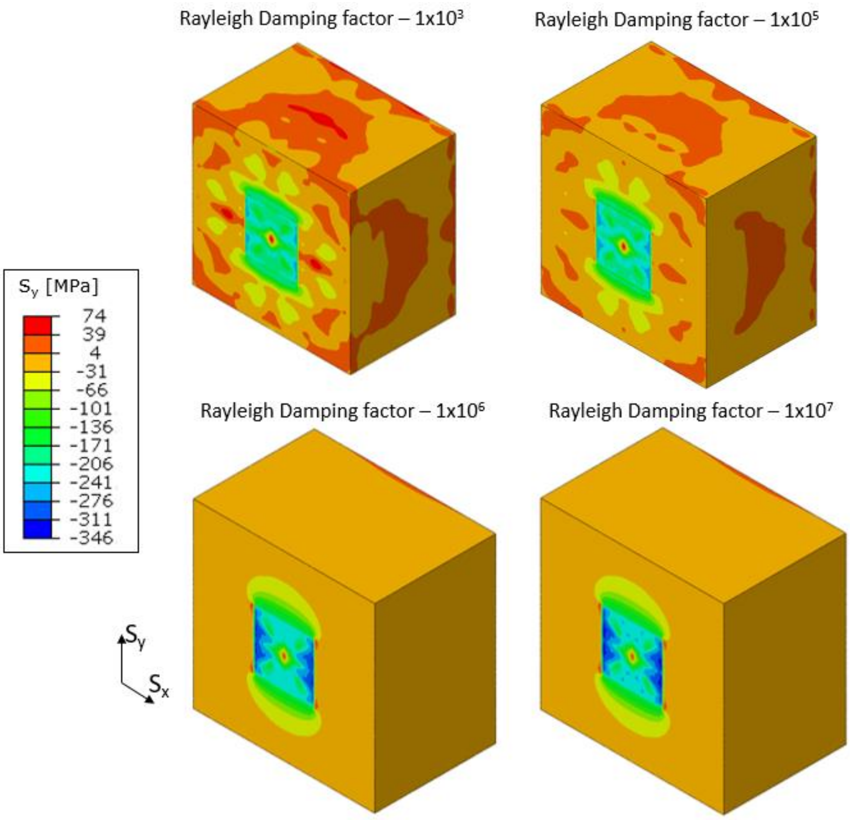

Figure 4.16: Effect of convergence rates on return of model equilibrium and the predicted residual stress

4.2.1.3. Mesh optimisation of laser shock peening model

Three-dimensional linear eight-node brick elements with reduced integration (C3D8R in ABAQUS) were used throughout and additional detail about these elements can be found in the ABAQUS user manual [17]. The mesh sensitivity and optimisation was carried out with the simulation of a simple single LSP shot. Figure 4.17 showed the single-shot model which was partitioned to have the LSP shot in the middle of the model and four thickness partitions (two clad layers, a fixed mesh area near the surface of the LSP spot and the remaining bulk thickness). Mesh refinement was conducted in the five critical areas indicated by the colour regions in Figure 4.17. Mesh size optimisation was extremely important with regards to an explicit simulation as element size defined the maximum critical time step, computation cost and general quality of the simulation outcomes.

An iterative optimisation process was conducted to obtain the best possible mesh structure whilst managing the computational cost of the model. The mesh was optimised according to the LSP spot edges (x-y), then the surrounding areas (x-y), then in the clad depth (y-z), followed by the near LSP depth edges (y-z) and finally the remaining bulk material (y-z). Table 4.3 provided the numerous mesh size combinations and final size which was judged to be the most optimal mesh strategy. Figure 4.18

provided the results for the listed mesh configurations for the single-shot LSP models. The mesh convergence was judged based on the predicated averaged equivalent plastic strain, the through-thickness residual stress at the centre of the LSP spot and surface deformation which was taken across the horizontal centre of the spot.

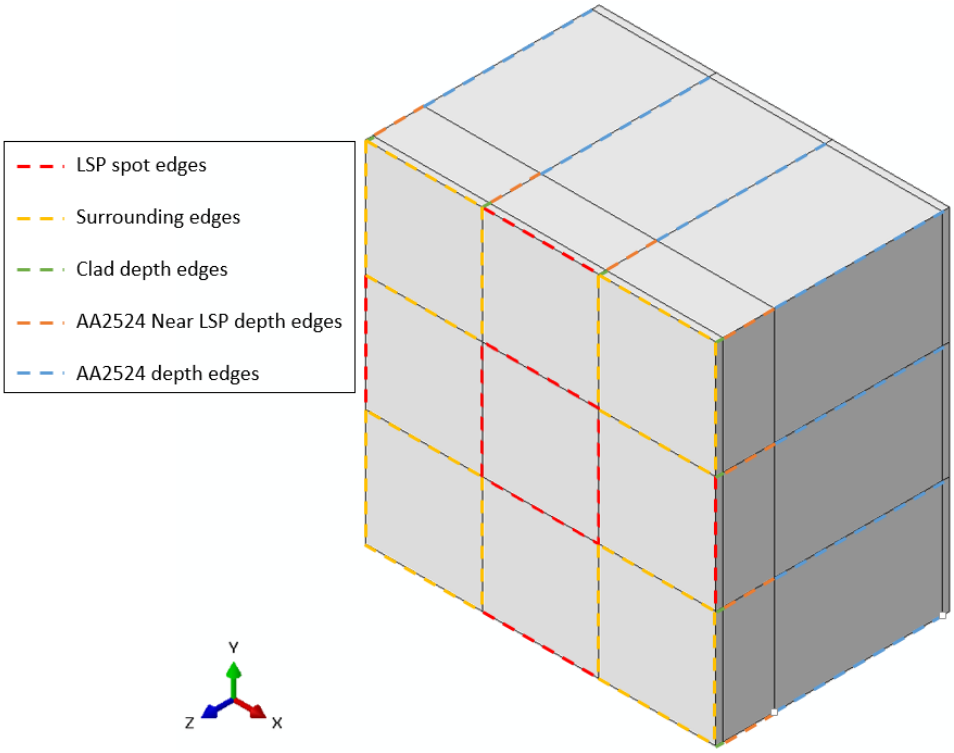

Figure 4.17: Single-shot model portioning strategy and specification of mesh sensitivity areas

Figure 4.18.a showed the results of the mesh optimisation across the edges of the LSP spot area. The surface deformation was most affected by the refinement around the LSP area. A mesh size of 50 µm was used in the LSP region as there was less than a 5% increase in residual stress and deformation with further refinement. Figure 4.18.b showed the result of the optimisation in the surrounding area to the LSP spot. A single increasing mesh bias was used to reduce the computational costs of the simulations. The starting size was fixed to the LSP spot edges to avoid sudden increases in mesh size. A gradual increase from 50 to 250 µm in this area was found to be appropriate and had little effect on the results. A larger maximum size was not used to avoid mesh elements with aspect ratios larger than 15.

Figure 4.18.c provided the refinement of the mesh in the depth of the clad region of the model. Three sizes were tested and a thickness of approximately 20 µm was found to provide the most accurate result of the surface deformation. As in the clad region, a mesh depth size of 20 µm was found to be appropriate in the AA2524 portion nearest the LSP surface of the model, as seen in Figure 4.18.d. Figure 4.18.e showed a mesh size in the remaining depth of the model which varied according to a double mesh bias of 20 - 250 - 20 µm which provided an acceptable accuracy of computation. The size of the

mesh in this region had very little effect and was specified mainly to increase the computation efficiency of the model.

Table 4.3: Mesh convergence specifications for a single shot laser peening model

Model area	LSP Spot Area	Surrounding LSP Spot	Clad Depth	AA2524 Near LSP	AA2524 Remaining	Figure Reference
	X-Y [µm]	X-Y [µm]	Z [µm]	Z [µm]	Z [µm]	
Across the LSP spot	100 x 100	100 - 150	40	40	40-120-40	Figure 4.18.a.
	50 x 50	50 - 150				
	35 x 35	35 - 150				
Surrounding LSP area	50 x 50	50 - 250	40	40	40-120-40	Figure 4.18.b.
		50 - 150				
		50 - 100				
Clad depth	50 x 50	50 - 250	80	40	40-120-40	Figure 4.18.c.
			40			
			20			
		50 - 150	20			
AA2524 Fixed depth	50 x 50	50 – 250	20	40	40-120-40	Figure 4.18.d.
				20		
AA2524 Remaining	50 x 50	50 – 250	20	20	40-120-40	Figure 4.18.e.
					20-120-20	
					20-250-20	

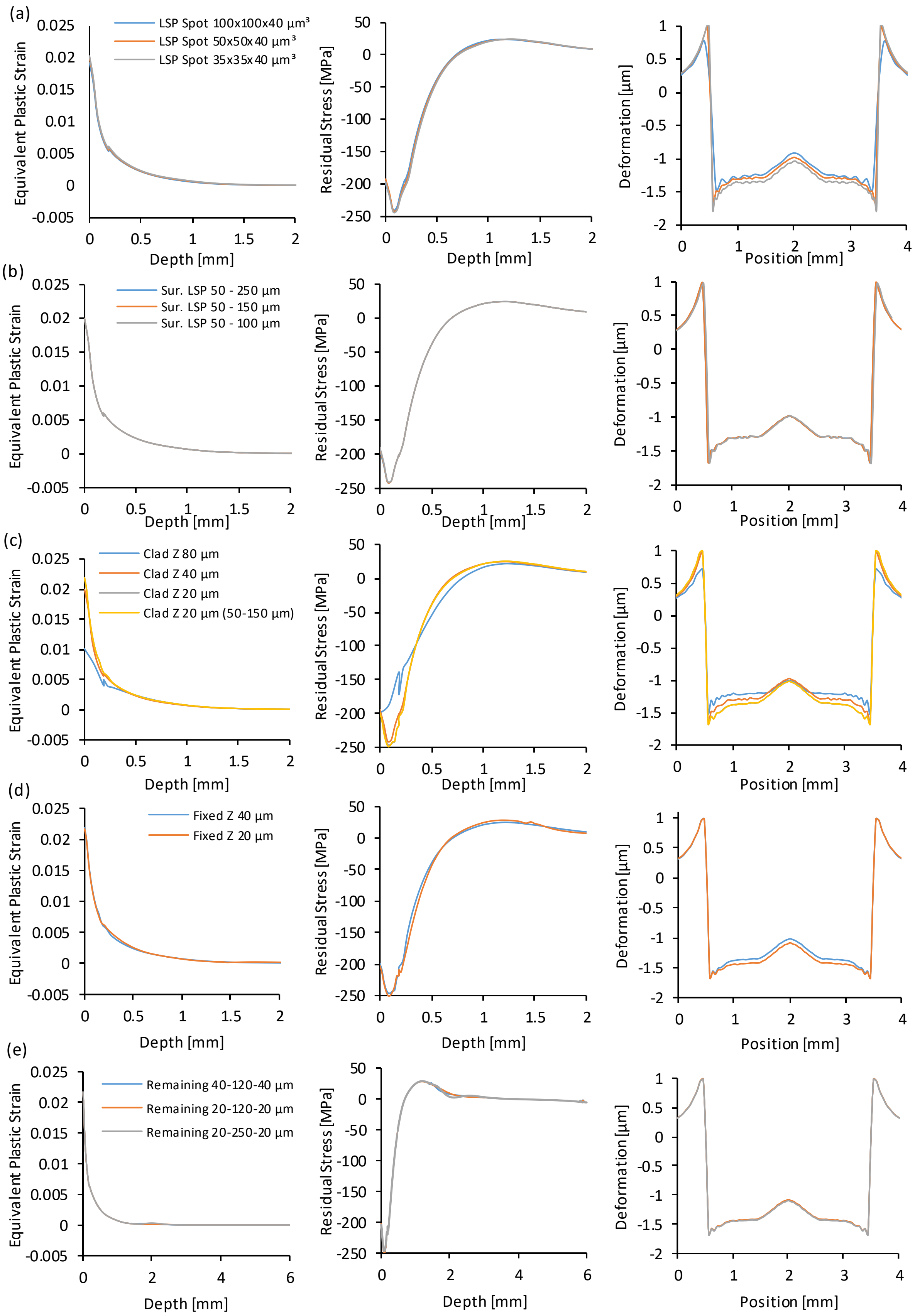

Figure 4.18: Results of mesh optimisation of single-shot laser shock peening model regions listed in table 4.3 (a) laser spot area, (b) surrounding spot area, (c) clad thickness, (d) near laser spot thickness, (e) remaining bulk thickness

4.2.1.4. Boundary conditions and model size

Keller et al showed that the measured residual stress in samples with various back surface contacts (free, in contact with steel and glued) only varied within the deviation of the measurement accuracy [18]. This result validated the assumption that any reflected shock waves from the free back surface would have no significant effect on the measured and simulated residual stress. In all cases, the model domains were fixed around the thickness surfaces in the three orthogonal modelling directions. The back surface to the LSP impact surface was set as a free surface that was not in contact with any support. This simplified the model by avoiding the need for simulating complicated non-linear contacts and was the most similar to the actual free surface which occurred during the peening process.

The size of the model which surrounds the LSP spot can greatly affect the rate of the completion and computational needs of the simulation. Coupled with the requirement for an extremely fine mesh structure, the model domain size should be optimised to ensure that the fixed boundary conditions did not influence the shock wave propagation and resulting residual stress. Table 4.4 listed the studied model domain sizes relative to the LSP spot geometry.

Table 4.4: Model size optimisation based on a single shot laser shock peening event

LSP Spot Size [mm]	Model Size [mm]	Model Size - LSP Spot Size Ratio	Number of elements
3 x 3	6 x 6	2	1 128 960
3 x 3	9 x 9	3	1 866 240
3 x 3	15 x 15	5	4 893 760

Figure 4.19 showed that the predicted residual stress was the most influenced outcome with regard to the proximity of the boundary. The best compromise between computational accuracy and solution efficiency was found with a domain-to-LSP spot size ratio of three.

4.2.1.5. Laser shock peening pulse loading

The plasma formed by the laser-material interaction was not directly modelled. Rather, the pressure loading from the laser pulse was determined using the analytical one-dimensional confined plasma model proposed by Fabbro et al. which was discussed in Chapter 2, section 2.2.1.3 [1]. The plasma pressure was applied over the laser spot area using time-varying surface traction. Initially, the plasma loading was applied as a spatially uniform pressure and was later refined by incorporating measured pre-focused laser spatial distribution which was discussed in more detail in section 4.2.1.6.2. No thermal effects were considered in the simulation as a protective ablative coating was used in the experimental LSP processing.

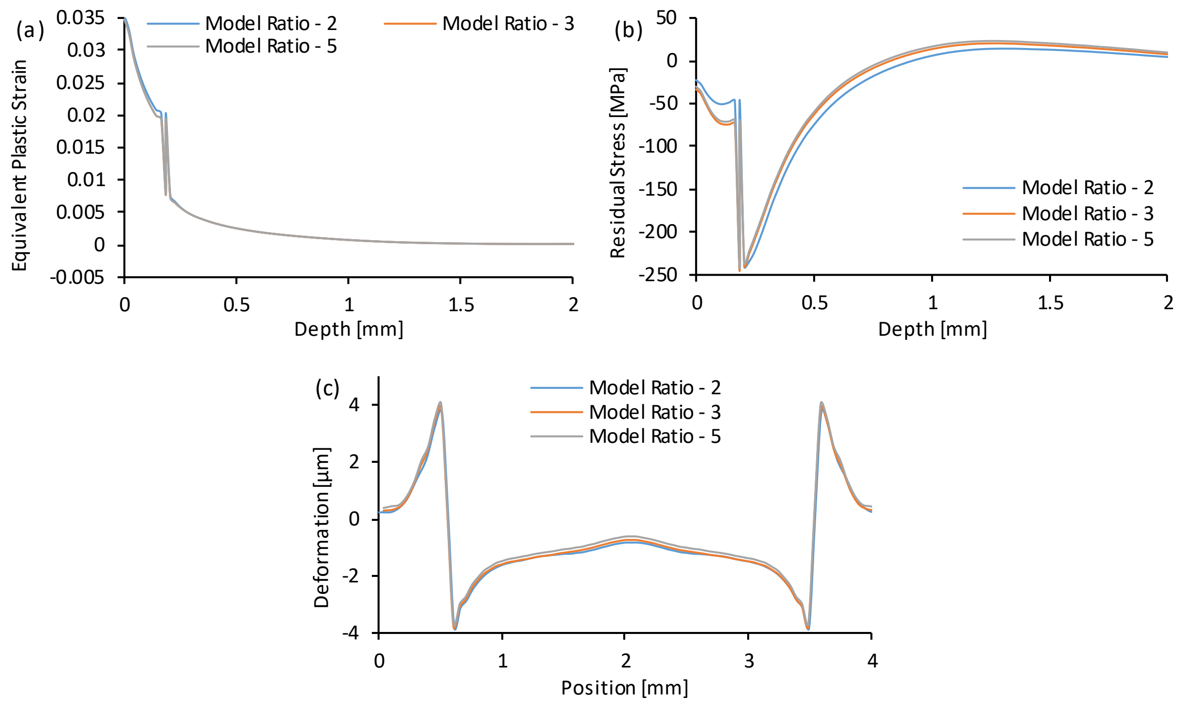

Figure 4.19: Effect of model size on the predicted (a) equivalent strain, (b) residual stress and (c) surface deformation due to a single laser shock peening event

Throughout this work, the experimental target surface assembly was made up of black polyvinyl tape ($Z_{coating} \approx 1.46\text{x}10^6$ g.cm^{-2}.s^{-1}) and the water confinement ($Z_{confinement} \approx 0.15\text{x}10^6$ g.cm^{-2}.s^{-1}). The combined acoustic impedance was $0.3\text{x}10^6$ g.cm^{-2}.s^{-1} which was determined according to equation 2-7.

The measured temporal profiles shown in Figure 4.1 provide an example of the time-varying plasma energy and by extension, the power density which was determined with equation 2-12. This equation incorporates the laser pulse widths listed in Table 4.1. The plasma pressure was analytically solved at each time step according to equation 2-4. The two pressure model coefficients were iteratively calibrated based on the comparison of the simulated and experimental results. This was discussed further in section 4.2.1.6. Figure 4.20 provided an example of the analytically determined plasma pressure distribution for each tested temporal profile. The plasma pressure steeply rose to its peak pressure within the first ten nanoseconds of the laser-material interaction. This correlated to the very quick rise time in the laser energy for each temporal profile. The most notable influence of the shape of the temporal profile was observed near the peak pressure, where the fluctuation in the pressure profile correlated to the reduction in laser energy. Close examination of this region showed that this mainly affected the double Gaussian profiles where a pressure reduction of approximately 400 MPa was observed over five nano-seconds. The lowest dashed-dot line in the figure corresponded to the Hugoniot Elastic Limit (HEL) of the material, this was determined with equation 2-13. The larger magnitude dashed lines corresponded to a simplification of the plasma pressure model in which a constant peak power density was assumed in determining the plasma pressure, this was achieved with equation 2-16. This simplification was proposed by Fabbro et al. and was used here to validate the numerical methods used to determine the pressure as the power density varied [1]. The model coefficients α and γ had to be slightly varied to achieve an approximately equivalent peak pressure of 1.6 GPa for each temporal profile, with the optimised coefficients for each temporal profile provided in the legend of the figure. It was evident that the α factor (which was directly proportional to the peak pressure) had to be increased to account for the reduction in overall energy delivery that occurred with the Gaussian-shaped temporal profiles. The γ (which defined the cooling rate of the plasma) was fixed across all the profiles. The total period of application of the plasma pressure was capped at 200 ns, as this was the most common value used by recently published works in this field (this was provided in table 2.4).

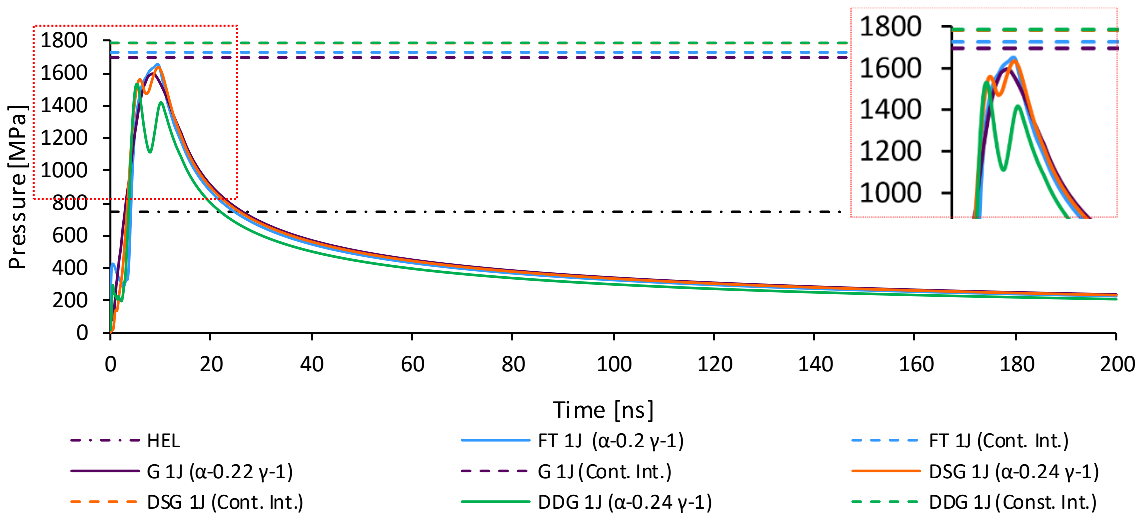

Figure 4.20: Example of pressure profiles determined by the various laser temporal profiles

It must be noted that this pressure model was purely based on measurable laser parameters only. As it was a pure pressure model it does not account for energy losses due to dielectric break down along the path of travel, thermal effects on the focusing lens and other optics, confinement absorption losses and reflections of the light (energy) upon striking the target surface.

4.2.1.6. Calibration of laser shock peening pulse pressure

An appropriate approximation of the plasma pressure loading was required to achieve an accurate prediction of the residual stress induced by each LSP shot. All parameters in the analytical plasma pressure model (equation 2-15) were known besides the plasma coefficients. These factors are typically determined based on a trial and error optimisation between the measured and predicted residual stress of a single LSP shot. In this work, the plasma coefficients for the FT and DSG temporal profiles were calibrated against the incremental hole-drilling residual stress measurements at the centre of the 3x3 mm^2 single shots at the two laser energy settings: the data was presented in Figure 4.3. These two profiles were selected due to the availability of experimental data. Additionally, it was concluded that the simulation of the two temporal profiles would be sufficient to demonstrate the accuracy of the model as there were no significant differences in the experimental data between the four profiles.

4.2.1.6.1. Spatially uniform plasma pressure

Initially, the FEA models were calibrated for each temporal profile assuming a perfectly uniform plasma pressure acted across the laser spot. This was not the case in reality and variations in the laser spatial profile were evident based on the non-uniformity of the surface deformations presented in Figure 4.9 and Figure 4.10. The FEA residual stress results were the averaged stresses over the equivalent volume of material that was removed by the numerous incremental hole drilling steps. The residual stress at the interface of the clad and AA2524 material was averaged to remove the step in the stress caused by the transition in the material. The alpha and gamma coefficients used to determine the plasma pressure that is applied in the FEA model are determined iteratively and are specified based on the values which provide the lowest discrepancy between the measured and predicted residual stress and surface deformation of a single LSP shot. Initial values of alpha and gamma were selected based on the published works listed in Table 2.5 and then incrementally changed to reduce the error between the predicted and measured results, as shown in Figure 4.12. The values for the plasma pressure coefficients have been listed in Table 4.5. A larger alpha coefficient was required for the DSG 1 J profile to account for the lower power density that was achieved with the measured pulse width listed in Table 4.1.

Figure 4.21 showed the comparisons between the measured and predicted residual stress with a uniform plasma pressure at the various power intensities and temporal profile combinations. It was possible to calibrate the uniform pressure pulse to achieve a good correlation between the experimental and predicted residual stress, especially with the peak compression and depth of compression. Figure 4.22.a-c. showed that the deformation was uniform in all directions of the spot geometry, with planes of symmetry occurring across the major axis of the model. This uniformity of the deformation resulted in an equal distribution of the residual stress in the two orthogonal directions. This was not the case in reality as a non-uniform deformation occurred in the experimental single shots, as shown in Figure 4.9 and Figure 4.10. An additional outcome of non-uniform experimental spot deformation was the establishment of a biaxial or anisotropic residual stress state that occurred from the single LSP shot.

Table 4.5: Plasma pressure model coefficients for a uniform and spatially varied laser shot

Temporal profile	Pulse energy & power density	Uniform plasma pressure		Spatial plasma pressure	
		Alpha (α)	Gamma (γ)	Alpha (α)	Gamma (γ)
Flat Top	1 J – 1.86 GW/cm^2	0.2	1	0.19	1
	3 J – 5.62 GW/cm^2	0.15	1	0.15	1
Double Shallow Gaussian	1 J – 1.70 GW/cm^2	0.24	1	0.23	1
	3 J – 5.08 GW/cm^2	0.15	1	0.15	1

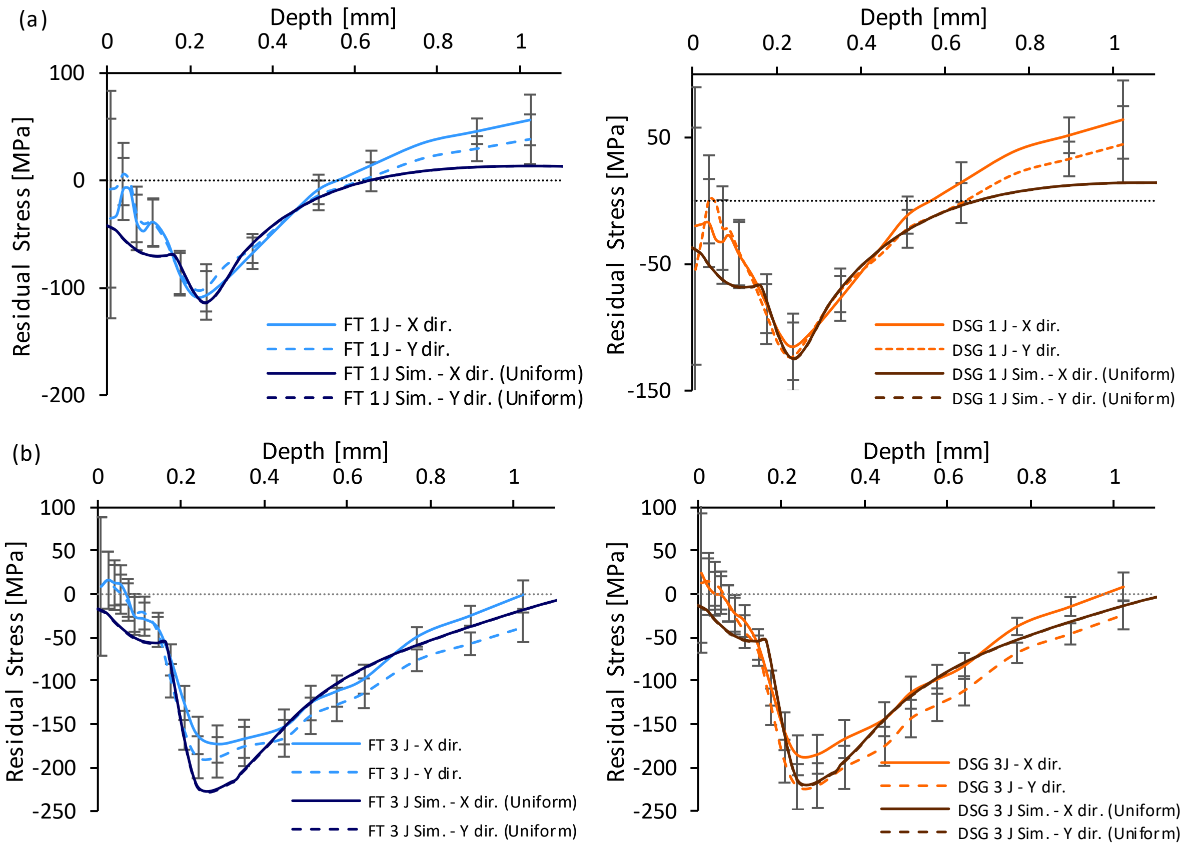

Figure 4.21: Comparison of spatial uniform pressure single-shot residual stress (a) flat top & double shallow Gaussian 1 J – 1.85 GW/cm^2, (b) flat top & double shallow Gaussian 3 J – 5.56 GW/cm^2

The simulated residual stress varied slightly from the experimental results in the near-surface (within the first 185 μm) due to the presence of the clad material. Due to limitations in the processing software, it had to be assumed that the mechanical properties of the clad layers were equivalent to the bulk AA2524 material when processing the experimental residual stress. The actual clad material was significantly softer and had a lower strength than the bulk material thus causing the much lower residual stress in this region. In the FEA analysis of this geometry, the clad ended at a distinct depth causing a large stress gradient at the interface of the clad and remaining AA2524 material. The stress at this depth was averaged between the two materials causing a distinct point in-depth profile where the stress tends to rapidly became more compressive due to the stronger AA2524 material. Additionally, the discrepancy between the experimental and simulated results in the clad region could have been exacerbated by the fact that exact JC material properties used in the modelling of this material could not be confirmed and it was assumed that the clad behaved similarly to pure aluminium.

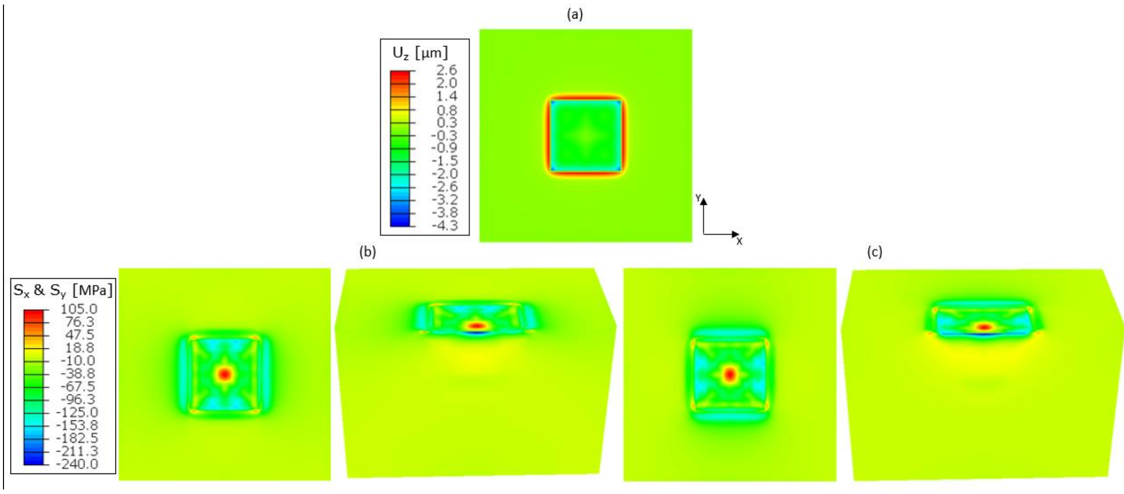

Figure 4.22: Spatial uniform pressure pulse simulation (a) surface deformation in the thickness direction, (b) residual stress in the x-direction, (c) residual stress in the y-direction

Figure 4.23 provided a comparison of the experimental and predicted surface deformation across the horizontal centre of the LSP shot. The experimental data was provided in Figure 4.11. The shaded region showed the local deformation range (maximum and minimum values used in the averaging of the deformation) caused by the LSP shot. At the lower pulse energy, the spatially uniform plasma pressure resulted in a predicted deformation that was similar in magnitude to the experimental results but failed to accurately capture the variations across the laser spot. The lack of accounting for the laser spatial variations significantly underestimated the predicted deformation at the higher pulse energy.

Overall, the simulation of the single LSP spot with a uniform plasma pressure distribution provided a reasonable first estimate of the residual stress and surface deformation at the four LSP parameter combinations. However, the main drawback of the single-shot LSP models was the inability to accurately predict the biaxial nature of the residual stresses in the two orthogonal directions. The uniformity of the simulated pressure pulse deformed the material equally resulting in near-identical residual stresses in the orthogonal directions. Additionally, the models underestimated the deformation in the central section of the spot and overestimated the peak deformation at the boundaries.

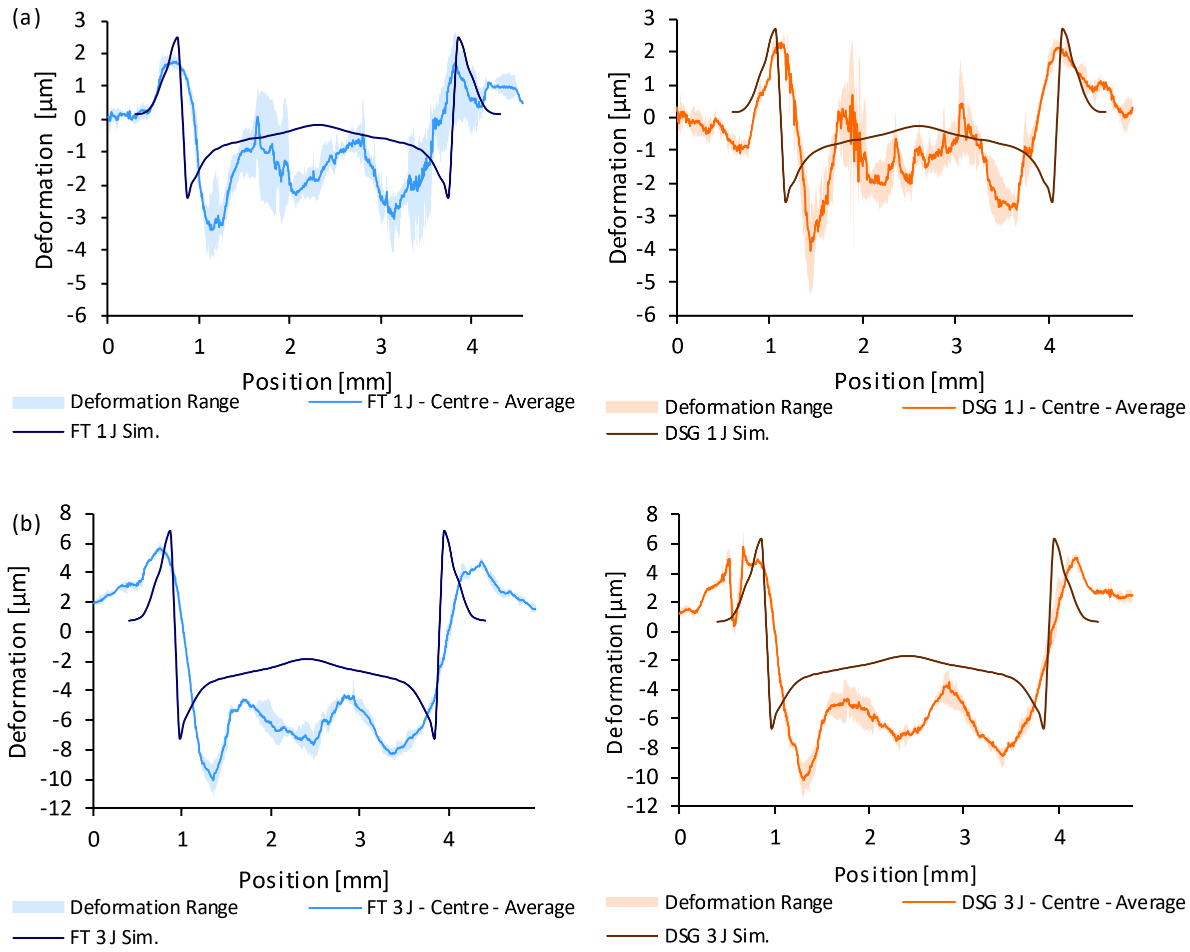

Figure 4.23: Comparison of experimental and simulated surface deformation across the horizontal centre of the laser shot with uniform pressure profile (a) flat top & double shallow Gaussian 1 J – 1.85 GW/cm², (b) flat top & double shallow Gaussian 3 J – 5.56 GW/cm²

4.2.1.6.2. Spatial distribution of the laser-plasma pressure

The previous simulation results showed that a purely uniform pressure led to inaccuracies in the simulated residual stress and surface deformation. Fabbro et al. showed that the spatial variations of a confined plasma pressure correlated fairly well to the local variations in the laser pulses power density [10]. In this work, the pre-focused laser spatial distribution was characterised using a diffractive optical element as shown in Figure 4.24.a. The diffractive optic element outputs an image of which it was assumed that the pixel intensity directly correlated to the variations in pulse energy, as provided in Figure 4.24.b. Le Bras et al. implemented a similar strategy in their assessment of an LSP pulse [19]. This indicated that Figure 4.24.a could be used as an estimation of the variations in power density and subsequently a manner in which the plasma pressure could be scaled in the FEA simulation.

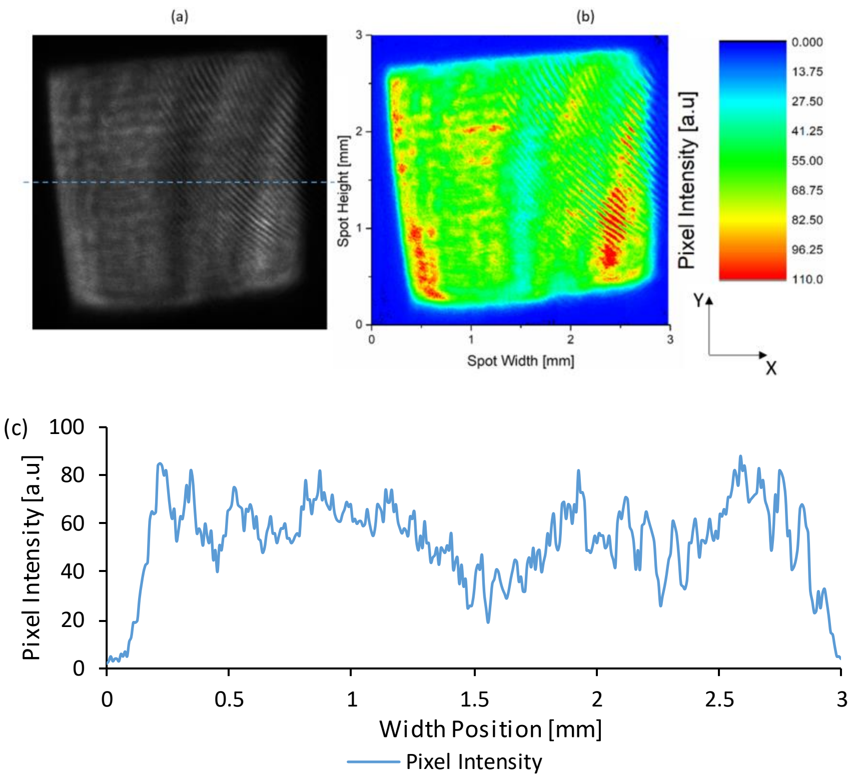

Figure 4.24: Spatial variation of the laser pulse energy (a) output from the diffractive optical element, (b) spatial laser energy variation as pixel intensity over the full spot, (c) spatial pixel intensity across the centre of the pulse

It was assumed that the spatial distribution did not drastically vary during the focusing and propagation of the laser beam. It must be noted that the spatial profile was characterised after the completion of the LSP experiment window thus minor differences between the presented and actual used spatial profile would be expected. The pixel intensity was normalised about a particular value to be incorporated into the one-dimensional plasma pressure model as a unitless pressure scaling factor. In the case of Le Bras et al., the spatial laser energy was normalised about the peak pixel intensity (maximum variance in intensity was 6%) [19]. Figure 4.24.c provided the pixel intensity across the centre of the laser spot (indicated by the blue dashed line). It was clear that laser spatial distribution was not statistically uniform as the intensity at the middle of the spot (≈1.5 mm) varied by as much as 128% to the maximum peak values at the edge of the spot (≈0.25 and 2.5 mm).

Figure 4.24.b showed areas of high intensity (indicated by the regions in red) which were grouped near the extremities of the laser spot. If Le Bras et al. normalisation strategy was used, the larger intensities would likely skew the normalised scaling value of the plasma pressure, resulting in an over and underestimation of the local plasma pressure across the spot. This was demonstrated in the pixel intensity frequency plot provided in Figure 4.25.a, where less than 30% of the pixels had magnitudes larger than the second peak of approximately 60 (Figure 4.24.a. was made up of 154 400 pixels). Figure 4.25.b provided the average pixel intensity across the laser spot at each height location (y-direction in

Figure 4.24.a) of the laser spot. The final normalising value was selected by averaging the intensities in Figure 4.25.b between the spot height positions of 0.3 and 2.7 mm, where the normalising value was represented as the black dotted line across the figure.

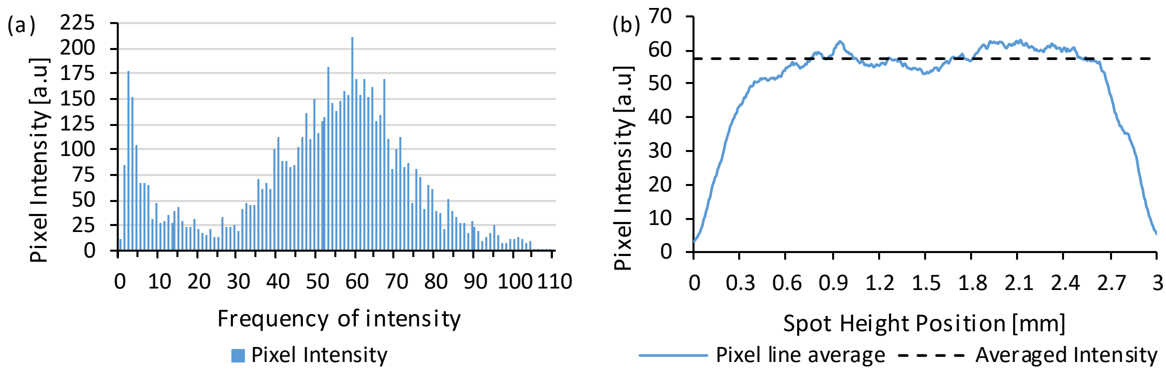

Figure 4.25: (a) Frequency of pixel intensity over the laser pulse, (b) representation of the average pixel line intensity

As previously indicated, the LSP plasma loading was represented as a time-varying surface pressure. ABAQUS applies the pressure load at the centre of the surface of each element that falls within the user-specified loading area. The LSP pressure area in all of the present simulations was made up of 3600 individual pressure points (60x60 elements). This led to the spatial distribution of the laser pulse (Figure 4.24.a, made up of 154 400 pressure points) being compressed to fit the optimised mesh structure of 3 600 points. The compression was achieved by averaging the measured laser intensity over the size of each mesh element, as represented by the grid overlay in Figure 4.26.a.

Figure 4.26.b. provided a direct comparison between the full and compressed laser spatial pressure distribution. It was to be expected that a loss in detail would occur due to the compression of the spatial profile. Overall, the compressed profile was accepted as it replicated the major features of the laser spatial profile. An increase in the spatial resolution of the profile would require a significant increase in the mesh structure size which would be computationally costly for a minimal increase in accuracy of the profile.

The per-element averaged pressure intensity was then set to act uniformly over each specific element of the mesh. This was achieved in ABAQUS by specifying an analytical field mapping function. This feature effectively scales the time-varying pressure according to a set of user-supplied coordinates (centre of the mesh elements) and scaling factors (averaged normalised pressure intensity). This was shown in Figure 4.26.c. A similar strategy can be implemented using an ABAQUS Vdload subroutine.

The coefficients in the confined plasma pressure model were re-optimised to account for the spatial variations of the plasma pressure. The values of the α and γ are listed in Table 4.5. The α values at the lower pulse energy were slightly reduced in both temporal profile cases to account for the localised increase in pressure caused by the spatial scaling. In all cases, the γ value was kept constant. The results of the simulations were validated against the experimental data provided in Figure 4.21 and Figure 4.23. The comparison was provided in Figure 4.28 and Figure 4.29.

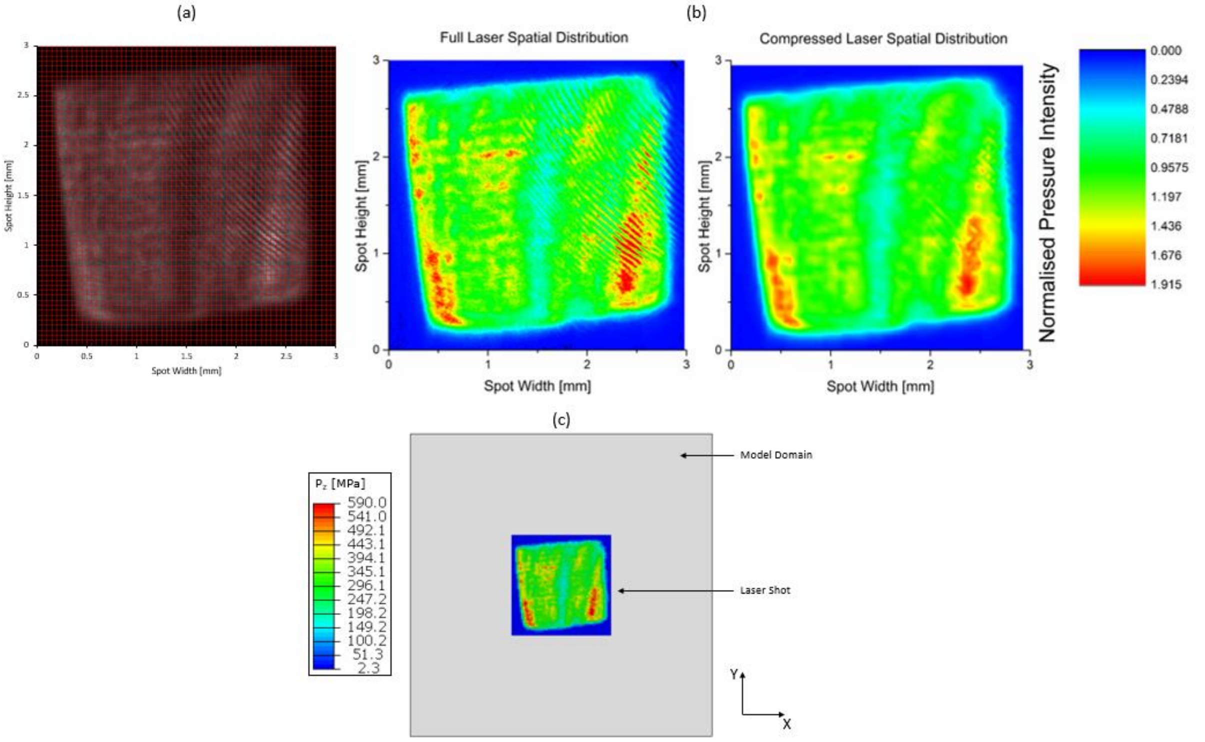

Figure 4.26: (a) Compression strategy of the laser intensity spatial distribution, (b) comparison of normalised laser pressure spatial distributions, (c) spatial variation of applied plasma pressure in a single shot laser shock peening model in ABAQUS

4.2.2. Single and multiple pulse laser shock peening modelling

The outcomes of each aspect associated with the LSP FEA modelling were incorporated to simulate three LSP processing strategies, namely a single LSP shot, a single layer of adjacent LSP shots and multiple layers of LSP shots. In these cases, the FEA results are validated and compared against experimental results, with only the FT and DSG temporal profiles being studied.

4.2.2.1. Overview of various laser shock peening simulation strategies

The mesh structure, computational settings and pressure loading of the LSP pulses were fixed for all three processing strategies. However, the modelling domains (the area surrounding the LSP shots) was increased to account for the sequential shots per the results in Table 4.4. Each LSP shot was modelled individually in the multi-shot simulations, with the solution of the previous shot being imported before the start of the pulse phase of the next sequential LSP shot. Figure 4.27.a-b showed the three-dimensional domains of the single and multiple shot LSP models.

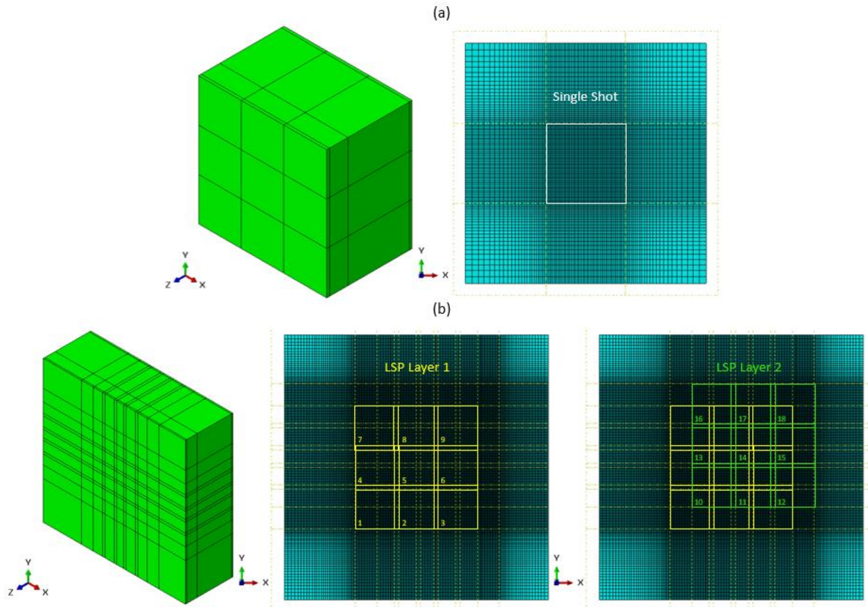

Figure 4.27: Laser shock peening spot locations and domain sizes (a) single-shot simulation, (b) multiple shot and layers simulation

In addition to the experimental results of this work, multiple sources in the literature have shown that sequential LSP shots will affect the induced residual stress [18,20]. Each LSP layer of sequential shots was made up of a three by three shot matrix (nine-shot sequence). The shots were applied in an X-Y raster pattern with overlapping areas that replicated the experimental processing. Both multiple shot LSP layer strategies were completed on the same model domain to reduce computational cost and the need for repeated simulations of the initial LSP layer. Figure 4.27.b. provided a schematic view of the domain partitioning and spot sequencing of each LSP layer on the FEA model. A sequence of nine shots was the smallest number of laser interactions to replicate a fully processed LSP patch. The fifth and fourteenth shots were the only shots that were fully affected by the adjacent LSP shots and layers. The size of the domain of the multiple shot simulation was selected to ensure a distance of at least three spot diameters from the top right corner of the final shot of layer 2.

4.2.2.2. Single-shot laser shock peening simulation

Finite element simulations of a single LSP spot were used to study the response of the processed material under four different peening conditions (two temporal profiles and two power intensities). These simulations clarify the individual effects of each spot on the residual stress and surface deformation without the influence of adjacent shots.

4.2.2.2.1. Comparison of experimental and simulated single-shot laser shock peening

Figure 4.28.a-b. provided a comparison of the residual stress as a function of depth at the centre of the LSP shot, with the spatial distribution of the laser incorporated into the FEA simulation. Comparison of

the residual stress profiles showed that the LSP simulations of the two temporal profiles and pulse energy of 1 and 3 J were within 12 MPa (10%) and 48 MPa (24%) of the measured peak compressive stress. The predicted depth of compression was within a maximum range of 0.1 mm (18%) of the experimentally measured values. A discrepancy between the measured and predicted residual stresses was observed post the stress transition depth in the low energy data. It was unclear if the variation was due to the modelling or measurement inaccuracies as a very good correlation was achieved in the residual stress profiles with the higher laser energy. Incremental hole drilling is known to have larger associated errors towards the maximum depth due to a reduction in the sensitivity of the gauge elements to fully capture the hole deformations at the depth. The lower laser energy pulse would have resulted in smaller strain relaxations that were increasingly more difficult to accurately transfer to the gauge elements towards the maximum depth of the measurements. This may have contributed to the observed variations between the experimental and simulated residual stress.

The addition of the laser spatial distribution greatly improved the LSP model's ability to replicate the biaxial nature of the residual stress in the two primary orthogonal directions. This was due to the non-uniform surface deformation created by the laser spatial distribution. In addition, Figure 4.26 showed that the LSP spot axis was partially inclined to the orthogonal directions. It was estimated that this slight spot rotation would contribute to the non-uniform deformation and increase the anisotropic stress state between the orthogonal directions. As this laser profile was not the exact distribution at the time of conducting the peening, it was expected that some variations will be present. However, this demonstrated the need for the inclusion of the spatial distribution of the laser profile in the simulation of the LSP process.

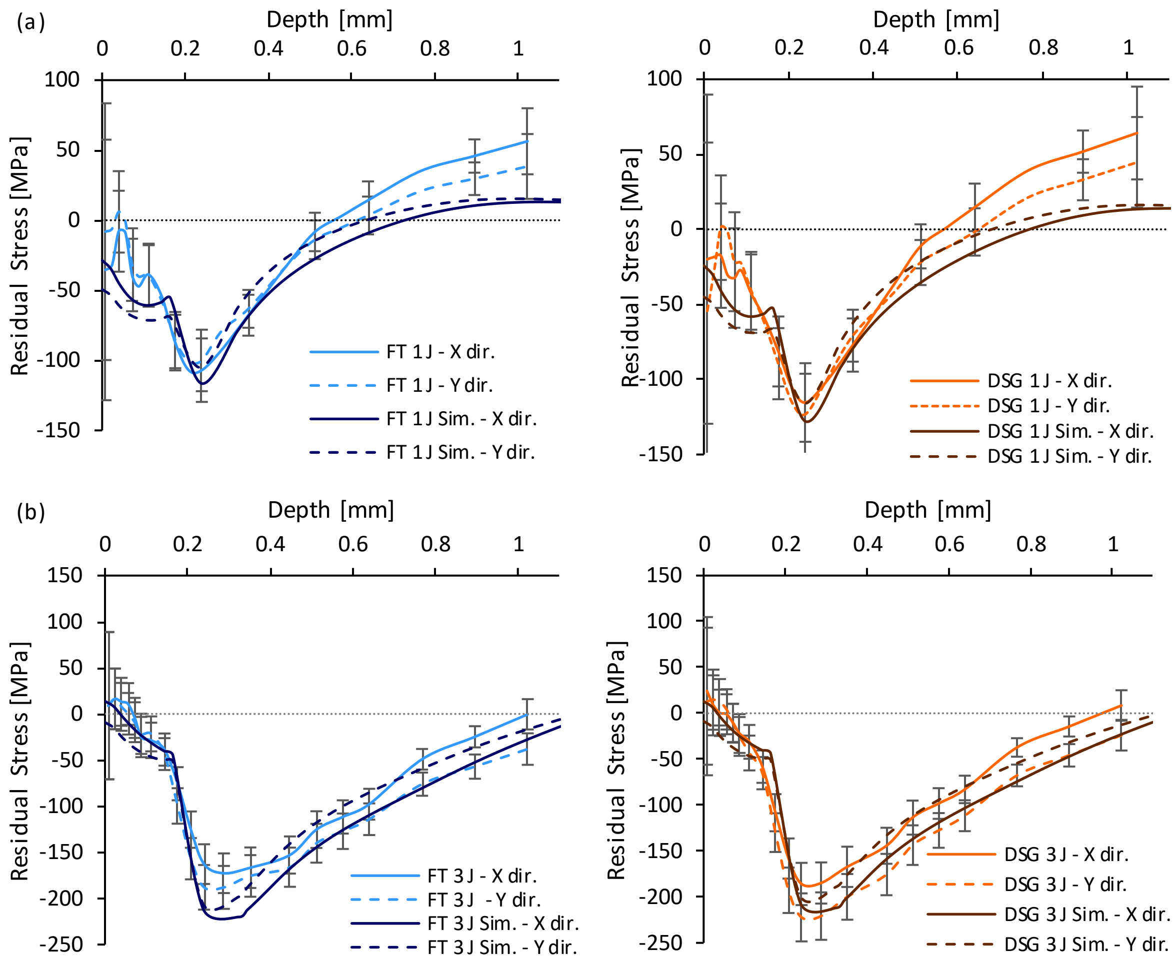

Figure 4.28: Comparison of single laser shot residual stress with the laser-based spatial distribution (a) flat top and double shallow Gaussian 1 J – 1.85 GW/cm^2, (b) flat top and double shallow Gaussian 3 J – 5.56 GW/cm^2

The FEA model was capable of representing the overall trend and approximate magnitude of the residual stresses in the clad region (first 185 µm). The largest variation in the magnitude of the stress occurred at the lower energy setting as the model consistently overestimated the compressive residual stress in this material region of the model. The discrepancy was attributed to possible inaccuracies in the material properties used in the FEA model and the calculation of the experimental residual stress. A very good correlation of the residual stress was achieved at the higher pulse pressure. This was attributed to the higher loading fully saturating the low strength clad material as the pulse pressure would have been many times larger than the HEL of this material.

Figure 4.29 provided a comparison of the surface deformation taken across the horizontal centre of the LSP shot. It was clear that the inclusion of the laser spatial profile greatly improved the correlation between the FEA and experimental deformation. An underestimation of the deformation was observed near the centre of the FEA shot due to the low-pressure intensity in this region caused by the spatial distribution of the laser shot, shown as the light blue region in the spatial distribution of Figure 4.26.

The improved correlation confirmed the Fabbro et al. conclusion that the local plasma pressure magnitude was dependent on the incident laser intensity [10].

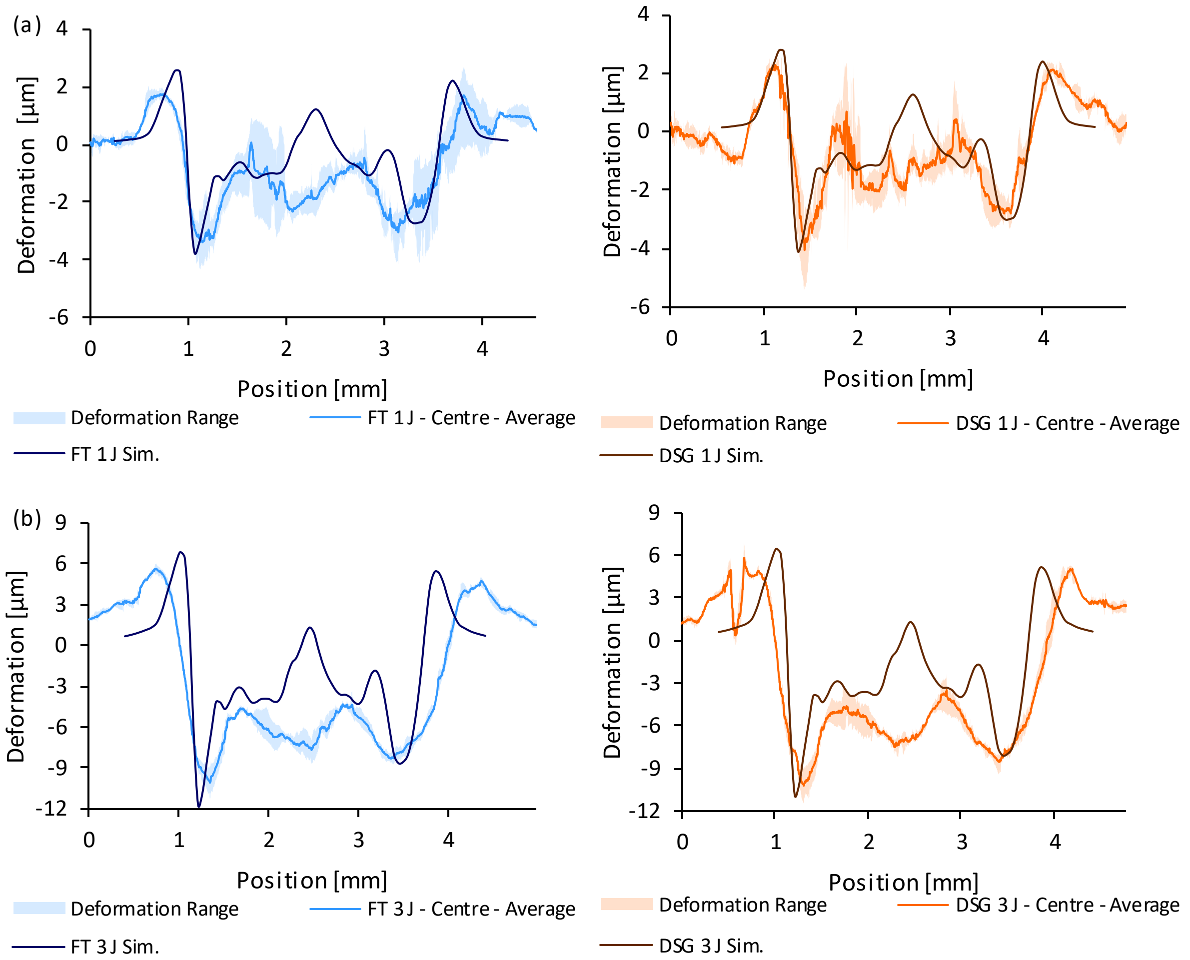

Figure 4.29: Comparison of surface deformation across the horizontal centre of the laser shot with the laser-based spatial distribution (a) flat top and double shallow Gaussian 1 J – 1.85 GW/cm², (b) flat top and double shallow Gaussian 3 J – 5.56 GW/cm²

The model was capable of predicting the surface deformation fairly well at the lower energy peening compared to that of the higher energy setting. Although the main features of the higher intensity experimental dimple were replicated in magnitude, the simulation did not fully represent the outward movement of the material due to the incident laser shot (experimental profiles are wider than the FEA profiles). The simulated deformation would naturally be smaller than the experimental impact as the simulations do not account for the lateral expansion of the plasma. This would be more prevalent at the higher peening intensity where a larger plasma would occur. This would indicate that the 3x3 mm^2 spot that was measured on the sample may have been caused by a smaller laser spot size, for example, a 2.7x2.7 mm^2 laser spot. This would have a knock-on effect on the actual laser power density, as the intensity would be higher than expected due to the approximate 10-20% uncertainty on the impact geometry. Overall, this model was deemed to provide a reasonably accurate representation of the surface deformation caused by a single LSP shot, with the inclusion of the spatial profile drastically improving the estimation.

The increased alignment of the surface deformation validated the calibration of the coefficients in the analytical plasma pressure model. These results added to the confirmation that the laser temporal profile had a negligible effect on the residual stress and surface deformation introduced by a single LSP event.

4.2.2.2.2. Effects of laser shock peening power density

The influence of the laser power density on the features of the residual stress depth profile was discussed as part of the model comparison with the experimental results. However, the simulated results provided a convenient view of the total through-thickness stress distribution caused by the single LSP shot.

Figure 4.30 showed the effects of increasing plasma pressure for a single shot. The contour plots represent a cross-section through the horizontal centre of the LSP spot and the colours representing the range of the in-plane residual stress component S_Y. The line plots represent the residual stress in the two orthogonal directions as a function of depth through the centre of the shot (originally shown in Figure 4.28). The maximum and average pressure-to-HEL ratios were provided to indicate the effect of the power density and laser spatial distribution. The maximum ratio was approximately double that of the average due to the scaling of the pressure pulse by the laser spatial distribution, as described in section 4.2.1.6.2.

From this figure, it was clear that the higher pressure loading increased the depth of the compressive stress into the thickness of the component. This was due to the associated increases in the material plastic flow with respect to the pressure. At both pulse pressure settings, the simulated results showed that the compressive depth was followed by a slightly tensile compensated region. The magnitude of the tensile stress was equivalent at both intensities. This suggested that the majority of the compensating tensile stress occurred towards the edges of the spot rather than directly below the centre and this was confirmed by higher magnitude tensile stresses that occurred at a pressure three times the HEL, as seen in the contour plots of Figure 4.30.

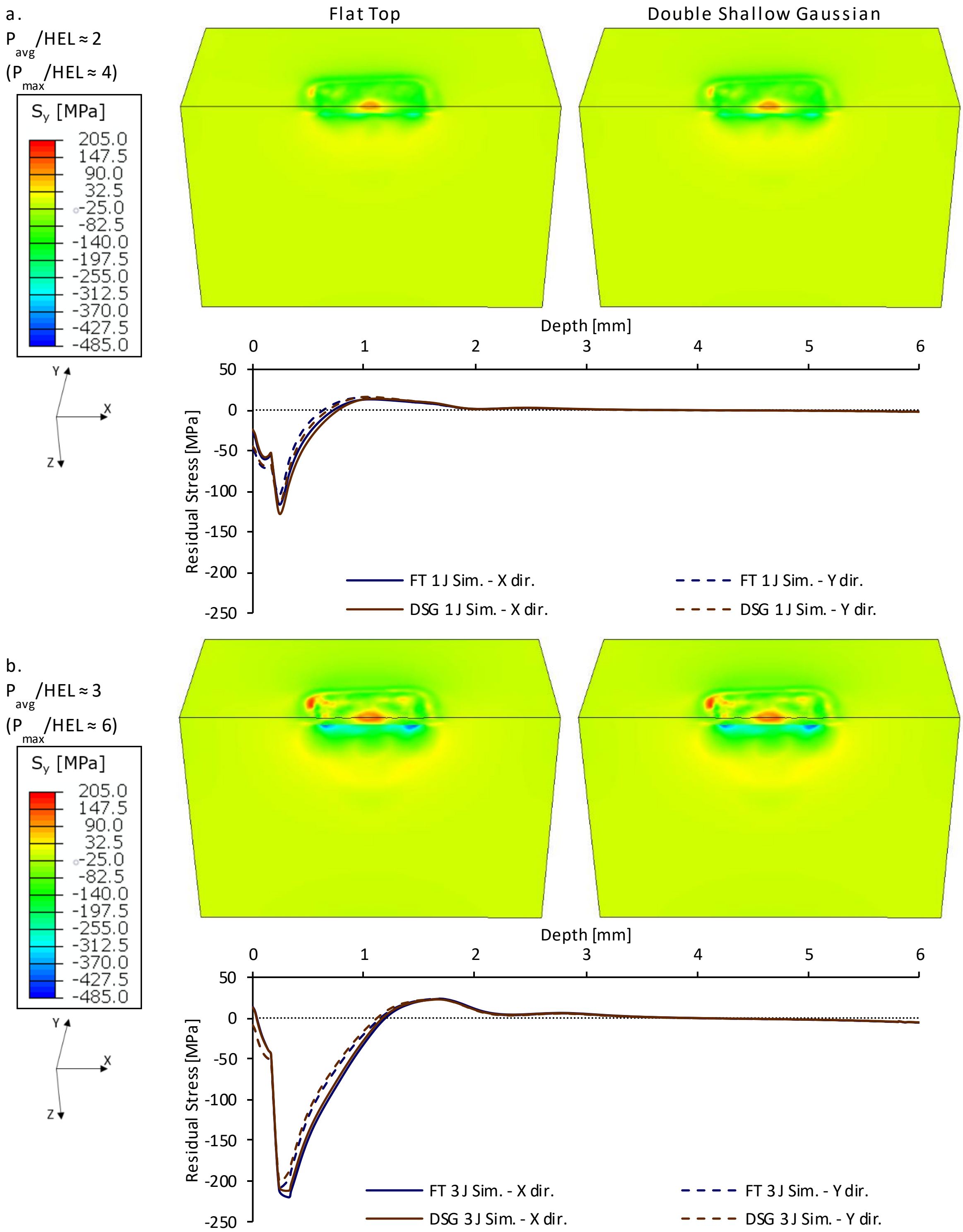

Figure 4.30: Effect of varying pressure loading for a single laser shock peening pulse (a) flat top and double shallow Gaussian 1 J – 1.85 GW/cm², (b) flat top and double shallow Gaussian 3 J – 5.56 GW/cm²

The full effects of the LSP shot fully tapered out at a depth of about 2 and 3 mm from the surface for the different pressure loadings. Additionally, the thickness of the sample prevented excessive stress reversal resulting from wave reflections off the back surface. This resulted in a smoother stress profile compared to what would be expected in the peening of a sample with a smaller nominal thickness, as shown by Langer et al. [20].

Figure 4.31.a-b indicated the effects of the plasma pressure on the residual stress across the surface of the LSP spot (surface of the clad material) and at the start of the AA2524 bulk material which was directly below the clad. The colour of the contour plots (Figure 4.31.a-b) represents equally the stress in the two orthogonal stress directions. The line plots (Figure 4.31.c) showed the distribution of the residual stress across the horizontal centre of each shot. The origin of the plot coincided with the spot centre. The boundaries of the original shot geometry are represented by the shaded region.

Both pressure loadings resulted in fairly non-uniform residual stress distribution on the surface of the clad. A tensile region at the centre of the laser shots was observed in both cases. The cause of this tensile region was due to the reverse plastic loading caused by the boundary effects of the laser shock, described further by Hu et al. [21]. The increased plasma pressure did not greatly affect the magnitude of the tensile region but did increase the relative size, as seen in Figure 4.31.b. It was concluded that the magnitude of the tensile stress was limited by the material properties of the clad layer (estimated yield strength of 200 MPa). The increased size of the region was intuitively linked to the increased amount of plastic deformation caused by the stronger plasma pressure. Additionally, the higher pressure increased the occurrence of pockets of tensile stresses on the surface. These pockets were attributed to the extremely high localised pressure loadings which in some cases was as large as six times the HEL of the material. The extremely large pressures would cause regions of the material to undergo localised reverse yielding resulting in increased amounts of tensile stress on the surface. These tensile pockets are purely related to the laser spatial distribution as similar sporadic tensile regions were not observed by Langer et al. who performed LSP simulations with a purely uniform pressure pulse under similar loading and material conditions [20].

Figure 4.31.c provided the comparison of the stress distribution of the clad surface (where the laser directly interacts with the material) and at the start of the AA2524 bulk material which was directly below the clad. All of the tensile stress present at the surface was fully contained within the clad materials thickness (185 μm). The stress distribution on the AA2524-T351 was fully compressive across the spot width and showed an improved stress uniformity. This was expected as the AA2524 material had a significantly higher ability to sustain higher pressure loads and magnitudes of compressive residual stress before reverse yielding occurs. Additionally, the LSP processing and simulations were considered as cold working mechanical processes due to the use of an ablative coating during peening and no thermal effects being incorporated into the FEA simulations. The higher pulse pressure tended to reduce the uniformity of the residual stress on the AA2524-T351 surface as the laser spatial distribution began to dominate the magnitude of the compressive stress. Additionally, the high-pressure pulse created a compressive stress state in the material surrounding the initial spot.

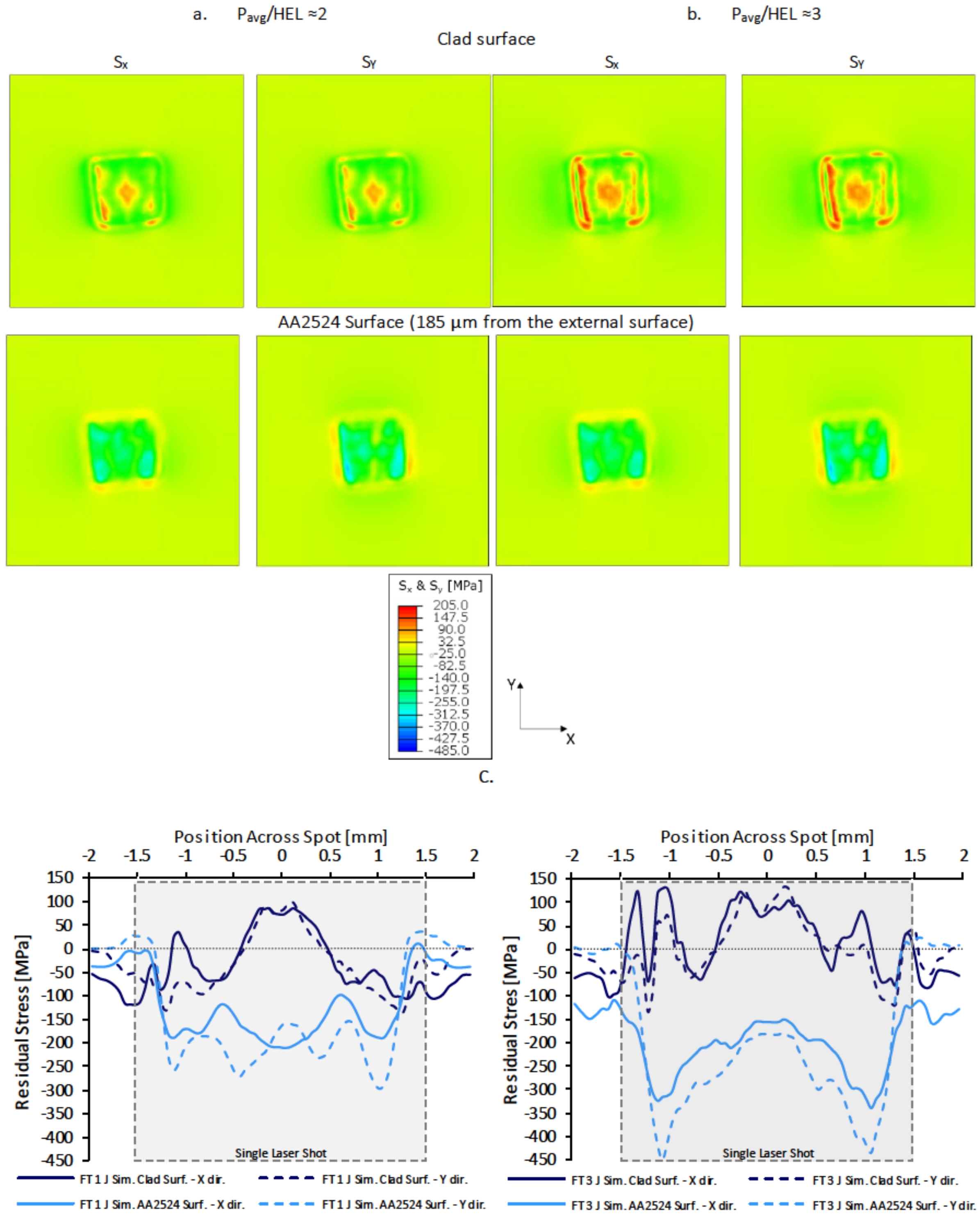

Figure 4.31: Surface residual stress across the centre of the single laser shot (a) flat top 1 J – 1.85 GW/cm², (b) flat top 3 J – 5.56 GW/cm², (c) comparison of surface residual stress in the clad and AA2524

Comparison of the contour plots at the two peening intensities in Figure 4.31, indicated that the laser temporal profiles had minimal effect on the predicted residual stress in both the depth and across the surface. The combination of the experimental and simulated results concluded that power density and laser spatial distribution are more influential parameters for affecting the LSP residual stress and surface deformation than that of the temporal profile. However, this outcome was only valid if the temporal profiles are equivalent in peak energy and pulse duration.

4.2.2.3. Multiple shot laser shock peening simulations

The single-shot simulation of the LSP process was a convenient and efficient method of calibrating the estimated plasma pressure and characterising the spatial distribution effects of the laser pulse. Additionally, it provided insight into the mechanics of the formation of the residual stress and surface deformation caused by the single LSP event. These simulations cannot capture the interactions between sequential LSP shots and multiple layers. In most engineering applications, LSP is applied to a component as a sequence of LSP shots with some overlapping area of the spot. The interaction of sequential LSP shots affects the residual stress field that was established by the preceding LSP interactions. Accurate FEA simulations of a representative number of LSP shots was an effective method to study the complex interactions of the laser shots, the material behaviour and the overall outcome of the peening process. The simulations provide insight into the residual stress which may not always be easily experimentally characterised. The multiple shot simulations were conducted with the pulse pressures that were optimised based on the single-shot results and with no other changes to the computational settings or mesh structure besides the overall domain size.

4.2.2.3.1. Effect of adjacent laser shock peening shots

As discussed in section 4.2.2.1, a three by three shot matrix (nine sequential LSP shots) was the smallest sample size to accurately represent the experimental LSP patch. Two experimental incremental hole drilling measurements were made on the single LSP layer sample per temporal profile. The measurement locations were approximately at the centre of the LSP shot and at the centre of the overlap area of four LSP shots, this was illustrated in Figure 4.2. The simulated residual stress results per depth position were averaged over a representative circular area as previously discussed. Additionally, the results were taken after the completion of the full nine-shot sequence at the centre of shot five and in the upper right overlapping region of the LSP patch (overlap of shots five, six, eight and nine in Figure 4.27).

Figure 4.32 and Figure 4.33 provided the comparison of the experimental and simulated in-depth residual stress at the two measurement locations of the LSP patch for the two peening intensities and temporal profiles. Figure 4.32 showed a fairly acceptable correlation in the peak compressive stress as the simulated values were overestimated but were within a 50 MPa range of the experimental values for both simulated temporal profiles. This was attributed to the fact that the constitutive material model was not adjusted to account for the LSP induced cyclic deformation effects, thus predicting a higher magnitude compressive residual stress. This was exacerbated in the overlap regions where a less compressive residual stress was experimentally measured due to the strain relaxation effects caused by the higher interactions of sequential LSP shots. The difference between the model and experimental peak compression at the overlap region was within 50 MPa at this laser energy setting. In all cases, the models predicted an increased uniformity of the residual stress field in the longitudinal direction (S_y) between the centre and overlap regions. The models were able to accurately predict the observed biaxiality of the residual stress field. The simulations showed a good correlation with the experimental depth of compression at the centre of the LSP spot, as the model predicted this transition point within a 0.15 mm range of the experimental result. The simulations did tend to underestimate the depth of compression in the overlap region. However, the simulated results were within the experimental error of the stress measurement in the overlap, the variation being attributed to the cyclic deformation effects that are not accounted for in the model.

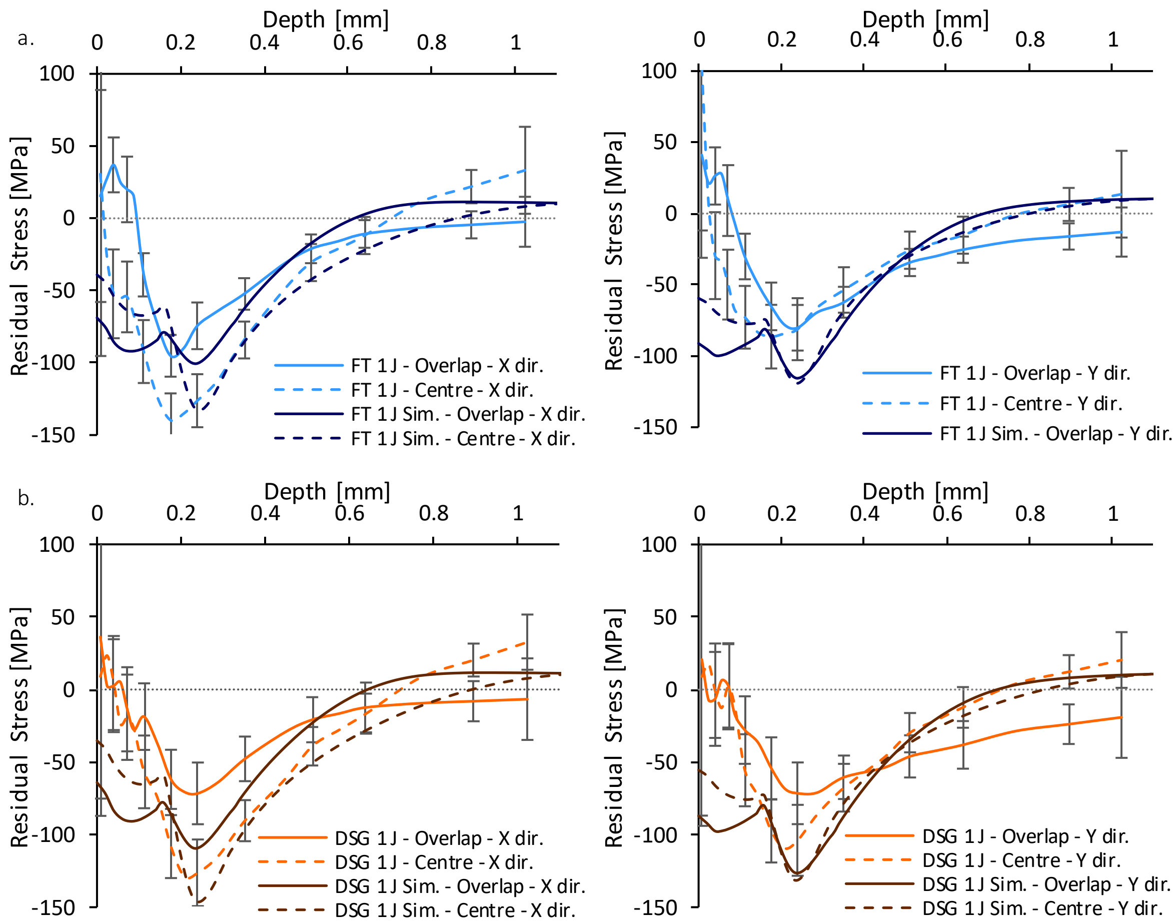

Figure 4.32: Comparison experimental and simulated residual stress at the centre of a laser shot and overlap region for (a) flat top 1 J – 1.85 GW/cm², (b) double shallow Gaussian 1 J – 1.85 GW/cm²

Figure 4.33 showed the comparison of the experimental and simulated in-depth residual stress at the two measurement locations with a higher LSP intensity. The correlation between the model and experimental results was drastically reduced at that higher power density. The peak compressive residual stress was overestimated by the models by a range of as much as 75 MPa. The simulated higher peening intensity followed the experimental trends in that a significant increase in the magnitude of the peak compressive stress and depth of compression was seen compared to that of the lower intensities. The model was capable of predicting the measured reduction in biaxiality of the residual stress in the longitudinal direction (y-direction), whereas a higher variation occurred in the transverse direction (x-direction), which was due to the spatial profile of the laser pulse. It could be inferred that the simulated residual stresses do not accurately represent the strain relaxation and saturation of the material which was seen in the experimental data. This limiting factor resulted in the model predicting higher residual stresses than were experimentally achieved.

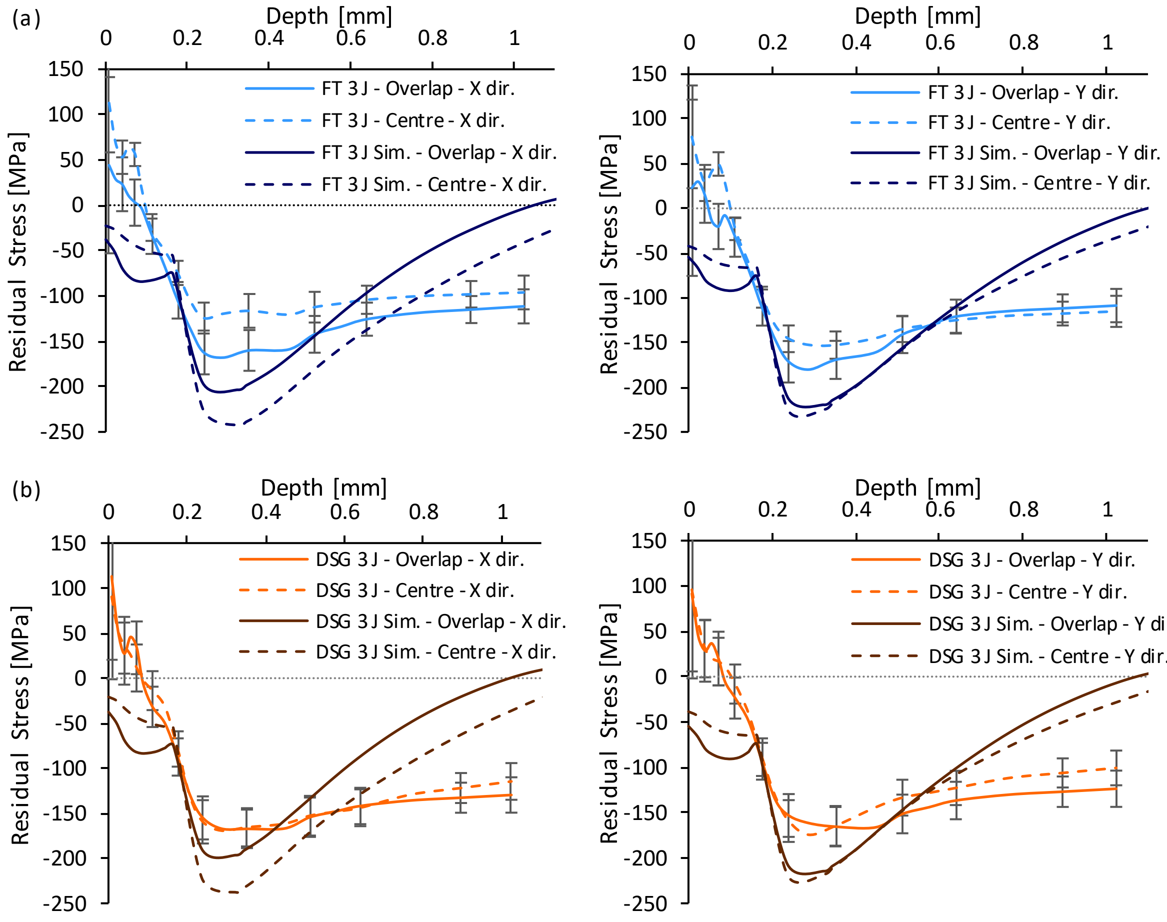

Figure 4.33: Comparison of experimental and simulated residual stress at the centre of a laser shot and overlap region for a single layer of laser peening (a) flat top 3 J – 5.56 GW/cm², (b) double shallow Gaussian 3 J – 5.56 GW/cm²

Figure 4.34 indicated the combined effects of peening pressure with multiple LSP shots on the in-depth residual stress. As in the case with the single-shot simulations, the majority of the balancing residual stress occurred in the surrounding subsurface material. Adjacent LSP shots increased the build-up of the balancing tensile stress in the regions below the laser spot overlap, as shown in Figure 4.34.a-b.

Figure 4.34.c showed the through-thickness line plots of residual stress at the centre of the domain geometry. The adjacent LSP shots tended to increase the depth of compression of a single-shot by as much as 35% (equivalent experimental value of 16%) at the lower energy set. Although a variation was observed between the experimental and simulated depths of compression, the models did predict the residual stress within the experimental measurement uncertainty bounds. The simulations predicted a 7% increase in depth of compression from the single-shot at the higher peening intensity with the multiple shots (no equivalent experimental value can be determined).

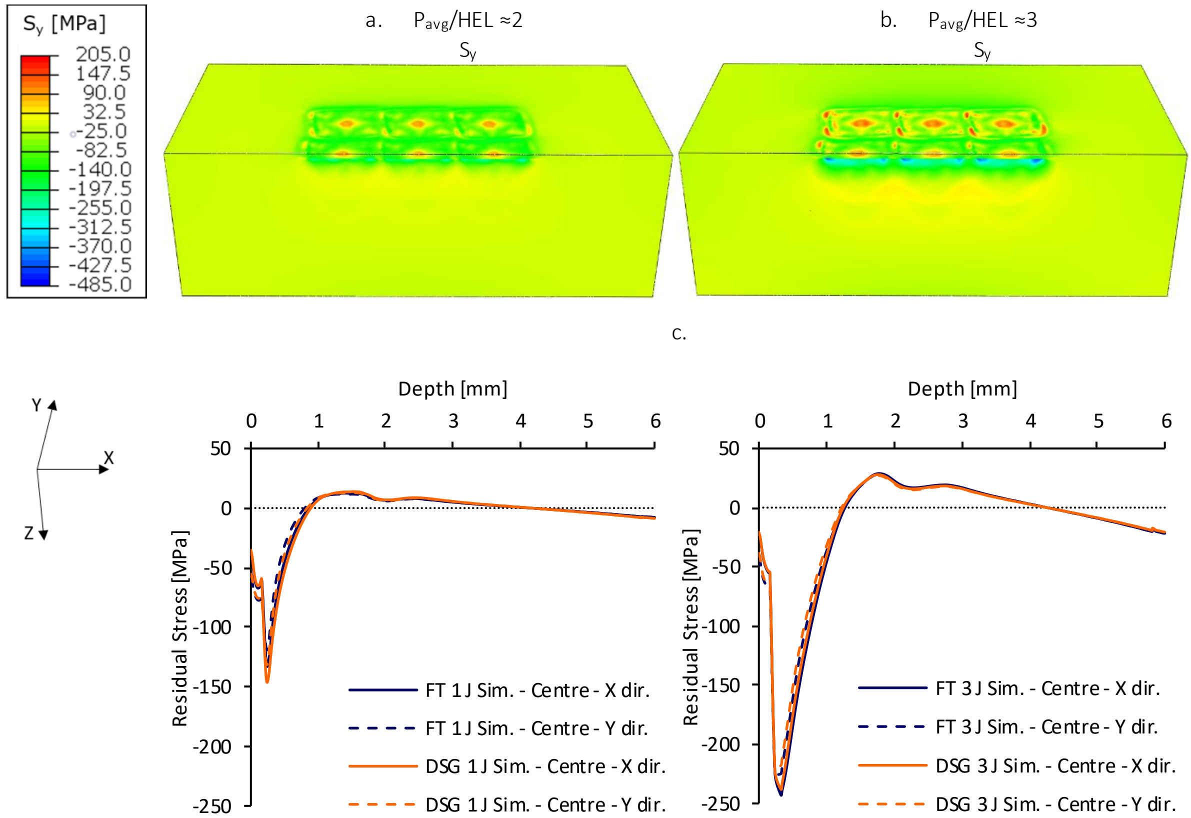

Figure 4.34: Effect of peening pressure on in-plane residual stress of laser peening sequence (a) flat top 1 J – 1.85 GW/cm², (b) flat top 3 J – 5.56 GW/cm², (c) through-thickness residual stress along the centre of the sample with two temporal profiles

Figure 4.34.c showed that the simulated through-thickness residual stresses were fairly uniform in the two orthogonal directions at both power intensities. This was contrary to the simulated results of Langer et al. who predicted a significantly anisotropic residual stress field in the two orthogonal directions [20]. This anisotropic stress state typically results in a larger state of compression in the longitudinal direction (laser stepping direction or y-direction) [22,23]. However, this was shown not to be the case by the experimentally determined residual stress depth profiles. In this case, the biaxial stress was not as severe and are mostly superficial and restricted to the first 0.2 - 0.4 mm in depth.

Figure 4.35 indicated the effects of peening pressure on the surface residual stress when peening a full sequence of LSP shots. As in the case of the single-shot, a tensile region forms at the centre of each laser shot.

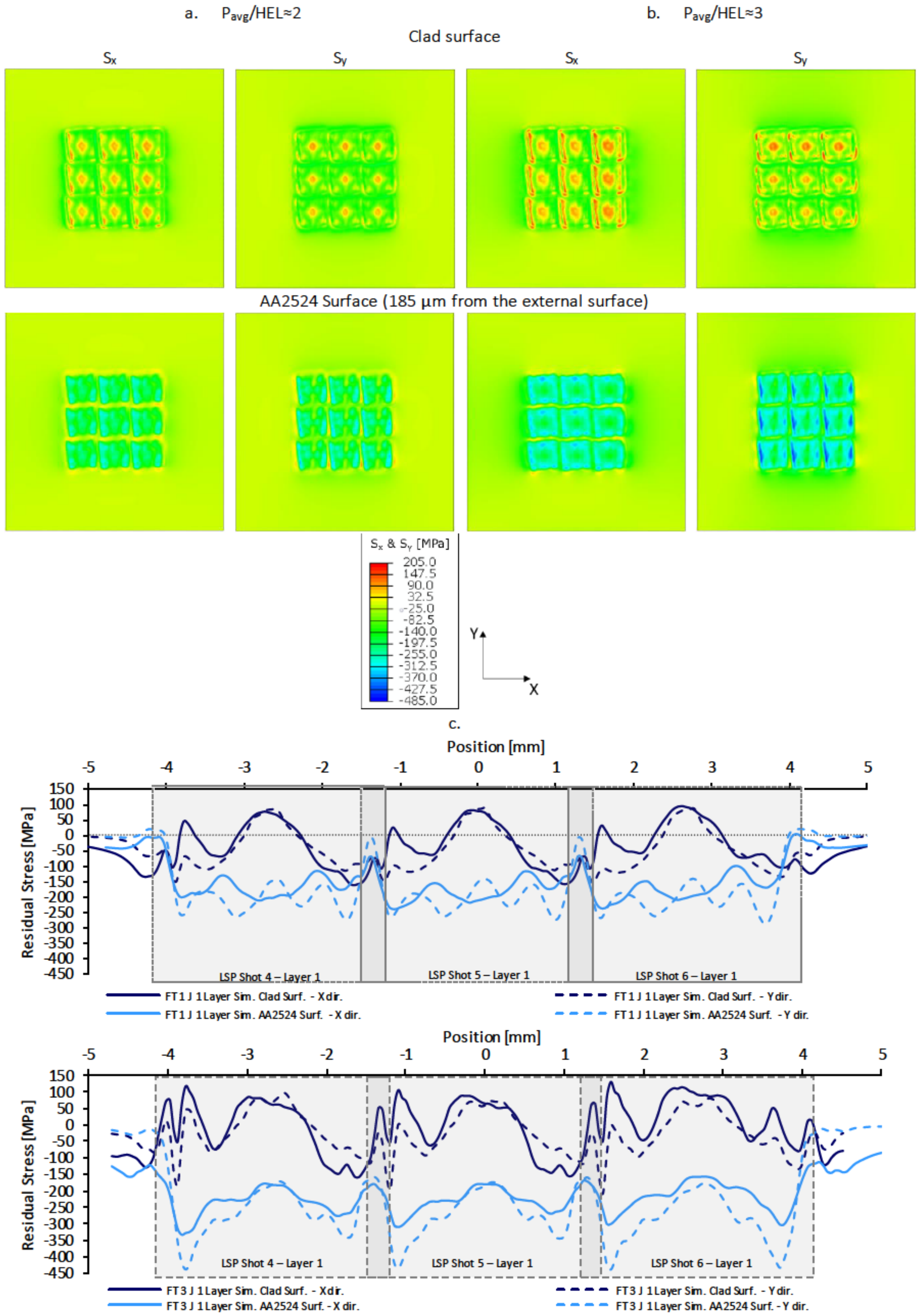

Figure 4.35: Single layer laser peening with a flat top temporal profile at 1 and 3 J pulse energy (a-b) Comparison of stress profiles across the surface of the clad and AA2524, (c) stress plot across the centre of the sample

The higher power density increased the general size of the surface tensile region, with the overlap of the laser pulses having no significant effect on the tensile regions which occurred toward the boundary of the spot. The magnitude of the surface tensile residual stresses was equivalent for the single shot and the full patch, as was observed by Langer et al. [20]. As previously stated, the additional laser pulses increased the depth and magnitude of the peak compressive stress. In addition to this, the adjacent LSP shot increased the uniformity of the residual stress on the surface of the AA2524.The shaded regions in Figure 4.35.c-d represent the geometry of the laser shot, it was clear that the stress in the overlapping regions was lower than that at the centre of the laser geometry. The cause of this was attributed to the combined effect of stress relaxation of the prior shot due to further peening and that the stress in this region was affected by the balancing tensile stresses which were pushed towards the boundaries of each laser shot.

Figure 4.36 showed a reasonably satisfactory comparison between the experimental and simulated surface deformation across the horizontal centre line of three sequential LSP shots. At a lower peening intensity (Figure 4.36.a), the model provided a fairly accurate representation of the periodic and maximum surface deformation induced by the three shots. Additionally, the use of spatial distribution of the laser resulted in the smaller deformation peaks roughly at the centre of each shot. The peaks associated with the edge of each laser spot did not occur at the higher peening intensity.

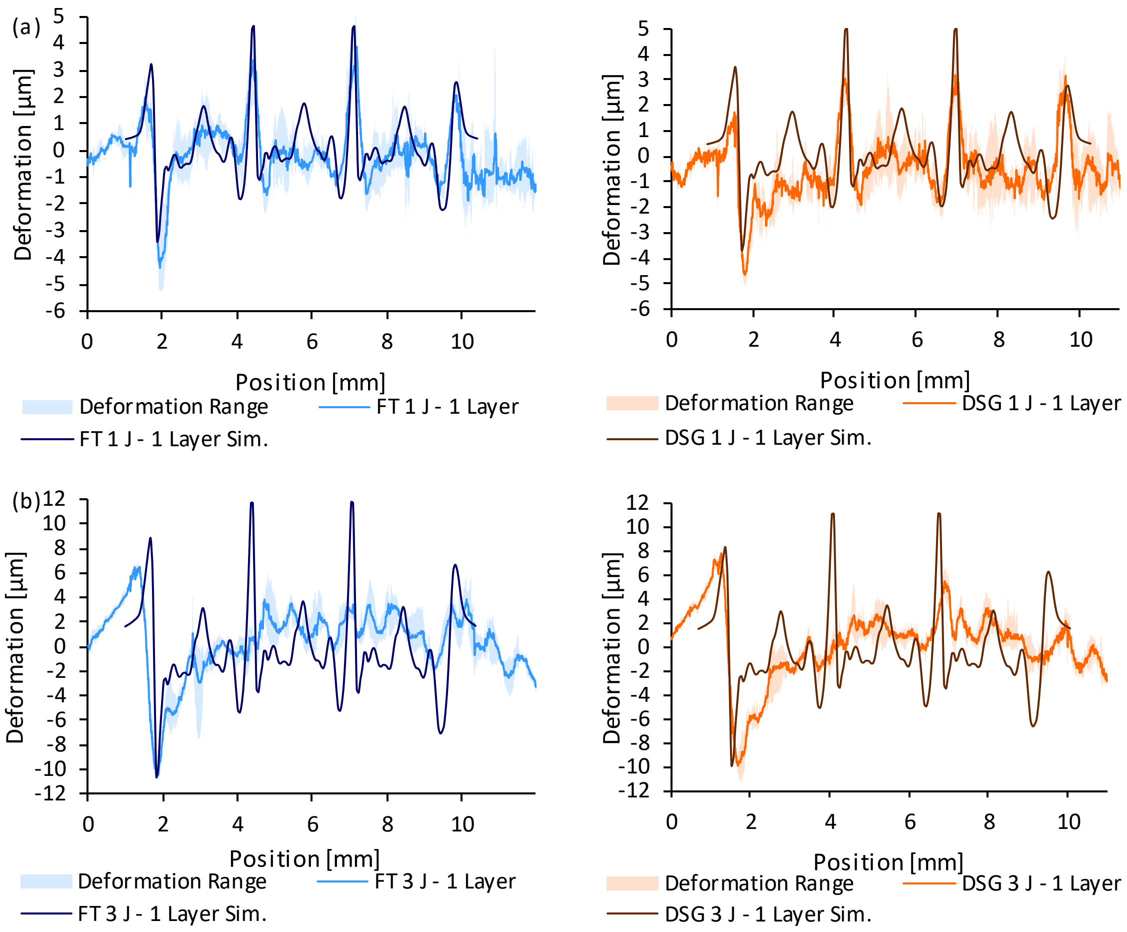

Figure 4.36: Comparison of experimental and simulated surface deformation across the horizontal centre of three sequential laser shots at two temporal profiles (a) 1 J – 1.85 GW/cm², (b) 3 J – 5.56 GW/cm²

This was caused by the lateral expansion of the plasma which was significantly larger than at the lower peening intensity. The interaction of the larger expanded plasma and the increased out-of-plane sample bending resulted in a smoothened deformation profile across the three experimental LSP shots. As the simulation did not account for plasma expansion this smoothing of the deformation would not be expected to occur and is thus not replicated in the data.

The experimental deformation at the lower intensity indicated that the sample did not deform drastically out of plane as the sample achieved static equilibrium with the induced LSP residual stress (this was shown in Figure 4.9.b-c and Figure 4.10.b-c). The fully constrained external boundaries of the model restricted the out-of-plane deformation of the simulated geometry. This effect was evident in the comparison of the simulated and experimental deflection at the higher power density. The two sets of data matched in magnitude and position at the start of the laser shot sequence but quickly deviate as the experimental sample deflected out of plane to achieve equilibrium. Inaccurate material properties which were assumed for the clad layer may have exacerbated the inconsistencies in the deformation of the surface.

4.2.2.3.2. Effect of multiple laser shock peening layers

Augmenting the single peening layer with an additional layer can often alleviate local tensile stresses, increase the magnitude of the compressive stress and drive the stresses to a deeper extent in the thickness. Figure 4.37 provided a comparison of the experimental and simulated residual stress in the depth of the sample. The averaging of the simulated residual stress over a circular area was taken about the centre of the central spot in the first LSP layer. It should be noted, that a measurement centred about the central LSP spot in the second layer had a similar magnitude of peak compression, displayed near isotropic residual stresses in the two directions and a similar magnitude in the depth of compression at all peening conditions. The main difference was slightly less compressive stress in the clad region but this corresponded to the tensile region that occurs at the centre of the current LSP shot.

The second LSP layer increased the magnitude of the peak compressive stress by as much as 14% and 4% at the 1 and 3 J energy settings. It was expected that a lower increase in peak compression was observed at the higher peening intensity as the initial LSP layer would have induced the majority of th e residual stress capable of being carried in the material before stress relaxation effects began to occur. As in the case of a single LSP layer, the simulation was capable of fairly accurately predicting the peak compressive stress with the lower peening intensity. The simulated residual stress was within the experimental uncertainty bounds at all depths apart from in the clad material. The inability of the simulated clad layer to accurately predict the stress was due to the previously mentioned inaccurate material properties. The peak compressive stress was found to be within a 50 MPa range of the experimentally determine d values at both temporal profiles and peening intensities.

A larger range in the variation of the depth of compression was observed between the models and experimental two LSP layers. At the lower intensity, the depth of compression was within an estimated range of approximately 0.2 mm, whilst a range could not be accurately determined at the higher power density due to the limitations in the incremental hole drilling. The models drastically underestimated the depth of compression at the higher peening intensity.

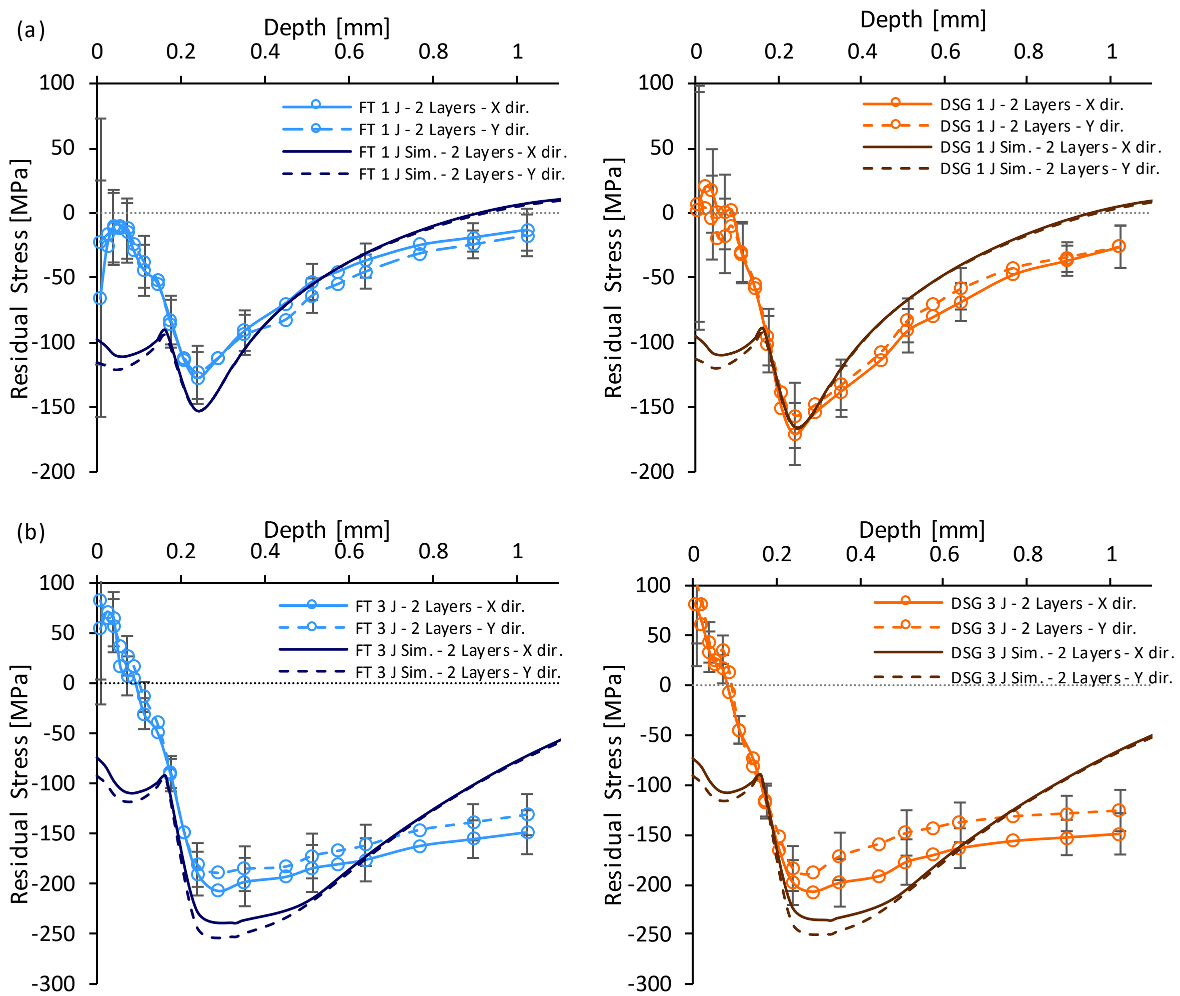

Figure 4.37: Comparison of experimental and simulated residual stress with two layers of laser peening (a) flat top and double shallow Gaussian 1 J – 1.85 GW/cm², (b) flat top and double shallow Gaussian 3 J – 5.56 GW/cm²

Figure 4.38 showed the in-plane residual stress across the cross-section of the sample geometry. It was clear that the second LSP layer overcomes the adjacent shallow subsurface balancing tensile stress which occurred from the initial LSP layer. It was found that the second offset layer pushed the balancing stresses deeper in the thickness and outward toward the overlapping region of the second layer.

Figure 4.39 showed the effects of the second LSP layer on the residual stresses on the clad and AA2524 surfaces. Figure 4.39.a-b indicated that the second layer reduced the central LSP spot tensile stress that occurred during the application of the first layer's shots. However, this tensile region merely shifts to the centre of the shots in the second LSP layer. The higher power density increased the size of this central tensile region, as seen with the single shot and single layer LSP processing. It must be noted that the presence of the initial layer of LSP shot had no noticeable influence on the size of this tensile region at the centre of each LSP shot.

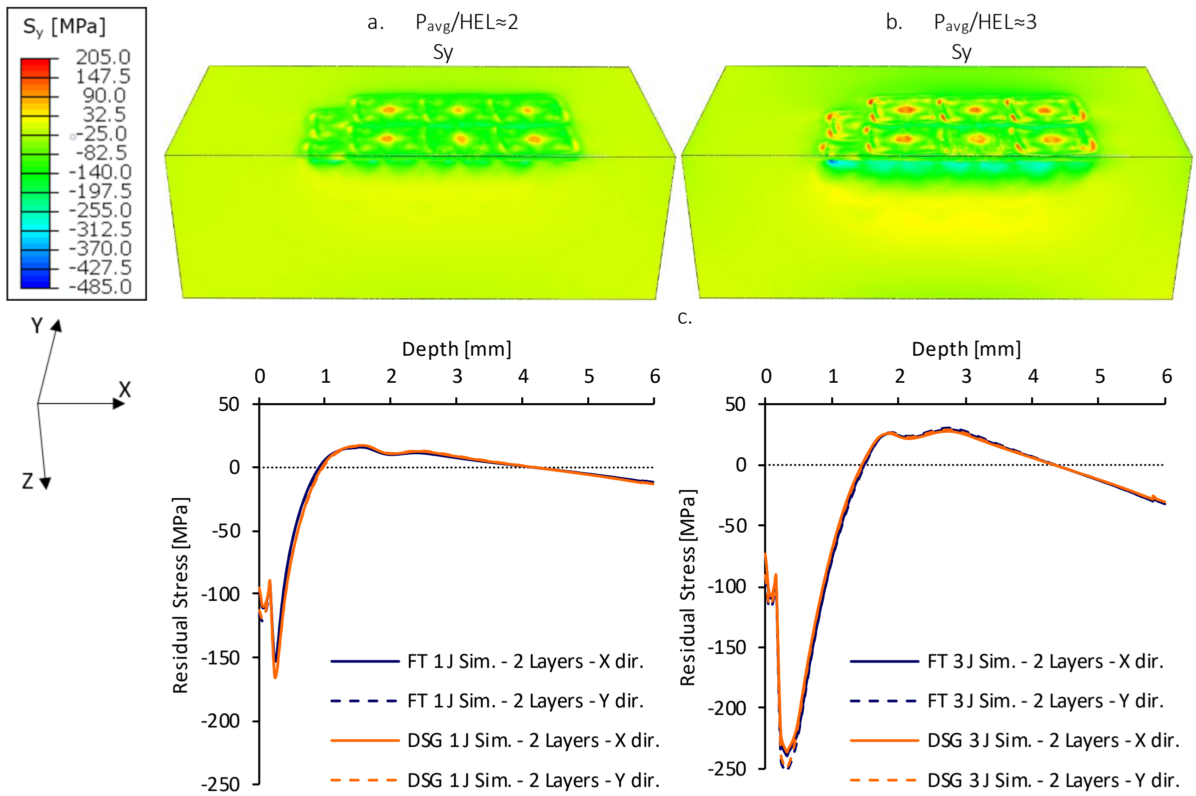

Figure 4.38: Effect of peening pressure on in-plane residual stress of two laser peening layers (a) flat top 1 J – 1.85 GW/cm², (b) flat top 3 J – 5.56 GW/cm², (c) through-thickness residual stress along the centre of the sample with two temporal profiles

Figure 4.39.c provided a comparison of the residual stress along the horizontal centre of the first layer of LSP shots (shots 4-6). The grey and red shaded regions indicated the shot boundaries of the first and second set of LSP layers respectively. At the lower peening intensity, the second layer increased the uniformity of the residual stress in the two measured directions. Additionally, it overcame the clad surface tensile stresses of the initial layer and left the area in question to a near full compressive residual stress state. This demonstrated the need for careful consideration when selecting the spot overlap strategy and number of LSP layers. Distinctive peaks or reductions in compressive stress were observed in the spot overlap regions of both LSP layers. These peaks correlated to the areas with the highest amount of peening.

The surface stress on the AA2524 at the higher peening intensity was only marginally more compressive than that at the lower peening intensity, indicating that the saturation effects had occurred and that little benefit to the surface would occur from additional peening. The clad surface was significantly more tensile at the higher intensity, with distinctive tensile peaks which were associated with the laser spatial features of the LSP shots in the second layer.

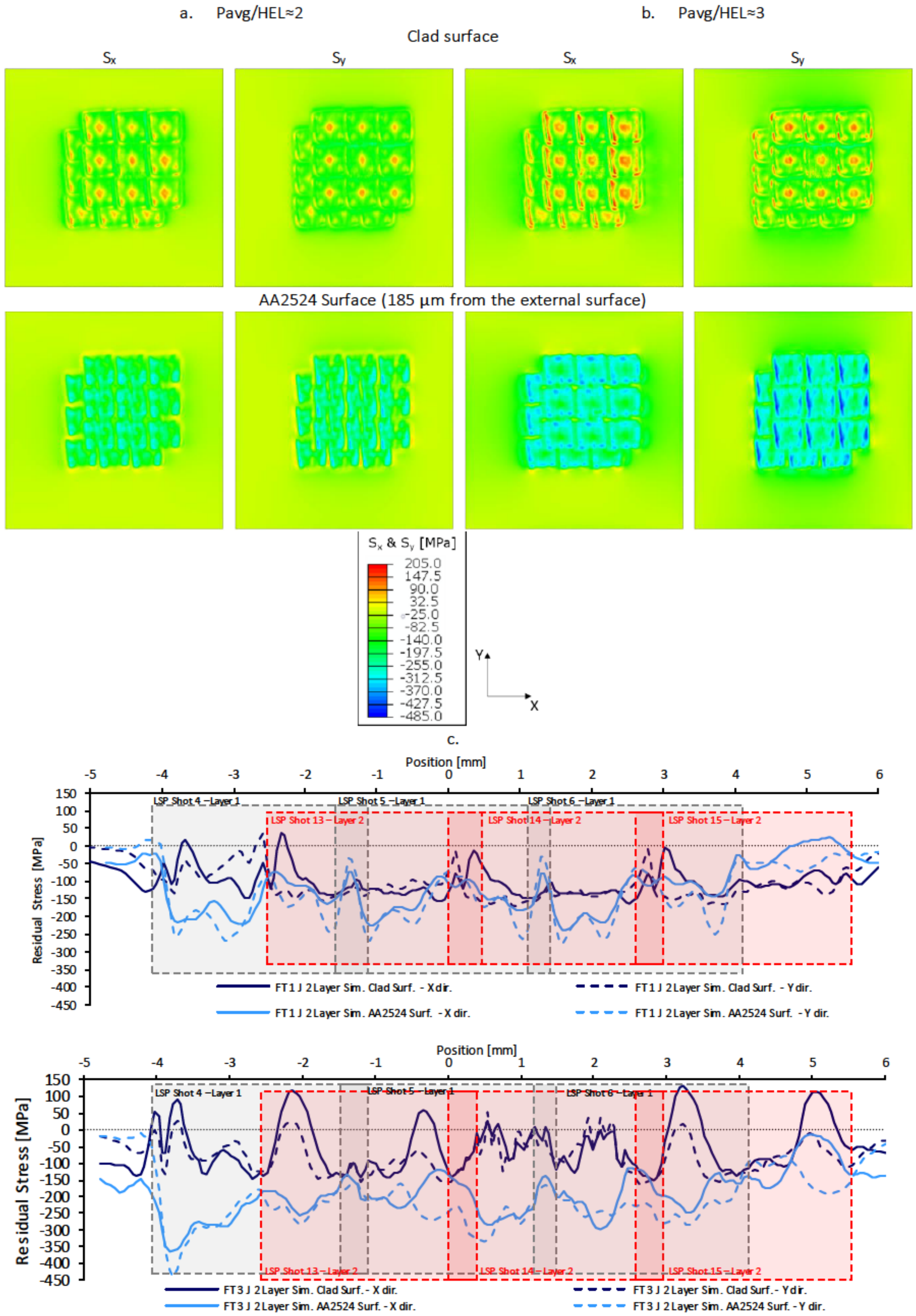

Figure 4.39: Two layers of laser peening with a flat top temporal profile at 1 and 3 J pulse energy (a-b) Comparison of stress profiles across the surface of the clad and AA2524, (c) stress plot across the centre of the sample

4.3. Conclusions

In this chapter, the effects of the laser pulse temporal profile and power density effects on the residual stress fields induced by laser peening were studied. The experimental work was augmented with a finite element analysis that provided substantiation to the observed results. The accuracy of the models was confirmed through the comparison of residual stress and surface deformation results. The following conclusions can be drawn:

- Short pulse variations in the laser temporal profile had no noticeable effect on the residual stress induced by laser peening. This was only valid if the profiles are of equivalent peak energy and pulse duration. It was concluded that the LSP established plasma will absorb the laser energy over a few nanoseconds whilst the resulting surface pressure was applied to the surface of the target over a few hundred microseconds. This significant difference in the order of magnitude of the time scale rendered the effects of the deviations in laser temporal profiles unnoticeable and inconsequential compared to other LSP parameters such as power density and LSP processing coverage.
- The laser power density had the largest influence on the LSP induced residual stresses. Larger intensities tended to drive the residual stresses to a deeper extent in the thickness of the material. However, careful consideration should be given to the selection of the intensity as a point of diminishing returns can quickly occur. Incorrect selection of the intensity can result in high magnitude tensile stress hot-spots which can be detrimental to the performance of the component.
- The complex interaction of the resulting LSP induced stress waves will always result in a region of low stress or even tensile stress at the centre of the LSP shot. The size and magnitude of the regions were greatly influenced by the laser power density and the material properties of the component. These regions can be mitigated by an additional layer of LSP shots, where the second layer reduces the tensile zone and compressive stresses can be established dependent on the LSP parameter.
- Finite element analysis of the LSP process was a convenient and reliable method of investigating the influence of the laser pulse parameters on the induced residual stresses. The inclusion of the laser spatial distribution was critical in achieving an accurate prediction of the surface deformation and anisotropic residual stress that was established on the target material. The accuracy of the simulation of the LSP patches was drastically reduced at higher LSP laser power intensities as a discrepancy between the measured and simulated in-depth residual stress profile significantly deviated from one another. It was concluded that this discrepancy was caused by the lack of the constitutive model not updating to account for the LSP-induced cyclic deformation effects which seemed to be most influential at higher peening intensities.

4.4. References

[1] Fabbro R, Fournier J, Ballard P, Devaux D, Virmont J. Physical study of laser-produced plasma in confined geometry. J Appl Phys 1990;68:775–84. https://doi.org/10.1063/1.346783.

[2] Montross CS, Wei T, Ye L, Clark G, Mai YW. Laser shock processing and its effects on microstructure and properties of metal alloys: A review. Int J Fatigue 2002;24:1021–36. https://doi.org/10.1016/S0142-1123(02)00022-1.

[3] Chen YL, Lewis JWL, Parigger C. Spatial and temporal profiles of pulsed laser-induced air plasma emissions. J Quant Spectrosc Radiat Transf 2000;67:91–103. https://doi.org/10.1016/S0022-4073(99)00196-X.

[4] Khan MK, Hainsworth S V., Fitzpatrick ME, Edwards L. A combined experimental and finite element approach for determining mechanical properties of aluminium alloys by nanoindentation. Comput Mater Sci 2010;49:751–60. https://doi.org/10.1016/j.commatsci.2010.06.018.

[5] Hu Y, Yao Z, Hu J. 3-D FEM simulation of laser shock processing. Surf Coatings Technol 2006;201:1426–35. https://doi.org/10.1016/j.surfcoat.2006.02.018.

[6] Ruschau JJ, John R, Thompson SR, Nicholas T. Fatigue crack nucleation and growth rate behavior of laser shock peened titanium. Int J Fatigue 1999;21:199–209. https://doi.org/10.1016/s0142-1123(99)00072-9.

[7] Peyre P, Fabbro R, Merrien P, Lieurade HP. Laser shock processing of aluminium alloys. Application to high cycle fatigue behaviour. Mater Sci Eng A 1996;210:102–13. https://doi.org/10.1016/0921-5093(95)10084-9.

[8] Clauer AH. Laser Shock Peening for Fatigue Resistance. In: Gregory JK, Rack HJ, Eylon D, editors. Surf. Perform. Titan., 1996, p. 217–30.

[9] Cao Y, Shin Y, Wu B. Parametric study on single shot and overlapping laser shock peening on various metals via modelling and experiments. J Manuf Sci 2010;132:61010–7. https://doi.org/https://doi.org/10.1115/1.4002850.

[10] Fabbro R, Peyre P, Berthe L, Scherpereel X. Physics and applications of laser-shock processing. J Laser Appl 1998;10:265–79. https://doi.org/10.2351/1.521861.

[11] Braisted W, Brockman R. Finite element simulation of laser shock peening. Int J Fatigue 1999;21:719–24. https://doi.org/10.1016/S0142-1123(99)00035-3.

[12] Brockman R, Braisted W, Spradlin T, Langer K, Olson S, Fitzpatrick ME. High Strain-Rate Material Model Validation for Laser Peening Simulation. J Eng 2015:1–8. https://doi.org/10.1049/joe.2015.0118.

[13] Angulo I, Cordovilla F, García-Beltrán A, Smyth NS, Langer K, Fitzpatrick ME, et al. The effect of material cyclic deformation properties on residual stress generation by laser shock processing. Int J Mech Sci 2019;156:370–81. https://doi.org/10.1016/j.ijmecsci.2019.03.029.

[14] Cuq-Lelandais JP. Etude du comportement dynamique de matériaux sous choc laser subpicoseconde. ISAE-ENSMA Ecole Nationale Supérieure de Mécanique et d'Aérotechique, 2010.

[15] Angulo I, Cordovilla F, García-Beltrán A, Smyth NS, Langer K, Fitzpatrick ME, et al. The effect of material cyclic deformation properties on residual stress generation by laser shock processing. Int J Mech Sci 2019;156:370–81. https://doi.org/10.1016/j.ijmecsci.2019.03.029.

[16] Brockman RA, Braisted WR, Olson SE, Tenaglia RD, Clauer AH, Langer K, et al. Prediction and characterization of residual stresses from laser shock peening. Int J Fatigue 2012;36:96–108. https://doi.org/10.1016/j.ijfatigue.2011.08.011.

[17] Dassault Systemes. ABAQUS User's Manual, version 6.14 2014.

[18] Keller S, Chupakhin S, Staron P, Maawad E, Kashaev N, Klusemann B. Experimental and numerical investigation of residual stresses in laser shock peened AA2198. J Mater Process Technol 2018;255:294–307. https://doi.org/10.1016/j.jmatprotec.2017.11.023.

[19] Le Bras C, Rondepierre A, Seddik R, Scius-Bertrand M, Rouchausse Y, Videau L, et al. Laser shock peening: toward the use of pliable solid polymers for confinement. Metals (Basel) 2019;9:1–13. https://doi.org/10.3390/met9070793.

[20] Langer K, Spradlin TJ, Fitzpatrick ME. Finite element analysis of laser peening of thin aluminum structures. Metals (Basel) 2020;10. https://doi.org/10.3390/met10010093.

[21] Hu Y, Gong C, Yao Z, Hu J. Investigation on the non-homogeneity of residual stress field induced by laser shock peening. Surf Coatings Technol 2009;203:3503–8.

https://doi.org/10.1016/j.surfcoat.2009.04.029.

[22] Dorman M, Toparli MB, Smyth N, Cini A, Fitzpatrick ME, Irving PE. Effect of laser shock peening on residual stress and fatigue life of clad 2024 aluminium sheet containing scribe defects. Mater Sci Eng A 2012;548:142–51. https://doi.org/10.1016/j.msea.2012.04.002.

[23] Peyre P, Merrien P, Lieurade HP, Fabbro R, Bignonnet A. Optimization of the residual stresses induced by laser shock treatment and fatigue life improvement of 2 cast Aluminium alloys. Fifth Int Conf Shot Peen ICSP 5 1993:301–10.

.

Chapter 5 Crack trajectory modifications by Laser Shock Peening residual stresses

This chapter investigated the feasibility of using Laser Shock Peening residual stresses to achieve a modification in the trajectory of a crack. The accurate positioning of LSP induced residual stress fields provided the unique possibility to determine whether the combination of applied loading and LSP residual stresses can result in a clear deviation of the crack path, reduce the crack growth driving forces and extend the life of a metallic component. Successful demonstration and characterisation of using LSP for this purpose may lead to the following future outcomes:

1) A possible reduction in the size and weight of fuselage tear straps and crack arrestors as the LSP residual stress may assist in driving crack turning whilst slowing the rate of crack propagation.
2) To use residual stress fields to promote the growth of concealed cracks in fuselage joints to an area of the structure which can be easily identified between inspection periods of the aircraft.
3) To potentially increase the fuselage residual strength capabilities as the LSP residual stresses work towards reducing the driving force of the propagating crack.

This chapter evaluated the LSP effects on AA2024-T3 alloy of 2.032 mm thickness which is representative of alloys used in the construction of fuselage structures. The influence of LSP on the geometry and surface finish of the coupons was assessed with a 3D optical profilometer. A residual stress analysis was performed with incremental hole drilling and neutron diffraction methods. The crack trajectory and crack growth rates were assessed with tension-tension crack growth rate testing. Finally, the experimental results are used to develop numerical models which provided further validation and insight into the outcomes of this chapter.

5.1. Effect of Laser Shock Peening on surface finish and sample geometry

Section 3.3.3 of chapter 3 provided a detailed overview of the middle tension sample configuration and general LSP parameters used for the processing of the samples. Five LSP configurations were manufactured in this study to investigate the effects of the LSP patch rotation angle and placement on the trajectory of the crack and overall FCGR. Figure 5.1 provided an example of the LSP sample configurations used in this study. The rotation angle, *LSP_Ang,* was referenced to the horizontal centre line of the sample. The patch spacing, *LSP_Dis*, refers to the rotated distance between the two LSP patches.

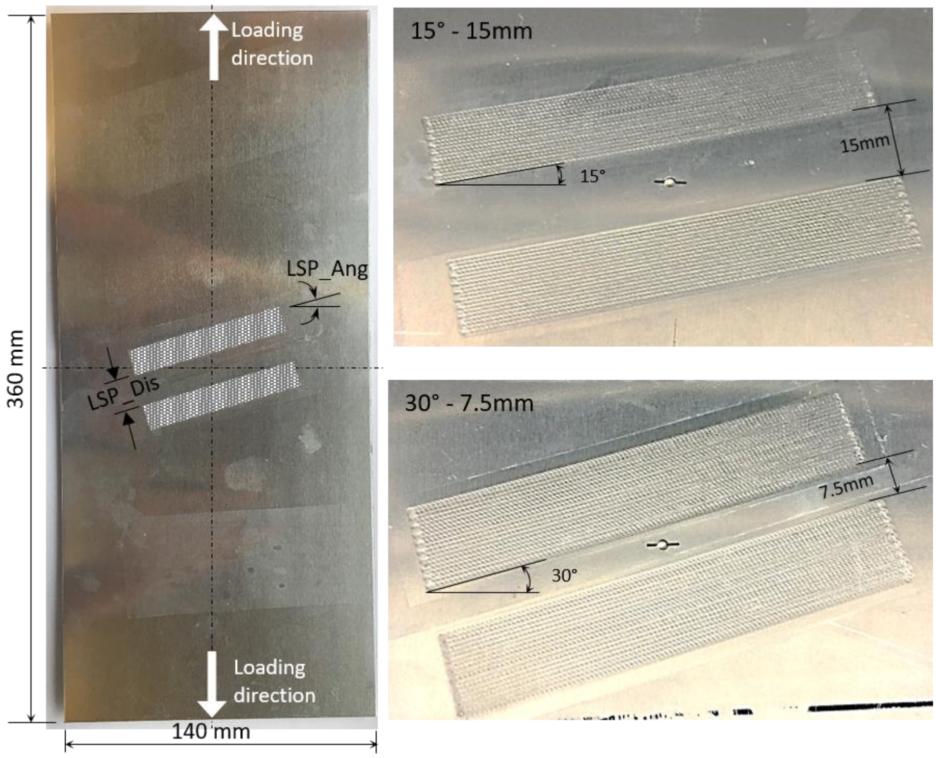

Figure 5.1: Example of the Laser Shock Peening patch orientations relative to the notch of the crack

5.1.1. Laser Shock Peening surface finish

The effects of the laser peening on the surface finish of the processed area are shown in Figure 5.2.a-b. These images were made with an optical microscope and Bruker 3D optical profilometer. Figure 5.2.a showed clearly the locations of the individual laser shots. Each dimple was made by two distinct laser shots as no layer offsets were used in the processing. Figure 5.2.b provided a topographical representation of a small region of the peened surface. The figure was overlaid with dotted shapes that approximated the laser shot diameter of 1.5 mm and overlap area. The laser shots tended to be more oval in shape as the target surface was placed at an approximate angle of 5 to 10 degrees to the incoming laser beam. This was done to avoid back reflections of the laser light which can potentially propagate back along the optical path, resulting in significant damage to the laser system. The largest surface deformations (orange-red regions) occurred at the centre of each shot, whilst the deepest (dark blue regions) localised surface deformation correlated to the approximate intersection of the sequential shots. All LSP patch orientations resulted in similar surface deformations.

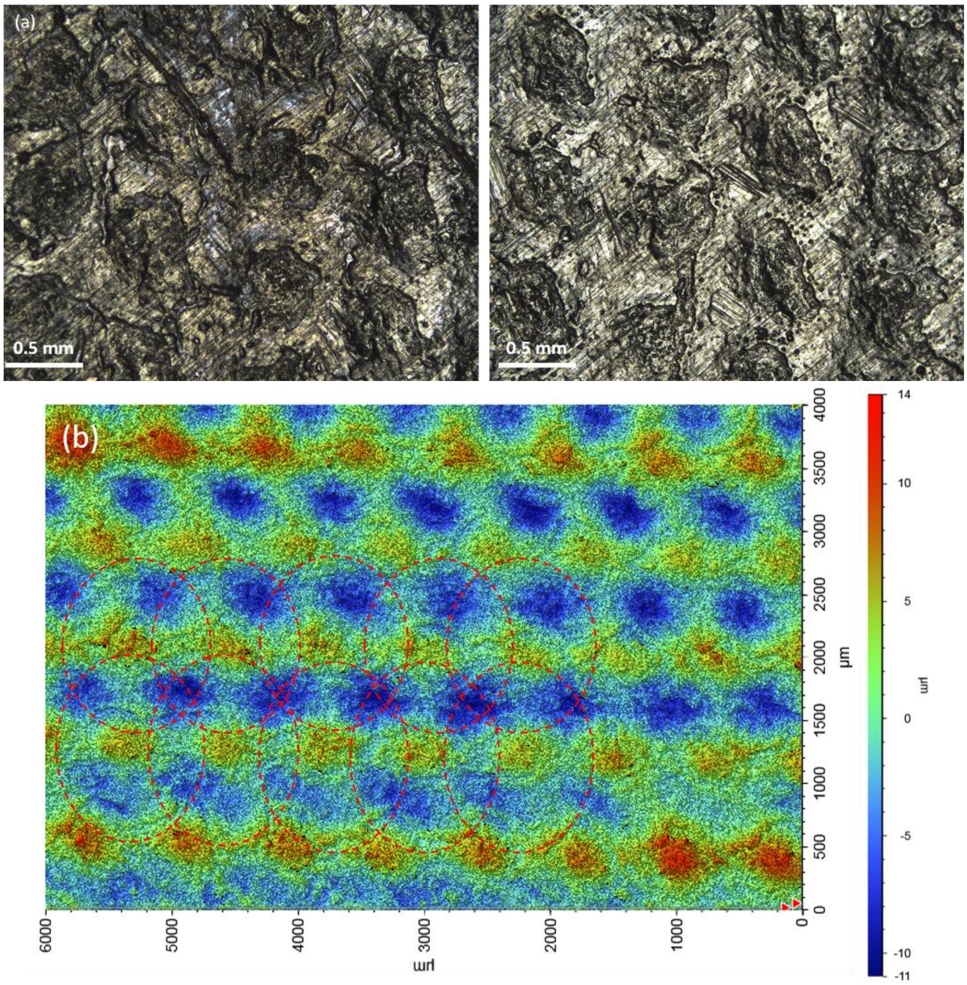

Figure 5.2: (a) Surface finish after laser peening treatment, (b) surface topography in the peened region

5.1.2. Residual stress-induced sample distortion

The introduction of residual stress by LSP resulted in the changing or deformation of the test samples original shape. The distortion occurred to maintain the equilibrium of the elastic stress field generated following the introduction of the LSP plastic deformation. The magnitude of the deformation was driven by the size of the applied LSP patch, laser parameters and the geometry of the sample. This deformation is most notable when processing thin structures as the volume of material is lower thus the elastic strains induced by the LSP processing leads to higher dimensional distortions. Figure 5.3 illustrated the process where a non-equilibrated LSP residual stress field was applied to the sample during peening. The distortion induced a balancing stress field which occurs as equilibrium was established in the test sample. The distortion of the sample can reduce the magnitude of the LSP compressive residual stress as the two components of the stress interact in a manner of superposition.

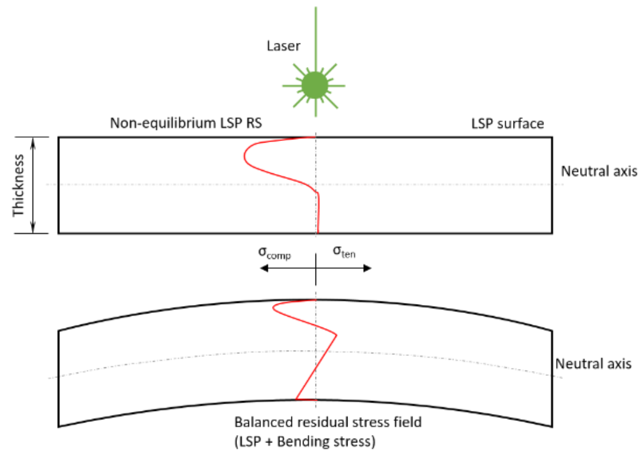

Figure 5.3: Effect of laser peening residual stress field on the sample distortion and resulting residual stress redistribution

LSP processing of both sides of the sample was not completed simultaneously which resulted in a bowed (convex/concave surfaces) sample shape after each application of the LSP processing. Figure 5.4 illustrated the full distortion process of the samples as the LSP was applied to each surface. The final resulting equilibrated stress field was the superposition of the distortion bending stresses and the LSP residual stresses. Throughout this chapter, LSP surface 1 (LSP layers one and three) and LSP surface 2 (LSP layers two and four) were referred to as the respective surfaces of the test sample. These surfaces are indicated by the blue and red '*x*' in Figure 5.4. The final sample deformation resulted in a concave shape for LSP surface 1 whilst LSP surface 2 was convex in shape.

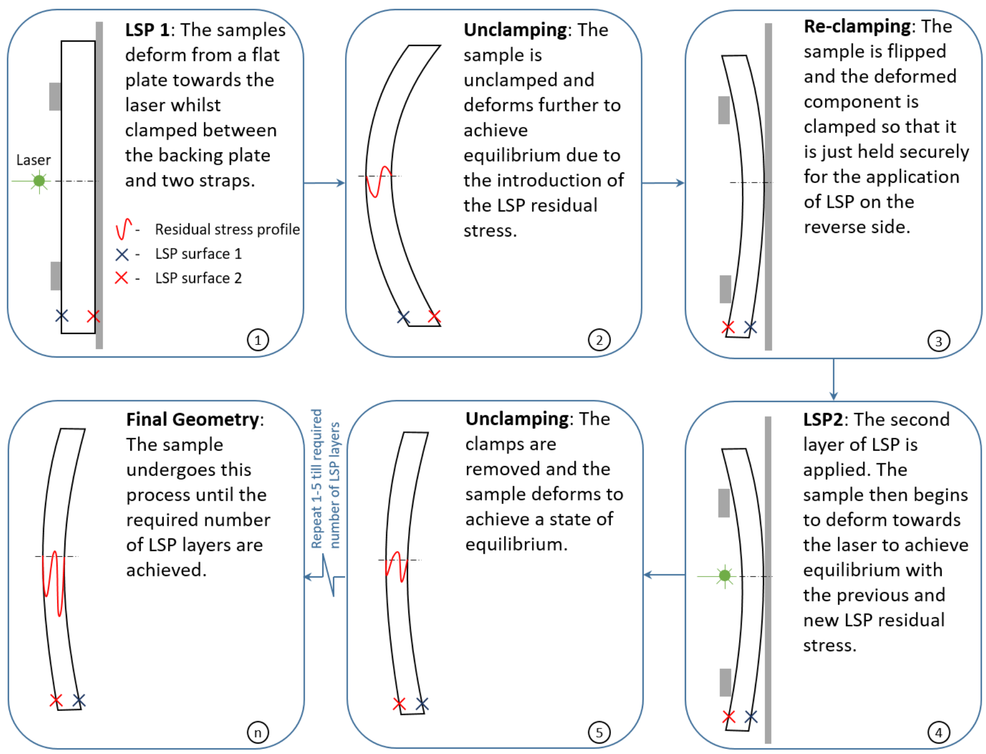

Figure 5.4: Illustration of the laser shock peening induced deflection over the full sample processing

Figure 5.5 demonstrated the influence that the number of applied LSP layers had on the overall peak distortion of the thin test samples. Three layers of LSP approximately doubled the total sample distortion from that of a two-layer peening strategy. The three-layer sample was found to distort extensively in both the longitudinal and transverse directions. The number of applied peening layers was limited to two to minimise the sample deformation.

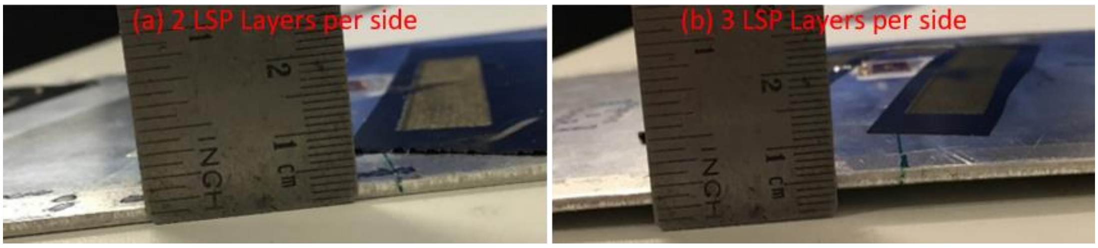

Figure 5.5: Effect of number of laser shock peening layers on the overall distortion of the test samples (a) two layers per side, (b) three layers per side

The final post-LSP shape of three samples per LSP configurations (five sets) was measured using a Coordinate Measurement Machine (CMM), as indicated by Figure 5.6.a. No measurements of the base-line samples were made, however, it was observed that the sample preparation (sample extraction from larger sheet and machining of the EDM notch) resulted in no significant sample distortion. Measurements were taken with a 1 mm diameter ball stylus along the length of samples in 0.5 mm measurement intervals at five width positions (L1 to L5), as seen in Figure 5.6.b. All measurements were made on the convex surface or LSP surface 2. The temperature and humidity were not controlled during the measurements but no significant change in operating conditions occurred in the laboratory during the time of the measurements.

The LSP induced distortion was confined to the peened areas with the maximum deflection occurring at the centre of the sample. Figure 5.7.a-e. provided an example of the measured deflections along the five locations of the most deflected or worst case sample of each LSP patch orientation. The edge of the LSP patches effectively acted as a pivot point where the remaining material returns to its non-deflected state over the remaining length of the sample. The two measurement lines which fell outside of the LSP area were typically just less than half the peak deflection at the centre of the sample and smoother along the length of the sample. The deflection of the samples was considered as the difference in height between the lowest position of the end of the sample and the position of the sample's mid-point.

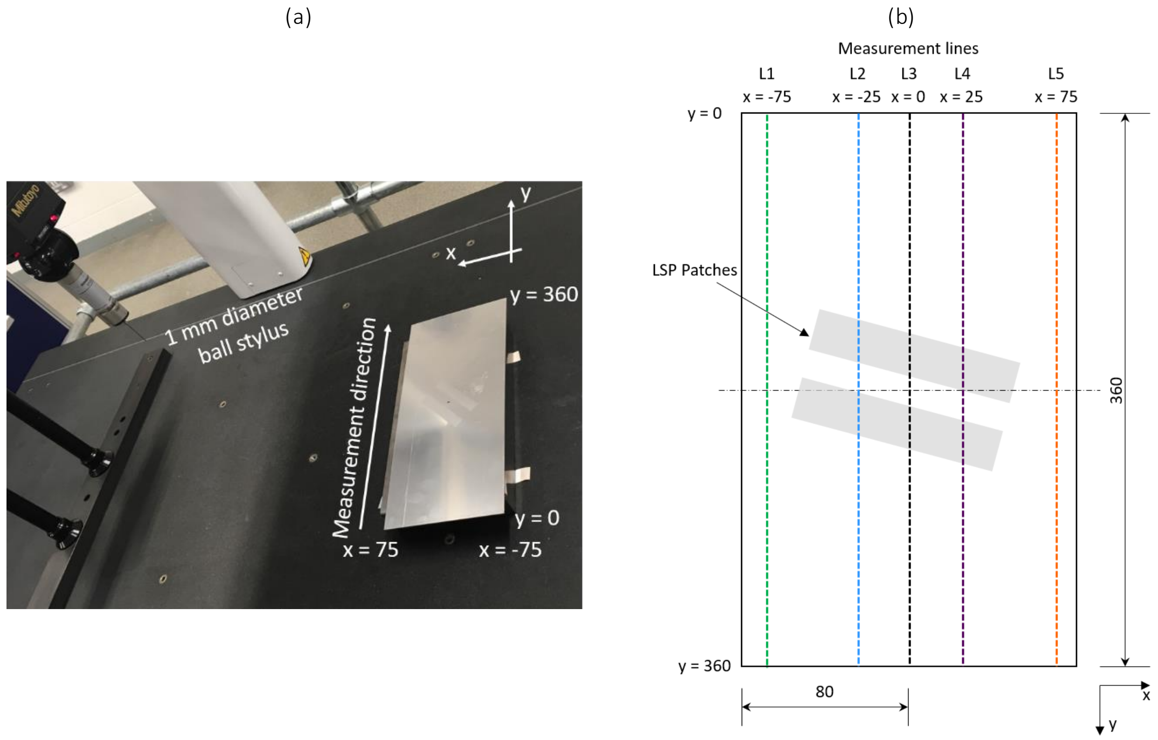

Figure 5.6: (a) example of sample layout during deflection measurement, (b) deflection measurement locations of crack trajectory samples

The peak deflection for all LSP orientations was within 4 - 5.5 mm except the sample set 30°-15 mm which fell between 2.5 - 3 mm, as shown in Figure 5.7.d. The exact cause of this inconsistency was unclear as there were no observed variations in the LSP parameters, application strategy and sample configuration. Additionally, the measured residual stress in this sample set was consistent across the other peening orientations. The only possible rationale for this lower deflection was due to inconsistent tightening of the securing straps between peening layers which influenced the final equilibrium deformation of the sample.

Figure 5.8.a-e provided a comparison of the central deflections and distortion angles of the three measured samples per LSP patch orientation. The multistep ‘to and fro’ like deformation process that each sample undertook in achieving its final geometry resulted in variations in the magnitude of the deflection peaks and angle between samples of each LSP patch orientation. The distortion angles were determined per sample as the intersection angle between the linear regions that flanked the LSP patches along the central measurement line; an illustration of this was shown in Figure 5.8.f. The peak deformation ranged between 3 - 5.5 mm with deflection angles ranging between 3 - 4.2° for the majority of the peening configurations, whilst the deflection ranged between 1.5 - 2.5 mm with angles of 2 - 2.5° at a 30°- 15 mm orientation. The occurrence of inconsistencies between sample deflections

with the same peening conditions indicated the sensitivity of the LSP process to how the thin samples were secured during processing. The steepest angle in each data set was associated with the sample with the highest deflection. The large deflections would likely result in the introduction of a secondary loading which will occur as the samples are pulled straight under the tension-tension loading and had to be accounted for in the FCGR testing.

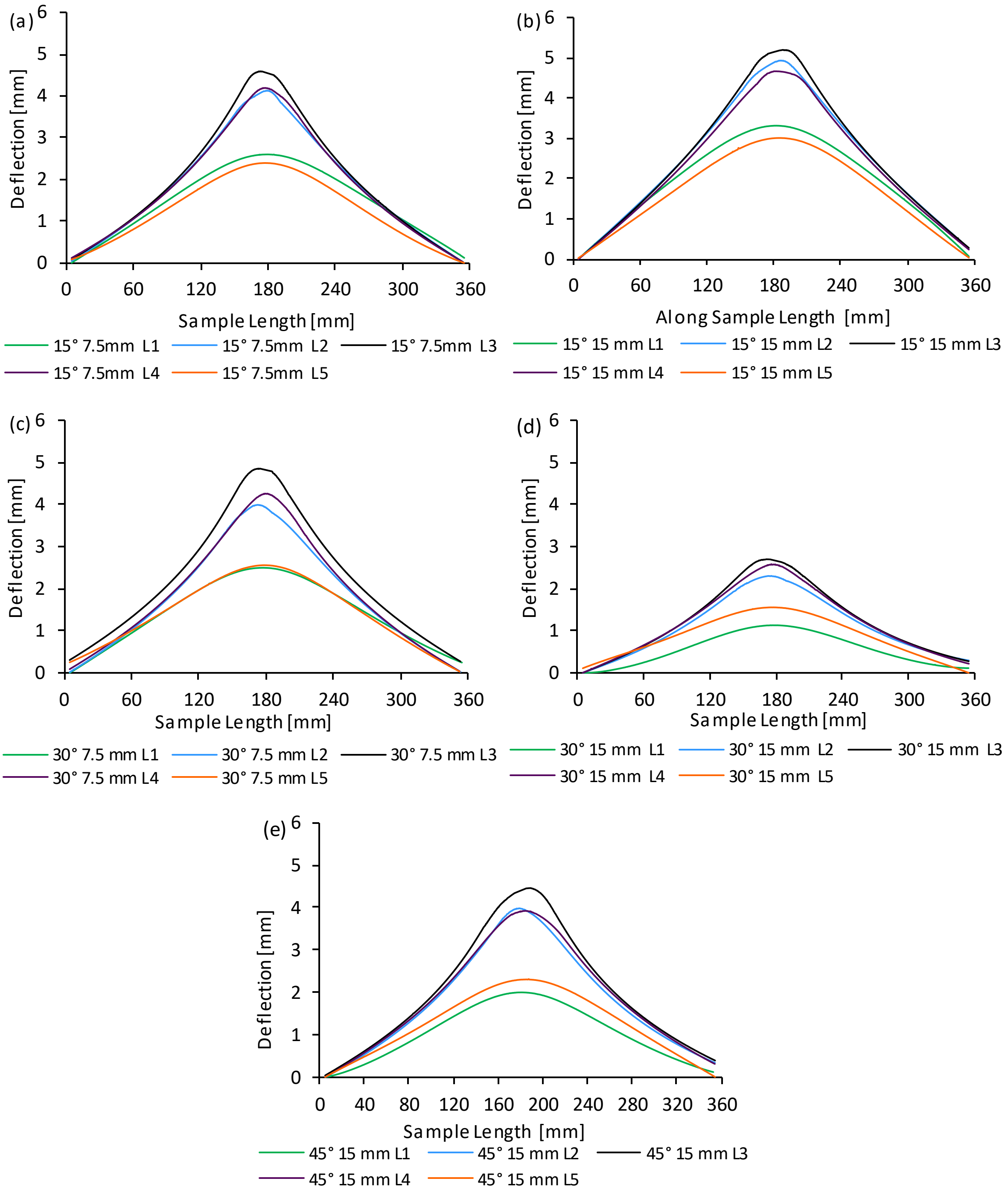

Figure 5.7: Induced deflection across each laser peening patch orientation (a) 15° - 7.5 mm, (b) 15° - 15 mm, (c) 30° - 7.5 mm, (d) 30° - 15 mm, (e) 45° - 15 mm

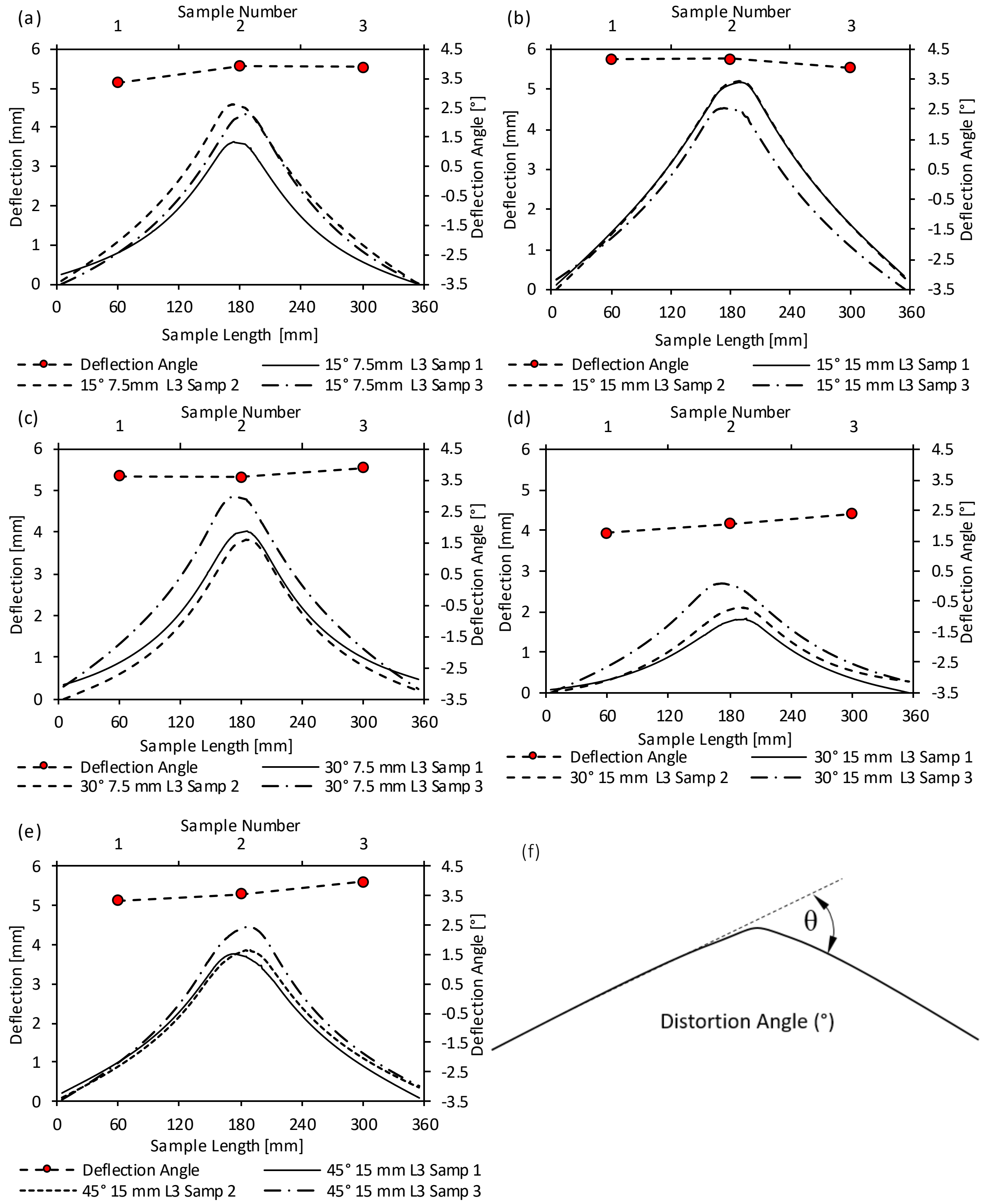

Figure 5.8: Comparison of centre (L3) deflection of measured laser shock peening orientations (a) 15° - 7.5 mm, (b) 15° - 15 mm, (c) 30° - 7.5 mm, (d) 30° - 15 mm, (e) 45° - 15 mm, (f) illustration of centrally measured deflection angle

5.1.3. Effect of induced residual stress distortion on applied loading

Due to the LSP residual stress-induced deflection of the samples, the applied load during the tension-tension crack growth testing was not purely uniaxial tension but a combination of tension and out of plane bending. An initial zero tension bending component was first initiated when the samples were clamped in the grips. An additional bending component was produced as the samples straightened under the application of the applied tensile load. Figure 5.9 illustrated the formation of the secondary out of plane bending throughout each step of the loading cycle.

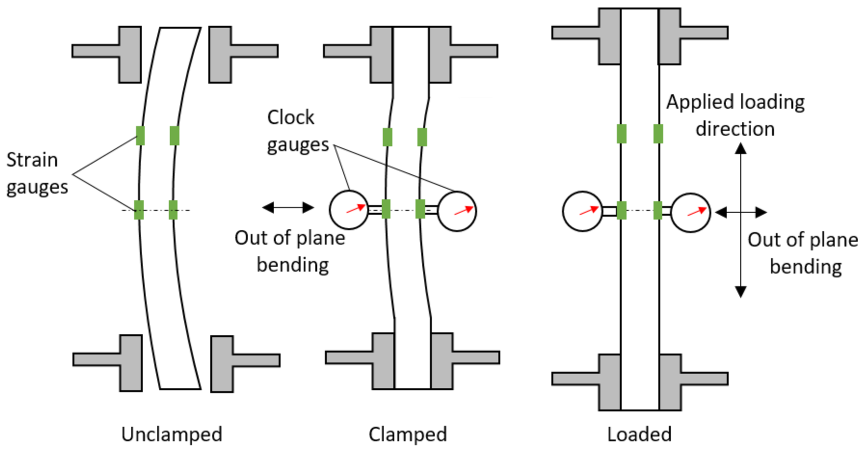

Figure 5.9: Illustration of out of plane bending load during crack growth test

Before commencing the FCGR testing, sample 2 and 3 of each LSP patch configuration was systematically loaded with a applied tensile stress that ranged from 9 to 200 MPa to characterise the deflection of the sample during loading. Dial indicator clock gauge instruments were placed on both sides of the samples just above the centre of the crack notch. As the samples were loaded the deflection of the gauges indicated the straightening of the samples, which was provided in Figure 5.10. The gauges were zeroed after clamping and at the minimum applied tensile stress of 9 MPa. In all LSP configurations, the samples undergo as much as half the total deflection within the first 50 MPa. The deflections tended to level off in the remaining 100 MPa of the loading cycle. The figures showed that LSP surface 2 (convex surface) underwent a higher deflection compared to the reverse surface.

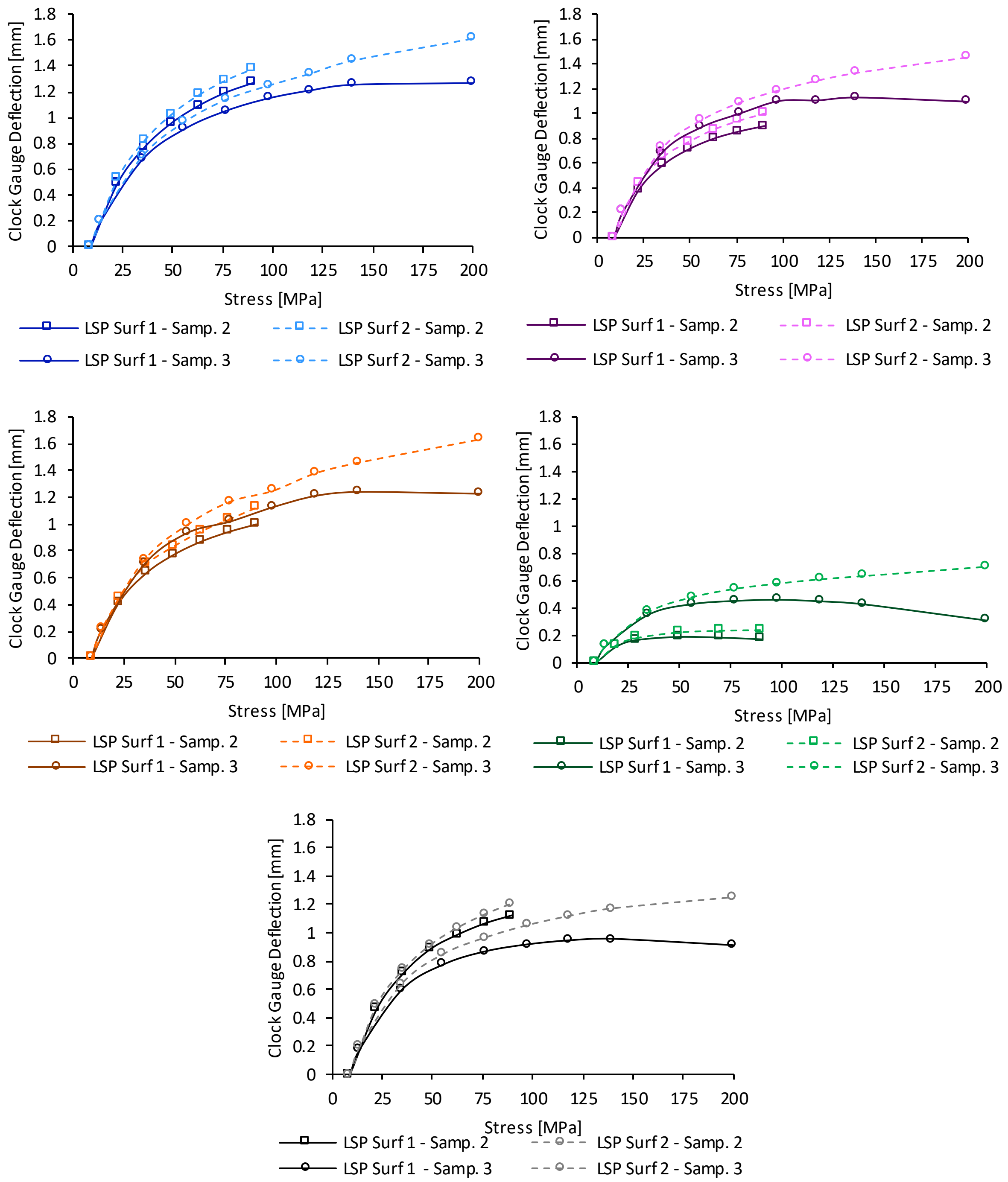

Figure 5.10: Central deflection of test sample surfaces through load cycle measured by clock gauge (a) 15° - 7.5 mm, (b) 15° - 15 mm, (c) 30° - 7.5 mm, (d) 30° - 15 mm, (e) 45° - 15 mm

The true surface strains were measured with uni-axial strain gauges that were bonded in multiple locations on both sides of the samples, as indicated in Figure 3.22 and Figure 5.11.a. The surface strains were measured throughout the fatigue loading cycle of three individual sample sets. All sample sets were exposed to a stress ratio of R 0.1, with sample sets 1 and 2 maximum applied stress set to 90 MPa and sample set 3 to 140 MPa. The maximum applied stress of sample set 3 was increased to overcome the distortion of the components. The calculated stresses in Figure 5.11 were determined using Hooke's law. Figure 5.11.b-e provided the surface stresses at the six measurement locations for the 30° - 7.5 mm LSP configuration, the remaining samples presented similar trends. Each line in Figure 5.11.b-e corresponded to the measured stress gradient through the samples thickness at the minimum and maximum applied stress. The zero-depth positions in the figures correlated to the concave surface or LSP surface 1. A single data set was provided as an example of the observed trends of all LSP configurations at the various loadings.

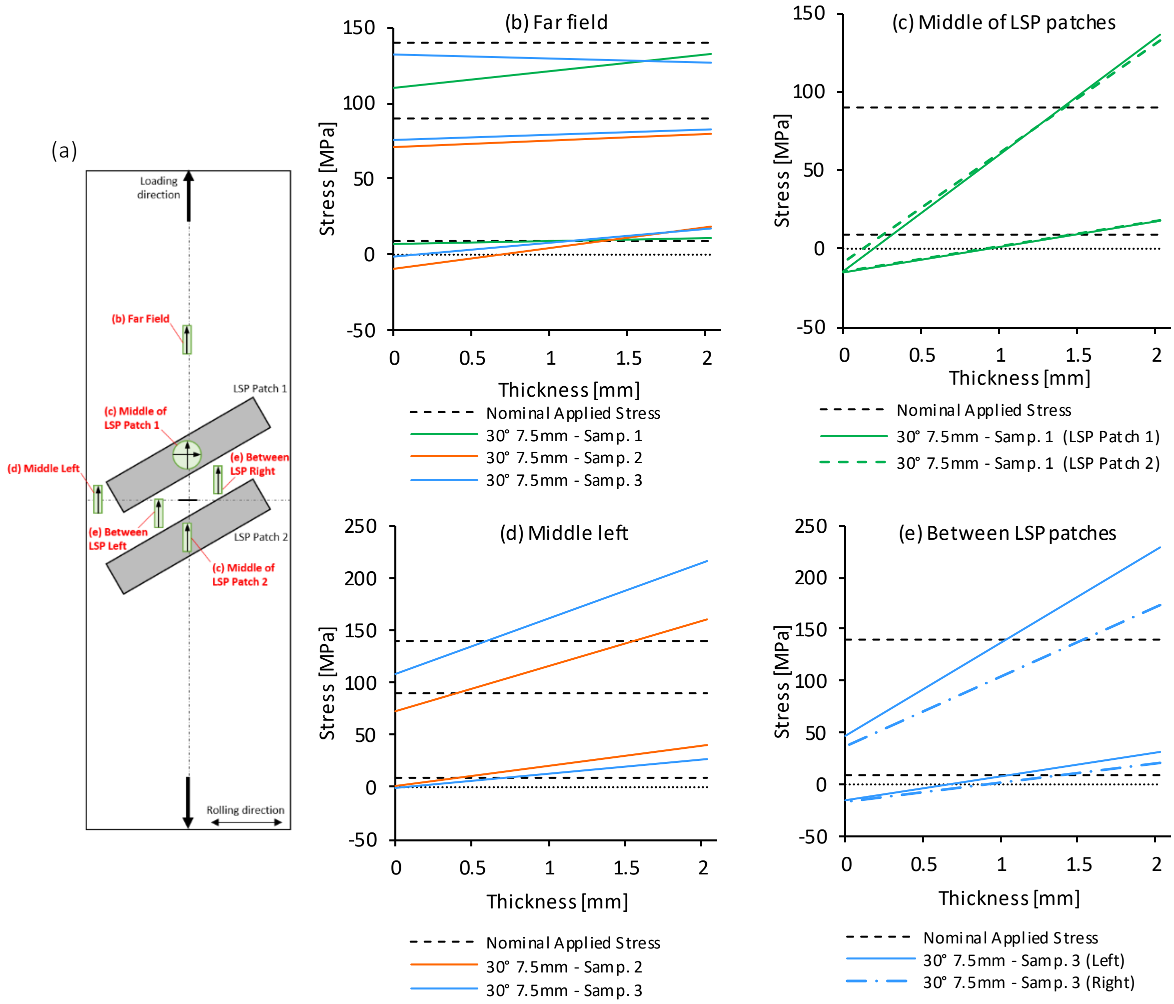

Figure 5.11: In situ surface stress applied during fatigue loading of 30° 7.5 mm laser peening configuration (a) strain gauge location on samples, (b) surface stresses at far-field gauge location, (c) surface stresses at the middle of laser peening patches, (d) surface stresses at the middle of sample and left offset location, (e) surface stresses between the laser peening patches on either side of the crack notch

Figure 5.11.b provided the surface stresses at the position which was considered to be outside the influence of the LSP compressive residual stress and was in the linear deflected region that flanked the LSP patches, so was considered in the far-field region. For the three samples, the stresses on LSP surface 2 generally were higher than those on LSP surface 1. At the minimum applied stresses of 9 (sample set

1 and 2) and 14 MPa (sample set 3), the calculated stress on LSP surface 1 was lower whilst the stress on LSP surface 2 was larger than the nominal applied stresses. The surface stresses were typically below the maximum nominal applied load, with the same surface stress differential occurring. This resulted in an effective R ratio and stress ranges that deviated from the nominal values of 0.1 and 81 MPa (sample 2) and 126 MPa (sample 3).

Figure 5.11.c provides the surface stresses at the centre of the LSP patches. At the maximum nominal applied load of 90 MPa, the surface stresses in LSP patch 1 were -14 MPa and 163 MPa on LSP surfaces 1 and 2 respectively. At the minimum load of 9 MPa, the surface stresses were -15 MPa and 18 MPa. This drastically affected the R ratio and the stress range on each surface. Figure 5.11.e provided the surface stresses at the mid-point between the two LSP patches and on either side of the crack notch. The maximum nominal stress was 140 MPa however the surface stresses on the left were 229 MPa and 47 MPa whilst on the right the stresses were 173 MPa and 37 MPa on LSP surface 2 and 1 respectively. This implied that the actual R ratio through the thickness varied between -0.38 and 0.18 at the left centre and -0.54 and 0.17 at the right centre, with stress ranges between 65 MPa and 188 MPa on the left and 57 MPa and 145 MPa on the right (nominal values were 0.1 and 126 MPa).

It was clear from the figures that the LSP induced deflection caused higher surface stress on the LSP surface 2 (convex surface) than what was observed on the LSP surface 1 (concave surface). Of particular note, was that a large loading differential occurred across the cross-section of the sample in the region where the crack was grown. This inevitably changed the loading that the crack experienced from its intended loading conditions. This fact was accounted for when considering the increase in life produced by the LSP and is discussed further in section 5.3. Similar trends were observed across all of the LSP configurations, with neither configuration presenting a benefit over another with respect to minimising the out of plane bending. Table 5.1 listed an example of the measured surface stresses at each of the locations for each LSP configuration, this was the data used in Figure 5.11 for sample 30° 7.5 mm. The table outlines the effective R ratio and stress range for each surface.

Table 5.1: In situ surface stress applied during fatigue loading of all sample configurations

		15° - 7.5mm		15° - 15mm		30° - 7.5mm		30° - 15mm		45° - 15mm	
		Surf. 1	**Surf. 2**	**Surf. 1**	**Surf. 2**	**Surf. 1**	**Surf. 2**	**Surf. 1**	**Surf. 2**	**Surf. 1**	**Surf. 2**
Far-field	Min load [MPa] (Appl. 14 MPa)	24.2	-2.5	23.4	-3.2	22.1	0.7	23.3	9.9	19.5	0.5
	Max load [MPa] (Appl. 140 MPa)	125.0	134.5	130.0	132.5	126.9	132.3	149.0	139.3	134.3	127.9
	R ratio	0.195	-0.019	0.18	-0.024	0.174	0.005	0.156	0.071	0.146	0.004
	Stress range [MPa]	100.6	137.0	106.7	135.7	104.8	131.6	125.7	129.5	114.7	127.4
Centre of LSP patch 1	Min load [MPa] (Appl. 9 MPa)	16.5	-15.7	5.4	11.6	18.1	-14.6	23.1	-10.7	18.9	-18.1
	Max load [MPa] (Appl. 90 MPa)	144.4	-18.1	85.7	77.4	132.6	-8.8	111.2	46.9	136.5	-6.1
	R ratio	0.11	0.87	0.06	0.15	0.14	1.7	0.21	-0.23	0.14	3.0
	Stress range [MPa]	127.9	-2.4	80.3	65.8	114.6	5.8	88.1	57.5	117.6	12.1
Middle left offset	Min load [MPa] (Appl. 14 MPa)	47.0	-1.1	46.6	-2.6	40.1	0.5	14.7	-5.2	40.4	-0.2
	Max load [MPa] (Appl. 140 MPa)	216.1	113.6	217.4	109.6	216.5	108.5	167.6	110.1	200.4	110.7
	R ratio	0.22	-0.01	0.21	-0.02	0.19	0.01	0.09	-0.05	0.20	-0.002
	Stress range [MPa]	169.0	114.7	170.8	112.2	176.4	108.0	152.9	115.3	160.0	110.9
Between LSP patches	Min load [MPa] (Appl. 14 MPa)	42.1	-20.8	41.1	-18.1	41.6	-17.8	40.1	-1.7	28.6	-15.9
	Max load [MPa] (Appl. 140 MPa)	229.1	38.7	205.7	66.1	229.2	46.9	195.5	107.4	171.0	75.9
	R ratio	0.18	-0.54	0.2	-0.27	0.18	-0.38	0.21	-0.02	0.17	-0.21
	Stress range [MPa]	187.0	59.5	164.6	84.3	187.5	64.7	155.4	109.1	142.4	91.8

5.2. Residual stress characterisation of Laser Shock Peened samples

The effects of the LSP processing and patch orientations were determined by incremental hole drilling and neutron diffraction techniques. Measurements were taken at multiple locations to determine the residual stress in and around the LSP patches.

5.2.1. Residual stress measured by incremental hole-drilling

5.2.1.1. Residual stress at the centre of the sample

Incremental hole drilling measurements were made at the centre of the sample and various locations in the LSP patches. An estimate of the through-thickness residual stress profile at the measurement locations were achieved through multiple incremental hole drilling measurements that were replicated on the two surfaces of the sample at the desired locations on individual samples.

The central residual stress profile was measured before the machining of the EDM notches. These residual stress measurements indicated the combined bending stresses and balancing LSP residual stresses that typically occur adjacent to the LSP patches. These results were later used to validate the residual stress simulation model. For the presented results, σ_x refers to the stress in the transverse direction of the sample and σ_y refers to the stress in the longitudinal (loading) direction. Figure 5.12.a-e. provided the central through-thickness residual stress for each of the LSP patch configurations. An acceptable agreement was achieved at the middle of the sample were the results of the two independent hole drilling measurements overlapped. In all measurements of the overlap region, the residual stress results were within the measurement error of each other.

As previously indicated, the steep variation in measured residual stress near the two external surfaces was due to the clad overlay on the material. The residual stress profiles at the centre of the sample were indicative of the out of plane bending of the samples, with the LSP samples highest magnitude of measured stress correlating to the most significantly deflected samples. The convex surface (LSP surface 2 which had the final layer of the LSP processing) tended to be in a larger amount of tensile residual stress than that of the concave surface which was in compression. Additionally, the rotation of the patches did not appear to influence the overall magnitude of the stress at the centre of the sample. However, the two samples with the smallest distanced patch placement of 7.5 mm had the largest magnitude of surface stress. Table 5.2 listed the averaged through-thickness stress at the centre of the samples.

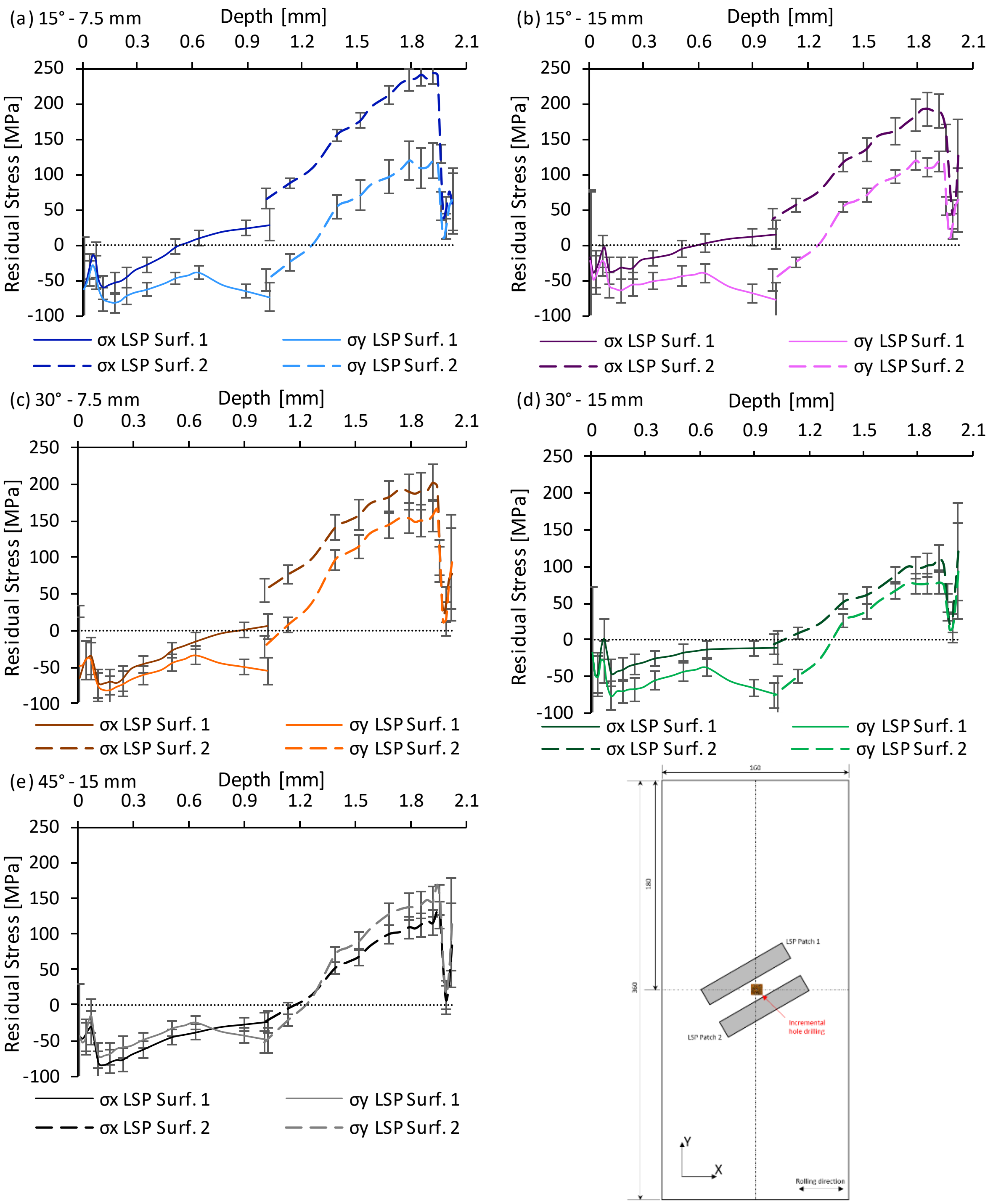

Figure 5.12: Through-thickness residual stress profile at the centre of samples (a) 15° - 7.5 mm, (b) 15° - 15 mm, (c) 30° - 7.5 mm, (d) 30° - 15 mm, (e) 45° - 15 mm, (f) schematic representation of incremental hole drilling position at centre of sample

Table 5.2: Summary of the average through-thickness residual stress at the centre of samples

Sample configuration	Average through-thickness stress at the centre of the sample	
	σ_x [MPa]	σ_y [MPa]
15° - 7.5mm	67	3
15° - 15mm	67	3
30° - 7.5mm	47	22
30° - 15mm	22	-7
45° - 15mm	10	22

5.2.1.2. Residual stress in the Laser Shock Peening patches

Figure 5.13 showed the through-thickness residual stress in the LSP patch 1 (top patch) in the as-received LSP configuration of 30°- 15mm. The strain gauges were aligned along the transverse (σ_x) and longitudinal (loading) directions (σ_y) of the sample. Measurements were located 20 mm from the left and right edges and along the centre line of the angled LSP patches: these positions were replicated on two individual samples to allow for the drilling of respective LSP surfaces. However, no measurement for the LSP surface 2 at the position right of the centre line was reported as the measurement failed due to the debonding of an area of the gauge during drilling. Due to the close correlation between the left and right measurements on surface 1, it was judged that the failed measurement would not need to be repeated as the obtained results did not vary significantly between measurements.

All residual stress measurements in the LSP patches exhibited the similar behaviour of having low surface stresses because of the clad layer. The LSP treatment resulted in a near fully compressive residual stress profile in the two orthogonal measurement directions. The peak compression of -250 MPa occurred at a depth of approximately 0.1 mm from the surface, which correlated to the transition depth from the clad to the bulk material. A slight tensile core of approximately 50 - 75 MPa was observed in the loading direction in the LSP patch. The depth of compression in both directions ranged between 0.7 - 0.9 mm. The magnitude of the stresses in the two directions was fairly similar throughout the first half of the measurement depths, with the longitudinal stress becoming more biaxial at approximately 0.55 mm. The two measurements on the LSP surface 1 had a fairly acceptable correlation, with the results being within the experimental uncertainty of the measurements. The largest deviation occurred towards the end of the measurement depth. This close correlation suggested that the residual stresses were fairly uniform across the LSP patches. As both patches were treated with the same LSP processing parameters, it was assumed that the through-thickness residual stress in both LSP patches had a similar residual stress profile to that presented in Figure 5.13. This assumption was partially validated by assessment of the measured sample deflections, shown in Figure 5.7. If the induced stresses vastly deviated between LSP patches then a significant difference in peak deflection and slope would have been observed about the centre of the figures.

A variation in the magnitude of the peak compressive stress was observed on the two LSP surfaces. This was caused by the superposition of the LSP residual stress and the out of plane bending stress of the sample. The compressive region of Figure 5.12 combined with the compressive LSP stress to increase the total compressive stress on this surface, whilst the tensile bending stress reduced the magnitude of the compressive stress on the reverse side.

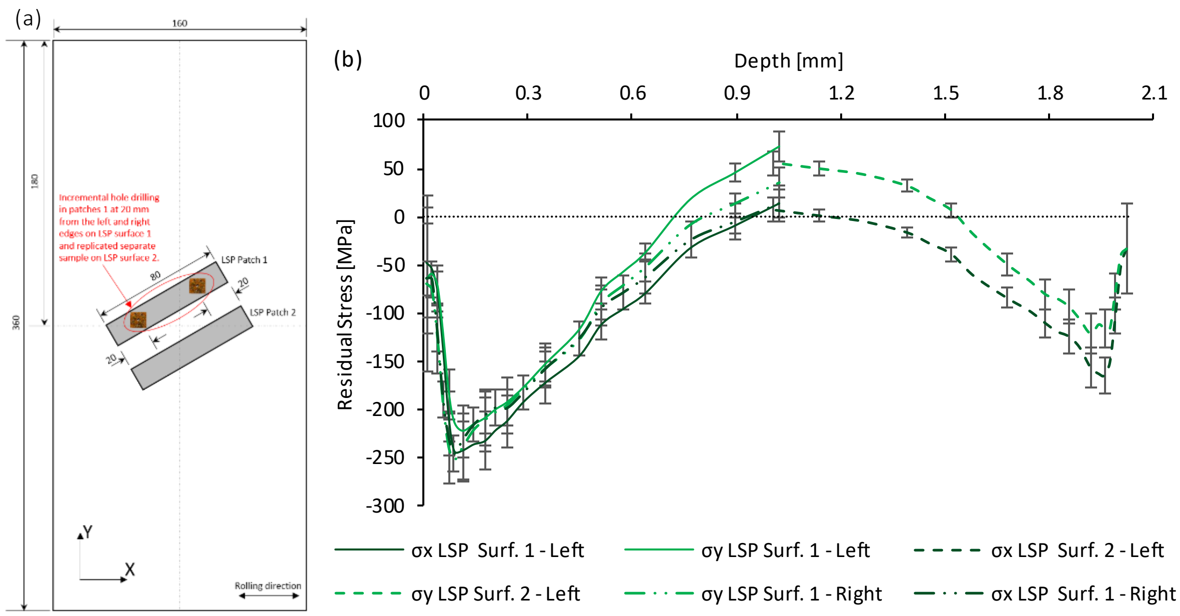

Figure 5.13: Through-thickness residual stress profile in the two laser peening patches in the 30° - 15 mm configuration (a) schematic representation of incremental hole drilling positions in patches, (b) measured residual stress profiles in both laser peening patches

The effect of the patch rotation angles on the residual stress was determined through incremental hole drilling measurements on samples that had undergone FCGR testing and had fully fractured, this is schematically shown in Figure 5.14.a. The measurements were made in approximately the same location as the as-received measurements, shown in Figure 5.13. Figure 5.14.b provided the measured LSP residual stress at each patch angle orientation but in fractured samples that had only been exposed to elastic loading. Due to the fracture of the samples, stress relaxation was expected and in addition, the residual stress would be affected by the removal of the bending stress. The main aim of the measurements, therefore, was not to accurately quantify the residual stress but rather to assess whether the various orientations resulted in residual stresses that were equivalent to the as-received sample in magnitude and trend. As in the previously presented data, the residual stress in the overlap depths of the measurements closely matched one another. This provided confidence in both the consistency of the LSP processing of the individual LSP patches and the use of the residual stress from individual samples in the assessment of the through-thickness residual stress.

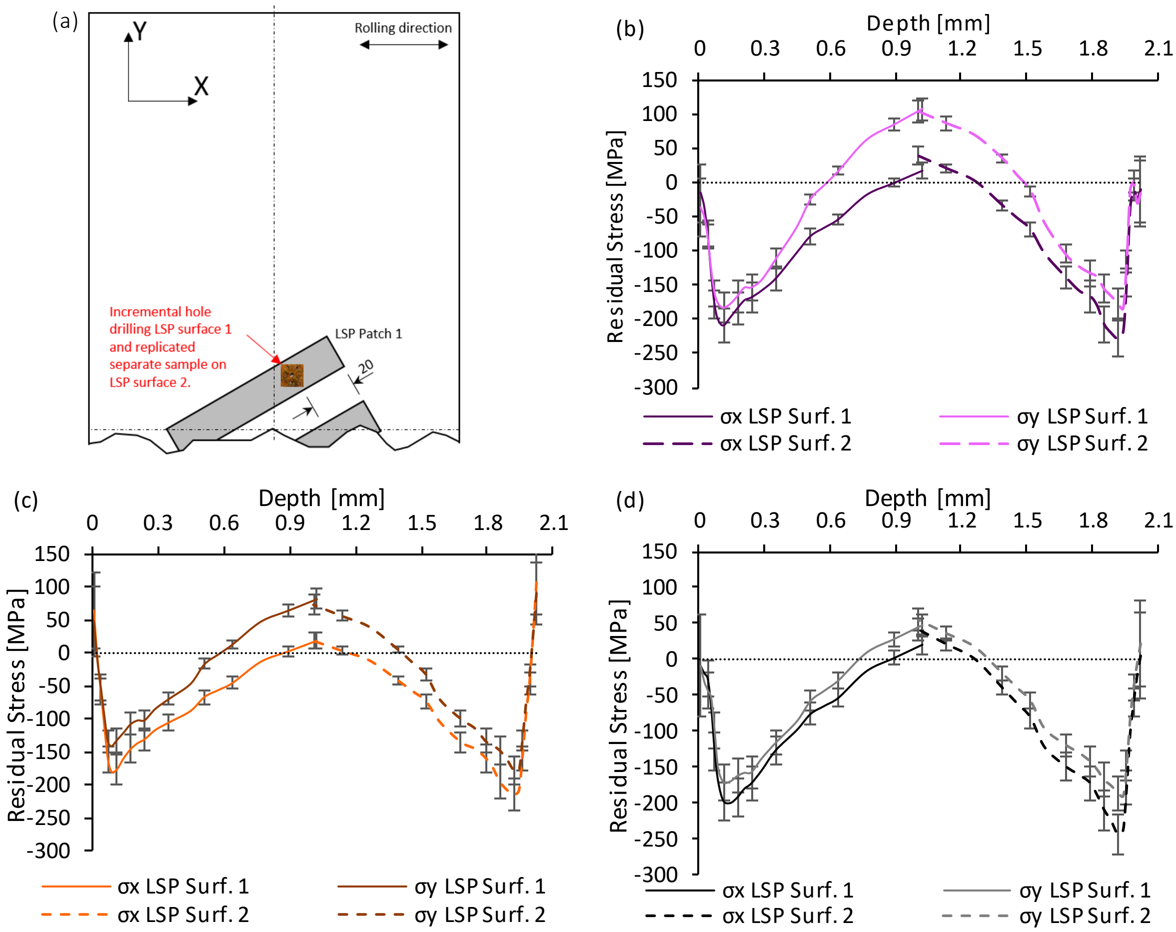

Figure 5.14: Through-thickness residual stress profile in fractured laser peening configurations (a) schematic representation of incremental hole drilling positions in patches, (b) 15° - 15 mm, (c) 30° - 7.5 mm, (d) 45° - 15 mm

All patch orientations resulted in a peak compressive residual stress that ranged between 150 - 225 MPa in compression on both surfaces, which was only slightly lower than the un-fatigued/damaged. The increased uniformity of the peak residual stresses was due to the removal of the bending stress. In addition, the residual stress in the LSP patches was predominantly compressive throughout the thickness, with a small tensile core in the loading direction. The peak tensile residual stress ranged between 50 -100 MPa for all patch orientations. The results suggested that the size of the tensile core tended to decrease with an increasing LSP patch rotation angle. The high patch rotations tended to reduce the magnitude of the biaxiality of the residual stress.

The measured residual stress in the LSP patches of both the as-received and fractured samples was compared in Figure 5.15. Comparison of the residual stress measurements made in patch 1 of the respective LSP samples indicated that the orientation and placement of the LSP patches had a minor effect on the magnitude and trends of the residual stress profiles, as the results were fairly similar. Additionally, the residual stress measurements at the various depths were within the experimental scatter of the measurements. As expected, the magnitude of the residual stresses in the LSP patch of the fractured samples was less than that of the equivalent position in the pristine sample. Similar depths of compression were achieved throughout the various LSP configurations (between 0.8 - 0.9 mm in the x-direction and 0.55 - 0.8 mm in the y-direction). This consideration may suggest that the fractured samples would likely have had an equivalent starting residual stress profile to that of the pristine 30° - 15 mm sample.

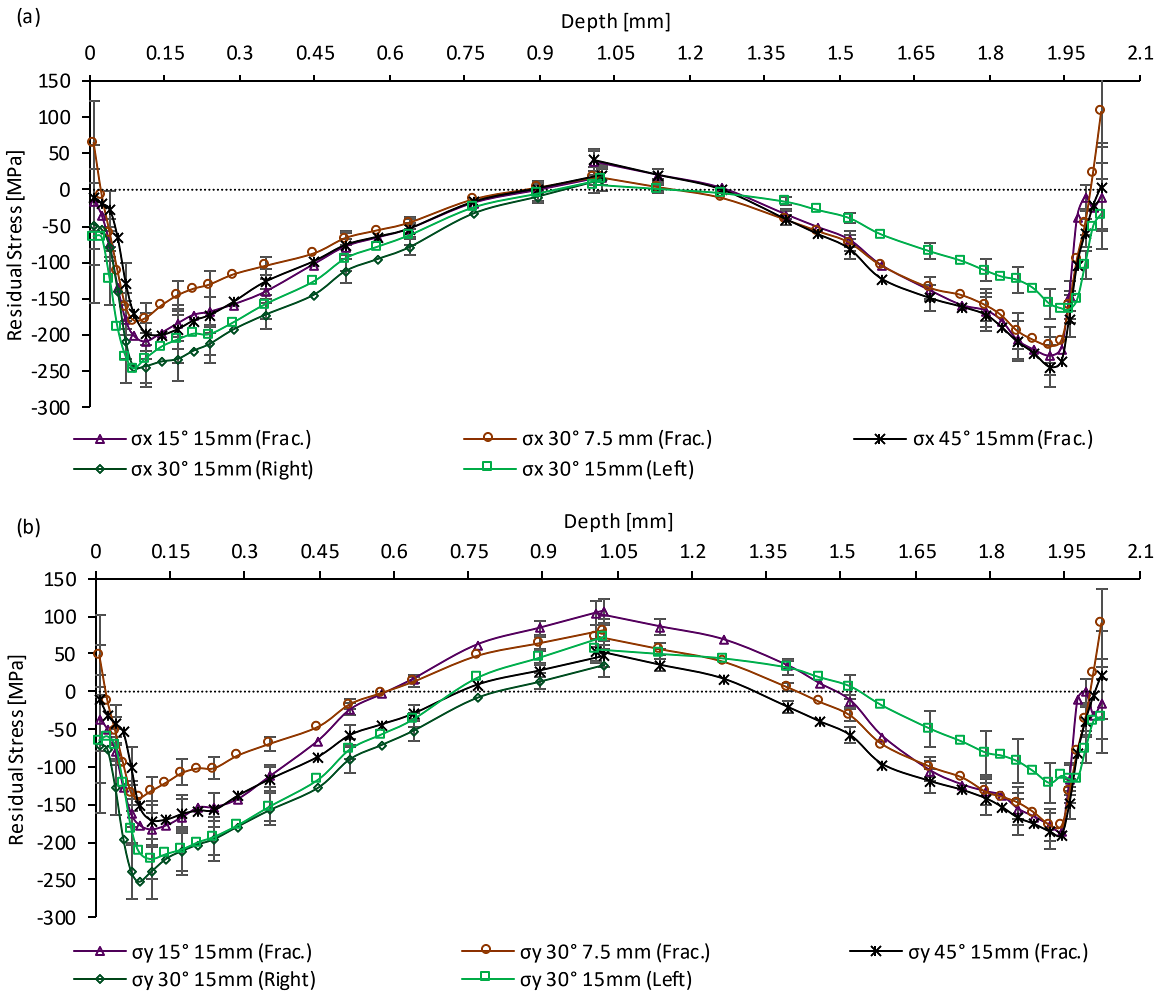

Figure 5.15: Comparison of the through-thickness residual stress of as peened and fractured samples in various patch configurations (a) residual stress in the transverse direction (x-direction), (b) residual stress in the longitudinal direction (y-direction)

Table 5.3 listed the averaged through-thickness residual stress which was measured in the LSP patches of the various orientations and spacings. In all cases, the LSP treatment was capable of inducing average residual stress that was compressive in nature. The average residual stress in the transverse directions tended to be more compressive than that of the longitudinal direction (in the loading direction). This was due to the lack of the tensile residual stress which occurred in the core of the sample.

Table 5.3: Summary of the average through-thickness residual stress in the laser peening patches

Sample configuration	Average through-thickness stress in the laser peening patch	
	σ_x [MPa]	σ_y [MPa]
15° - 7.5mm	Not measured	Not measured
15° - 15mm	-102	-66
30° - 7.5mm	-88	-55
30° - 15mm*	-109	-79
45° - 15mm	-103	-80

5.2.2. Residual stress measured by neutron diffraction

Neutron diffraction measurements were made on the 45° - 15mm rotated LSP sample at ISIS on the ENGIN-X instrument. Lines of measurements were made across the horizontal centre line and along the longitudinal direction 11 mm from the centre of the sample, as shown in Figure 5.16. At each location, three thickness positions (z - 0.75 mm, 1.00 mm and 1.25 mm) were measured. Additional z positions were avoided as the deformed shape and curvature of the samples made it extremely difficult to ensure the full gauge volume was immersed in the sample as the z positions approached the surface. Secondly, all of the unmeasured depth was made up of the clad material.

Figure 5.17.a-b showed the averaged through-thickness residual stress per location are provided in the longitudinal directions. These figures indicated a low magnitude tensile residual stress region occurred between the LSP patches. The averaged through-thickness incremental hole-drilling residual stress results are included to provide a comparison with the neutron diffraction data and showed a reasonable correlation between the two sets of measurements.

* Measurement was made on a pristine LSP sample.

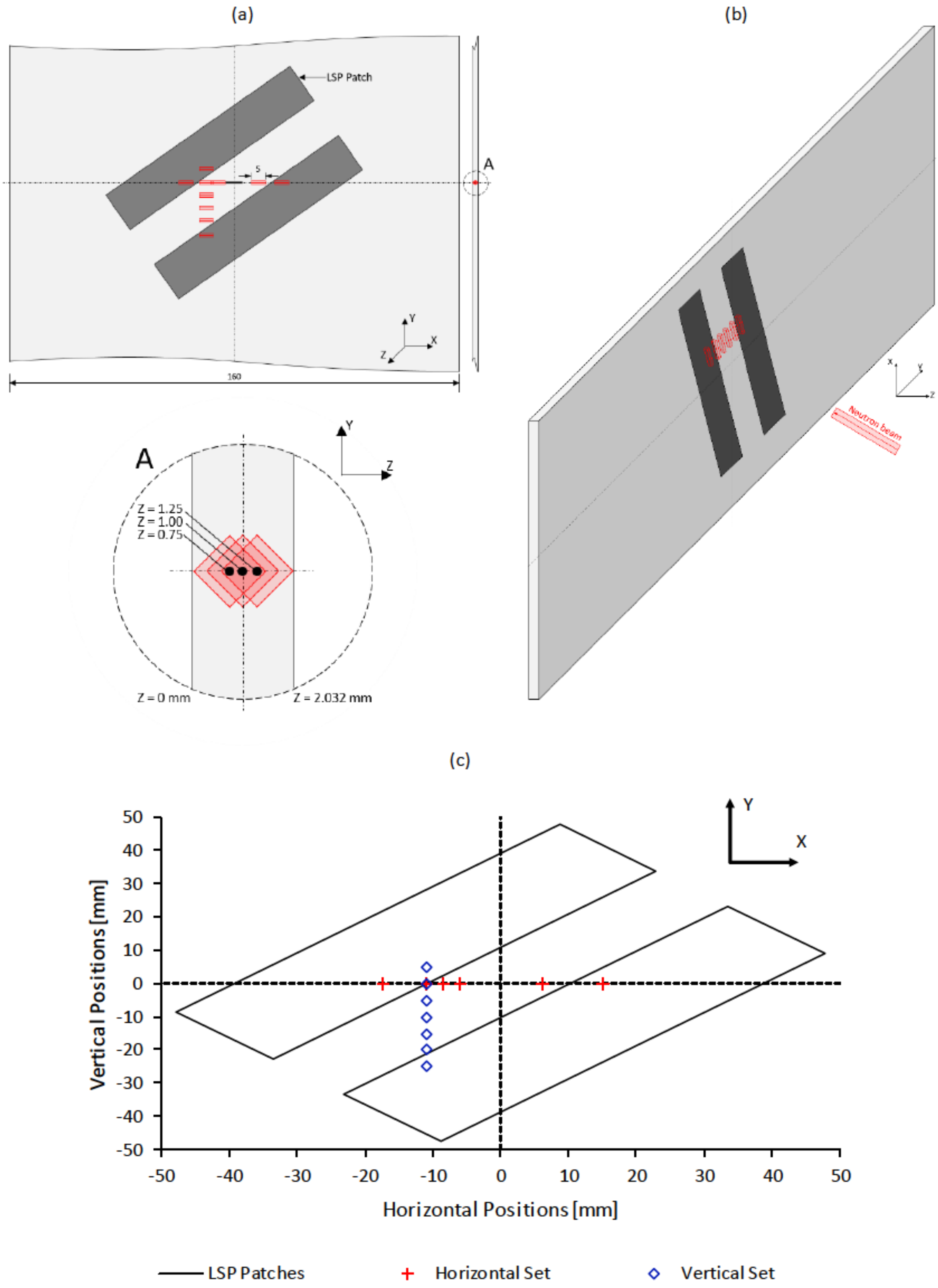

Figure 5.16: Schematic of neutron diffraction measurement locations (a)accurate representation of gauge volume across the face and in the thickness of the sample, (b) 3D representation of neutron measurement, (c) exact positioning of the gauge volume centre at various measurement locations

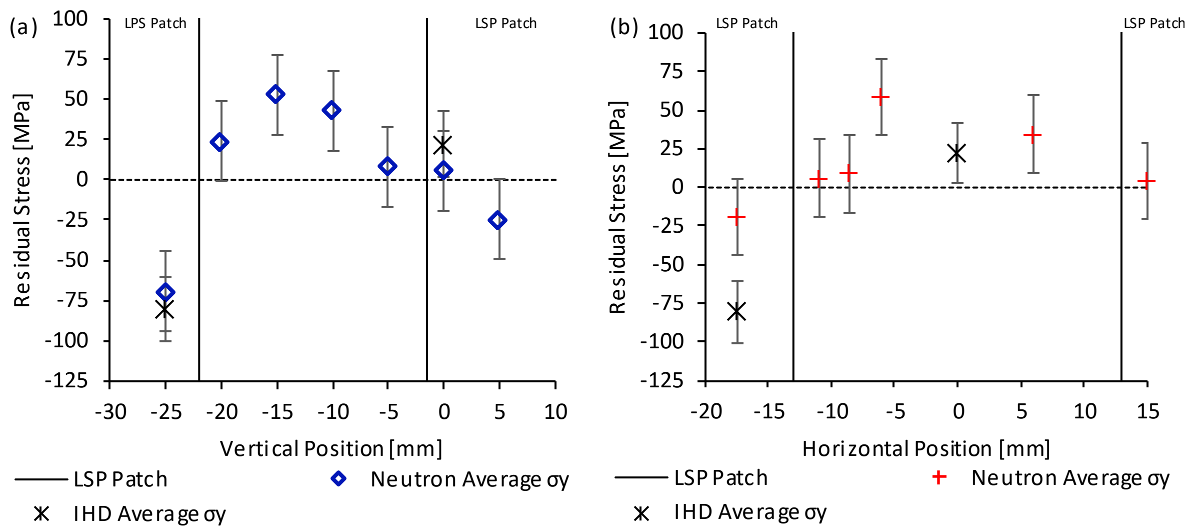

Figure 5.17: Averaged through-thickness neutron diffraction residual stress measurement results for rotated laser peening patches at 45°-15mm in the longitudinal direction (a) along the vertical measurement positions (b) along the horizontal measurement positions

The averaged through-thickness neutron diffraction measurements in the LSP area tended to be lower in magnitude than those of the incremental hole drilling. This was due to the fact that the neutron measurement was not taken at the centre of the LSP patch, where the compressive stress was more uniform and not affected by the stress transition that occurred near the edge of the LSP patches. The neutron gauge volume was elongated in the length direction which exacerbated the issue of sampling more of the lower transitional LSP stress.

5.3. Crack growth and trajectory modifications due to laser shock peening

The crack growth results for the baseline and laser peened middle tension samples were provided to show the influence of the LSP induce residual stress on the crack growth behaviour. The crack paths were measured to determine the effect of the LSP configurations on the overall trajectories. The baseline crack growth results were used to develop the Walker model coefficients for the 2024-T3 aluminium alloy. Table 5.4 has been reproduced from chapter 3, to specify the loading configurations used during the experimental fatigue crack growth testing of the samples.

Table 5.4: Fatigue crack growth experimental test matrix

Sample ID	LSP configuration (Angle-Spacing)	Cross-sectional area [mm^2]	Loading frequency [Hz]	R - ratio	Nominal max applied stress [MPa]
MT-BL-1	-	325	10	0.1	80
MT-BL-2	-	325	10	0.1	80
MT-BL-3	-	285	15	0.1	90
MT-BL-4	-	285	10	0.1	140
MT-BL-5	-	285	7.5	0.1	200
MT-BL-6	-	285	15	0.3	90
MT-BL-7	-	285	15	0.5	90
MT-15-7.5-1	15° - 7.5 mm	325	10	0.1	80
MT-15-7.5-2	15° - 7.5 mm	285	15	0.1	90
MT-15-7.5-3	15° - 7.5 mm	285	10	0.1	140
MT-15-7.5-4	15° - 7.5 mm	285	10	0.1	200
MT-15-15-1	15° - 15 mm	325	10	0.1	80
MT-15-15-2	15° - 15 mm	285	15	0.1	90
MT-15-15-3	15° - 15 mm	285	10	0.1	140
MT-30-7.5-1	30° - 7.5 mm	325	10	0.1	80
MT-30-7.5-2	30° - 7.5 mm	285	15	0.1	90
MT-30-7.5-3	30° - 7.5 mm	285	10	0.1	140
MT-30-15-1	30° - 15 mm	325	10	0.1	80
MT-30-15-2	30° - 15 mm	285	15	0.1	90
MT-30-15-3	30° - 15 mm	285	10	0.1	140
MT-45-15-1	45° - 15 mm	325	10	0.1	80
MT-45-15-2	45° - 15 mm	285	15	0.1	90
MT-45-15-3	45° - 15 mm	285	10	0.1	140

5.3.1. Formation of applied stress during fatigue crack growth testing

The ASTM E647-15 standard for the measurement of FCGR specifies a sample aspect ratio (half-length to width ratio (L/W)) of at least two when using mechanical wedge grips to ensure a uniform stress field at the centre of the sample, a schematic of this ratio was provided in Figure 5.18 [1].

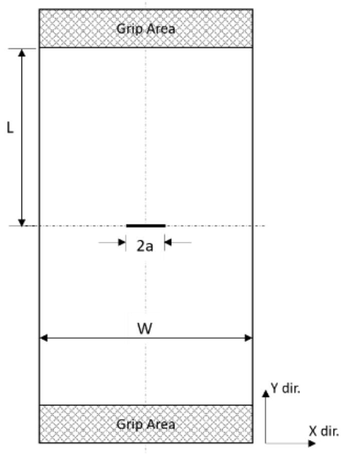

Figure 5.18: Schematic of middle tension geometric ratio

The MT LSP samples discussed in previous sections of this chapter were reduced in width from 160 mm (L/W – 0.875) to 140 mm (L/W – 1) before completing the crack growth experiments. This was done to increase the L/W ratio and promoted a uniform stress field in the samples. The samples had been initially manufactured to 160 mm to increase the amount of material which aided in the prevention of excessive deflection of the samples during LSP. The gripping area was the full width and the last 40 mm of the length on both ends of the coupon. Finite element modelling was used to show that the L/W ratio of 1 was sufficient for a uniform stress field to occur when the samples were loaded to 90 MPa with mechanical wedge grips. Full three-dimensional modelling of the samples was achieved by simulating the jaws of the test rig as non-deformable solids with a high coefficient of friction at the interface. Figure 5.19 provided a comparison of the averaged through-thickness stress along the length of the centre line of MT samples. The figure compares the effect of L/W ratios with a fixed sample width of 140 mm. It was clear from the figure that a uniform stress field occurred at the centre of both configurations as the average through-thickness stress in the σ_y (loading direction) was within 0.17% of the expected 90 MPa. Additionally, the stress in the σ_y direction did not exceed a 2% variation from the applied loading in the first 50 mm of length from the horizontal centre. Additionally, the figure showed that the stress perpendicular to the loading direction (σ_x) was less than 2 MPa.

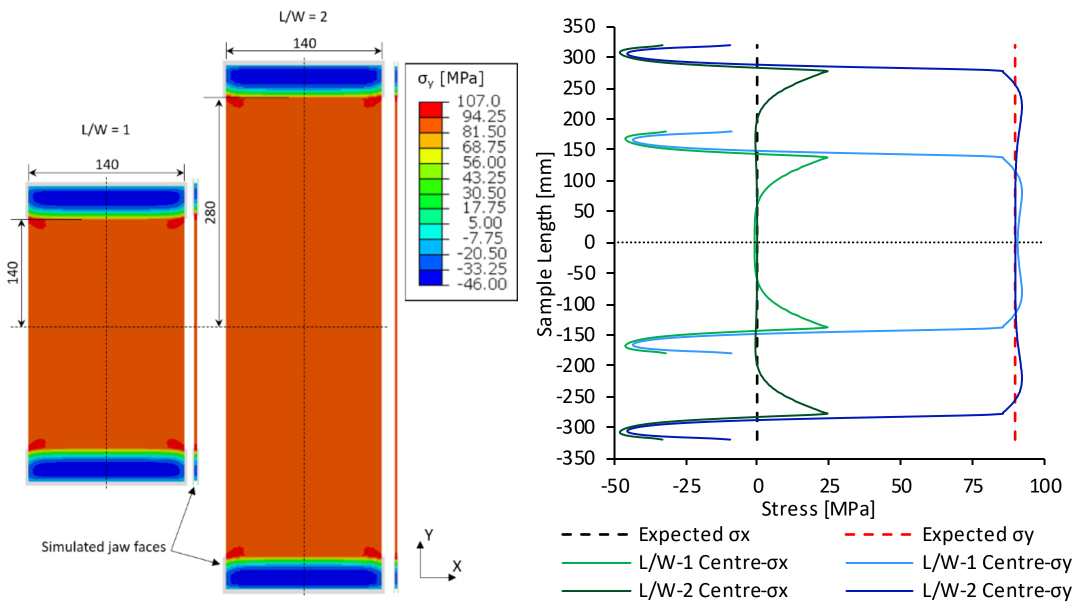

Figure 5.19: Comparison of averaged through-thickness stress along the length of the Middle tension sample (width 140mm)

Although no loading was intentionally applied in the σ_x (perpendicular to the loading direction), the action of applying the load through mechanical grips caused stress in this direction. The FEA results in both geometric cases estimated that the stress in the σ_x was less than 0.5 MPa at the centre and did not exceed ±1 MPa in the first 50 mm of length from the horizontal centre, thus was deemed negligible. This showed that the grip induced stresses did not contribute to any biaxial loading at the crack front which may have influenced the experimental trajectory of the fatigue cracks.

5.3.2. Experimental baseline fatigue crack growth

Fatigue crack growth rates (*da/dN*) throughout this chapter were determined from the crack length versus elapsed cycles (*a-N*) data by using the ASTM E647-15 proposed secant method [1]. The stress intensity was calculated using equation 2-49, which was applicable to a centre crack in a finite width body. No modifications to the intended test loading conditions were applied during pre-cracking of the samples to a crack extension length of 1 mm (half crack length of 4 mm, 3 mm EDM notch with a 1 mm pre-crack), this was used throughout.

Figure 5.20 provided the log-log FCGRs for the baseline material at three stress ratios (R 0.1, 0.3 and 0.5). This figure illustrated the effect of the stress ratio (R-ratio) and applied mean stress in that the FCGRs increased with increasing R-ratio. Data from replicated samples were combined and linear regressions were fitted to the linear regions of each set of data to determine the Paris coefficients, as discussed in section 2.3.3.

Table 5.5 lists the determined Paris coefficients for the three R-ratios. All R-ratios entered into Paris's defined region III of the FCGR range. The data sets were trimmed at various stress intensities when determining the linear regressions, the upper limits for each R-ratio were listed in the table. This was done to improve the accuracy of the linear fit, with the quality of the fits being judged on the correlation coefficients (R^2) in the linear regions. The correlations with the test data were deemed very good. A significant reduction was observed in the correlation factors of the complete test data (Paris region I-III). This was expected as the linear fits only described the stable crack growth region II, whilst the full data sets extended into region III.

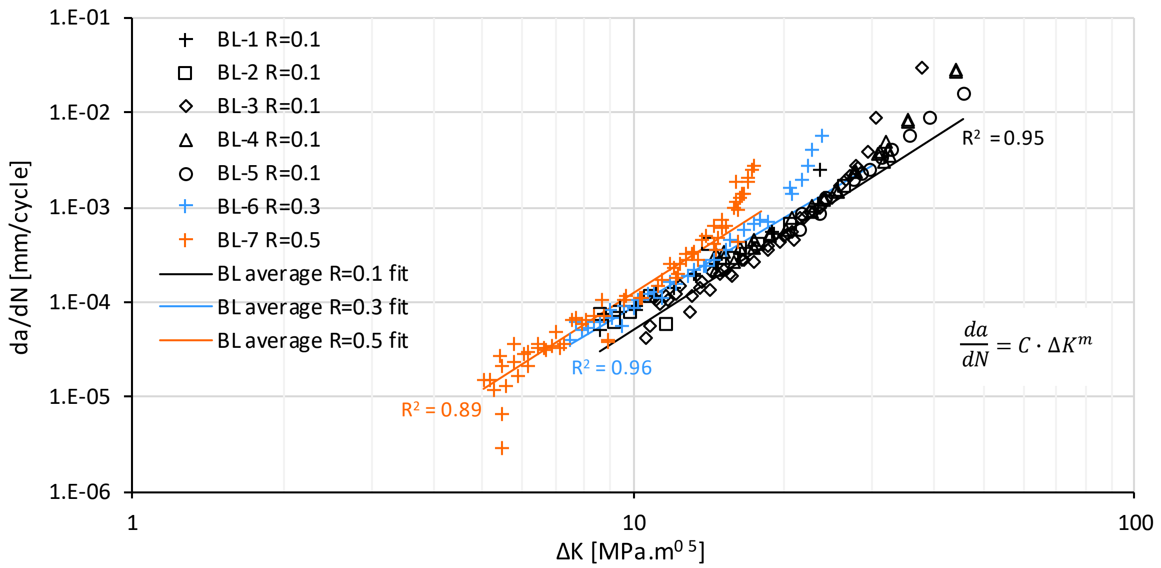

Figure 5.20: Baseline crack growth rate (da/dN) – stress intensity range (ΔK) test for three R-ratios (R=0.1, R=0.3, R=0.5)

Table 5.5: Determined Paris coefficients and correlation values with tested data

R-ratio	Paris coefficients for trimmed data range (region II)			R^2 correlation factor with region-II	R^2 correlation factor with complete data range
	C [mm/cycle]	m	ΔK limit of data trim [MPa.m$^{0.5}$]		
0.1	2.12×10^{-8}	3.38	25	0.95	0.78
0.3	6.54×10^{-8}	3.13	20	0.96	0.44
0.5	5.20×10^{-8}	3.38	15	0.89	0.50

5.3.2.1. Baseline Walker material coefficients

The Walker coefficients were determined to allow for the accurate prediction of FCGRs whilst considering mean stress effects, this was particularly useful when considering the influence of residual stresses on FCGRs. The baseline samples that were tested at the three R-ratios were used to develop the model for this material and sample configuration. This was achieved by collapsing the different stress ratio data in a single curve through the use of an effective stress intensity range (ΔK_{Eff}) at an R-ratio of 0, this value was calculated according to equation 2-59. Figure 5.21 showed the collapsed data for each R-ratio. The gamma parameter was iteratively determined to maximise the correlation factor of the linear fit, resulting in a γ-value of 0.59 (R^2 value of 0.91). The determined gamma factor was found to be of a similar value to those determined by Busse γ-value of 0.59 AA2524-T3 [2] and Melson γ-value of 0.564 AA7075-T6 [3]. The correlation factor was good, however, the model did deviate from the experimental data at the regions of the higher ΔK-values for the respective R-ratios.

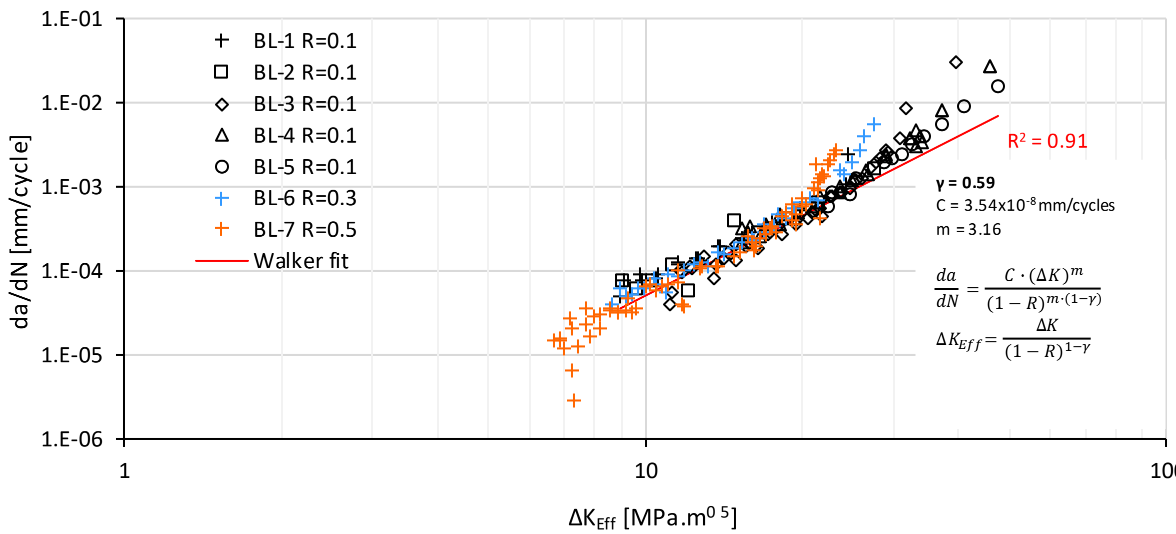

Figure 5.21: Walker fit for AA2024-T3 crack growth test data for three R-ratios (R=0.1, R=0.3, R=0.5)

The determined Walker equation was cross-checked and compared against the test data at the three R-ratios. Figure 5.22.a-c. showed a fairly good correlation between the predicted model and the respective experimental FCGRs. The experimental data from Busse (AA2524-T3) and Hudson (AA2024-T3) at equivalent R-ratios was included [2,4]. The agreement in FCGRs validated the used experimental procedure and methodology and confirmed that the results were within the expected range of previously published results.

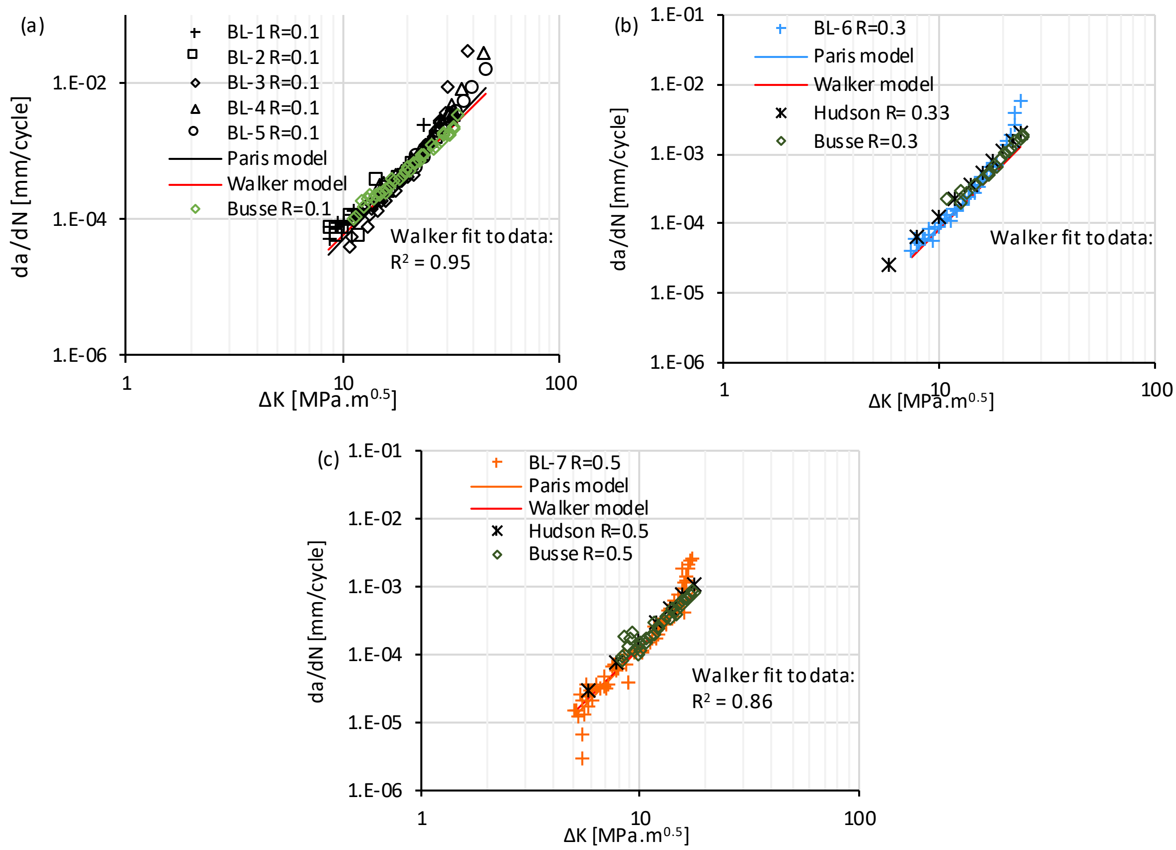

Figure 5.22: Comparison of Paris and Walker models against test data (a) R=0.1, (b) R=0.3, (c) R=0.5 (comparative published data at equivalent stress ratios [2,4]

5.3.3. Experimental Laser Shock Peened fatigue crack growth rate

Five LSP patch configurations were applied to the MT samples, as illustrated in Figure 5.23.a-e and previously defined in chapter 3. The patches were orientated about the centre of the samples at three angles (15°, 30° and 45°) and two patch spacings (7.5 and 15 mm). The LSP conditions were fixed throughout and defined in section 3.3.3.

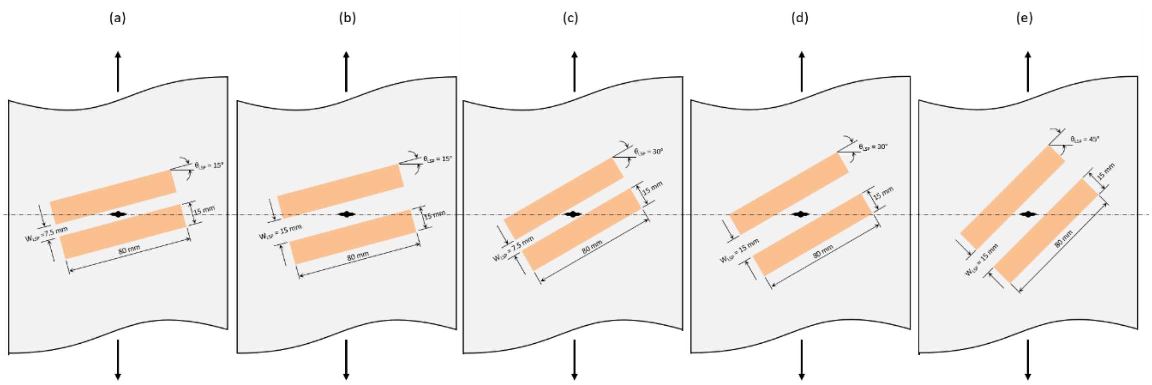

Figure 5.23: Laser peening patch configurations (a) 15°-7.5 mm (b) 15°-15 mm (c) 30°-7.5 mm (d) 30°-15 mm (e) 45°-15 mm

All tests were done in laboratory air at ambient temperature, with no significant variations occurring during the experimentation. All samples sets were tested with a stress ratio of 0.1, sample set 1 had loading spectrum of σ_{max} = 90 MPa and σ_{min} = 9 MPa and sample set 2 had σ_{max} = 140 MPa and σ_{min} = 14 MPa. The applied maximum loading was increased by 50 MPa between sample sets to overcome the deflection of the samples as shown in Figure 5.10. Figure 5.24.a-f. provides the measured crack growth life of the baseline and each LSP configuration. Test 1 and 2 referred to the left and right crack of the MT samples for each loading configuration. The average crack length was taken between these values.

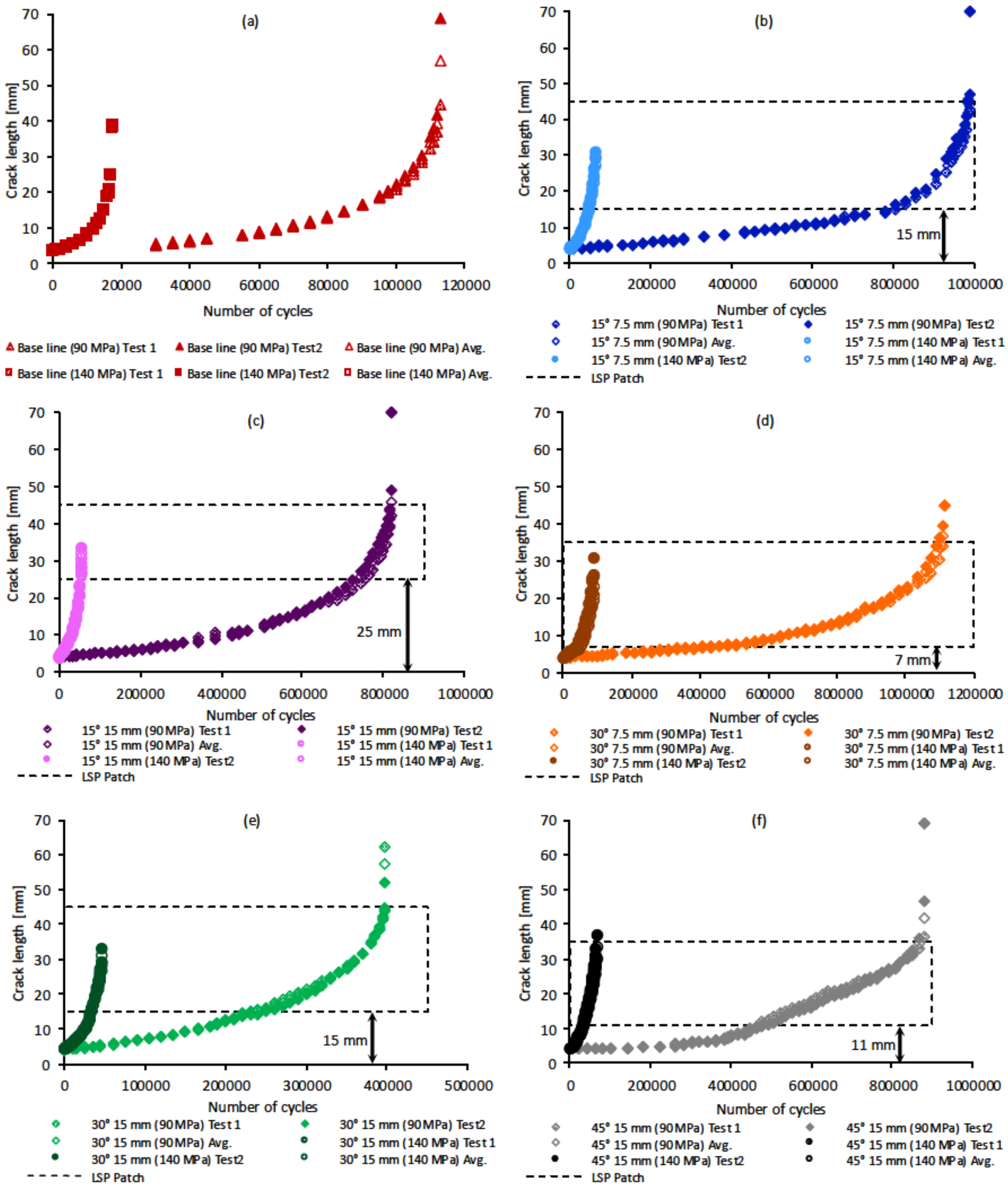

Figure 5.24: Measured and averaged crack growth life (a-N) of tested samples (a) baseline material, (b) laser peened patch configuration 15° - 7.5 mm , (c) laser peened patch configuration 15° - 15 mm, (d) laser peened patch configuration 30° - 7.5 mm, (e) laser peened patch configuration 30° - 15 mm and , (f) laser peened patch configuration 45° - 15 mm

Table 5.6 listed a summary of the average total post pre-cracking number of cycles (crack growth life) required for the samples to completely fracture. The average horizontal distance from the notch tip to the edge of the LSP patches for each LSP configuration was listed. These distances were measured before the FCGR testing and whilst under the maximum applied load. The data tended to show that the LSP configuration with the slowest FCGR or highest extension in crack growth fatigue life was achieved by placing the LSP patch closest to the notch tip (30° - 7.5 mm, a distance of approximately 7 mm). This trend was observed and confirmed by Pavan [5], Busse [2] and van Aswegan et al. [6], who investigated the effects of the placement of a single vertical LSP stripe of finite thickness relative to a crack tip in aluminium samples.

Table 5.6: Summary of cycles to failure and extension in crack growth life due to laser peening patches

LSP configuration	Horizontal length to LSP patch [mm]	Average cycles to failure (post pre-cracking)		Extension in crack growth life	
		Set 1 (σ_{max} - 90 MPa)	Set 2 (σ_{max} - 140 MPa)	Set 1 (σ_{max} - 90 MPa)	Set 2 (σ_{max} - 140 MPa)
15° - 7.5 mm	15	986 470	62 000	8.74	3.54
15° - 15 mm	25	817 985	57 000	7.25	3.26
30° - 7.5 mm	7	1 113 217	89 818	9.86	5.13
30° - 15 mm	15	397 907	63 000	3.52	3.6
45° - 15 mm	11	879 561	64 000	7.79	3.66

Baseline material σ_{max} 90 MPa – 112 884 cycles

Baseline material σ_{max} 140 MPa – 17 500 cycles

Figure 5.25 to Figure 5.29 were made up of two respective plots which provided (a) standard crack growth rate (da/dN vs ΔK) and (b) crack growth rate as a function of crack length (da/dN vs a) for each LSP patch configuration. The two loading conditions and the baseline material were included to provide additional context. The average boundaries of the LSP patches which were measured along the crack length of the samples and were indicated by the dashed rectangle were appropriate.

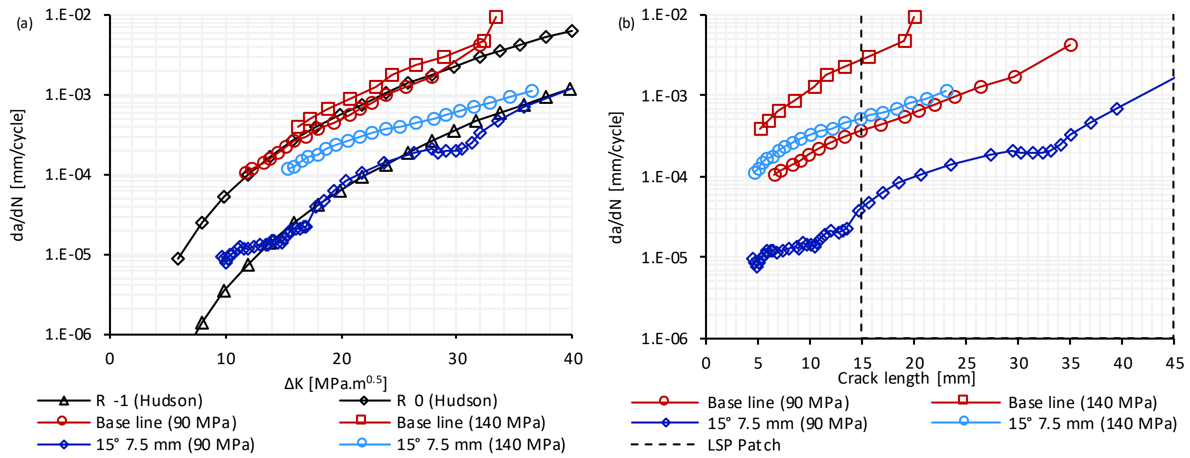

Figure 5.25: Laser peened patch configuration 15° - 7.5 mm (a) crack growth rate (da/dN-ΔK) [4], (b) comparison of crack growth rate and crack length (da/dN-a)

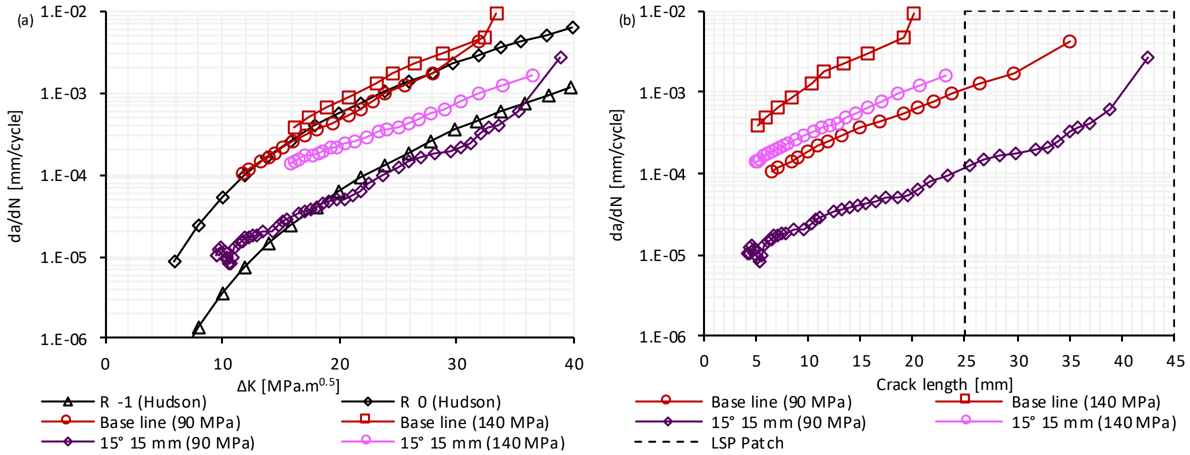

Figure 5.26: Laser peened patch configuration 15° - 15 mm (a) crack growth rate (da/dN-ΔK) [4], (b) comparison of crack growth rate and crack length (da/dN-a)

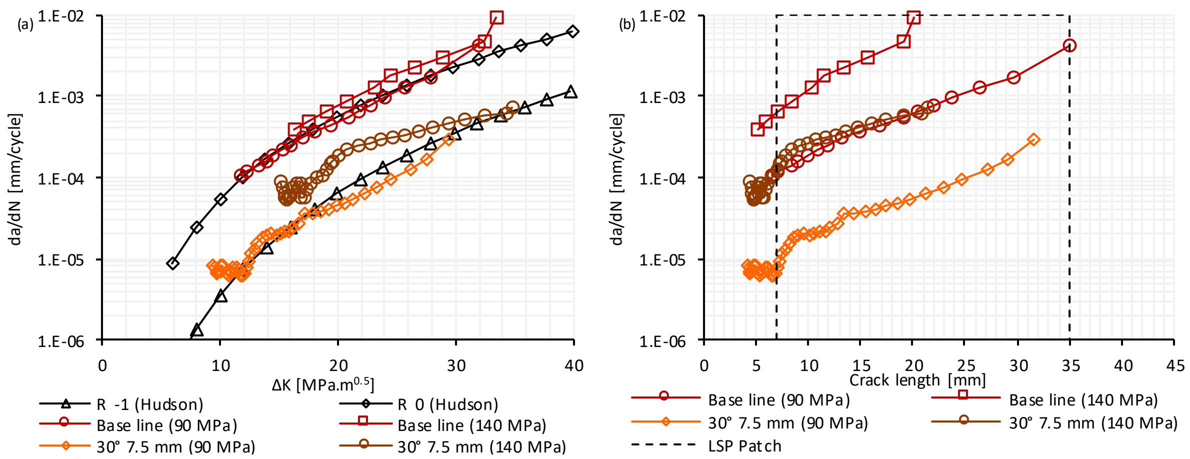

Figure 5.27: Laser peened patch configuration 30° - 7.5 mm (a) crack growth rate (da/dN-ΔK) [4], (b) comparison of crack growth rate and crack length (da/dN-a)

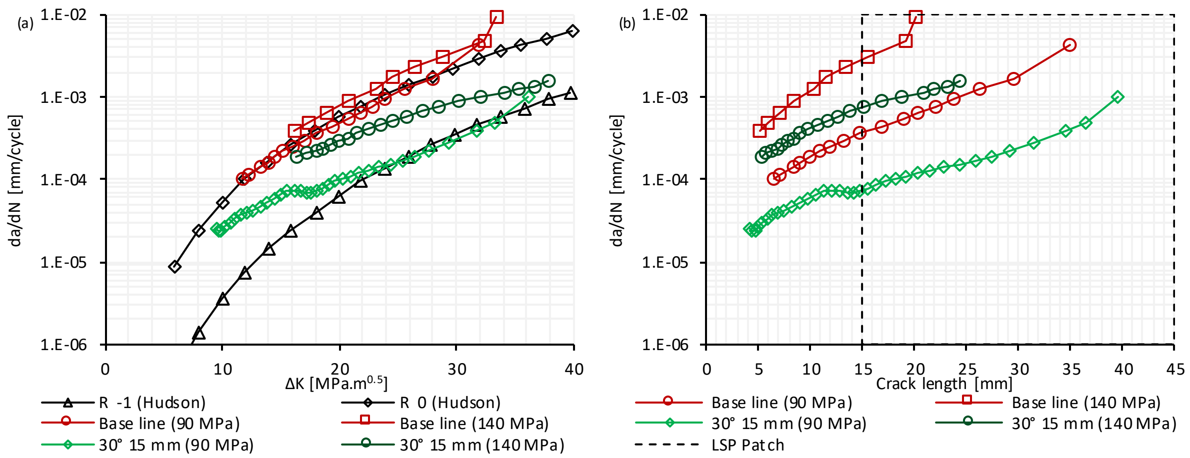

Figure 5.28: Laser peened patch configuration 30° - 15 mm (a) crack growth rate (da/dN-ΔK) [4], *(b) comparison of crack growth rate and crack length (da/dN-a)*

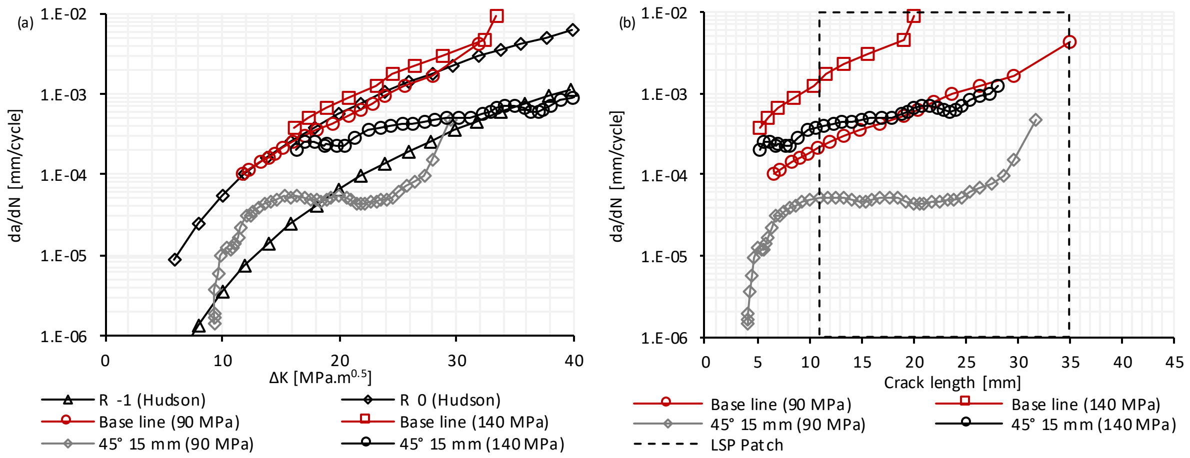

Figure 5.29: Laser peened patch configuration 45° - 15 mm (a) crack growth rate (da/dN-ΔK) [4], *(b) comparison of crack growth rate and crack length (da/dN-a)*

Assessment of Figure 5.25 to Figure 5.29 indicated that the LSP processing in combination with the deformation of the samples resulted in a significant reduction in the fatigue crack growth rate of each LSP sample configuration. The comparison of the experimental results at the lowest loading condition of 9 and 90 MPa and those from Hudson showed that the compressive residual stresses induced by the LSP acted against the applied loading, reducing the crack driving force and resulted in an actual stress ratio of approximately -1. This was plausible as the average residual stress in the LSP patches was found to be compressive and within a value of – 100±15 MPa for all configurations. This would also imply that crack closure effects would likely have occurred during the loading spectrum. The crack growth rate prior to the cracks entering the LSP processed are were slower than that of the base material for all LSP configurations and load cases, implying that compressive stresses were present at those crack lengths.

The out of plane bending would have also influenced the crack growth rate as the applied stress was not uniform throughout the sample thus the load at the crack would have been drastically reduced compared to that seen by the baseline material. The influence of the out of plane bending was reduced by increasing the range of the loading spectrum to 14 and 140 MPa. This was determined as the FCGR in the central unpeened regions of these samples were more similar to that base material. However, even with the increased loading, the LSP compressive stress was capable of reducing the FCGR of all samples.

Assessment of Figure 5.30.a-d indicated that each LSP configuration resulted in a fairly similar FCGR. Initially, the measured FCGR are slightly slower than that of the base material. However, the FCGR tended to reduce due to the compressive residual stress introduced by the LSP. The rotated LSP patches placed a larger amount of the crack path into a significantly compressive residual stress which would naturally reduce the FCGR. The LSP configuration of 30º - 15 mm had the fastest FCGR due to it being the least deflected thus having the lowest out of plane bending acting to reduce the loading.

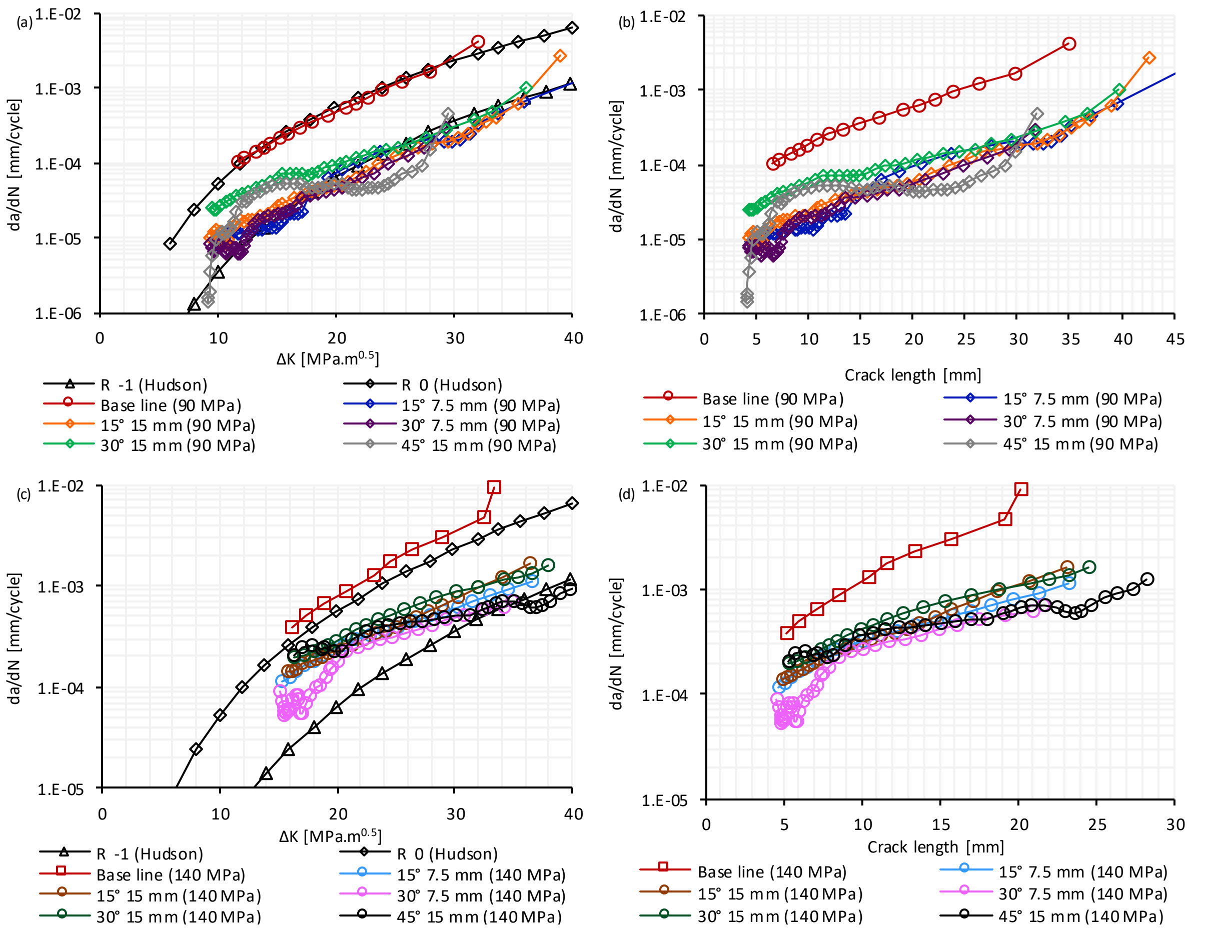

Figure 5.30: Comparison of the all tested laser peening configurations (a) crack growth rate (da/dN-ΔK) at 90 MPa [4], (b) comparison of crack growth rate and crack length (da/dN-a) at 90 MPa, (c) crack growth rate (da/dN-ΔK) at 140 MPa [4], (d) comparison of crack growth rate and crack length (da/dN-a) at 140 MPa

The overall trend of the FCGR was that the LSP processing produced a complex residual stress field which when combined with the effects of out of plane bending likely produced a stress field that was compressive in nature along the width of the sample. This compressive stress would result in a K_{res} value that would actively reduce the overall ΔK, thus reducing the crack growth rate and increasing the overall crack growth life of the samples. In each LSP configuration, a slight slope change was observed in the da/dN plots when the crack entered the respective LSP regions. This indicated a further slowing of the crack due to the higher magnitude compressive residual stress in the LSP regions.

5.3.4. Laser Shock Peened fatigue crack trajectory

The experimental fatigue crack trajectory of each sample (both sides of the starter notch) were captured using a digital optical travelling microscope. Multiple images were taken along the crack path and later stitched together using the methodology defined by Preibisch et al. [7]. Figure 5.31.a-f. provided an example of the captured trajectories at both loading conditions (R 0.1, σ_{max} 90 MPa & 140 MPa) for each sample configuration. The crack trajectories on each side of the notch were recorded, with Figure 5.31 showing the best case deviation per LSP side of the sample. Scale markers that represent a 1 mm spacing were included in addition to the vertical scribe marks (equally spaced at 1 mm). The samples approximate horizontal centre line and starting edge of the LSP patches was designated in each image to provide a reference for the orientation of the various cracks. Figure 5.31.a showed the baseline crack trajectory which indicated that the crack tended to grow fairly straight and predominantly perpendicular to the applied loading. Figure 5.31.b-f. showed that the presence of the LSP residual stress patches did affect the trajectory of the cracks as they tended to deviate towards the inclined LSP patches. The deviation was most noticeable in Figure 5.31.c (15°-15mm) where the cracks tended to propagate fairly straight and then began to deviate upon nearing the LSP patches. In all of the LSP configurations, the LSP residual stress was not capable of producing a significant deviation of the cracks which would be considered comparable to the turning of the crack as achieved by fuselage structural tear straps.

Figure 5.32.a-e showed the averaged measured crack trajectories for all tested sample configurations and LSP patch orientations. The presented trajectories were determined as the average of the surface trajectories on both sides of the samples (convex and concave LSP surfaces). The start of the LSP patches was indicated by the inclined dashed lines in the figures. Slight misalignment of the patches occurred during LSP processing as each sample had to be reoriented and clamped between the application of the next LSP layer. The largest crack deviations were observed with the LSP configurations

which were placed further away from the starter notch. The crack deviation then tended to reduce back towards a perpendicular path upon entering the LSP patches. The fundamental mechanism behind this was expectedly due to the presence of a higher mode II loading condition which is established by the transverse residual stresses in the area between the LSP patches, and this is confirmed in later chapters.

5.3.4.1. Fracture surface

An example of the fracture surface of each LSP orientation and loading configuration was provided in Figure 5.33. The main purpose of this figure was to show that the observed crack deviations were not of the consequence of the crack shape transformation from a flat to a slanted surface or in regards to crack growth mode transition from tensile to shear. Typically, the beginning of the transition process is associated with the formation of shear lips that are oriented at 45° from the original flat crack surface. This was illustrated on the base material. The 45° inclination of the crack surface could be misconstrued as actual crack deviation. In a number of the LSP configurations, the crack deviations occurred within the region of flat and stable crack growth thus indicating the deviations were the consequence of the residual stress rather than the underlying fracture mechanisms.

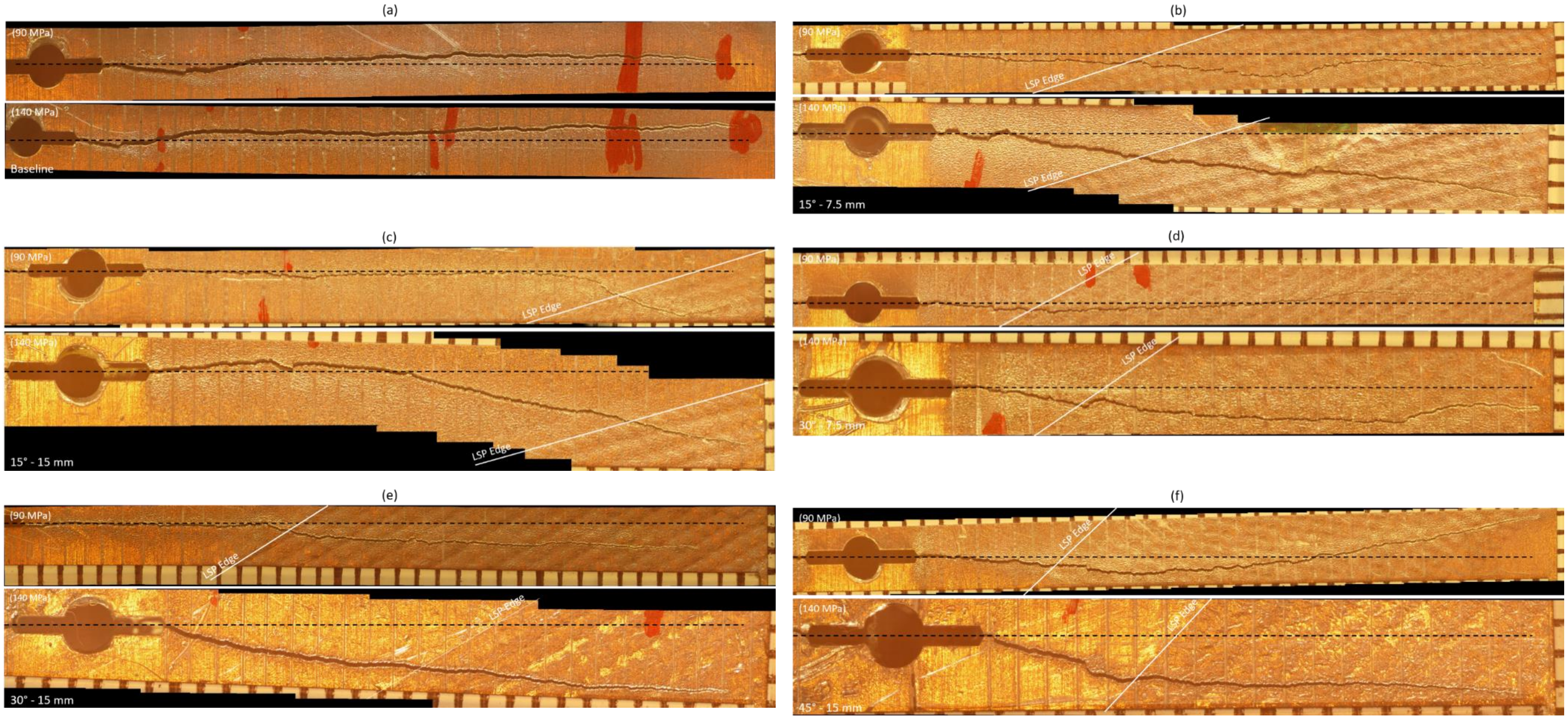

Figure 5.31: Example of the measured crack trajectory at each loading condition (a) baseline, (b) 15°-7.5mm, (c) 15°-15mm, (d) 30°-7.5mm, (e) 30°-15mm, (f) 45°-15m

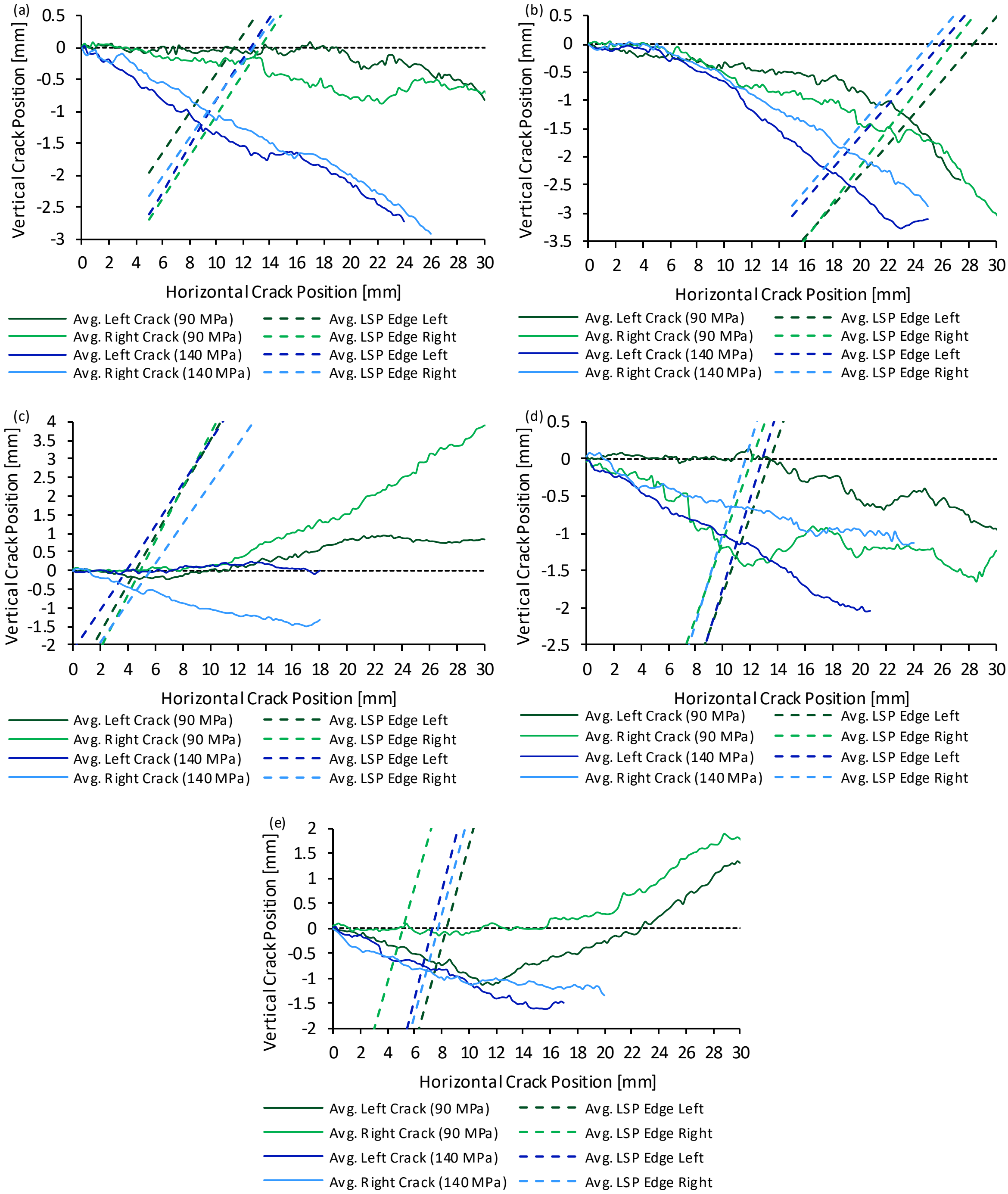

Figure 5.32: Averaged crack trajectory measured on both external surfaces with the dashed lines indicating the averaged starting edge position of the laser peening patches (a) 15°-7.5mm, (c) 15°-15mm, (d) 30°-7.5mm, (e) 30°-15mm, (f) 45°-15mm

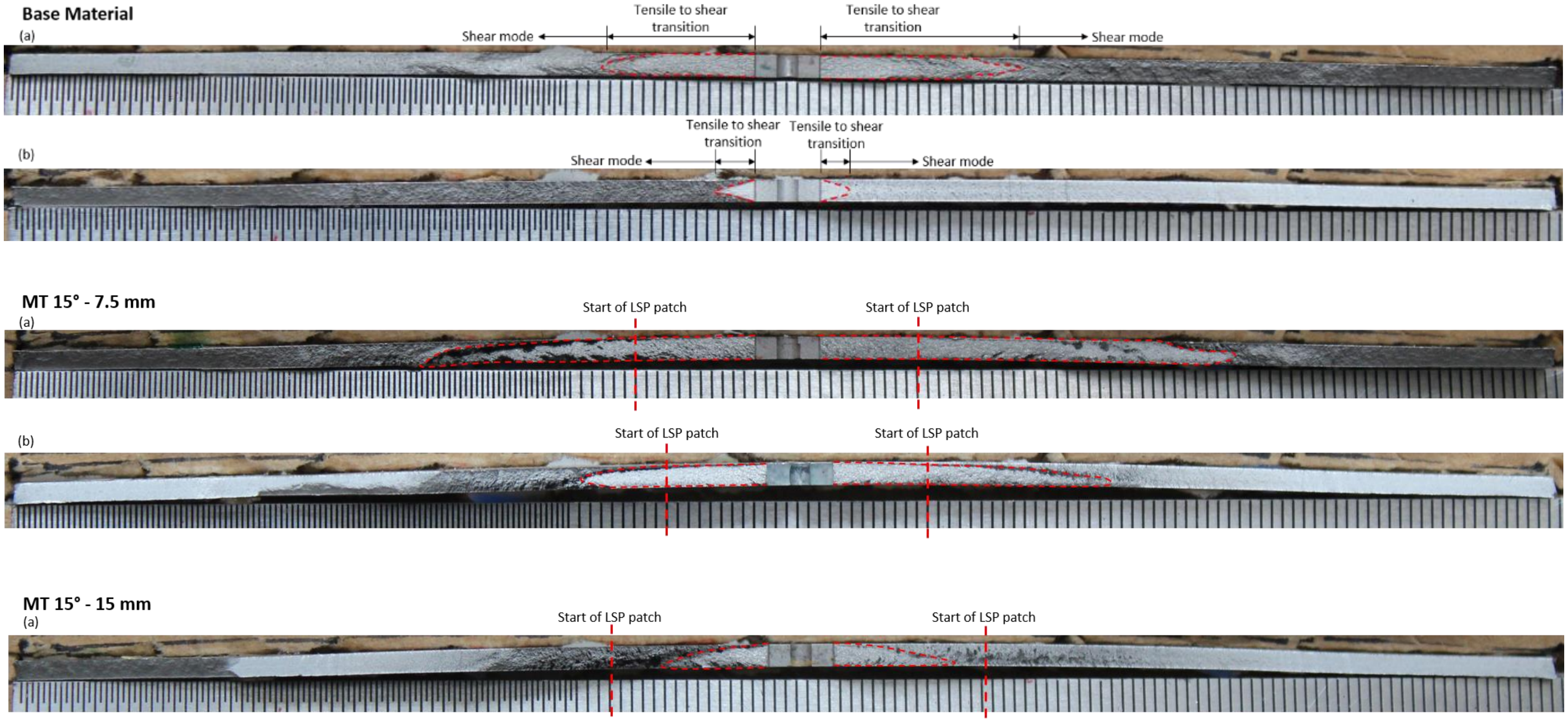
Base Material
(a)
Tensile to shear transition
Tensile to shear transition
Shear mode
Shear mode
(b)
Tensile to shear transition
Tensile to shear transition
Shear mode
Shear mode
MT 15° - 7.5 mm
(a)
Start of LSP patch
Start of LSP patch
(b)
Start of LSP patch
Start of LSP patch
MT 15° - 15 mm
(a)
Start of LSP patch
Start of LSP patch

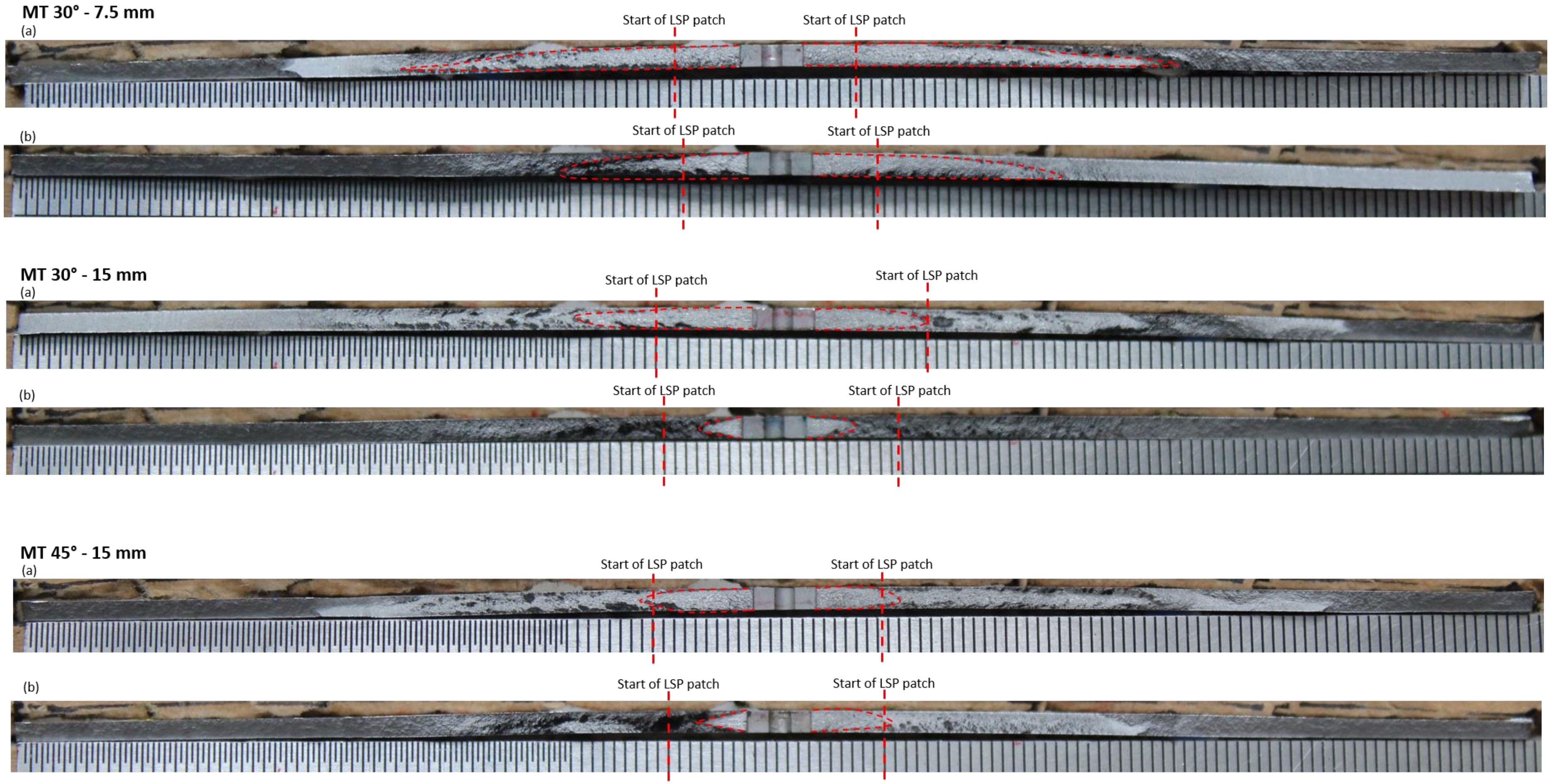

Figure 5.33: Fracture crack surface variation due to crack growth mode transition for all sample configurations (a) σ_{max} 90 MPa, (b) σ_{max} 140 MPa

5.4. Numerical modelling of rotated Laser Shock Peened samples

Accurate modelling of crack growth in complex residual stress fields is a critical tool for the further development and implementation of LSP in advanced aerospace applications. This section outlines the used numerical modelling strategy and results that provided additional understanding to the underlying mechanisms of the fatigue crack growth life extension and the crack deviation. The main aim of this modelling work was to predict the following:

1. Accurately predict the induced residual stress within the MT sample 30^{o}-15mm. This sample was selected as the most experimental residual stress data was available for this configuration.
2. Characterise the fundamental mechanisms associated with the deviation of the fatigue crack whilst propagating through a complex residual stress field.

To achieve the aims of this study, accurate predictions of the LSP residual stress, sample deformation and the per-crack-length stress intensity factors were required. An adaptation of the three-step modelling approach that has been successfully used by Pavan [5], Busse [2] and Smyth [8] to predict SIFs in LSP residual stress fields were used. Figure 5.34 illustrated the three-step FE modelling approach used to determine the influence of the LSP residual stress on the propagating crack and the overall sample's fatigue life. Step one required the accurate prediction of the LSP residual stress through the use of an optimised eigenstrain approach. The second step consisted of a fatigue crack growth simulation, where the crack front was incrementally advanced along with the sample and through the residual stress field. Finally, the SIF from step two was used in the prediction of the fatigue crack growth life and crack trajectory.

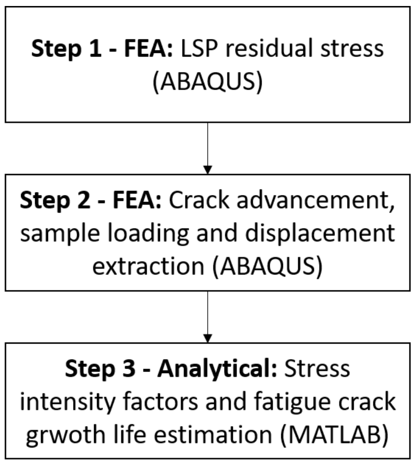

Figure 5.34: Three-step finite element modelling procedure to determine the influence of the rotated laser peening residual stress fields on the fatigue crack growth, crack growth life estimation and crack trajectory

The first two steps were completed using the commercial finite element software ABAQUS 6.14 [9] and the final step was completed in the commercial software MATLAB 2020b [10].

Although the thickness of the samples would inevitably result in the development of a plane stress condition, full 3D models of the samples were carried out to accurately determine the full residual stress field. Although a 3D model was significantly heavier from a computational perspective, it was preferred for the residual stress simulation as it represented a closer approximation of the real samples. Figure 5.35 illustrated the full 3D model of the LSP sample. The green rectangles indicated the positions of the respective LSP patches.

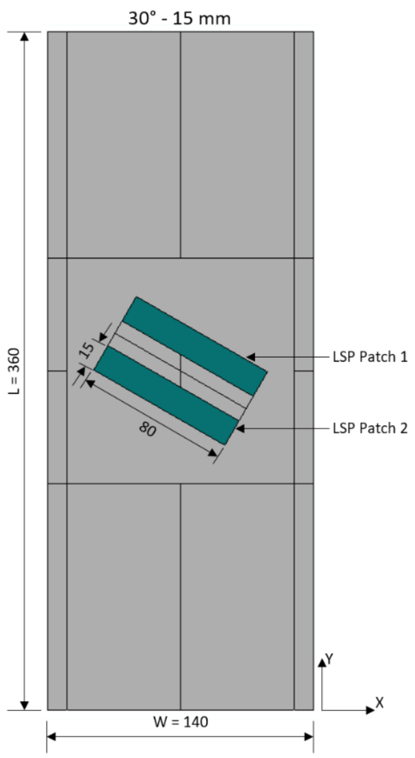

Figure 5.35:Illustration of the residual stress model

The rotated MT samples were required to be modelled as a full component as no planes of symmetry naturally occurred in these configurations. The material behaviour used throughout the FE models was linear elastic with the bulk properties listed in Table 3.3. Static general solvers were used in both the residual stress and fracture simulations, with the inclusion of the ABAQUS Nlgeom feature enabled (this includes nonlinear effects due to large sample displacements).

5.4.1. Residual stress input model

As an alternative to the modelling of the LSP process by simulating each laser shot, as done in chapter 4, the residual stress field and resulting sample deflection were introduced through an iterative algorithm method. The proposed algorithm method used an optimised eigenstrain approach which was adapted from the methods presented by Hill et al. [11], Correa et al. [12] and Coratella et al. [13].

In this method, each application of the LSP process or LSP layer was replicated by the application of a set of optimised eigenstrain values. The residual stress and final distorted equilibrium shape were established over four consecutive simulations as illustrated in Figure 5.36. This effectively replicated the experimental LSP processing in which the residual stress was built up through multiple applications of the LSP processing. It was clear from the figure that the modelled sample undergoes a similar "to and fro" deformation as experimentally observed during the LSP processing. The eigenstrains are applied simultaneously to both patches and are only effective in the LSP processed area. This strategy allowed the residual stress in the surrounding areas to occur naturally as the component achieves equilibrium.

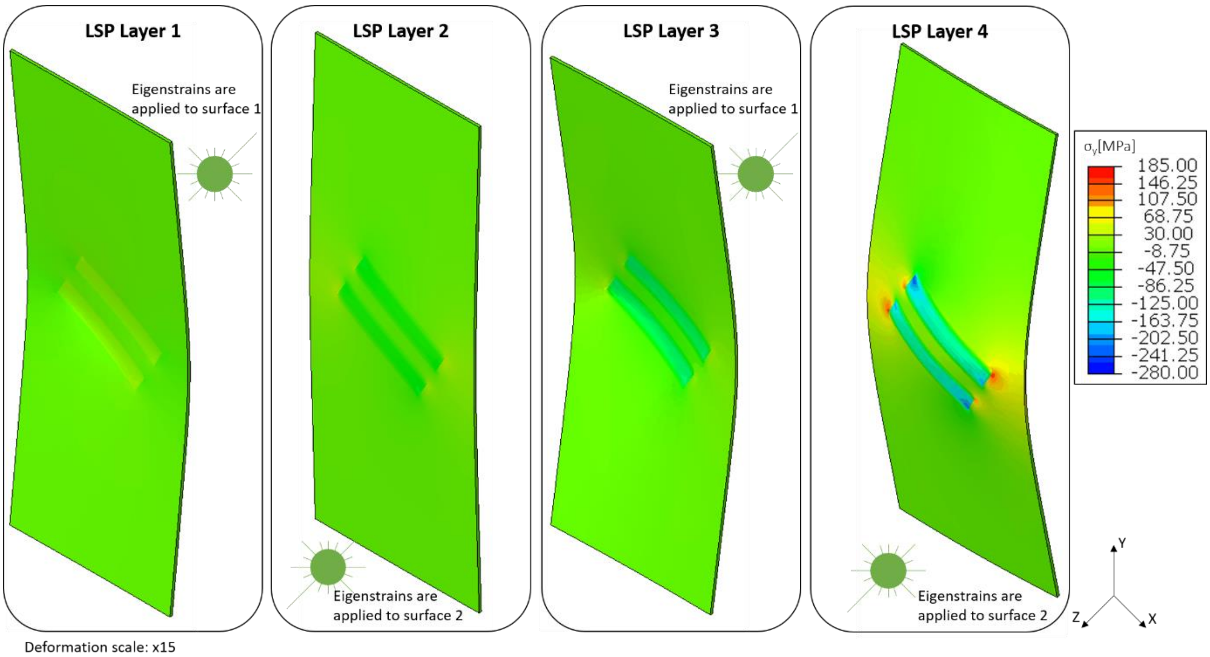

Figure 5.36: Illustration of the multi-layer eigenstrain residual stress simulation that replicates each experimental application of the laser peening

The LSP induced eigenstrains were introduced as anisotropic thermal expansion coefficients, α_{LSP}. The resulting stress field was achieved by applying a unit temperature variation (ΔT = 1) to the model. After the thermal simulation, the elastic strains in the LSP areas are $\varepsilon_e = \alpha_{LSP} \cdot \Delta T$, the sample then elastically deformed and the residual stress distribution per layer was achieved. The expansion coefficients were introduced into the models with the aid of a multi-staged ABAQUS user subroutine USDFLD. This is a FORTRAN program that allows the user the functionality to define material properties (thermal expansion coefficients) at individual elements within the relevant section.

The initial estimation of the eigenstrains was obtained through the use of equation 2-20 and the assumption that plane stress conditions occurred in the samples. The initial estimate of $\sigma_{LSPx}(z)$ and $\sigma_{LSPy}(z)$ was based on the measured residual stress provided in Figure 5.13 and then undergoes a series of value refinements to achieve the targeted residual stress profile at the various control points on the sample. Due to the objectives of this work, both orthogonal components of the residual stress had to be considered in this model. The model's residual stress optimisation steps can be further explained as followed and illustrated in Figure 5.37:

1. The targeted residual stress at the centre ($\sigma_{meas,centre,x}$ and $\sigma_{meas,centre,y}$) of the sample and in the LSP regions ($\sigma_{meas,LSP,x}$ and $\sigma_{meas,LSP,y}$) are defined according to the experimental residual stress measurements. The values vary according to the residual stress distribution through the thickness of the sample.
2. An initial estimate of $\sigma_{LSP,x,n}$ and $\sigma_{LSP,y,n}$ for each layer of the LSP processing was made, where *n* refers to the applied LSP layer (n=1,2,3,4). The eigenstrain profiles are then calculated for each LSP layer, $\alpha_{LSP,x,n}$, $\alpha_{LSP,y,n}$ and $\alpha_{LSP,z,n}$ and applied to the standard ABAQUS model through the subroutine.
3. The four sequential models are run by applying the unit temperature change, with the results of the previous simulation acting as the starting equilibrium state for the current simulation of the current LSP layer.
4. The final simulated residual stress field at the control points ($\sigma_{sim,centre,x}$ and $\sigma_{sim,centre,y}$, $\sigma_{sim,LSP,x}$ and $\sigma_{sim,LSP,y}$) was extracted and compared to the measured residual stress.
5. An optimisation loop that compares the final balanced residual stress with the measured stress field was initiated. On each repetition of the loop, the values $\sigma_{LSP,x,n}$ and $\sigma_{LSP,y,n}$ per layer are updated until the averaged through-thickness values of $\sigma_{sim,LSP,x}$ and $\sigma_{sim,LSP,y}$ are within 10 MPa of the $\sigma_{meas,LSP,x}$ and $\sigma_{meas,LSP,y}$ profiles. Additionally, the total sample distortion was required to be within the boundaries of the three experimentally measured shapes of the samples along the three control lines.

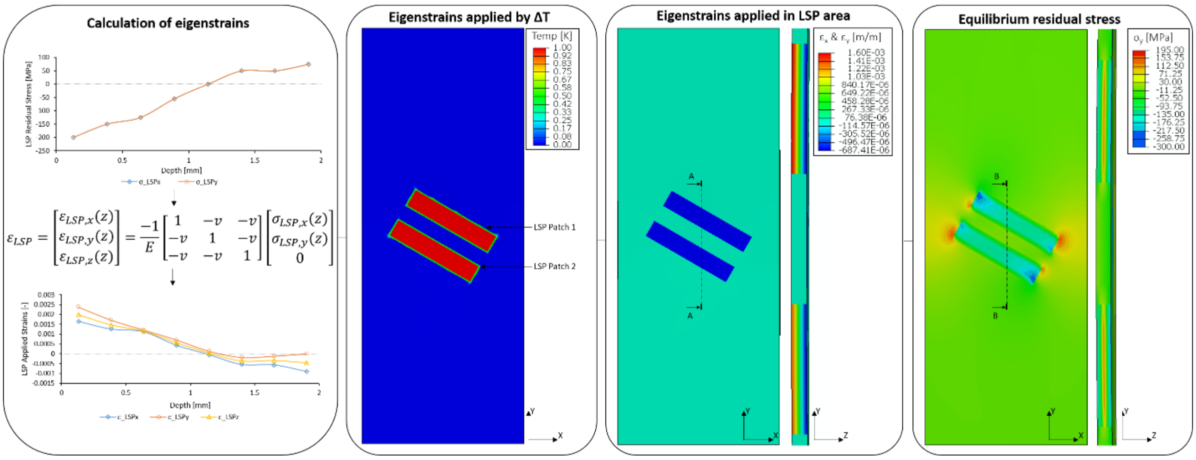

Figure 5.37: Illustration of the associated steps of the eigenstrain residual stress modelling technique

The comparison between the measured and the FE generated residual stress was carried out at specific control points located at the centre of the sample and in the LSP patches, as shown in Figure 5.38. The central control point was used as a reference to ensure that the balancing residual stresses which were determined during the simulation agreed with the experimental measurements. Additionally, the final FE sample deformation was compared to the experimental deformation along the three longitudinal control lines. The alignment of the deformation verified that the overall balanced solution was correct not only at the control points but also over the entire model's volume. The compared residual stress that was taken from the model was averaged over a similar surface area as the sampled area in the experimental hole drilling measurements.

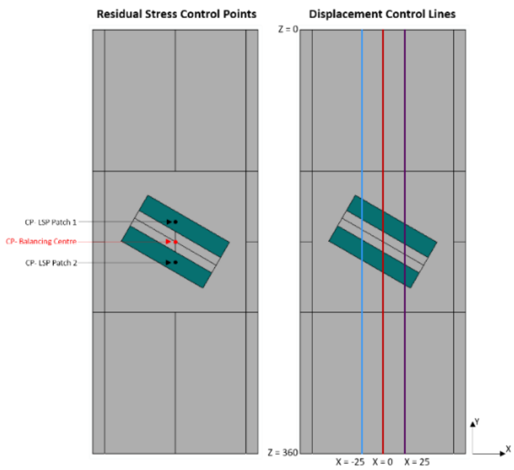

Figure 5.38: Schematic of residual stress control points and distortion measurement lines

The used mesh for the residual stress modelling was kept consistent throughout this step. The model had to be portioned to apply the localised temperature variation to the LSP areas, allow for the placement of appropriate boundary conditions and to allow for mesh refinement in specific areas of interest, as shown in Figure 5.35.

Eight-node linear brick elements with reduced integration (C3D8R) were used throughout. The element size within the LSP region was fixed at 1.5 mm with seven elements through the thickness (0.3 mm). A swept hexagonal structure was allowed in the surrounding LSP area. This was used as a transition area to allow for a structured mesh in the adjacent areas. An overview of the mesh structure was provided in Figure 5.39.a. This mesh size was specified based on previous simulation results that showed that further refinement resulted in a variation of the results of less than 2%. Further refinement was avoided as the residual stress optimisation loop was only stopped once the simulated results sufficiently matched the experimental results. Remeshing of the distorted model would be required before conducting the SIF analysis. The results from the final residual stress model are imported and effectively interpolated to the corresponding element points on the new mesh thus providing a further opportunity to refine the mesh before the fine analysis step.

As a full model was simulated, strategic boundary conditions had to be applied to the model to constrain the model within the domain. These boundary conditions do not influence the formation of the residual stress but rather just fixes the model in space. Figure 5.39.b. provided a schematic representation of the boundary conditions as they were applied to the model.

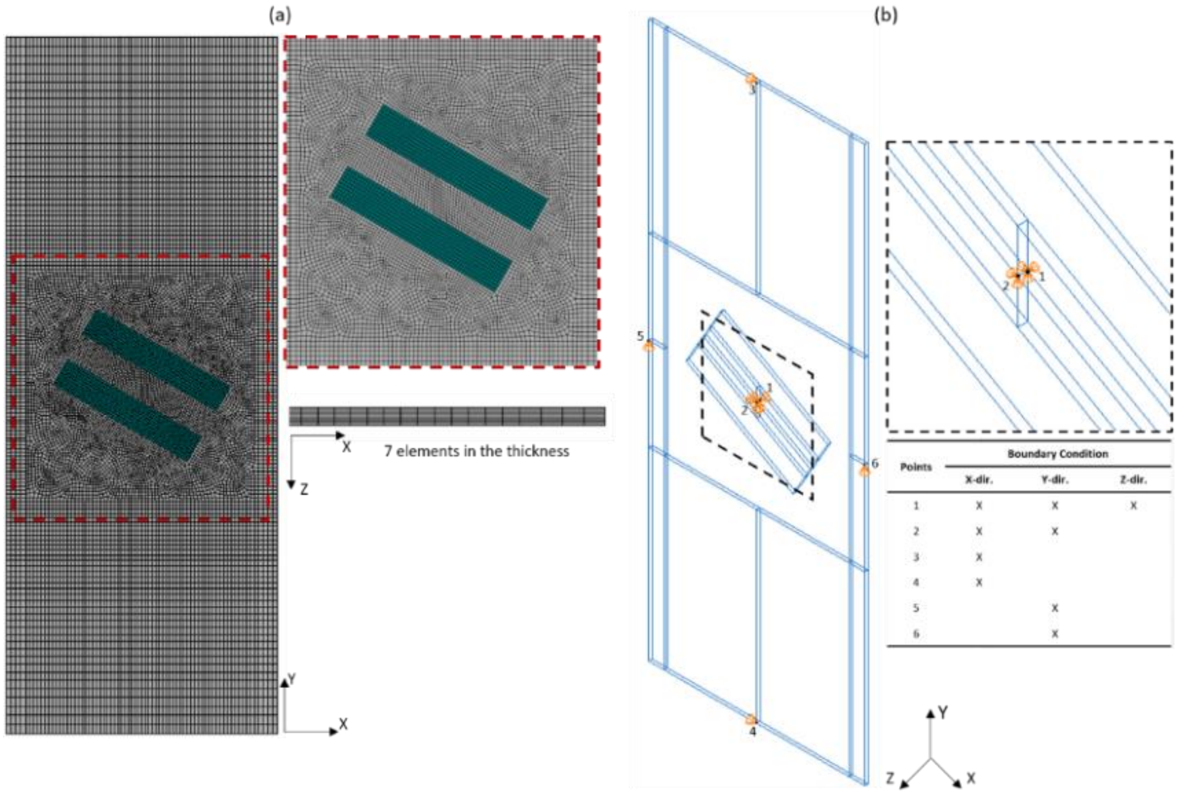

Figure 5.39: Residual stress modelling, (a) full mesh structure, (b) applied boundary conditions

5.4.1.1. Validation of residual stress model

The model was judged to have converged to its optimal solution once the specific criteria were met, as defined in section 5.4.2.1. Due to the nature in which the residual stress was achieved in the model, localised optimisation of the stress field was difficult. The multi-objective optimisation of the model increased the difficulty to obtain the ideal solution at every position in the model. Although the results were judged to be representative and accurate some consideration must be made for variability in the stress field between samples. The variation in the deflection measurements of each sample under the sample LSP configuration in Figure 5.8 provided a good example of this variation. This possible deviation was inherent in the LSP processing of thin metallic structures.

The residual stress FE model was validated according to the acquired experimental data at the respective control locations. Figure 5.40.a-b provided the comparison between the experimental and simulated through-thickness residual stress distribution in the LSP patches and at the centre of the sample. The thin clad layer was not considered in this model as it was assumed to have little structural consequence. This was the cause of the poor correlation of the stress near the surfaces. A good correlation in the LSP residual stress was achieved in the first half-thickness of the model. The model predicted a higher magnitude tensile region in the core of the material. To achieve the desired averaged through-thickness residual stress, the optimisation algorithm increased the magnitude of the compressive stress in the remaining thickness.

Table 5.7 listed the average through-thickness residual stresses at the two control points. Although an exact replication of the stress profiles was not achieved in the simulations, the models were judged to have converged upon being within 10 MPa of the experimental results.

Table 5.7: Averaged through-thickness residual stress comparison at control locations.

Control point	Experimental		Simulated	
	σ_x [MPa]	σ_y [MPa]	σ_x [MPa]	σ_y [MPa]
LSP patch	-109	-79	-99	-72
Sample centre	22	-7	33	-17

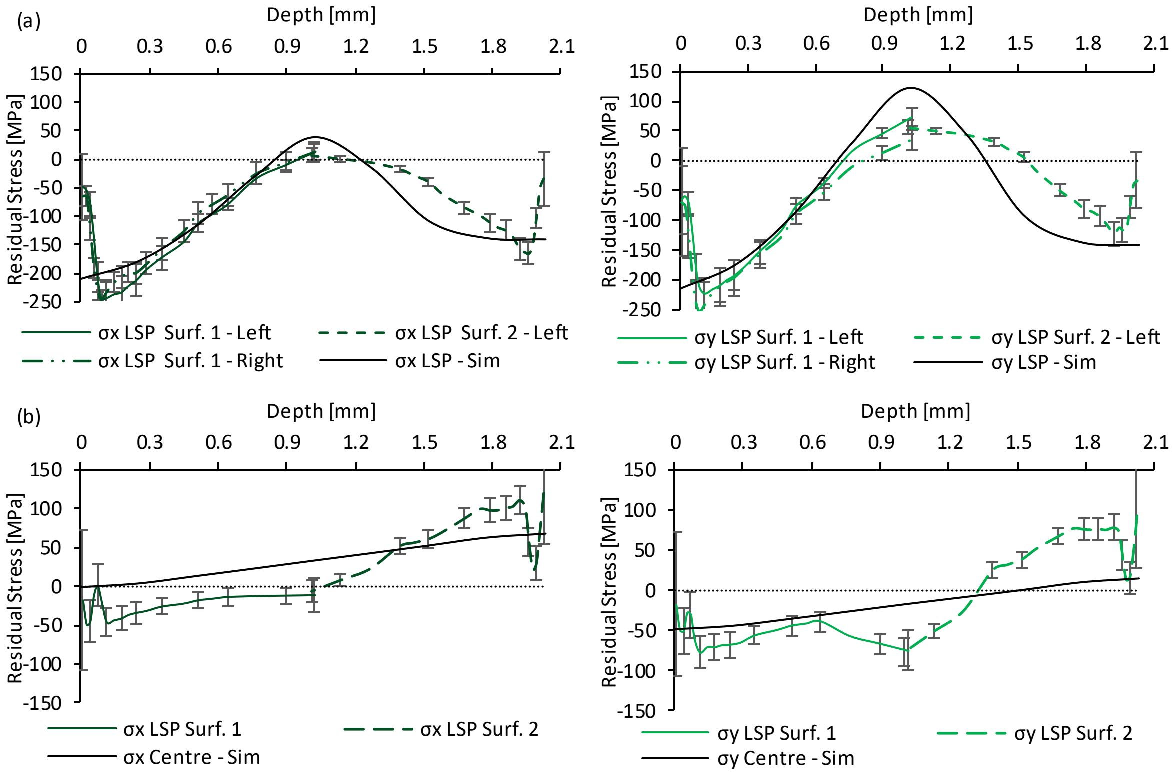

Figure 5.40: Comparison of the through-thickness residual stress at the simulated control locations in orthogonal directions (a) laser peening patch, (b) centre of the sample

The sample distortion was used to validate that the total balanced residual stress field correlated to what was observed in the experimental sample. As a large variation in the experimental deflection of the samples was observed, the final simulated deflection was judged appropriate if all control positions were within the experimentally measured variation. Figure 5.41. provided the comparison of the simulated and experimental deflection.

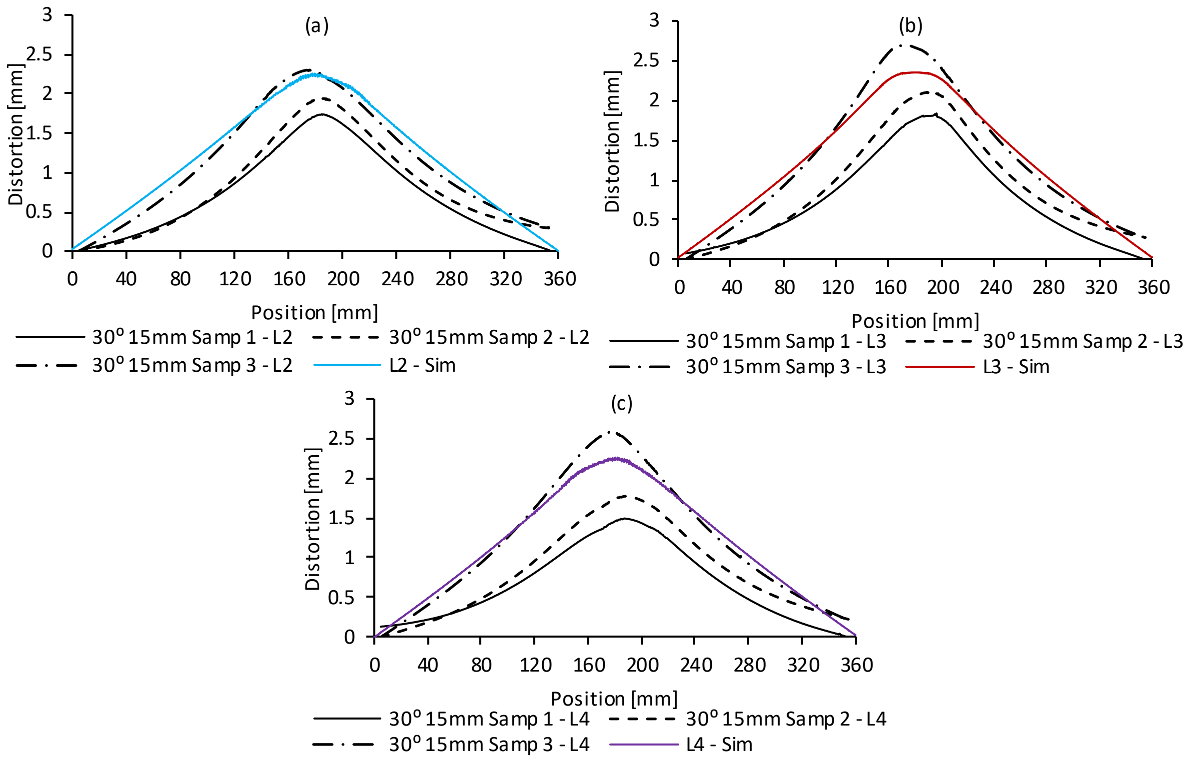

Figure 5.41: Comparison between experimental and simulated sample distortion, (a) experiment line 2, (b) experiment line 3, (c) experiment line 4

Figure 5.42 showed the averaged through-thickness residual stress along the horizontal centre line of the sample in the transverse and longitudinal directions. The averaged through-thickness experimental residual stress has been included for comparison. The LSP experimental average was shifted to the centre of the LSP patch based on the assumption that the stress was consistent throughout. The validated simulated residual stress showed that the averaged longitudinal stress between the LSP patches was compressive. This was in line with the experimental observations seen in FCGR testing, where the LSP crack growth rate was significantly longer than that of the base material. Additionally, Pavan [5] and Busse [2] (LSP patches were applied vertically along the sample and were perpendicular to the crack propagation direction) both observed an acceleration of the FCGR in the region between the patches due to the presence of the balancing tensile residual stresses. In the present LSP configuration, the tensile balancing residual stresses are shifted toward the extremities of the LSP patch and sample, as seen in Figure 5.43, resulting in a residual stress field that was more conducive to the fatigue crack growth life extension of the sample.

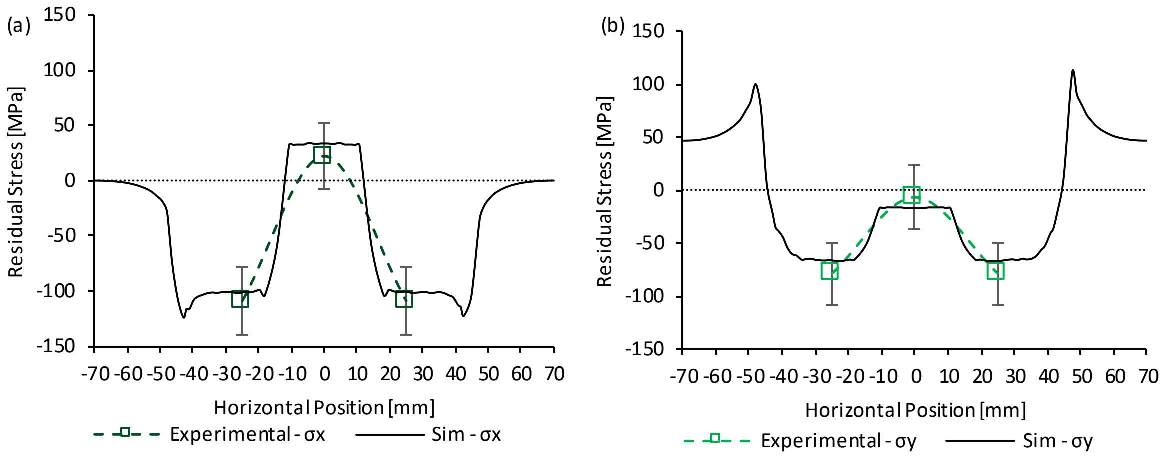

Figure 5.42: Simulated averaged through-thickness residual stress across the horizontal centre of the sample (a) transverse residual stress (σ_x), (b) longitudinal residual stress (σ_y)

The severity of the sample deflection of the 3D model of the LSP samples resulted in significant errors in the behaviour of the sample under applied loading during linear elastic fracture mechanics simulations. This issue caused the simulations to continuously fail or result in unrealistic deflection. No combination of the boundary conditions could be determined which resulted in the accurate behaviour of the deflected sample under the application of the external loading. This issue was exacerbated by the fact that symmetrical boundary conditions could not be applied to resolve the issue. To counteract this, the 3D residual stress model was converted to a 2D model which replicated the 3D stress field as a through-thickness average. This method of representing the stress field as the averaged stress field was used by Busse [2] and Symth [8]. The move to a 2D model removed the out of plane deflection resulting in a simpler model that was still representative of the sample's residual stress field. It was noted that the out of plane deflection would inherently apply an additional bending moment as the sample deflected due to the tension-tension loading. This extra loading would likely have influenced the combined loading that the samples were exposed to during the experimental FCGR testing but was mitigated by using the least deflected sample.

As the deflection was no longer a considered factor, the ABAQUS SIGINI subroutine was used to transfer the averaged through-thickness 3D stress field to the 2D representative model. Figure 5.43 provided a comparison of the stress field in two and three dimensions. Figure 5.43.a showed the contour comparison of the averaged 2D residual stress and 3D surface residual stresses (2D was lower as the 3D contour plot shown has not included the sub-surface tensile residual stress core). This figure indicated that the 2D model adequately represented the characteristics of the 3D model and the balancing stresses adjacent to the LSP patches. Figure 5.43.b was the most appropriate comparison as it showed a good correlation between both models with the experimental data.

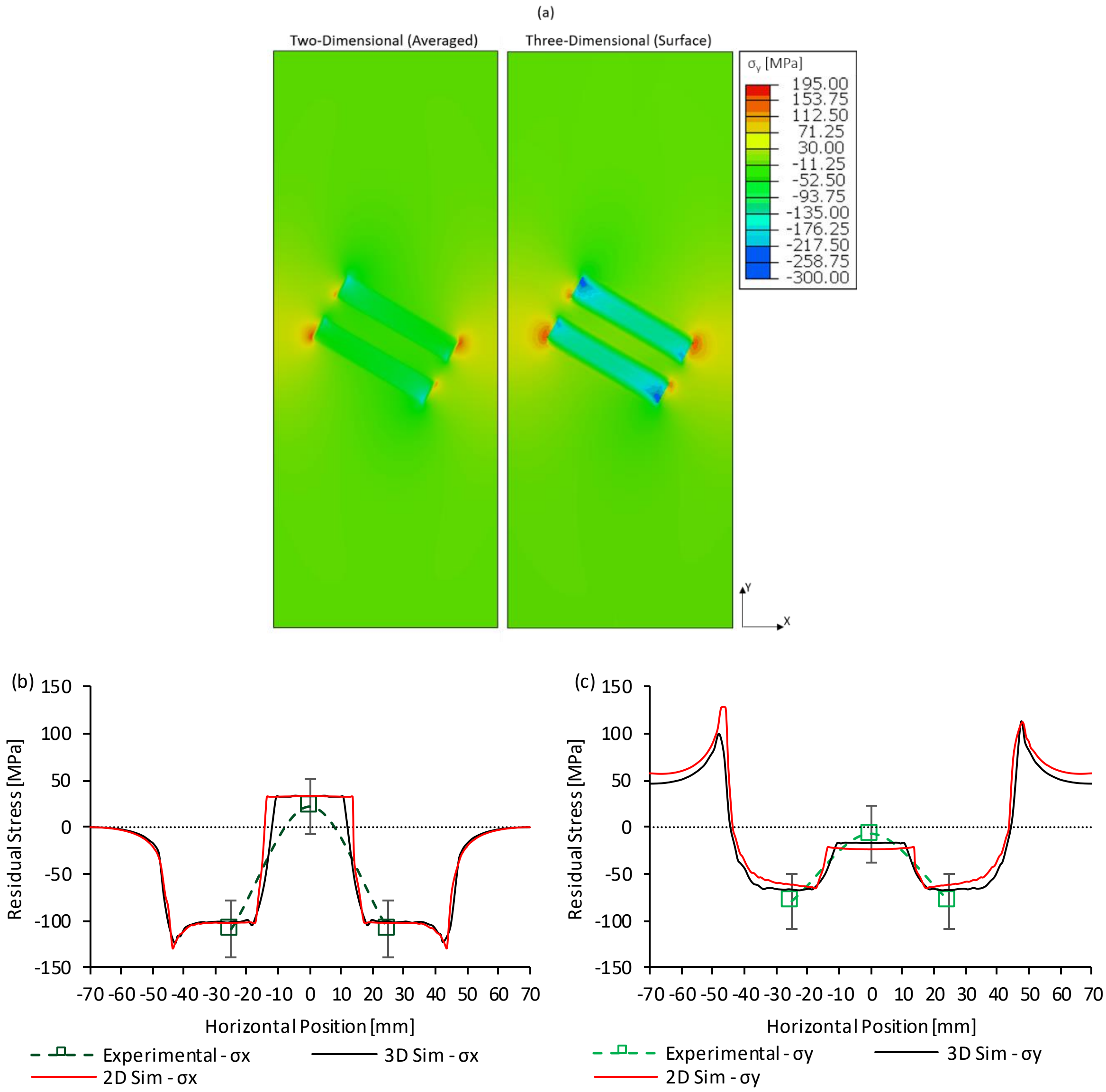

Figure 5.43: Comparison of two and three-dimensional residual stress fields (a) contour comparison of longitudinal residual stress, (b)averaged transverse residual stress (σ_x), (c) averaged longitudinal residual stress (σ_y)

The same boundary conditions, geometry partitioning and mesh seeding strategy were used to achieve an equivalent two-dimensional mesh as shown in Figure 5.39. Plane stress elements with reduced integration (CPS4R) elements were used to replicate the residual stress.

5.4.2. Fatigue crack growth model

The second step of the presented finite element strategy was the simulation of the linear elastic fracture of the sample in the residual stress field.

5.4.2.1. Introduction of residual stresses into the linear elastic fracture mechanics model

The application of the LSP residual stress resulted in the two-dimensional deformation of the simulated MT geometry. To account for this in the Linear Elastic Fracture Mechanics (LEFM) simulation, the deformed body was imported from the results file of the residual stress model. ABAQUS imports the deformed structure as an orphan mesh that was converted to a solid geometric body using the built-in feature “2D Part from 2D Mesh”. However, the boundaries of body geometry were defined by many small increments which were associated with the converted orphan mesh. The ABAQUS “Virtual Topology” feature was used to merge all geometric feature lengths which were smaller than 50 mm. This resulted in the boundaries of the geometry being defined as single continuous edges. This increased the ability to re-mesh the structure to achieve a consistent and structured mesh that was appropriate for the simulation of the crack growth in the residual stress field.

The contribution of the residual stress to the total stress intensity was defined as K_{res}. To evaluate this factor, the 2D residual stress field was mapped onto the re-meshed deformed structure using the ABAQUS command “Un-balanced Stresses”. This feature propagates the stress field from one mesh structure to another by providing integration points for the stress to be determined on the new mesh. This was done at the initial stage of the simulation and an additional standard step was included to allow for the stress field to achieve equilibrium. By defining a relatively small mesh seed, there was no significant loss in detail of the stress field due to the interpolation on the new mesh. Figure 5.44 provided a comparison of the residual stress from the initial mesh structure and the equilibrated mapped residual stress. An excellent correlation in the stress fields was achieved between the mesh structures with this method. The LEFM Sim stress profile was then imported at the start of each simulation of the various crack lengths and allowed to achieve equilibrium before any application of additional forces.

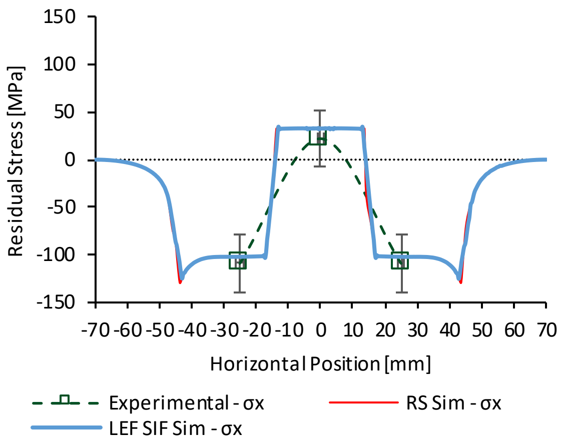

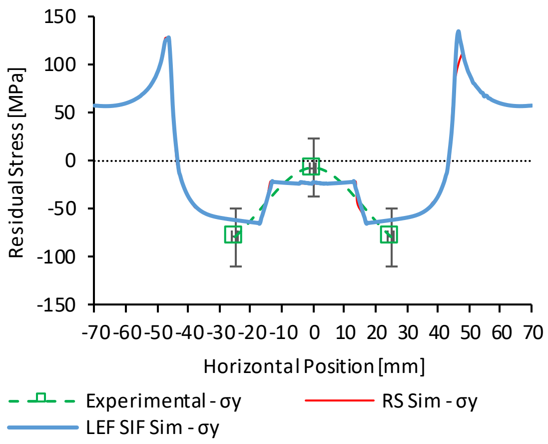

Figure 5.44: Comparison of the residual stress along the horizontal centre line for the residual stress and fracture mesh structures

5.4.2.2. Stress intensity calculation using the displacement extrapolation method

The stress intensity factors were determined based on the displacement extrapolation method defined by Zhu [14] and Zhu [15]. There are several alternative methods to determine the SIF in FEM, such as the J-integral method, virtual crack closure and eXtended Finite Element Method (XFEM). The XFEM is mesh independent but this method cannot be used in the presence of a residual stress field due to its path independence. The J-integral method is path-dependent as the residual stress is accounted for as an initial strain field, but this method requires a specific mesh structure to accurately define the singularity at the crack tip [16]. The virtual crack closure method, which calculates the SIF from the strain energy release rate, could not be easily implemented as the force at the crack tip was not easily determined due to the lack of symmetry conditions in the current sample configuration [17].

The displacement extrapolation method was selected due to simplicity and reduced demand on the mesh structure. The crack tip displacement field can be defined by equations 2-44 to 2-46. This method can be used to determine the stress intensity at a crack tip based on the respective displacement of the material points that fall along the crack surface under mixed-mode loading, these are defined by Equation 2-1.

$$K_I = \sqrt{2\pi}\frac{G}{1+\kappa}\frac{|\Delta v|}{\sqrt{r}}$$
$$K_{II} = \sqrt{2\pi}\frac{G}{1+\kappa}\frac{|\Delta u|}{\sqrt{r}} \qquad \textit{Equation 5-1}$$
$$K_I = \sqrt{2\pi}\frac{G}{1+\kappa}\frac{|\Delta w|}{\sqrt{r}}$$

Where G was the shear modulus of the elastic material and κ was defined by Equation 5-2. Due to the nature of the experimental samples (the thickness was an order of magnitude smaller than other dimensions), it was assumed that plane stress conditions applied throughout.

$$\kappa = \begin{cases} 3 - 4v & Plane\ strain \\ \dfrac{3 - v}{1 + v} & Plane\ stress \end{cases}$$ *Equation 5-2*

Figure 5.45 provided a schematic representation of the relative displacement of one crack face with respect to its corresponding point on the alternative crack surface. The relative displacements for points K and M would be, $|\Delta v| = |v_k - v_m|$ and $|\Delta u| = |u_k - u_m|$ [15].

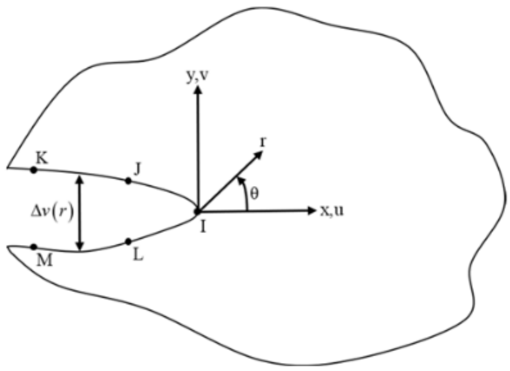

Figure 5.45: Schematic of relative displacement of material points on the crack face [15]

The actual SIF at the crack tip can then be extracted by determining the y-intercept of the plot of the relative SIF and distance from the crack tip, as shown in Figure 5.46. Only the linear region of the relative stress intensity factors needed to be taken into account in determining the total stress intensity.

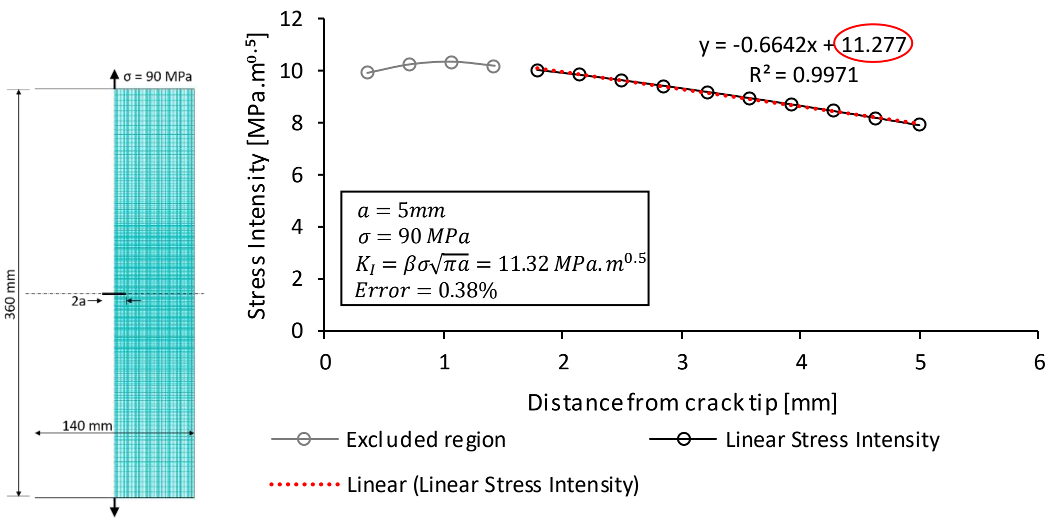

Figure 5.46: Two-dimensional example of the displacement extrapolation model

5.4.2.3. Boundary conditions and crack advancing scheme

The external load was applied to the upper and lower horizontal edges of the samples as a distributed pressure load that only acted in the vertical direction. For each crack length both minimum and maximum loading conditions (σ_{min} and σ_{max}) were applied to determine the corresponding stress intensity factors.

As a full model was used, the sample was constrained in the x-direction at the two opposite ends of the sample along the vertical centre line and in the y-direction along the horizontal centre line.

The crack was introduced into the module through the use of the ABAQUS built-in "Seam" feature. This application effectively splits the model along the assigned edge allowing a closed region to open during the analysis. The software places overlapping duplicate nodes along the seam when the mesh is generated.

The natural crack surface contact which happened during the dynamic loading of the experimental samples was modelled by placing a "hard contact" interaction property on the two surfaces of the crack. This was achieved by placing a fixed analytical rigid wire of an equivalent length to the current crack length in the centre of the sample. As this feature has no actual thickness, it does not interfere with the behaviour of the sample whilst the crack was fully open. Crack closure was effectively simulated by assigning a "hard contact" interaction property between the relative surfaces as a master and slave pair that prevents the two surfaces from penetration one another whilst allowing for separation after contact, effectively simulating rigid crack closure. Contact elements were used in this work due to their ease of implementation and realistic behaviour. This configuration was illustrated in Figure 5.47, during crack closure the gap between surfaces will be fully removed.

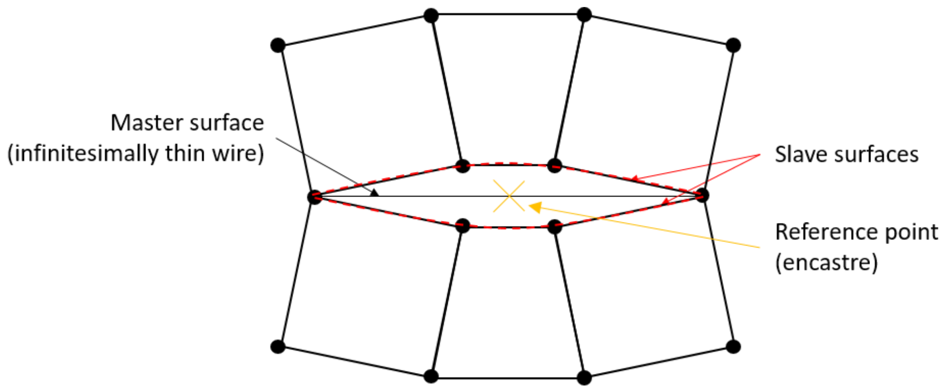

Figure 5.47: Illustration of crack contact model

The crack propagation was simulated by creating multiple models with varying lengths of the seam crack. To determine K_{res}, the crack was only extended along the horizontal direction. The crack length was increased in 4 mm increments from 4 mm, equal to the initial crack length after pre-cracking, to 48 mm. The final crack length was chosen as this was one crack increment larger than the experimental crack length at failure with an applied stress of 90 MPa. The crack front was assumed to be straight and uniform as no thickness effects could be accounted for in the two-dimensional analysis. Crack tunnelling commonly occurs in fatigue crack growth in the presence of residual stresses. This effect causes the crack front to elongate in the mid-thickness, however, these effects were not considered in this analysis. Finally, plane stress conditions at the crack tip were assumed for all crack lengths.

5.4.2.4. Validation of linear elastic fracture mechanics model

To verify the implementation of the displacement extrapolation method, the case of a centre crack sample (representative of the experimental samples) exposed to pure mode I tensile loading was simulated at the relevant crack lengths. The empirical formulation was originally developed by Feddersen in 1966 and was reported in equation 2-49 [1]. The relative error between the FEA and ASTM SIF at each crack length at the two maximum loading values (σ_{max} 90 MPa & 140 MPa) was calculated according to Equation 5-3 .

$$K_{error} = \frac{K_{FEA} - K_{ASTM}}{K_{ASTM}} \cdot 100\% \qquad \text{Equation 5-3}$$

As previously discussed, the LSP model was re-meshed after the completion of the residual stress simulation. Throughout this LEFM analysis, plane stress 8-node biquadratic quadrilateral elements (CPS8) were used. The effect of the number of exclusion points on the accuracy of the stress intensity was determined at a crack length of 15 mm, with a mesh size of 1 mm along the crack propagation direction and a σ_{max} of 90 MPa. Figure 5.48 showed the variation of the stress intensity with the number of exclusion points (as discussed in section 5.4.2.2) and the corresponding relative error to the ASTM value. It was determined that the number of exclusion points should be increased until the linear fit correlation factor (R^2) was approximately equal to 0.997 - 0.998. This correlation point was found to be the ideal range at which point all non-linearity in the SIF near the crack tip is removed and sufficient points remain to obtain an accurate linear fit.

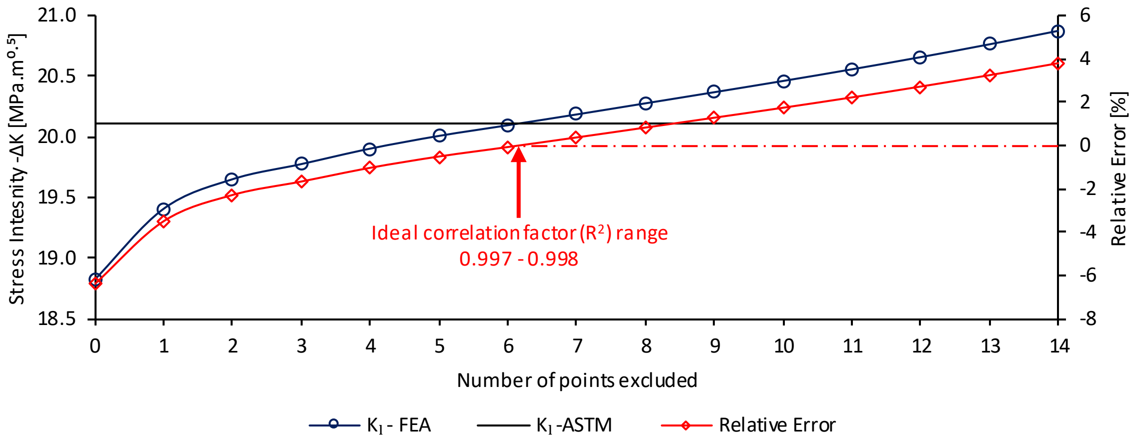

Figure 5.48: Influence of number of exclusion points on calculated stress intensity

To determine the influence of the mesh size on the predicted SIF, several element sizes, ranging from 0.25 – 2 mm were used along the crack propagation direction. The half crack length was fixed at 15 mm which corresponded to a SIF of 20.11 MPa.m$^{0.5}$ with a σ_{max} of 90 MPa. The SIF values were selected based on the minimum number of exclusion points required to obtain the desired fit. Table 5.8 listed the results of the mesh convergence study. The results of this showed that for all tested mesh sizes, the SIF was within 1% of the empirical value. A final mesh size of 0.5 mm was selected as this provided an excellent correlation with the empirical equation, a small enough mesh to fully represent the initial residual stress field and was not computationally expensive.

Table 5.8: Influence of mesh size on predicted stress intensity

Element size [mm]	Stress intensity [MPa.m$^{0.5}$]	Relative error [%]
0.25	20.122	0.06
0.5	20.144	0.17
1	20.163	0.26
2	20.185	0.37

Figure 5.49 provided the simulated SIF ($K_{I,app}$) for the two σ_{max} values of 90 MPa & 140 MPa at the various crack lengths. The relative error between the simulated SIF and empirical ASTM standard was within 1% for all crack lengths. In addition, the mode II stress intensity was found to be 0 MPa.m$^{0.5}$ at each crack length. This was expected as no residual stress or transverse forces were included.

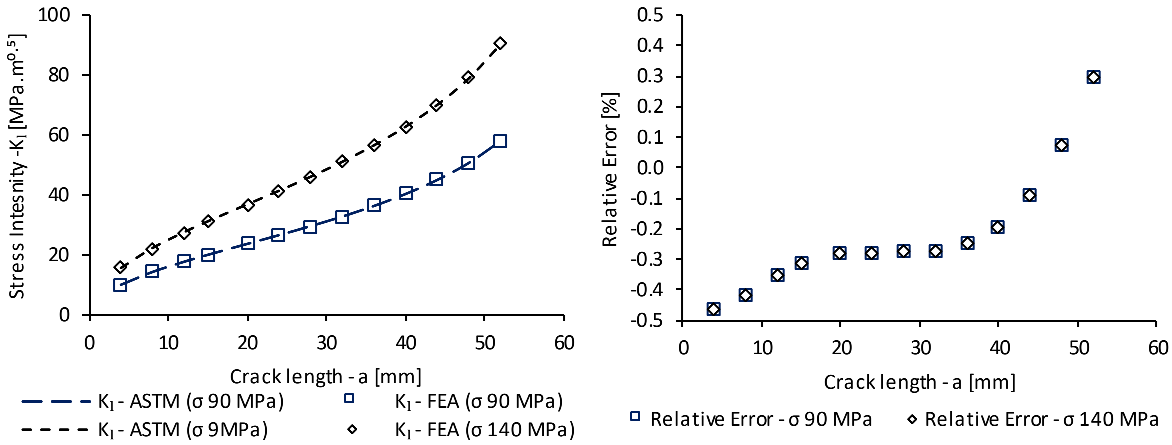

Figure 5.49: Comparison of empirical and simulated mode I stress intensity of a middle tension crack specimen at σ_{max} 90 MPa & 140 MPa, (a) stress intensity variation with crack length, (b) the relative error variation with crack length

5.4.2.5. Fatigue crack growth rate predictions

The FCGR for the simulated sample was predicted using Walker's empirical crack growth equation provided in equation 2-58. This formulation took into account the experimental test data of the base material and subsequently derived material coefficients from section 5.3.2. The influence of the residual stress on the SIF and stress ratio was analysed with the superposition based and crack-closure-based techniques provided in section 2.3.3.

The FCGR prediction methods incorporate the influence of the residual stress field on the total SIF as K_{res}. To avoid errors that may have occurred during the modelling on a nonlinear contact, K_{res} was determined when both the residual stress and the applied load acted simultaneously in the FEA model [18]. This ensures that the crack was fully open (Δu>0 in Equation 2-1) at all positions of the crack face. K_{res} was then evaluated based on the superposition principle, shown in Equation 5-4 [19].

$$K_{res} = K_{tot} - K_{app} \qquad \text{Equation 5-4}$$

In this work, K_{res} was determined as the average between the two individual values of K_{res} determined at a σ_{max} of 90 MPa and 140 MPa. For all crack lengths, the maximum percentage difference between the two values was less than 7%. Figure 5.50 showed the initial residual stress distribution and the determined mode I and II K_{res} values with respect to the various crack lengths (a). The mode I K_{res} (solid red line) was negative for all crack lengths due to the compressive residual stress in the longitudinal direction (y-direction). The residual stress in the two orthogonal directions tended to increase in compression upon approaching the LSP area and stabilised until exiting the processed area.

The occurrence of a mode II K_{res} distribution indicated that the LSP residual stress introduced an additional loading component on the crack. The use of the absolute value of the Δv term in the displacement extrapolation method and Equation 5-4, coupled with the fact that $K_{II,app} = 0$ for a centre crack sample, would always result in the mode II $K_{res} > 0$ for all crack lengths. This limiting factor of the displacement extrapolation method prevented the precious determination of the crack extension direction and only provided an estimate of the magnitude of the mode II K_{res}. Figure 5.50 showed that mode II K_{res} tended to increase in value as the crack propagated toward the LSP area and then steadily reduced with increasing crack length. This behaviour was linked to the transverse residual stress distribution (short dash black line).

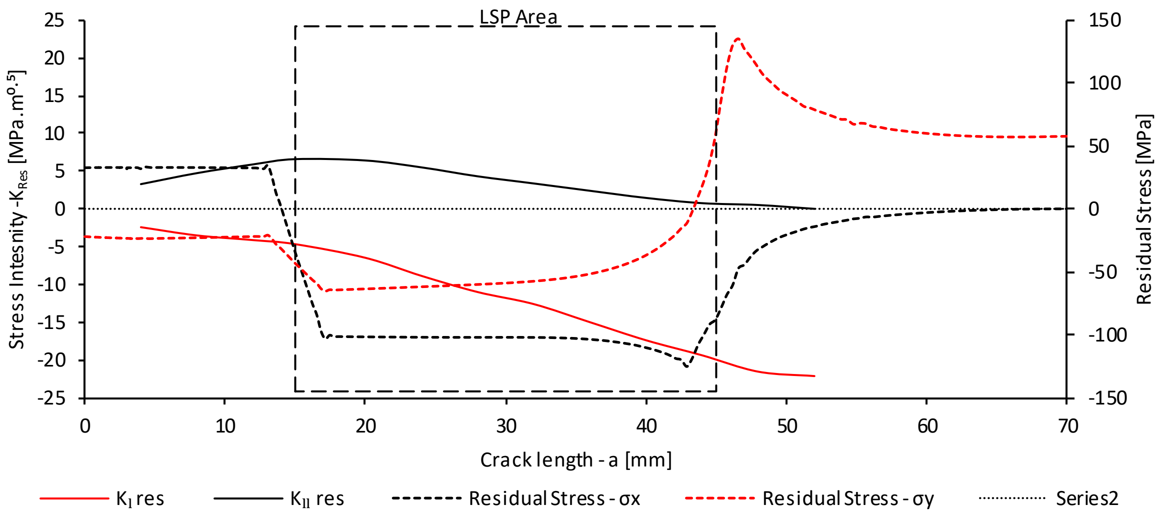

Figure 5.50: Mode I and II residual stress intensity distribution with varying crack length

The mode I component was only considered in the simulated prediction of the FCGR for the baseline and LSP rotated sample 30⁰ - 15mm. The Superposition (S), Modified-Superposition (MS) and Superposition Contact (SC) methods were used to describe the $\Delta K_{I,eff}$ and $R_{I,eff}$, these methods were discussed in section 2.3.3. Figure 5.51.a showed the $K_{tot,min}$ and $K_{tot,max}$ distributions according to the three FCGR predictive models (Superposition, Modified Superposition and the Superposition Contact), together with the $K_{app,min}$ and $K_{app,max}$ for the loading condition of σ_{max} 140 MPa. The lower loading condition was excluded as the effects of the sample deflection were found to affect the accuracy of the FCGR models as the 2D FEA model did not fully account for the reduction in the SIF due to the out of plane bending.

The $K_{tot,max}$ for the three models were all equal as no crack closure occurred at the maximum applied loading. However, the $K_{tot,min}$ of the Modified Superposition model did deviate from the other two models as it was the only technique to enforce rigid crack closure, restricting the value from becoming less than zero. By consequence, Figure 5.51.b showed that this resulted in a lower predicted $\Delta K_{I,eff}$ for the MS technique. As the crack was fully closed by K_{res} for all crack lengths at the lowest applied loading, the Superposition and Superposition Contact techniques have an equivalent $\Delta K_{I,eff}$ value to the base material. This was due to the removal of the K_{res} term in the expression, as derived in section 2.3.3. Figure 5.51.c provided the estimation of the effective stress ratio: the Superposition and Superposition Contact models both predicted equivalent negative stress ratios for all crack lengths. These two models had the same behaviour to each other and resulted in $K_{tot,min} < 0$ for all crack lengths as K_{res} was significantly negative. As the MS model enforced crack closure, the effective stress ratio was limited to zero for all crack lengths as $K_{tot,min} < 0$. Although a positive applied stress ratio of 0.1 was applied, the lack of tensile residual stresses between the LSP patch areas prevented an increase in the stress ratio.

Figure 5.52.a-b provided a comparison of the experimental and simulated FCGRs. Only the maximum applied loading case has been included as these measurements were least influenced by the deflected nature of the samples. The comparison of the predicted and experimental baseline showed good agreement until the nearing the end of crack propagation. The predictions in these regions may not be fully valid as region III of the crack propagation was approached.

The three predictive models tended to have a very good correlation with the experimental LSP data in the regions between the LSP patches. The comparison of the simulated and experimental FCGR reduced slightly upon the crack entering the LSP region. This implied that the magnitude of the compressive residual stress in the LSP area was slightly underestimated, suggesting that K_{res} would have been marginally more compressive. An additional contributing factor to the overestimation of the FCGR was the effects of the sample deflection not being incorporated into the predictive model. Ideally, the samples would not have been so significantly deflected in any real-world application. As the MS FCGR was within 10% of the experimental results for all crack lengths it was judged the most suitable method to describe the fundamental mechanisms associated with the fatigue crack growth life extension of the samples.

Figure 5.52 showed that the Modified Superposition technique provided the best fatigue crack growth life estimation with a predicted total number of cycles to failure of 45 003 cycles, 5% less than the averaged experimental equivalent value. The remaining two methods provided a further conservative prediction that was 18% lower than the experimental data.

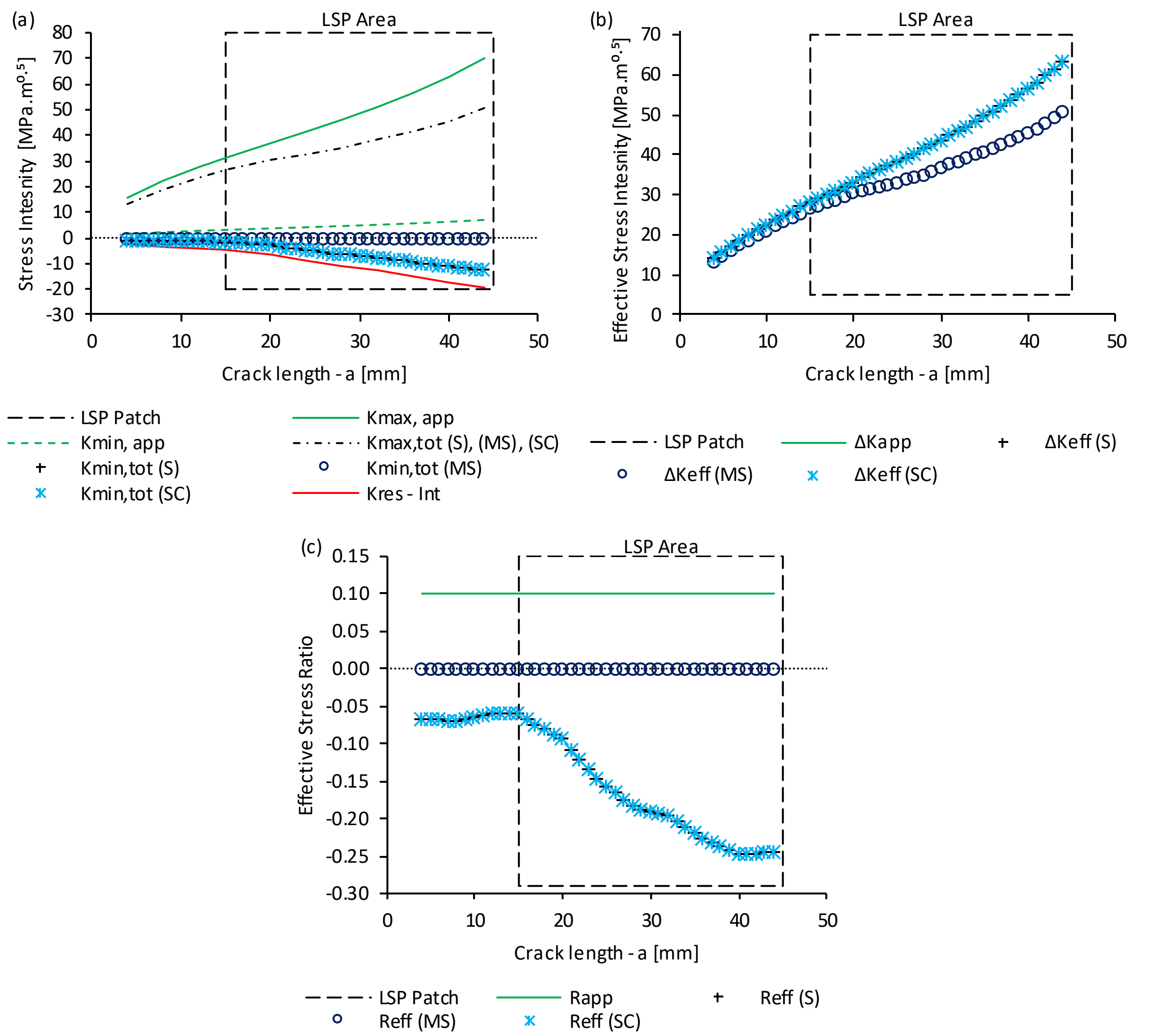

Figure 5.51: Fatigue crack growth rate predictive models (a) maximum and minimum stress intensity per method, (b) effective stress intensity, (c) effective stress ratio

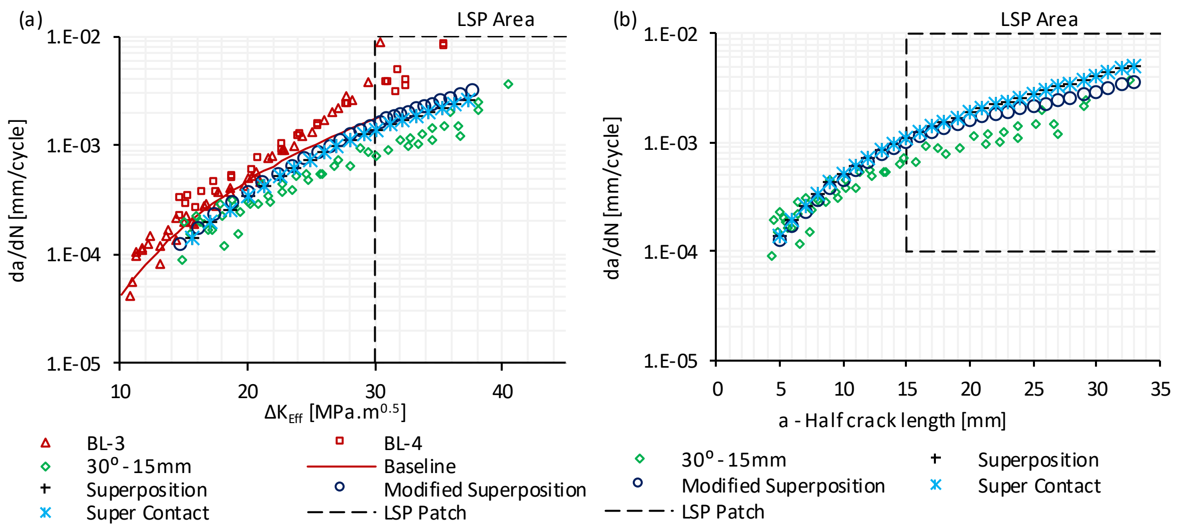

Figure 5.52: Comparison of predicted fatigue crack growth rates

5.4.2.6. Influence of residual stress on the crack trajectory

Figure 5.50 showed that the presence of the transverse component of the residual stress would give rise to an increased mode II K_{res}. Although the magnitude was found to be relatively low (less than 5 MPa.m$^{0.5}$) compared to the mode I SIF, this additional SIF would likely promote the modification of the crack trajectory.

Due to the manner in which the SIF are determined with the displacement extrapolation method, the exact direction of the crack extension angle could not be precisely determined. Rather the crack deviation angle was determined per crack length to provide a quantitative representation of the crack's likelihood to deviate from the straight path that was assumed in the FEA analysis. The Maximum Tangential Stress criterion, defined in equation 2-71, provided an estimation of the crack deviation angle as the crack extends. This formulation relates the crack deviation to the mode I and II SIF at the crack tip. Figure 5.53 illustrated the trajectory deviation potential of the crack by assuming the absolute values of $K_{I,tot,max}$ and $K_{II,tot,max}$. The averaged crack trajectory showed the largest deviation prior to the crack entering the LSP area. This was replicated in the calculated deviation angle which predicted the largest deviation angles prior to entering the LSP patch. The crack deviation potential steadily reduced as the crack extended into the LSP patch which was replicated in the experimentally measured crack trajectory. Additional FEA modelling would be required to accurately determine an estimated crack trajectory.

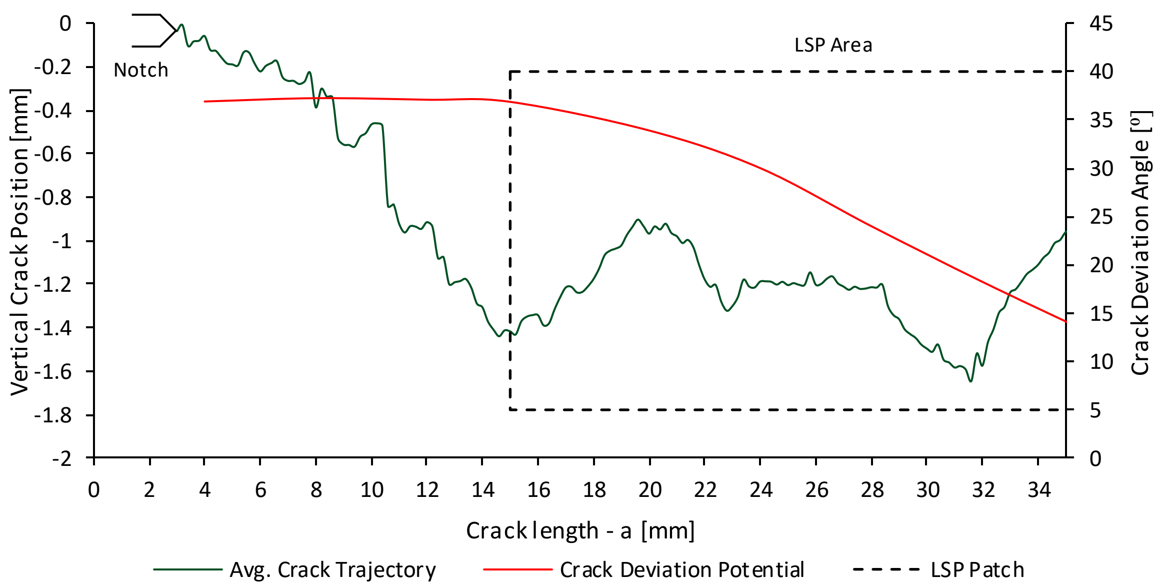

Figure 5.53: Crack trajectory deviation potential

5.5. Conclusions

The following conclusions can be drawn from this chapter:

- The LSP residual stress was capable of introducing small crack redirections by creating an additional mode II K_{res} value and drawing the crack towards the LSP patches.
- Only small scale deviations were achieved, indicating that the LSP could not be used as a direct replacement for aircraft structures such as tear straps. However, angled LSP patches can increase the efficacy in which crack deviation is achieved.
- The highest deviation was achieved by placing the LSP patches further away from the initial starting crack tip. The crack trajectory deviation tends to reduce upon entering the LSP patch as the residual stresses become less biaxial in magnitude.
- The presence of the LSP compressive residual stress resulted in a fatigue crack life extension of at least three times the original crack growth life of the samples.
- The highest extension in crack growth life was achieved by placing the LSP patch as close as possible to the initial starting crack.

5.6. References

[1] ASTM International. ASTM E647 - Standard Test Method for Measurement of Fatigue Crack Growth Rates. ASTM B Stand 2016;03:1–49. https://doi.org/10.1520/E0647-15E01.2.

[2] Busse DO. Extending fatigue life of aircraft fuselage structures using laser peening. Cranfield University, 2017.

[3] Melson JH. Fatigue Crack Growth Analysis With Finite Element Methods And A Monte Carlo Simulation. Virginia Polytechnic Institute and State University, 2014.

[4] Michael Hudson C. Effect of stress ratio on fatigue-crack growth in 7075-T6 and 2024-T3 aluminium alloy specimens. Eng Fract Mech 1969;1:429–46. https://doi.org/10.1016/0013-7944(69)90003-4.

[5] Pavan M. Laser Shock Peening for Fatigue Life enhancement of Aerospace Components. Coventry University, 2018.

[6] van Aswegen DC, Polese C. Experimental and analytical investigation of the effects of laser shock

peening processing strategy on fatigue crack growth in thin 2024 aluminium alloy panels. Int J Fatigue 2021;142:105969. https://doi.org/10.1016/j.ijfatigue.2020.105969.

[7] Preibisch S, Saalfeld S, Tomancak P. Globally optimal stitching of tiled 3D microscopic image acquisitions. Bioinformatics 2009;25:1463–5. https://doi.org/10.1093/bioinformatics/btp184.

[8] Smyth N. Effect on Fatigue Performance of Residual Stress induced via Laser Shock Peening in Mechanically Damaged 2024-T351 Aluminium Sheet 2015. https://doi.org/10.1017/CBO9781107415324.004.

[9] Dassault Systemes. ABAQUS User's Manual, version 6.14 2014.

[10] MathWorks. MATLAB User's Manual, version R2020b 2020.

[11] Dewald AT, Hill MR. Eigenstrain based model for prediction of laser peening residual stresses in arbitrary 3D bodies : Part 1 model description. J Strain Anal Eng Des 2009;44:1–11. https://doi.org/10.1243/03093247JSA417.

[12] Correa C, Gil-Santos A, Porro JA, Díaz M, Ocaña JL. Eigenstrain simulation of residual stresses induced by laser shock processing in a Ti6Al4V hip replacement. Mater Des 2015;79:106–14. https://doi.org/10.1016/j.matdes.2015.04.048.

[13] Coratella S, Sticchi M, Toparli MB, Fitzpatrick ME, Kashaev N. Surface & Coatings Technology Application of the eigenstrain approach to predict the residual stress distribution in laser shock peened AA7050-T7451 samples. Surf Coat Technol 2015;273:39–49. https://doi.org/10.1016/j.surfcoat.2015.03.026.

[14] Zhu WX, Smith DJ. On the use of displacement extrapolation to obtain crack tip singular stresses and stress intensity factors. Eng Fract Mech 1995;51:391–400. https://doi.org/10.1016/0013-7944(94)00319-D.

[15] Zhu N, Oterkus E. Calculation of stress intensity factor using displacement extrapolation method in peridynamic framework. J Mech 2020;36:235–43. https://doi.org/10.1017/jmech.2019.62.

[16] Boni L, Fanteria D, Lazzeri L, Furfari D. Numerical prediction of fatigue crack propagation in Cold-Expanded Holes. Proc 29th Symp Int Comm Aeronaut Fatigue 2017:1–10.

[17] Krueger R. Virtual crack closure technique: History, approach, and applications. Appl Mech Rev 2004;57:109–43. https://doi.org/10.1115/1.1595677.

[18] Bao R, Zhang X, Yahaya NA. Evaluating stress intensity factors due to weld residual stresses by the weight function and finite element methods. Eng Fract Mech 2010;77:2550–66. https://doi.org/10.1016/j.engfracmech.2010.06.002.

[19] Janssen M, Zuidema J, Wanhill R. Fracture Mechanics. 2nd ed. Springer; 2004. https://doi.org/10.1007/978-3-319-24999-5.

Chapter 6 Conclusion

This is a conclusive chapter for the presented thesis. Section 6.1 provided a summary of the research where the achievements of the objectives are addressed. The novel findings of this research are outlined in section 6.2. A list of suggestions for future works which is based on the carried out research is provided in section 6.3.

6.1. Summary of the research

The research presented in this thesis addressed the mechanisms of LSP parameters on the formation of residual stresses and the use of these induced stresses to influence the fatigue crack growth behaviour of aluminium samples. The experimental results were used in the formulation of a pulse-by-pulse dynamic simulation of the LSP process and combined residual stress and fracture mechanics model that provided additional context in the mechanisms associated with the observed crack deviation and extension in fatigue crack growth life.

An extensive literature review of the fundamentals of LSP revealed that due to restrictions in laser infrastructure a systematic study into the effects of the laser temporal profile had not yet been completed. The four individual laser temporal shapes were designed to have an equivalent intensity and time duration of 6 ns at the FWHM whilst fitting within the total pulse time of 14 ns. All other critical LSP parameters such as peak power intensity, spot size and coverage were maintained. Residual stress and surface deformation measurements indicated that there was little to no discernible influence of the various pulse shapes on the measured outcomes whilst maintaining the other LSP parameters. In all of the trialled profiles, the step rise time in the laser intensity provided the required energy to establish plasma over an extremely short time scale. The determined analytical model of the plasma pressure showed that pressure was applied to the sample surface for at least an order of magnitude longer than that of the laser temporal profiles. Indicating that over a short pulse duration (at least less than 14 ns) the temporal profiles had no distinguishable influence on the measured residual stress.

This research has confirmed the published outcome that the magnitude and depth of the compressive residual stress are directly related to increasing the power density and extent of the LSP processing. However, the thickness of the sample or item being processed greatly influences the induced residual stress and the selection of the LSP parameters. A greater understanding of the influence of the LSP parameters can have a significant effect on the further progression and development of lasers and full commercial LSP systems, as the main focus should be placed on parameters such as the power density and coverage rather than the temporal profile.

The laser temporal experimental test campaign was advanced by the development of an LSP pulse-by-pulse dynamic simulation methodology. The accuracy of the analytical plasma pressure model was drastically improved through the inclusion of the measured laser spatial variations. This spatial varying of the pressure when introduced in the model greatly improved the predicted surface deformation and the anisotropic nature of induced residual stresses. These models showed that the current Johnson-Cook material model is appropriate to use in the prediction of the residual stress by LSP and the input parameters of the pressure model should be calibrated to minimise the deviation between the experimental and predicted results. However, the cyclic hardening effects that occur during multiple applications of LSP shots should be included in future models as this will likely increase the accuracy of the material response. The development of realistic LSP models that accurately account for the characteristics of the laser source is critical in the wider implementation of the technology as a design and repair tool for the aerospace industry. By being able to predict the LSP process drastically reduces the need for extensive process development and parameter optimisation. Additionally, the effects of the LSP can be easily determined and implemented into more advanced modelling campaigns that aim to investigate the influence of the LSP residual stress on other mechanical behaviours such as fatigue and crack propagation.

In the final chapter, the applicability of using LSP induced residual stresses to control the behaviour of fatigue cracks was investigated. The positional accuracy of the LSP process allowed for the placement of LSP patches which were oriented at various angles relative to a centrally notched sample. As the crack propagated and approached the peened area, the cracks tended to deviate away from the preferred failure direction (perpendicular to the loading direction). The presence of the LSP residual stress induces a secondary loading condition at the crack tip which resulted in mixed mode loading capable of causing a deviation of the crack trajectory. It was found the highest deviation of the crack occurs in the region which is just before the LSP processed area. This was due to the increase in the magnitude of the transverse residual stresses that occurred in this region. In all LSP patch configurations, the crack tended to deviate towards the centre of the LSP patch, this was counter to the initial idea that the crack propagation would be maintained in the unprocessed area between the two parallel LSP patches. Of all the tested LSP configurations, it was found that the highest deviation in crack trajectory was achieved by placing the LSP patch further along the crack path and at lower patch rotation angles. All of the trialled LSP patch configurations were capable of significantly reducing the fatigue crack growth rate of the samples and extended the crack growth life. This was caused by the induced longitudinal compressive residual stresses. These stresses tended to reduce the driving force of the applied loading and resulted in a significantly lower loading condition at the crack tip. Of all the tested LSP configurations, it was found that the highest extension in crack growth life was achieved by placing the LSP patch as close to the notch as possible and that patch rotation angle had little influence on the crack growth life.

A reverse optimisation eigenstrain based modelling technique was used to induce the accurate final residual stresses and component deformation in the middle tension samples. This technique used multiple applications of unbalanced thermal strains to replicate the experimental residual stress and deformation caused by the application of each LSP layer. The benefit of this technique was that a comprehensive residual stress model that accurately determined the deformation of the component can be produced with minimal experimental results and at a low computational expense.

The full three-dimensional residual stress state was mapped to a simplified two-dimensional simulation case to determine the residual stress associated mode I and II K_{res} factors along the various crack lengths. The displacement extrapolation method was used in this thesis to determine the stress intensity at the various crack lengths. However, this method was hindered by the inability to determine the exact sign of the stress intensity factor and restricted the analysis of the crack propagation angle and direction. The FEA analysis did confirm that the highest mode II K_{res} occurred just prior to the LSP processed area, indicating that this region had the highest potential for a crack deviation. The modified superposition methodology provided the closest estimate to the average experimental fatigue crack growth life of all other tested methodologies. This was due to the fact that this methodology accounts for the influence of crack closure.

In conclusion, this work has ideally assisted in the understanding and further progression of LSP as an industrial application that is suitable for the replacement of less effective technologies such as shot or ultra-sonic peening. This work has provided clear outcomes on the influence of previously unstudied process parameters and will likely assist in the further development of commercial LSP systems. In addition, this research has shown a new application for the use of LSP residual stresses to assist in the control of fatigue cracks. Additional research is required to fully optimise the LSP patch configuration which will maximise the crack deviation in aircraft structures and has promising potential to assist in the prolonging of ageing aircraft.

6.2. Contribution to the knowledge

Several novel findings were achieved during this research. The main aspects are listed below:

- The selected temporal profile of a short-pulsed laser (less than 14 ns) has little to no noticeable influence on the formation of the LSP residual stress for equivalent power density, pulse energy and spot size.
- A method for accurately representing the laser pulses spatial and pressure variations in FEA simulations of the LSP event was put forward. This method greatly increased the accuracy of the predicted surface deformation that occurred during the simulated LSP event. It also increased the accuracy of the predicted anisotropic residual stresses that occur during LSP.
- LSP residual stresses do modify the trajectory of fatigue cracks in thin metallic structures. The cracks tend to propagate towards the centre of the processed LSP area. The highest deviation occurs in the final few millimetres outside of the processed area.

6.3. Suggested work

Some possible future works that can form the initiation point for additional research:

- Evaluate the effects of various laser temporal profiles on the formation of the LSP plasma and cavitation bubbles with the use of high-speed imaging techniques to assess if the variation in pulse energy influences the behaviour of these LSP phenomena.
- The time scale of the laser pulse plays a significant role in the formation of the laser-induced plasma. Although the plasma is formed within a few nanoseconds whilst the laser is supplying it with energy, it will take an order of magnitude of time longer for its effects to fully decay due to energy losses. It is suggested that research be dedicated to the development of µsecond long temporal profiles through the use of multiple laser sources. This time scale would be equivalent to the rate at which the shockwave propagates with the material thus a prolonged plasma could constructively interact with the reflected shockwaves increasing the extent of the plastic deformation and magnitude of compressive residual stress.
- Build in the effects of cyclic hardening into the pulse-by-pulse LSP predictive model to increase the accuracy of the material response to multiple applications of LSP processing.

- Alternative geometries of the LSP patches should be developed to attempt to increase the crack deviation whilst minimising the out of plane bending of the component.
- The consideration of pairing LSP with manufacturing techniques such as cold gas dynamic spraying, allowing for the design of unique crack propagation pathways in which LSP can be used to control the localised residual stress field and cold spray can be used to increase the stiffness of component in the desired location. This combined effect may result in a crack pathway which might result in a higher opportunity to deviate a crack.
- An alternative analytical/FEA method such as the virtual crack closure technique should be used to accurately determine the resulting stress intensity factors. This energy release rate method allows for the directionality of the propagating crack to be determined thus can be used to validate the experimentally observed crack deviations. This can also be used to explore alternative LSP strategies and determine LSP patch configurations which can be used to maximise the crack deviation.
- The simulation of full three-dimensional components should be simulated when determining the stress intensity factor of the heavily deflected samples. This will include the influence of the out of plane bending component on the determined stress intensity factors.

Appendix A Incremental hole drilling residual stress uncertainty evaluation

This section outlines the analytical method used to estimate the uncertainty in residual stress measurements by incremental hole drilling. The uncertainty at each nominal residual stress depth was determined by combining the ASTM 837-20 standards integral method [1] with the propagation of uncertainty using a Monte Carlo method as described in Smit et al. [2] and Peral et al. [3]. Unlike classical partial derivative uncertainty propagation methods, the Monte Carlo method incorporates bounded random number variations of the input variables to discern the measurements uncertainty limits. Figure A.1 provided a flow chart describing the Monte Carlo incremental hole drilling uncertainty method.

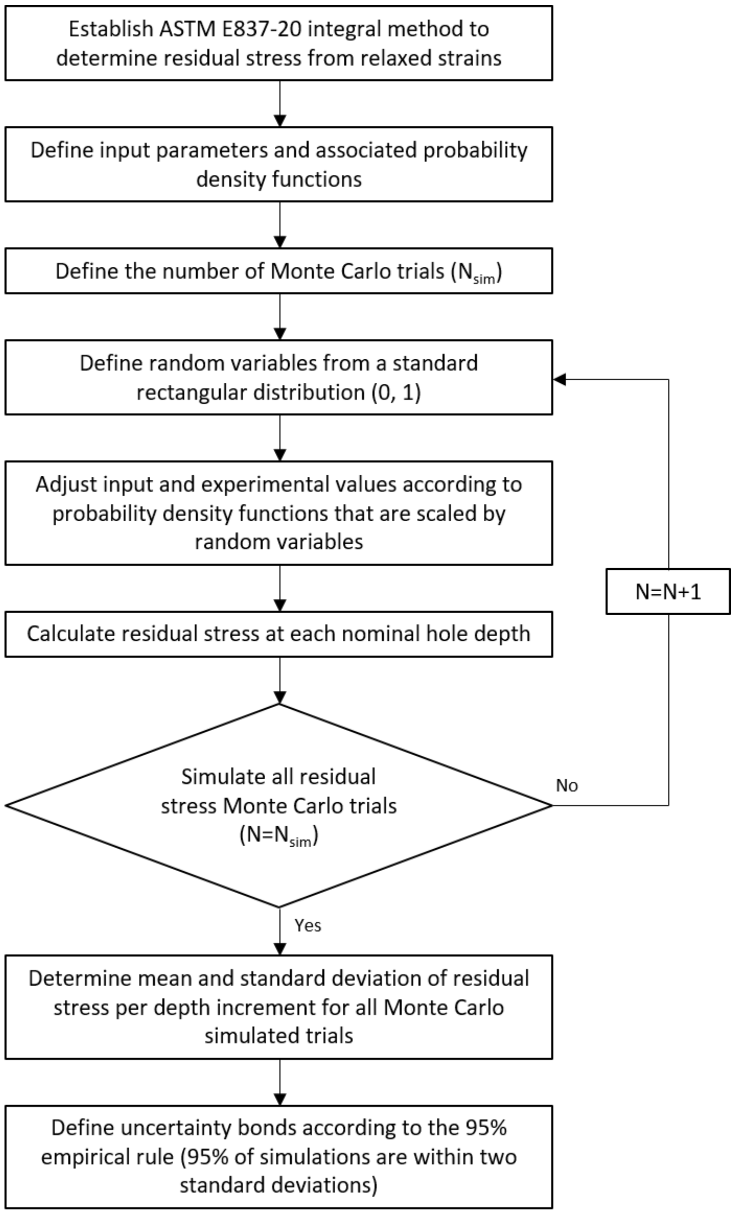

Figure A.1 - Flowchart of the Monte Carlo incremental hole drilling uncertainty method

A.1. Review of ASTM 837-20 standard test method for determining residual stresses by the hole-drilling strain-gauge method

This standard provides the experimental and analytical procedures for determining the residual stress profile within the first 2 mm from the surface using the incremental hole-drilling strain gauge method. This method involves recording the relieved strains at the surface as incremental amounts of material are removed at the gauge's geometric centre. The following lists the key elements and assumptions taken directly from the ASTM standard [1]:

1) All material behaviour is assumed to be linear-elastic and the residual stress does not exceed approximately 80% of the materials yield strength for blind hole drilling.
2) Measurement locations must be at a flat uniform surface area away from the sample's edges and other irregularities.
3) Non-uniform stress fields that vary in the thickness are represented as a staircase distribution. The thickness of the steps corresponds to the incremental drilling depths. Figure A.2.a provides a schematic representation of the staircase residual stress distribution and the nomenclature of the gauge and drilled hole [1]. D is the gauge diameter and D_{ICH} is the drilled hole diameter. Figure A.2.b provides an example of Type A, three-element strain gauge rosette used throughout this work. All used gauges had a D value of 5.13 mm.

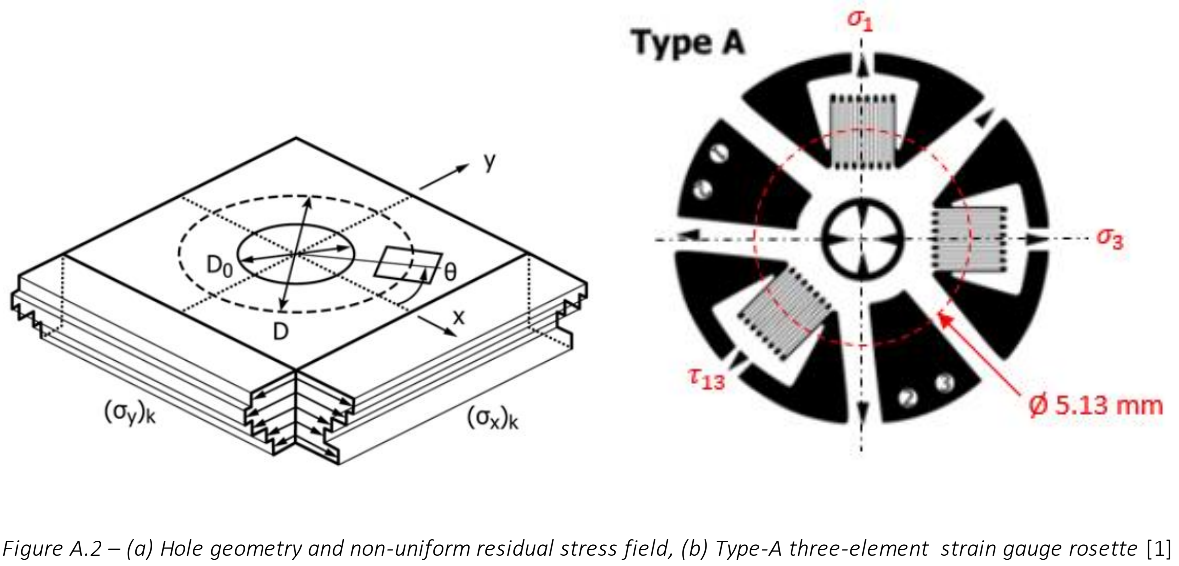

Figure A.2 – (a) Hole geometry and non-uniform residual stress field, (b) Type-A three-element strain gauge rosette [1]

4) The standard defines workpiece thicknesses up to 1.2825 mm ($0.25D$) as 'thin', whilst a workpiece thickness greater than 3.078 mm ($0.6D$) as 'thick'. A workpiece thickness between the specified limits is considered as 'intermediate'.
5) The residual stresses that were initially present in the material are evaluated from the measured relaxed strains (ε_1, ε_2 and ε_3) in *j* (number of hole depth steps) and are based on linear elasticity

theory. The calculated stresses along the axis of the strain gauge are defined as σ_1 (gauge 1) and σ_3 (gauge 3) and the shear stress orientated at 45° as τ_{13}, as shown in Figure A.2.b. The combination strains (Equation 3–1 to Equation A–3) and combination stresses (Equation A–4 to Equation A–6) can be evaluated for a sequence of stress depths (k), with $k \leq j$. Equation A–7 to Equation A–9 provide an estimate of the standard error in the combination strains (Equation 3–1 to Equation A–3). n is the number of sets of strain data at the various hole depths steps. The error in the measured strains should be characterised, as small errors in the strains that can cause proportionally larger errors in the calculated stress

$$\mathrm{p_j} = \frac{(\varepsilon_3 + \varepsilon_1)_\mathrm{j}}{2} \qquad \textit{Equation A–1}$$

$$\mathrm{q_j} = \frac{(\varepsilon_3 - \varepsilon_1)_\mathrm{j}}{2} \qquad \textit{Equation A–2}$$

$$\mathrm{t_j} = \frac{(\varepsilon_3 + \varepsilon_1 - 2\varepsilon_2)_\mathrm{j}}{2} \qquad \textit{Equation A–3}$$

$$\mathrm{P_k} = \frac{((\sigma_3)_\mathrm{k} + (\sigma_1)_\mathrm{k})}{2} \qquad \textit{Equation A–4}$$

$$\mathrm{Q_k} = \frac{((\sigma_3)_\mathrm{k} - (\sigma_1)_\mathrm{k})}{2} \qquad \textit{Equation A–5}$$

$$\mathrm{T_k} = (\tau_{13})_k \qquad \textit{Equation A–6}$$

$$p_{std}{}^2 = \sum_{j=1}^{n-3} \frac{(p_j - 3p_{j+1} + 3p_{j+2} - p_{j+3})^2}{20(n-3)} \qquad \textit{Equation A–7}$$

$$q_{std}{}^2 = \sum_{j=1}^{n-3} \frac{(q_j - 3q_{j+1} + 3q_{j+2} - q_{j+3})^2}{20(n-3)} \qquad \textit{Equation A–8}$$

$$t_{std}{}^2 = \sum_{j=1}^{n-3} \frac{(t_j - 3t_{j+1} + 3t_{j+2} - t_{j+3})^2}{20(n-3)} \qquad \textit{Equation A–9}$$

The integral method relates the above equations through the matrix relations defined in Equation A–10 to Equation A–12 (where the bar accent indicates a matrix and the arrow accent a vector). E and v are the elastic modulus and Poisson's ratio of the material and $\bar{a}$ and $\bar{b}$ are lower triangular calibration matrices.

$$\bar{a}\vec{P} = \frac{E}{(1+v)}\vec{p} \qquad \textit{Equation A–10}$$

$$\bar{b}\vec{Q} = E\vec{q} \qquad \textit{Equation A–11}$$

$$\bar{b}\vec{T} = E\vec{t} \qquad \textit{Equation A–12}$$

6) The calibration matrix $\bar{a}$ in Equation A–10 is defined as the strain relaxation caused by unitary isotropic stress in the increment j of a hole depth k, as shown in Figure A.3 [3]. The calibration matrix $\bar{b}$ in Equation A–11 to Equation A–12 has the same physical interpretation but consides the shear stresses. The components of the matrixes are determined based on polynomial coefficients provided in the ASTM standard. These coefficients are established by FEA calibration for various hole diameters and strain gauge types. The ASTM standards outline specific procedures to interpolate the provided coefficients according to the used strain gauge type, sample thickness and the final experimentally determined hole diameter. The ASTM standard should be consulted for additional information relating to determining the polynomial coefficients and respective analytical procedures per category of thickness.

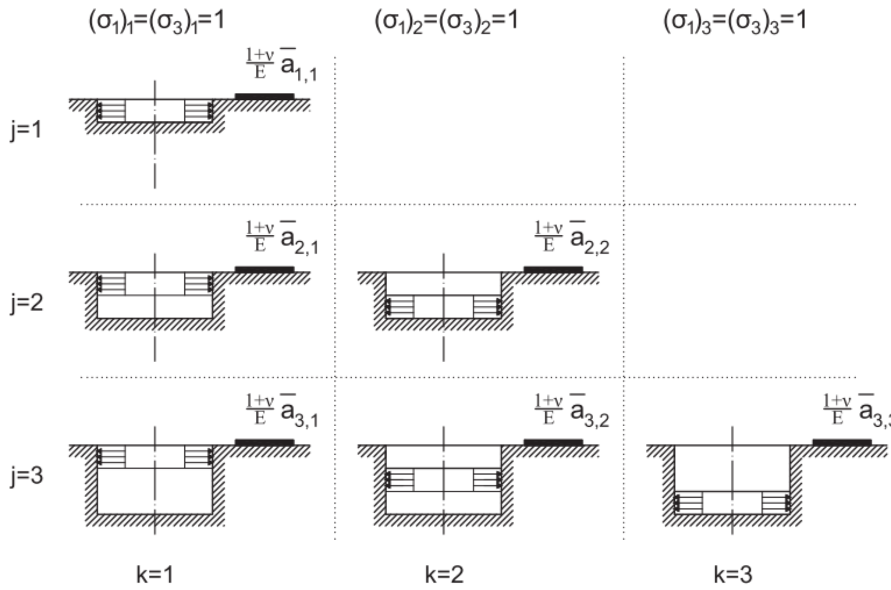

Figure A.3 – Principle of the integral hole drilling method and physical interpretation of how the calibration coefficients are obtained at the sequential depths of the measurement [3]

7) Tikhonov regularization is suggested as a method to reduce the matrices $\bar{a}$ and $\bar{b}$ from becoming ill-conditioned when a large number of hole depths are used in the measurements. If regularization is neglected, small errors in the measured strains can cause large errors in the calculated stresses. A tri-diagonal "second derivative" matrix (c) is formed, where the number of rows is equal to the number of hole depth steps used in the calculation. The first and last rows contain all zeros, with all other rows having [-1 2 -1] centred along the diagonal. Equation A–10 to Equation A–12 are augmented with the Tikhonov second-derivate (smooth model) as defined in Equation A–13 to

Equation A–15. The factors α_P, α_Q and α_T control the amount of regularization. Values in the range of 10^{-4} to 10^{-6} are typically suitable. Due to the regularization, the unregularized strains do not precisely correspond to the actual strains. The resulting strain "misfit" vectors ($\vec{p}_{misfit}$, $\vec{q}_{misfit}$ and $\vec{t}_{misfit}$) can be determined by Equation A–16 to Equation A–18Equation A–25 and the root mean square of this vector can be determined by Equation A–19 to Equation A–21. The regularization factors must be optimised according to Equation A–22 to Equation A–24 until the mean square of the misfit vector is within 5% of the standard error (Equation A–7 to Equation A–9) of the combination strains (Equation 3–1 to Equation A–3).

$$(\bar{a}^T\bar{a} + \alpha_P\bar{c}^T\bar{c})\vec{P} = \frac{E}{(1+v)}\bar{a}^T\vec{p}$$ *Equation A–13*

$$(\bar{b}^T\bar{b} + \alpha_Q\bar{c}^T\bar{c})\vec{Q} = E\bar{b}^T\vec{q}$$ *Equation A–14*

$$(\bar{b}^T\bar{b} + \alpha_T\bar{c}^T\bar{c})\vec{T} = E\bar{b}^T\vec{t}$$ *Equation A–15*

$$\vec{p}_{misfit} = \vec{p} - \frac{1+v}{E}\,\bar{a}\vec{P}$$ *Equation A–16*

$$\vec{q}_{misfit} = \vec{q} - \frac{1}{E}\,\bar{b}\vec{Q}$$ *Equation A–17*

$$\vec{t}_{misfit} = \vec{t} - \frac{1}{E}\,\bar{b}\vec{T}$$ *Equation A–18*

$${p_{rms}}^2 = \frac{1}{n}\sum_{j=1}^{n}{(\vec{p}_{misfit})_j}^2$$ *Equation A–19*

$${q_{rms}}^2 = \frac{1}{n}\sum_{j=1}^{n}{(\vec{q}_{misfit})_j}^2$$ *Equation A–20*

$${t_{rms}}^2 = \frac{1}{n}\sum_{j=1}^{n}{(\vec{t}_{misfit})_j}^2$$ *Equation A–21*

$$(\alpha_p)_{new} = \frac{{p_{std}}^2}{{p_{rms}}^2}(\alpha_p)_{old}$$ *Equation A–22*

$$(\alpha_q)_{new} = \frac{{q_{std}}^2}{q^2}(\alpha_q)_{old}$$ *Equation A–23*

$$(\alpha_t)_{new} = \frac{{t_{std}}^2}{{t_{rms}}^2}(\alpha_t)_{old}$$ *Equation A–24*

8) The Cartesian stresses at each nominal depth can then be determined according to Equation A–25 to Equation A–27. The principal stresses and directions are determined by Equation A–28 and Equation A–29.

$$(\sigma_1)_j = P_j - Q_j \qquad \textit{Equation A–25}$$

$$(\sigma_3)_j = P_j + Q_j \qquad \textit{Equation A–26}$$

$$(\tau_{13})_j = T_j \qquad \textit{Equation A–27}$$

$$(\sigma_{max})_k, (\sigma_{min})_k = P_k \pm \sqrt{{Q_k}^2 + {T_k}^2} \qquad \textit{Equation A–28}$$

$$\beta_k = \frac{1}{2}\tan^{-1}\left(\frac{-T_k}{-Q_k}\right) \qquad \textit{Equation A–29}$$

A.2. Sources of uncertainty

This uncertainty analysis of incremental hole drilling accounts for the three primary groups of uncertainty in the measurement. These variation sources are related to material properties, calibration matrices produced from the ASTM E837-20 standard, and measurement related uncertainties (strains, hole diameter and hole depths).

Material Properties:

The material properties considered in this assessment were the elastic modulus and Poisson's ratio. The presence of a clad layer in all 2XXX series aluminium alloy samples resulted in a higher estimated uncertainty variation in the elastic modulus to the ±3% suggested by Oettel [4]. Khan et al. determined that the elastic modulus of the clad material varied from the bulk alloy by as much as ±4% [5].

Strain Reconstruction Matrices:

A critical part of deriving the calibration matrices $\bar{a}$ and $\bar{b}$ was to determine the individual numerical values of the calibration constants. These values can be evaluated based on polynomial coefficients interpolated from tabulated finite element analyses results [1] or by analytical functions [6]. In this work, all values were determined from the tabulated values in the ASTM standard [1]. It fell out of the scope of research to carry out finite element analysis of the strain relaxations and hole deformations for each LSP residual stress distribution found in this research. The ASTM standard defines that the cumulative calibration matrices $\hat{a}_{jk}$ and $\hat{b}_{jk}$ are evaluated for each hole depth based on a polynomial equation. An uncertainty probability was applied to the tabulated polynomial coefficients that are listed in the ASTM standard to account for inaccuracies in the FEA models. Hole diameter and depth position variations were included in determining the strain reconstruction matrices for each Monte Carlo simulation thus making the uncertainty in the strain reconstruction matrices cross-correlated with some experimentally determined parameters.

Measurement uncertainty:

The effects of the drilled hole eccentricity, plastic strains and induced stresses due to the milling of the hole have been neglected from this assessment. It was reported by Parel et al. to have negligible effects if the test fell within the standard limitations of the measurement [3]. This method assumed that all the holes were near-perfectly centrally aligned with the gauges. Additionally, the gauge thermal effects were considered small and have been accounted for as part of the instrumentation probability density function as there was no significant change in temperature during the measurements.

a) Hole depth measurements – Each hole depth was determined by the encoder on the motors which had an estimated accuracy of ±2 μm on the depth position. Twenty-three hole depth increments to make a total depth of 1408 μm were used throughout (in order from the zero position - six increments of 16 μm, five increments of 32 μm, six increments of 64 μm and six increments of 128 μm).
b) Zero depth detection – The zero-depth was considered the position where the gauge and adhesive had been completely removed and the drill was 'just in contact' (no material has been removed) with the surface of the material. The strain readings were set to zero at this point to remove any gauge reading fluctuations which may have occurred whilst milling through the gauge. The unique operational feature of the Stresscraft apparatus allows for small amounts of material to be removed in stages (≤ 4 μm per layer) resulting in a high degree of confidence in determining the zero-depth position. The zero-depth was determined optically as small amounts of the gauge and adhesive material were removed incrementally. The largest depth of cut whilst removing gauge material was 4 μm and was reduced to 2 μm whilst removing the adhesive layer.
c) Hole diameter – The hole diameter was measured on the surface of the sample using the hole drilling positioning microscope and validated with an optical microscope. At least three diameter measurements were taken along each horizontal and vertical axis to determine an averaged hole diameter. The three measurements validated that the drilled hole eccentricity was within ±20 μm [1].
d) Measured strains – The Stresscraft incremental hole drilling apparatus directly outputs the measured strains, with the three gauge rosette's nominal gauge factor used in the calculation. As variations due to changes in temperature, external vibrations and change in resistance of the lead wires were not captured during the measurements, it is impossible to determine the strain uncertainty based on resistance variations. However, the recorded strains per depth increment

were recorded once the sum of the absolute difference of strains from the three channels was equal to or less than 2 με. This protocol allowed for strain reading stabilisation and attempted to negate any thermal effects during the removal of the material. Any additional resistance in the lead wires was not directly accounted for but was considered to be small. Although every effort was made to eliminate any external factors (vibrations in the laboratory and removal of heat-emitting lights), there were unavoidable small strain variations. These were accounted for by including a strain probability density function which was in accordance with the suggested values from Oettel [4].

e) Strain instrumentation noise – As previously stated, there were slight variations in the observed strain readings during the experiments (less than 2 με). A portion of the observed variations was considered as always-present noise that cannot be removed experimentally. In addition, this factor allowed for an uncertainty budget in the rosette's strain sensibility and any uncertainty associated with the gauges' manufacture.

As provided in Chapter 3, Table 3.7 listed the probability density functions of all the mentioned sources of uncertainty used in this analysis.

Table A.1 - Uncertainty limitations for measurements and mechanical properties

Category of uncertainty	Source of uncertainty	Uncertainty range
Material property	Elastic modulus	±4%
	Poisson's ratio	±3%
Measurement	Instrumentation noise (encompassing thermal effects)	±2 με
	Strain variation	±2 με
	Final hole diameter	±50 μm
	Zero depth position	±2 μm
	Depth increments	±2 μm
Computational	Cumulative strain relaxation polynomial coefficients (ASTM E837)	±2% $\hat{a}_{jk}$ & $\hat{b}_{jk}$

A.3. Monte Carlo propagation of uncertainty in incremental hole drilling residual stress

The Monte Carlo method is a numerical technique for solving mathematical problems utilizing random variable simulations [7]. This method allows for the uncertainty in the residual stress measurements to be discerned by simulating random variations of the measurement parameters bound by the respective probability density functions. The random variables used in the Monte Carlo Simulations are selected from a rectangular random variable uniformly distributed in the interval (0, 1). Matlab R2020a software was used to generate the random functions. Figure A.1 provides an overview of the method. The final uncertainty bound of the residual stress at each hole depth was defined as approximately two standard deviations of the total Monte Carlo simulated data set at each hole depth. This value was selected as it corresponded to a 95% coverage interval which refers to a 95% probability this uncertainty estimation will produce an interval containing or covering, the actual value of the residual stress at that depth.

JCGM 101:2008 suggests a total of 10^6 Monte Carlo trials will often be expected to deliver a 95% coverage interval [7]. However, it is computationally expensive to assume that this larger number of Monte Carlo trials is appropriate for all cases. The number of Monte Carlo trials should be appropriately selected to achieve the desired numerical tolerance of the uncertainty output quality and coverage probability whilst managing computational resources. To achieve this, the number of Monte Carlo trials should be incrementally increased until the stabilisation and convergence of the mean and standard deviation per stress depth are achieved.

A.4. Practical example of the Monte Carlo incremental hole drilling uncertainty estimation

The data from the incremental hole drilling measurement of the LSP flat top temporal profile sample (sample ID TP-FT-1.85-1-1) were used to illustrate this method and to determine the required number of Monte Carlo simulations to be used throughout in achieving a 95% confidence in the uncertainty bounds of the residual stress uncertainty.

A.4.1. Residual stress calculation and model validation

A summary of the samples used in this example was provided in Chapter 3. The AA 2524-T3 sample was 6 mm thick with a 0.185 mm thick protective clad layer, LSP processed with a flat top temporal profile, power intensity of 1.85 GW/cm^2, pulse energy of 1 J/pulse, a wavelength of 1060 nm, a square spot of 3x3 mm^2, with an ablative coating and a thin water confinement layer. A Vishay Micro-Measurements type A rosette (CEA-13-062UL-120/SE) was used with a gauge diameter of 5.13 mm (Figure A.2.b). The equipment included a Stresscraft orbital milling incremental hole drilling apparatus equipped with an electric motor drilling system. The data acquisition system was a Vishay P3 strain indicator and recorder. The average hole diameter was measured as 1.95 mm (averaged over six measurements of the diameter). Table A.2 listed a select number of experimentally measured total cumulative strains at their corresponding depths. The full set of data was used to calculate the residual stress profile up to a depth of 1.024 mm.

Table A.2 - Example of select measured strains

Hole Depth (mm)	Strain 1 (μm/m)	Strain 2 (μm/m)	Strain 3 (μm/m)
0	0	0	0
0.048	-3	0	-3
0.08	-4	-6	-10
0.16	1	-1	-5
0.32	33	40	32
0.512	68	89	58
0.768	96	124	71
1.024	109	140	74
1.28	115	145	75
1.408	116	146	75

The incremental hole-drilling residual stress profiles were made up of twenty individual stress depths spatially biased towards the sample surface. To provide an accurate sample calculation and for the sake of a better understanding, the cumulative calibration matrices $\bar{a}$ and $\bar{b}$ without any uncertainty propagation has been provided in Table A.3 and Table A.4. Only a portion of the depth increments was listed in the tables due to space constraints.

Table A.3 - Example of the calculated cumulative calibration matrix $\bar{a}$

Matrix $\bar{a} \cdot 10^{-5}$

Stress increment	Hole depths [mm]	Stress depths [mm]									
		0.008	0.024	0.04	⋯	0.208	0.24	0.288	⋯	0.896	1.024
1	0.008	-825									
2	0.024	-895	-1732								
3	0.04	-962	-1870	-1789							
⋮	⋮		⋮		⋱						
10	0.208	-1514	-2995	-2945		-4112					
11	0.24	-1593	-3156	-3110	⋯	-4565	-4068				
12	0.288	-1701	-3374	-3330		-5155	-4711	-6119			
⋮	⋮		⋮		⋱		⋮		⋱		
19	0.896	-2374	-4717	-4672	⋯	-8023	-7700	-10920	⋯	-5582	
20	1.024	-2363	-4709	-4682		-8248	-7937	-11284		-7511	-3421

Table A.4 - Example of the calculated cumulative calibration matrix $\bar{b}$

Matrix $\bar{b} \cdot 10^{-5}$

Stress increment	Hole depths [mm]	Stress depths [mm] 0.008	0.024	0.04	⋯	0.208	0.24	0.288	⋯	0.896	1.024
1	0.008	-1634									
2	0.024	-1735	-3411								
3	0.04	-1832	-3610	-3523							
⋮	⋮		⋮		⋱						
10	0.208	-2657	-5300	-5270		-8372					
11	0.24	-2781	-5552	-5528	⋯	-9112	-8399				
12	0.288	-2951	-5897	-5880		-10093	-9470	-12816			
⋮	⋮		⋮		⋱		⋮		⋱		
19	0.896	-4078	-8161	-8158		-15291	-14931	-21647		-20428	
20	1.024	-4084	-8196	-8220	⋯	-15716	-15374	-22326	⋯	-24557	-16578

Figure A.4 provided a direct comparison between the calculated residual stress profiles on gauge 1 and 3 using the commercial Stresscraft software and the developed Matlab code of the ASTM integral method without error propagation included. The ASTM E837 residual stress profiles were determined with the cumulative calibration matrices listed above and Tikhonov regularization (the factors that control the amount of regularization were determined according to the ASTM standard and were found to be α_p - 10^{-4}, α_q - 10^{-4} and α_t - 19^{-5}). This comparison validates the developed ASTM model as both residual stress profiles have been calculated according to the integral method and are closely matched. However, slight variations are expected in the profiles as the Stresscraft software assumes an infinitely thick sample, unlike the developed ASTM model which corrects the cumulative calibration matrices according to the sample thickness. Additionally, the Stresscraft software uses proprietary polynomials to determine the cumulative calibration matrices, whereas the developed ASTM model uses the published tabulated values along with Tikhonov regularization.

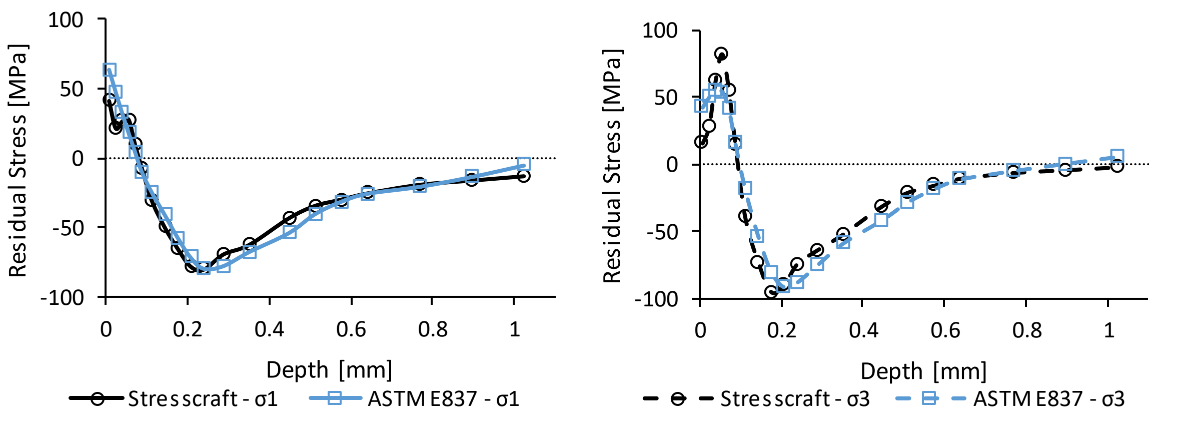

Figure A.4 – Comparison of Stresscraft and ASTM E837 residual stress profile (a) Stress on gauge 1 (b) stress on gauge 3

A.4.2. Required number of Monte Carlo simulations

As described in section A.3, the number of Monte Carlo trials that provide an adequate confidence level needs to be determined. The validated ASTM residual stress integral model and the probability functions listed in Table 3.7 were used to determine the required number of trials. This was done by incrementally increasing the number of Monte Carlo trials until the stabilisation of the normalised mean and standard deviation of the simulated results at each stress depth and root mean square difference of the total outcomes per gauge. Figure A.5 shows these results for several selected stress depths. The primary purpose of using the normalised mean and standard deviation was to allow for a direct comparison of the results at each stress depth and to increase the clarity of the presented figures. The data sets at each stress depth were normalised about the mean and standard deviation achieved with 100 Monte Carlo simulations. These values were chosen as the normalising values as they were the result of the first iteration. Across all of the tested Monte Carlo sample sets, the mean and standard deviation varied by less than 15% from the values achieved with 100 Monte Carlo simulations, with the maximum outlier of 57% of the normalising values in the simulated residual stress outcomes on gauge 3. This was attributed to low strains near the surface and the variation in stress observed in the first 0.1 mm of Figure A.4.b.

Figure A.5 clearly shows that the largest variations in the mean and standard deviation per stress depth were damped out within 25 000 Monte Carlo simulations and fully converge by 50 000 simulations (there was less than 0.5% variation in results with additional Monte Carlo trials). Based on these results, a Monte Carlo sample size of 50 000 simulations was appropriate for the statics to converge.

Table A.5 listed the determined mean and standard deviation of four iterations of 50 000 Monte Carlo trials for the two orthogonal gauges. The model was considered very repeatable as the maximum range in the mean and standard deviation was less than 0.5 MPa across all four iterations of this uncertainty model. The highest variation occurred at the first stress depth near the surface, which corresponded to the region of highest variance in uncertainty was due to the difficulties in determining the residual stress near the surface of the sample. This indicated that the Monte Carlo sample size was adequately selected to provide consistent results even though the method was based on random variations in the input values.

Table A.5 - Repeatability of Monte Carlo predicted residual stress mean and standard deviation of strain gauge 1 at various stress depths for 50000 simulations

Strain Gauge - σ_1 [MPa]										
	Iteration 1		Iteration 2		Iteration 3		Iteration 4			
Depth [mm]	Mean	Std. Dev.	Mean	Std. Dev.	Mean	Std. Dev.	Mean	Std. Dev.	Mean Range	Std. Dev. Range
0.008	67.5	37.0	67.3	36.7	67.6	36.9	67.1	36.9	0.04	0.3
0.04	29.4	9.5	29.4	9.4	29.5	9.4	29.4	9.4	0.1	0.1
0.072	4.1	11.4	4.1	11.3	4.0	11.3	4.1	11.3	0.1	0.1
0.144	-37.2	6.3	-37.2	6.3	-37.1	6.3	-37.1	6.3	0.1	0.1
0.208	-74.0	7.7	-73.9	7.6	-73.9	7.7	-73.9	7.6	0.1	0.1
0.352	-63.6	5.57	-63.6	5.5	-63.6	5.5	-63.5	5.5	0.1	0.1
0.512	-35.9	5.0	-36.0	5.0	-36.0	5.0	-36.0	5.0	0.1	0.01
0.768	-23.4	3.7	-23.4	3.7	-23.4	3.75	-23.4	3.6	0.04	0.03
1.024	-2.0	8.6	-2.0	8.6	-2.0	8.6	-2.0	8.6	0.04	0.1

Strain Gauge - σ_3 [MPa]										
	Iteration 1		Iteration 2		Iteration 3		Iteration 4			
Depth [mm]	Mean	Std. Dev.	Mean	Std. Dev.	Mean	Std. Dev.	Mean	Std. Dev.	Mean Range	Std. Dev. Range
0.008	-3.6	36.3	-3.4	35.9	-3.4	35.9	-3.2	36.2	0.4	0.4
0.04	58.6	10.0	58.5	10.0	58.5	10.0	58.5	10.0	0.1	0.1
0.072	66.1	12.4	66.0	12.4	66.0	12.4	66.0	12.4	0.2	0.1
0.144	-58.6	7.1	-58.5	7.0	-58.5	7.0	-58.5	7.1	0.1	0.1
0.208	-101.1	8.5	-101.0	8.5	-101.0	8.5	-101.0	8.5	0.1	0.1
0.352	-61.6	5.4	-61.5	5.4	-61.5	5.4	-61.5	5.4	0.1	0.02
0.512	-28.0	4.8	-28.0	4.7	-28.0	4.8	-28.0	4.8	0.04	0.1
0.768	-5.9	3.5	-5.9	3.5	-5.9	3.5	-5.9	3.5	0.04	0.02
1.024	6.7	8.6	6.7	8.6	6.7	8.6	6.7	8.6	0.1	0.03

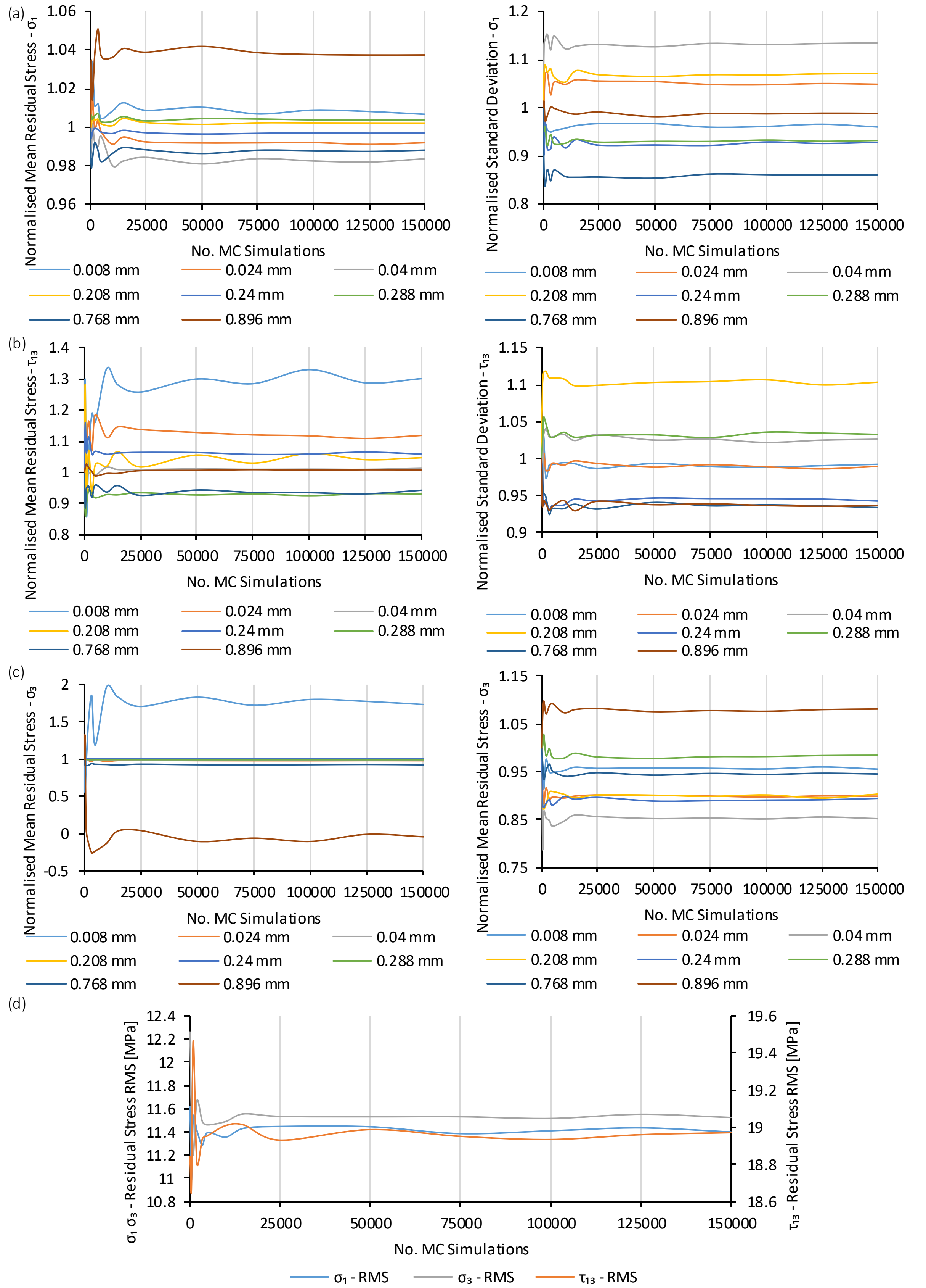

Figure A.5 - Variation of the Monte Carlo simulation statistics based on sample size (a) Normalised mean and standard deviation on gauge 1, (b) Normalised mean and standard deviation on gauge 2, (c) Normalised mean and standard deviation on gauge 3, (d) Root mean square difference of simulated residual stress results for each gauge

A.4.3. Results of Monte Carlo uncertainty estimation

In this assessment, the simulated uncertainty bounds of the residual stress at each stress depth have been represented by two standard deviations or a 95% confidence limit. This was based on the statistical empirical rule which defines the percentage of values that lie within a band around the mean in a normal distribution [8]. Figure A.6 compares the Monte Carlo mean per stress depth with the results in Figure A.4. The mean values are combined with the standard uncertainty from all sources listed in Table 3.7. The shaded regions in Figure A.6 represent the uncertainty bounds.

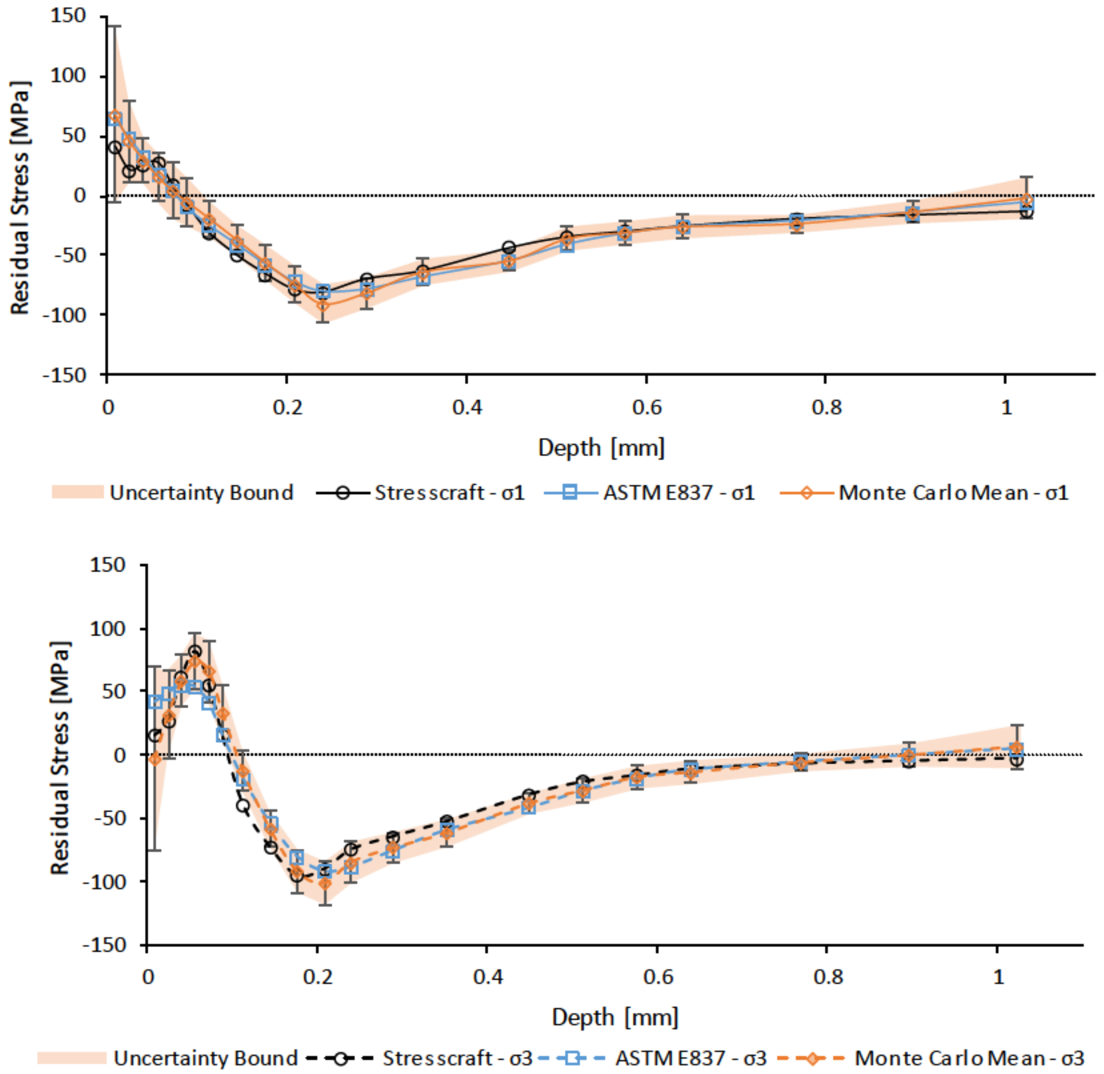

Figure A.6 - Incremental hole drilling uncertainty determined with 50 000 Monte Carlo simulations a) Stress on gauge 1 (b) stress on gauge 3

The highest error shown in Figure A.6 was near the surface; this was attributed to the increased spatial resolution near the surface (finest depth increments) and the strain values being of an equivalent magnitude to the strain variation probability functions. Additionally, errors in the detection of the zero-depth position contributed the most near the surface. This aligns with the understanding that it is difficult to accurately measure the residual stress near the surface by incremental hole drilling [9]. The residual stress profile predicted by the Stresscraft software fell within the uncertainty bounds of the ASTM and MC residual stress model.

Figure A.7.a and b provide the probability density functions of the predicted Monte Carlo simulations on the orthogonal gauges at a select number of stress depths. A normal fitted curve was superimposed to indicate the distribution of the simulated results. The general probability density functions were all roughly symmetrical about the mean.

(a)

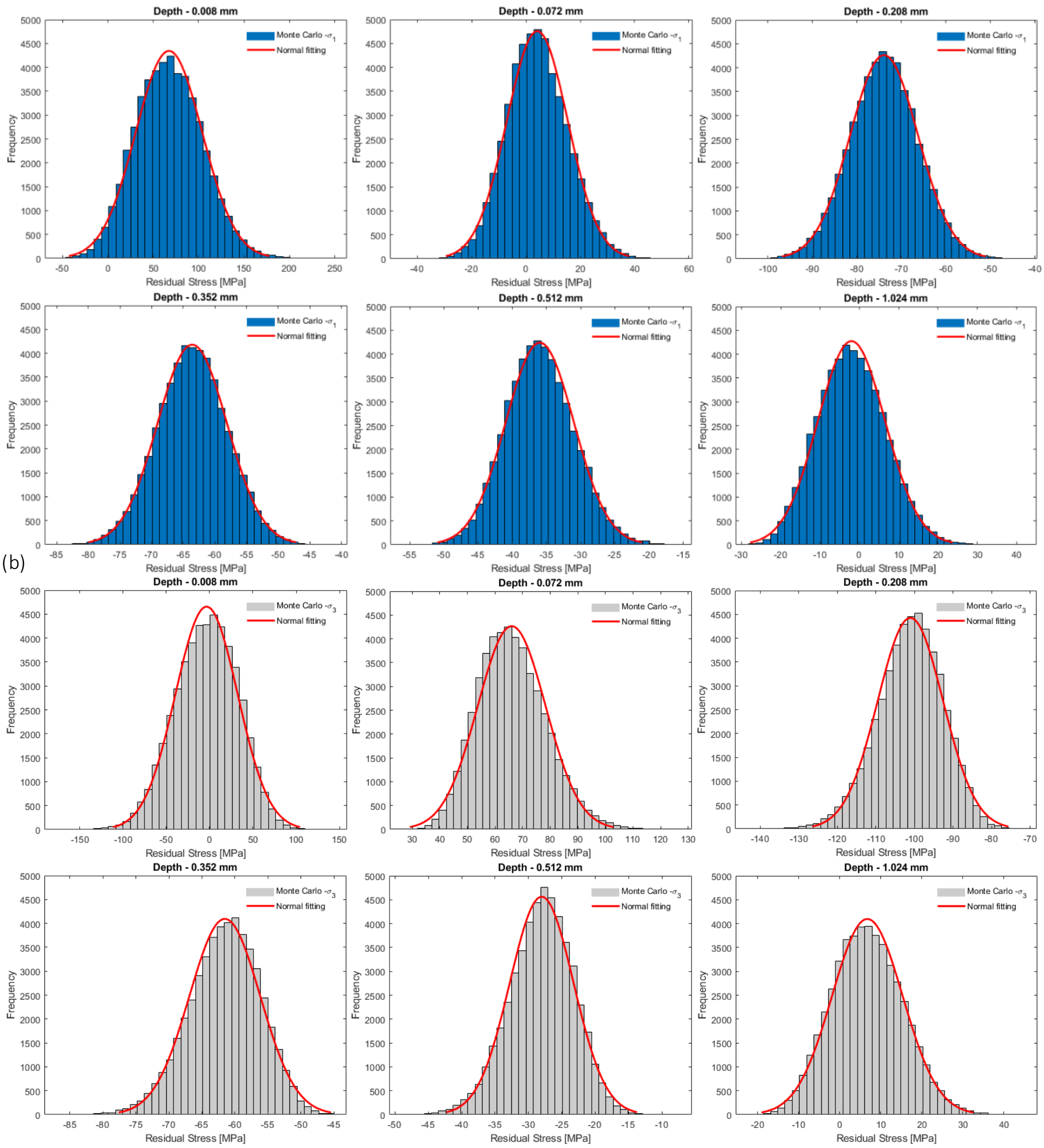

Figure A.7 – Monte Carlo residual stress (50 000 simulations) probability density functions at select stress depths in (a) stress directions 1 and (b) stress direction 3

A.5. Conclusions

The following provides the concluding remarks of this section:

- The Monte Carlo propagation of uncertainty method is a convenient and reliable method for predicting the associated uncertainty in incremental hole drilling measurements.
- The predicted uncertainty trends conformed to the well-established understanding that the highest variance in the measurement occurred at the sample's surface.

A.6. References

[1] ASTM International. ASTM E837-20 Determining Residual Stresses by the Hole-Drilling Strain-Gage Method. vol. i. 2020. https://doi.org/10.1520/E0837-13A.2.

[2] Smit TC, Reid RG. Residual Stress Measurement in Composite Laminates Using Incremental Hole-Drilling with Power Series. Exp Mech 2018;58:1221–35. https://doi.org/10.1007/s11340-018-0403-6.

[3] Peral D, de Vicente J, Porro JA, Ocaña JL. Uncertainty analysis for non-uniform residual stresses determined by the hole drilling strain gauge method. Meas J Int Meas Confed 2017;97:51–63. https://doi.org/10.1016/j.measurement.2016.11.010.

[4] Oettel R. The Determination of Uncertainties in Residual Stress Measurement (Using the hole drilling technique) 2000:18. https://doi.org/10.1007/bf02327502.

[5] Khan MK, Hainsworth S V., Fitzpatrick ME, Edwards L. A combined experimental and finite element approach for determining mechanical properties of aluminium alloys by nanoindentation. Comput Mater Sci 2010;49:751–60. https://doi.org/10.1016/j.commatsci.2010.06.018.

[6] Beghini M, Bertini L. Analytical expressions of the influence functions for accuracy and versatility improvement in the hole-drilling method. J Strain Anal Eng Des 2000;35:125–35. https://doi.org/10.1243/0309324001514071.

[7] Joint Committee For Guides In Metrology 101. JCGM 101: Evaluation of measurement data - Supplement 1 to the “Guide to the expression of uncertainty in measurement” -Propagation of distributions using a Monte Carlo method 2008. https://www.bipm.org/en/publications/guides/gum.html.

[8] Moore DS, Notz WI, Flinger MA. The basic practice of statistics. 6th ed. New York: W.H. Freeman and Company; 2013.

[9] Grant P V, Lord JD, Whitehead P. The Measurement of Residual Stresses by the Incremental Hole Drilling Technique. Meas Good Pract Guid No 53 - Issue 2 2006:63. https://eprintspublications.npl.co.uk/2517/.

Appendix B Innovative solid confinement for Laser Shock Peening applications

This chapter was associated with the development of an innovative polymer-based solid confinement medium that could be used as an alternative to the industry standard of water. Flowing water has been identified by aircraft manufacturers as a critical hindrance to the full integration of LSP into manufacturing lines and onsite applications. Most identified applications of LSP will be in areas of the airframe which might be near electrical systems or in corrosion critical areas thus the use of water poses an obvious issue. The pooling of LSP confinement water after the processing could potentially lead to significant corrosion of the airframe structure. Additionally, most industrial applications of LSP would likely be carried out on complex geometries which often give rise to confinement flow issues, as maintaining the laminar flow of the water overlay becomes more difficult on complex three-dimensional shapes.

The fundamental concept of this confinement medium was based on the patent "Overlay Material for Laser Shock Peening" [1]. The patent or proposed invention defined two primary criteria of the novel solid overlay material:

1) "the solid overlay is structured and adapted to a shape of a surface of a component to be treated by laser shock peening" – this required that the confinement medium be capable of being applied in a manner that allowed it to adhere to the contour of the component.
2) "the solid overlay is configured to be producible by additive manufacturing" – this enforced how the solid medium was to be produced and restricted the possible type of materials that could be used in this application.

To achieve the imposed requirements of the solid confinement medium, a near optically clear 3D printed polymer-based material was identified and trialled for its suitability as an alternative replacement to the industry standard of water.

B.1. Solid 3D printed polymer confinement

The 3D printed confinement overlays were manufactured and purchased from Luximprint N.V. [2]. The confinement media were 3D printed directly to the aluminium substrate through sequential droplet layer deposition of a mono-acrylic liquid that was later cured solid by UV light. Figure B.1 provided a schematic overview of the 3D manufacturing processing as the printer head deposits droplets of the liquid material directly onto the substrate and then cures the material into a solid layer [2]. This process was repeated multiple times until the desired thickness of the confinement layer was achieved. The overlays do not require additional post-processing after curing. This method was ideal, as the droplets would naturally take the shape of the imperfections of the substrate surface as the overlay was cured.

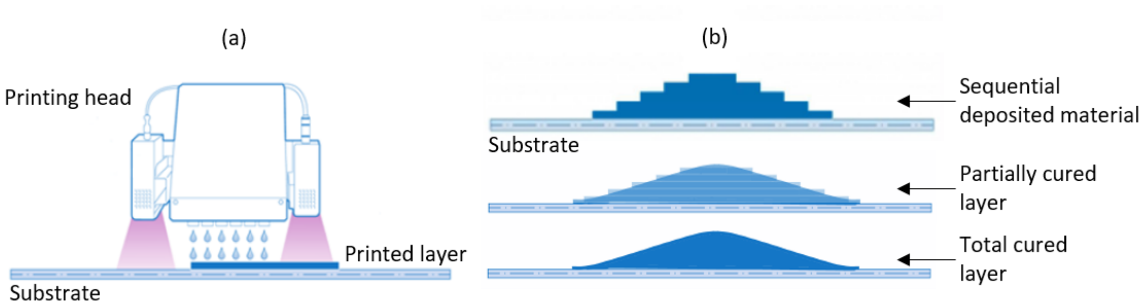

Figure B.1: Schematic overview of liquid droplet deposited additive manufacturing of solid confinement for laser shock peening (a) total printing process, (b) sequential building of 3D printed layers [2]

This study was conducted on flat confinement mediums of 1 mm, 2 mm and 3.5 mm in thickness, as this would provide the required proof of concept for later further developments. The thickness of the overlays was measured at ten random locations using a micrometre and it was found that the largest variation in each confinement thickness was ±0.03 mm from the nominal thickness value. Each confinement layer was printed in the shape of a rectangle of 26x28 mm on a bare (no ablative tape layer) 40x40x2mm AA2024-T351 (no clad) substrate. The substrate material had undergone a process of chemical milling to remove the clad overlay. No LSP ablative coating was used as this would reduce the adhesion between the substrate and the 3D printed overlay. Figure B.2 provided an example of each overlay thickness as printed directly to the aluminium substrate. Although an increase in yellow hue occurred with increasing overlay thickness, no geometric inconsistencies were observed with the increased thickness and all overlays were firmly adhered to the substrate surface.

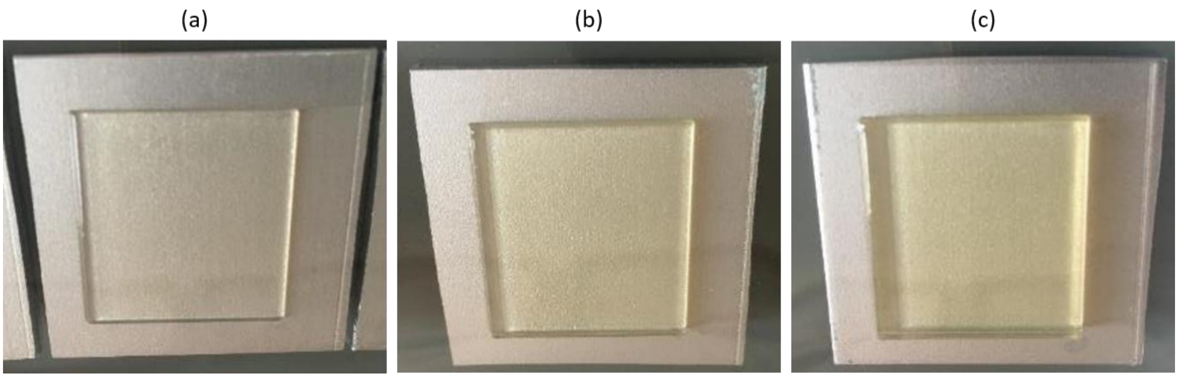

Figure B.2: 3D printed solid confinement on AA2024-T351 substrate (a) 1 mm thick, (b) 2 mm thick, (c) 3.5 mm thick

B.2. Laser Shock Peening of 3D Printed Solid Confinement

All LSP activities with this medium were completed at the HiLASE laser facility in the Czech Republic through their Open Access program. The details of this facility are outlined in Chapter 3 section 3.2.1.

During the LSP processing, the solid confinement samples were clamped between two external plates. The front plate had a 20x20 mm opening at the centre and had a 0.5 mm deep recess around the parameter of the opening to seat the sample. The external plates applied direct pressure to an area around the parameter of the overlay material, which assisted in maintaining the contact between the confinement and substrate. A schematic of the clamping strategy was provided in Figure B.3.

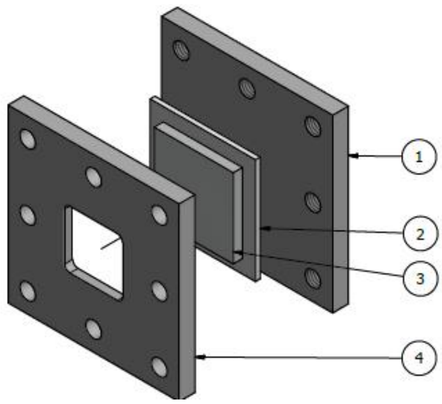

Item Number	Part Name
1	Backing plate
2	AA2024 substrate
3	3D printed solid confinement
4	Front plate

Figure B.3: 3D Printed Laser Shock Peening clamping strategy whilst processing

B.2.1. Influence of 3D printed solid confinement on the laser propagation

The 3D printed overlay material was rated by the manufacturer at a 90% total light transmissibility for wavelengths between 600 to 850 nm [2]. The light transmissibility of the overlays had to be experimentally determined as the Hilase LSP processing was completed at a longer wavelength of 1030 nm. A sample of each overlay thickness was printed without an aluminium substrate as shown in Figure B.4. This allowed for the characterisation of overlay thickness effects on the through-put of the laser beam energy. The laser energy of the unfocused beam was initially measured at the laser source with a Gentec energy meter. Each overlay was placed in the optical path of the laser pulse and the energy of the pulse was then measured upon exiting the reverse surface of the solid medium. Table B.1 listed the results of the measurements. These tests were completed at two laser pulse energy settings, a lower energy setting of 120 mJ and a higher energy setting of 510 mJ.

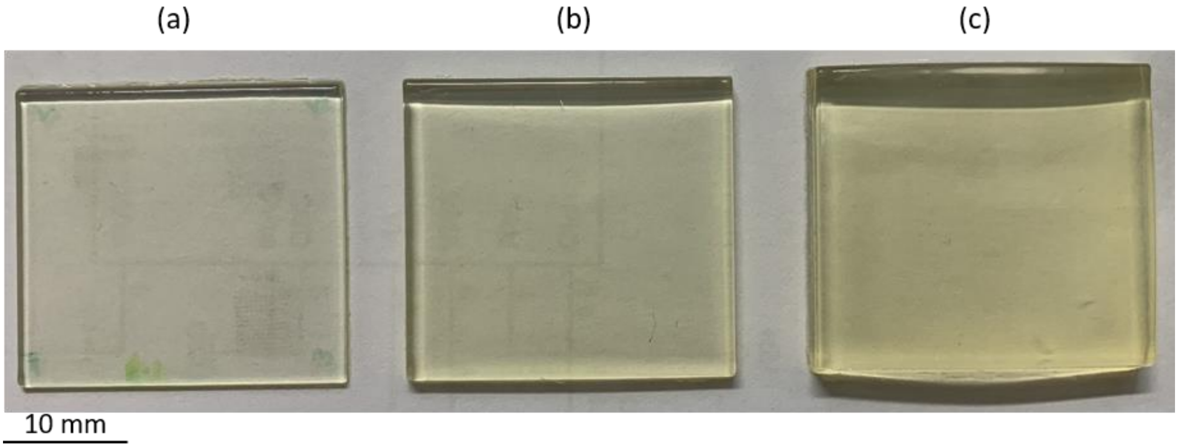

Figure B.4: Solid confinement medium with no substrate (a) 1mm, (b) 2mm, (c) 3.5mm

Table B.1:Averaged power loss due to solid confinement medium

	Confinement Thickness [mm]	1.0	2.0	3.5
Low energy setting (120 mJ)	Energy in [mJ]	117.0	121.0	121.0
	Energy out [mJ]	107.0	107.5	105.5
	Percentage drop [%]	8.5	11.2	12.8
High energy setting (510 mJ)	Energy in [mJ]	571.0	572.0	571.0
	Energy out [mJ]	513.0	511.7	498.0
	Percentage drop [%]	10.2	10.5	12.8
Average Percentage energy drop [%]		9.4	10.9	12.8

The energy drop per confinement thickness was determined as the average per energy setting. Figure B.5 showed that for both energy settings the average beam energy reduction due to the confinement medium increased with increasing confinement thickness. The average energy loss was found to be approximately 11% which was equivalent to the manufacturer's reported transmissibility of the material properties. It was suspected that the fundamental mechanism of the energy drop was due to a portion of the laser light being reflected at the surfaces rather than being significantly absorbed and or reflected by the medium. This was justified as there was less than a 5% variation in the energy drop between the three overlay thicknesses. The average energy drop was used from here on out in the calculation of the power density.

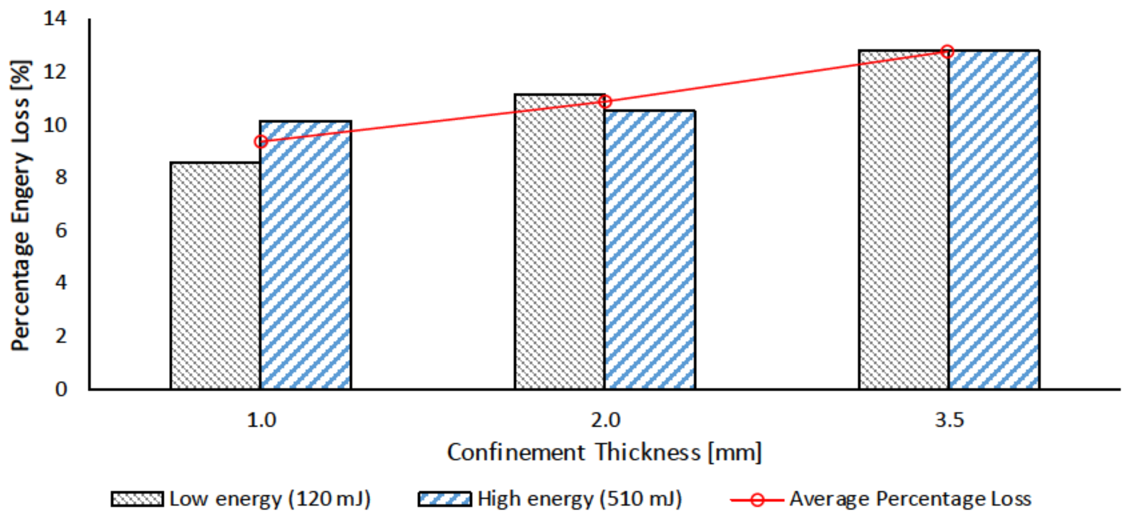

Figure B.5: Characterisation of energy absorption of solid confinement medium

B.2.2. Confinement degradation due to Laser Shock Peening

The high temperatures and pressures associated with the LSP process drastically reduced the damage threshold of the polymer-based confinement medium. A 2 mm thick overlay was used to investigate the effect of the processing on the quality of the confinement medium. An LSP patch of 15x15 mm was created with a power density of 1 GW/cm^2, pulse energy of 200 mJ and a 10% spot overlap, the resulting damage was shown in Figure B.6.a-d. Figure B.6.a showed the overlay sample in its as-received condition. The small cracks which originated from the confinement/substrate interface surface occurred during the 3D printing process and were only present in this single overlay. Figure B.6.b indicated the effects of the LSP processing, in that the overlay was entirely delaminated from the substrate. In addition, clear degradation of the overlay was present on both surfaces of the confinement material. Figure B.6.c showed the damage to the external surface, where the laser pulses entered the medium. The interaction with the laser pulse caused the final build layer of the overlay to flake and break up. Figure B.6.d indicated multiple dark black regions which were indicative of scorching or burning at the interface between the confinement medium and substrate.

The degraded confinement was exposed to the same laser energy drop test that was conducted in section B.2.1. Table B.2 listed the results of this experiment at two pulse energy settings. The degradation caused by the LSP processing caused a further 64% reduction in the throughput energy of the LSP beam. This indicated that with a single application of LSP processing, the overlay materials effective energy transmissibility was reduced by as much as 75%. In addition to the delamination and surface damage at the two confinement surfaces, it was concluded that this confinement strategy should be a single-use consumable and should be replaced between each layer of LSP processing.

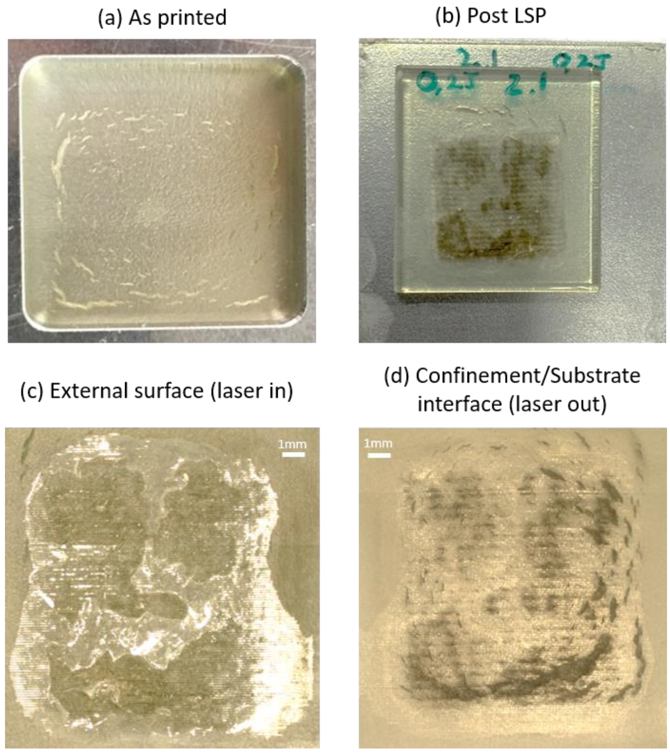

Figure B.6: Degradation of 3D printed solid confinement medium (a) as printed on the substrate, (b) post-laser peening, (c) external surface of the overlay where the laser enters, (d) confinement and substrate interface surface of the overlay where the laser exited

Table B.2: Energy loss due to degradation of solid confinement medium

Degraded 2 mm thick confinement overlay		
Low energy setting (200 mJ)	Energy in [mJ]	200.0
	Energy out [mJ]	78.0
	Percentage drop [%]	61.0
High energy setting (642 mJ)	Energy in [mJ]	642.0
	Energy out [mJ]	215.0
	Percentage drop [%]	66.5
Average Percentage energy drop [%]		64.0

B.2.3. Single-shot confinement delamination

Delamination of the confinement medium caused by a single LSP shot at the fixed power density of 1 GW/cm^2 was investigated with two different laser spot sizes and energy settings (varied to maintain power density). The two square spot sizes were 1.4x1.4 mm^2 and 2.45x2.45 mm^2 and the pulse energy was set to 200 mJ and 600 mJ respectively. This power density was selected as it was the lowest reasonable setting that is typically capable of inducing compressive residual stress within this aluminium alloy.

It was found in both cases that the single LSP shot tended to cause localised delamination of the confinement medium. Figure B.7 showed the formation of a delamination bubble under the surface of the 1mm thick confinement layer after each single LSP shot. Figure B.7.a was completed with an average pulse energy of 200 mJ, a square spot size of 1.45x1.45 mm^2 and a power density corrected for energy loss of approximately 1.19 GW/cm^2. Figure B.7.b was completed with larger parameters of average pulse energy of 600 mJ, a square spot size of 2.45x2.45 mm^2 and a power density corrected for energy loss of approximately 1.24 GW/cm^2. Close inspection showed the delamination occurred radially outwards with two delamination fronts occurring: full delamination of the overlay occurred near the LSP shot and partial delamination radially outward from the initial shot. The radii of the full and partial delamination rings at the smallest LSP spot were approximately 3.2 mm and 5.25 mm and 7.4 mm and 9.8 mm for the larger LSP spot. This indicated that the larger spot size and higher energy increased the delamination ring size even though the power density was kept constant.

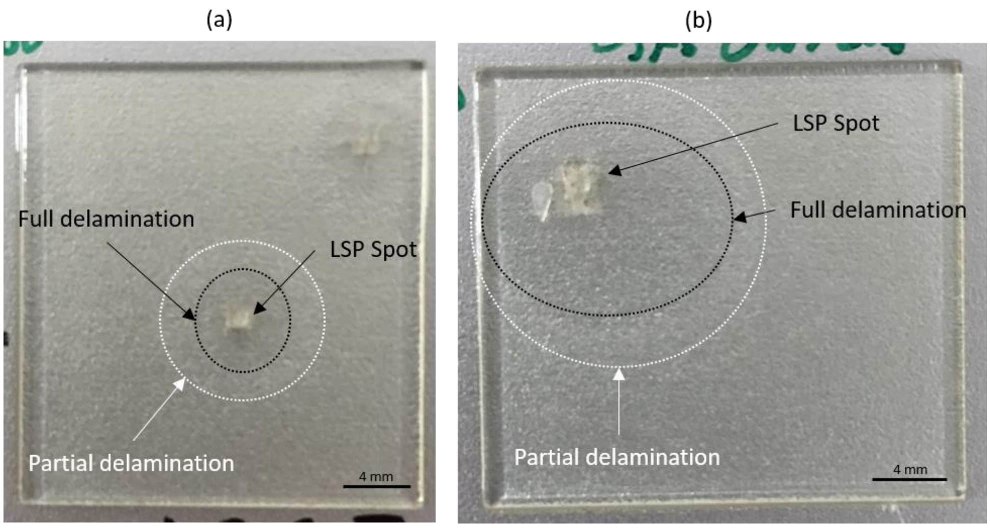

Figure B.7: Localised confinement layer delamination due to single laser peening shot (a) small singe shot 1.45x1.45 mm – 200mJ – 1.19 GW/cm^2, (b) larger single shot 2.45x2.45 mm – 600 mJ – 1.24 GW/cm^2

B.2.4. Multi-shot confinement delamination

Laser shock peening is typically applied to a component as a sequenced array of laser shots such as those shown in chapters 4 and 6. To adequately achieve this type of processing strategy with the present solid confinement samples, the spot size and pulse energy were iteratively reduced, whilst maintaining a 1 GW/cm^2 power density. This was repeated until large scale localised delamination no longer occurred with a single LSP shot. The optimised LSP parameters were found to be a pulse energy of 16 mJ and an approximate spot size of 0.4x0.4 mm^2. Figure B.8 provided a measure of the spot size and temporal distribution of the laser pulse energy at the optimised parameter setting. These have been provided to confirm the laser parameter combination as these settings neared the lowest operating conditions of the laser.

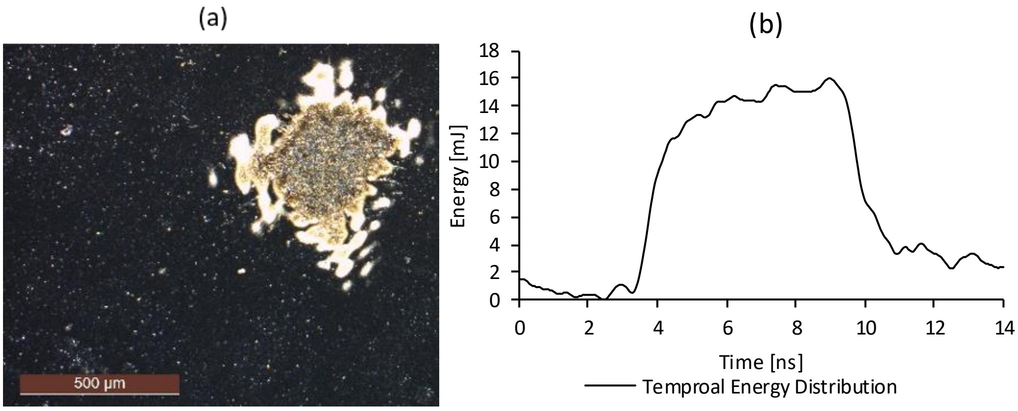

Figure B.8: Optimised parameters for Laser Shock Peening with solid confinement media (a) attenuated spot size measured at 0.4x0.4 mm^2 (b) temporal distribution of laser pulse energy

The reduced energy and spot size combination produced favourable results in that the delamination per spot was significantly reduced. Figure B.9 showed that minimal overlay delamination occurred after peening a 5x5 mm^2 patch with 0% spot overlap. This result indicated that the LSP parameters had to be fixed to <20mJ with a corresponding spot size of <0.5 mm in dimension.

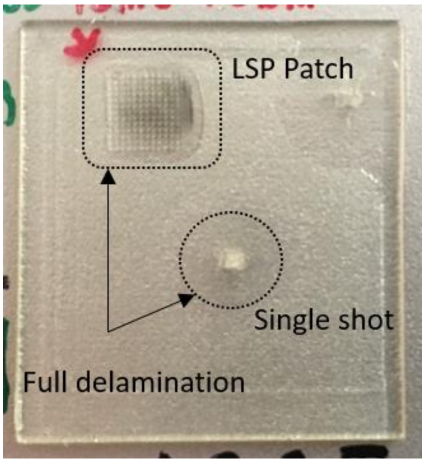

Figure B.9: Minimising overlay delamination at low energy Laser Shock Peening

Maintaining the contact between the confinement and substrate was vitally important for the success of LSP with the solid medium. If a large gap between the substrate and confinement was introduced by each spot, as in the case of Figure B.7, the effectiveness of subsequent spots would be drastically reduced as the plasma will no longer be confined by the overlying material but rather will be confined by air. As shown in Figure 2.21, an air confined plasma (no confinement) rapidly expands away from the target surface reducing the pressure applied to the surface and reducing the effectiveness of the LSP processing.

B.2.4.1. Water confined benchmark sample

Samples were replicated with the standard water confinement at the ideal LSP conditions of 1GW/cm^2, 16 mJ, 0.4x0.4 mm^2, single layer and 0% spot overlap. This sample was manufactured as the benchmark to assess the outcomes of the solid confinement LSP processing. The processing was completed without an ablative coating. Figure B.10.a showed the characterisation of the surface of the six individual patches that were produced with a thin sheet of flowing water as the confinement medium. Figure B.10.b-c provided the topographic representation of the post-LSP surface, with deformation dimples caused by the LSP shots as deep as 25 µm. The average deformed surface was produced as the mean deformation across three horizontal measurement lines across the LSP patch. Notable surface deformation was induced in the surface of the sample even though a relatively low power density, pulse energy and spot size were used. This result showed an exciting potential for future LSP applications at the micro-LSP scale.

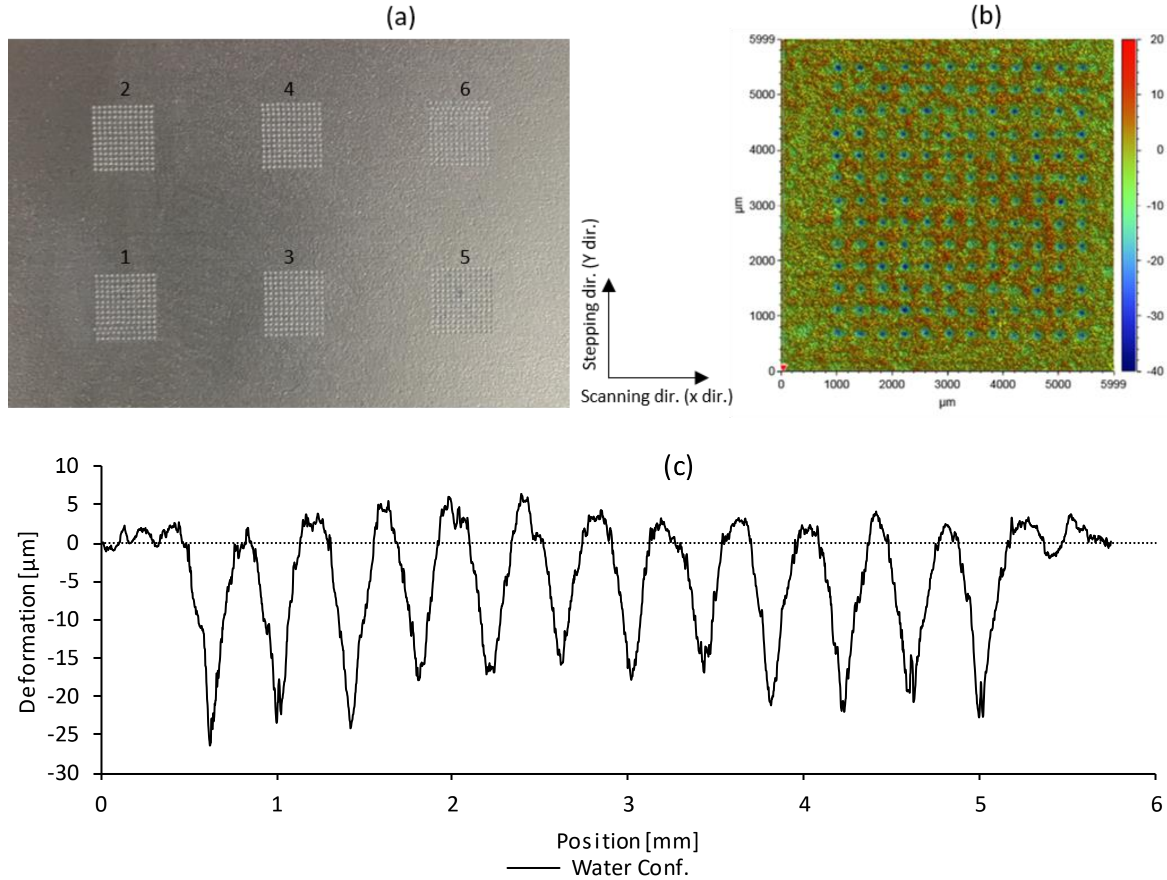

Figure B.10: Surface deformation of water confined laser peening sample at ideal processing parameters (a) post-laser peening surfaces of the six patch sample, (b) surface topology over a laser peened patch, (c) averaged surface deformation across three lines of laser shots

The residual stress of the water confined LSP patches were characterised using both incremental hole drilling and laboratory XRD techniques. XRD techniques with layer removal via electropolishing were used at Hilase to characterise the residual stress in the first 50 µm of the solid confinement samples thus the residual stress in the remainder of the depth was completed with this technique upon the return to Coventry University. Incremental hole drilling was used on the water confined sample to validate the measurement procedure and results achieved with the XRD method.

A 1 mm diameter hole was made in a Vishay Microsmeasurements EA-06-031RE-120 three-element strain gauge, which allowed for the characterisation of the residual stress to a depth of 0.5 mm from the surface. Sixteen depth increments that were biased toward the surface were used to determine the residual stress variation in the sample. The orthogonal gauge elements were aligned approximately with the stepping (Y direction) and scanning (X direction) directions of the LSP processing.

A 2 mm diameter collimator with five tilt angles to 45°/-45° and a count time of 20 seconds per tilt were used in the characterisation of the residual stress by XRD [3]. A copper X-ray source with measurements on the {422} diffraction plane was used to achieve an approximate penetration depth of the gauge volume which varied between 30 and 40 μm in the aluminium substrate [4]. The XRD measurements per depth were the arithmetic mean of nine individual measurements where the centre of the collimator was shifted in ±0.3 mm intervals in the X and Y directions relative to the centre of the LSP patch. This was done to increase the number of grains sampled in each depth measurement.

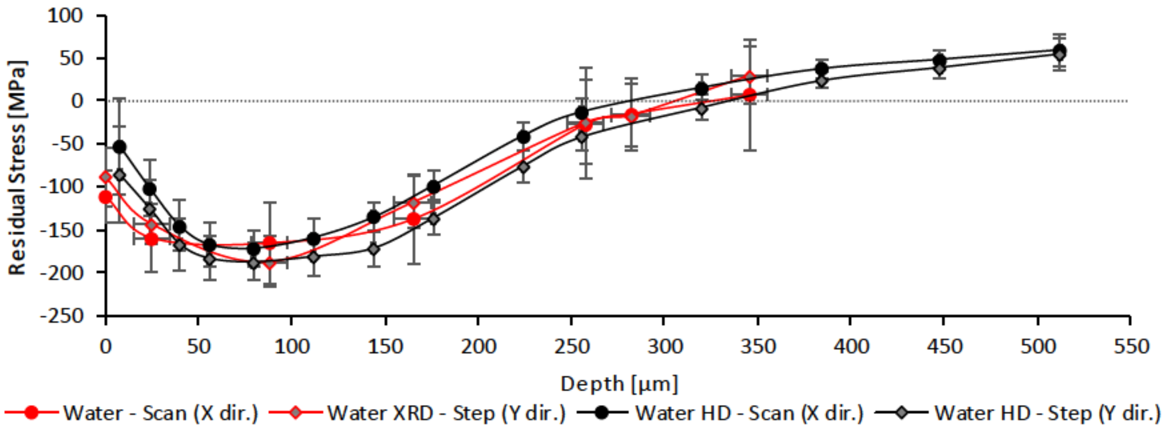

Figure B.11: Comparison of water confined residual stress measured with incremental hole drilling and x-ray diffraction with layer removal

An acceptable correlation between the two measurement techniques was achieved with a water confined sample. The XRD measurements provided a slightly more compressive surface than that of the incremental hole drilling measurements. The cause of this may have been due to the slight underestimation of the surface position in the hole drilling measurements (the zero surface position may have been slightly in the adhesive layer). The XRD residual stress measurements were slightly more biaxial than that predicted by the incremental hole drilling measurement. However, the measurements were all within the expected experimental uncertainty of each respective measurement technique.

B.2.4.2. Influence of solid confinement delamination during patch processing

This strategy of LSP confinement was found to be extremely susceptible to delaminating from the substrate during processing. This resulted in insufficient confinement of the plasma and reduced the magnitude of the effective plastic deformation of the target surface. Clear interactions between the laser pulse and the substrate were seen as a recast layer typical of LSP processing without an ablative coating was formed on the surface, as shown in Figure B.12.a.

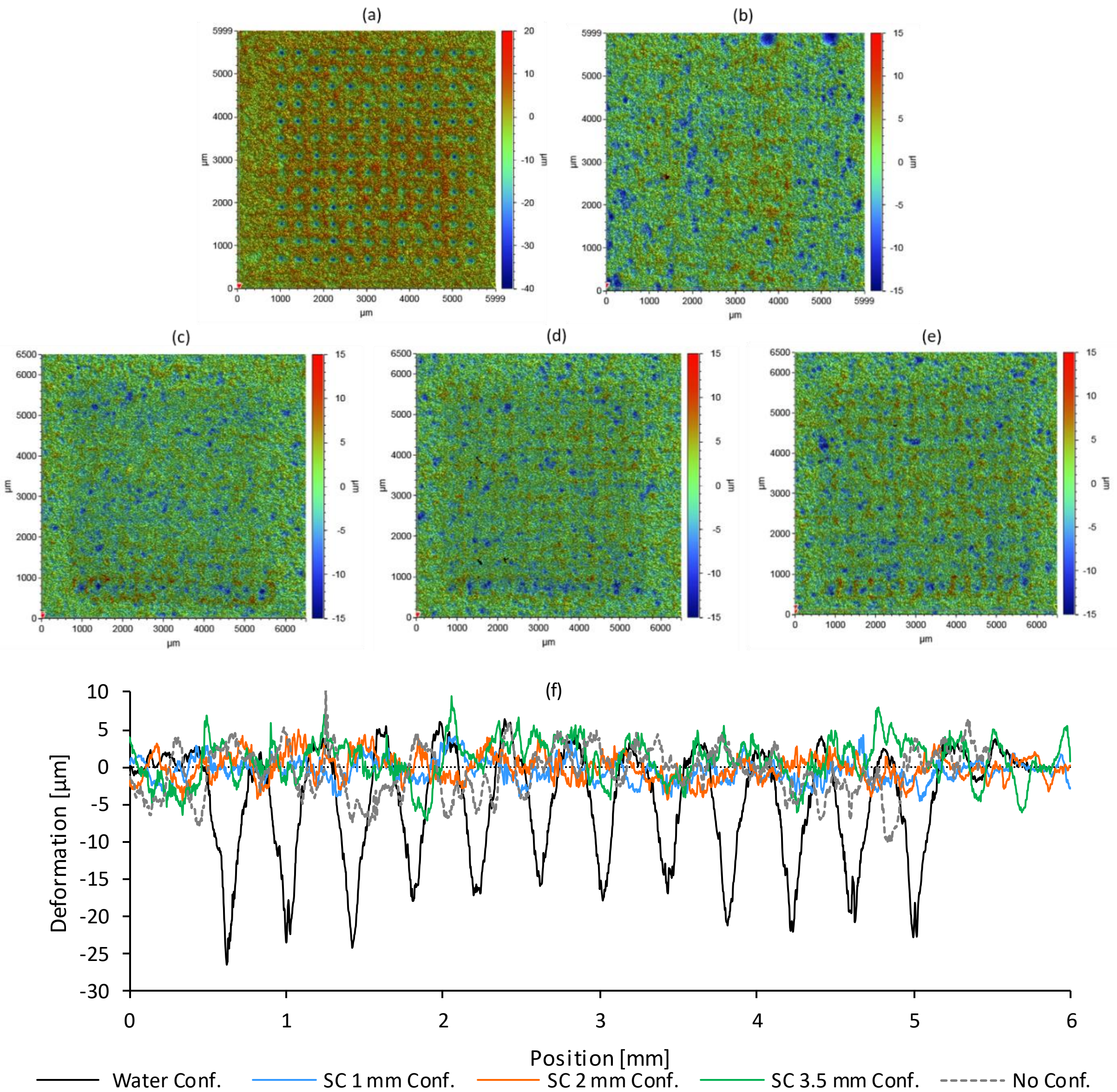

Figure B.12: Influence of inadequate confinement during patch laser peening (a) water confined surface, (b) no confinement, (c) 1 mm solid confined surface, (d) 2 mm solid confined surface, (e) 3.5 mm solid confined surface, (f) average surface deformation across the laser peened surfaces

This was effectively considered as a region where the laser pulse ablated the target surface, establishing a weak plasma that affected the surface through direct ablation, localised high temperatures and created a new shallow recast layer. However, no substantial deformation below this layer was observed when the solid confinement was delaminated. This was due to the plasma being relatively unhindered in its rapid expansion away from the target surface. Figure B.12.b-c provided the comparison of the average surface deformation across the LSP patches with LSP processing with no confinement (laser directly striking the surface), a thin layer of water confinement and the three thicknesses of the 3D printed confinements. From the results of the deformed surfaces shown in Figure B.12, when the LSP processing causes a significantly large enough gap at the interface between the solid confinement and the target surface no substantial surface deformation was observed. This is because the plasma escapes, resulting in an insufficient strengthened shockwave to penetrate the material. A suspected cause of the overlay delamination was due to the large mismatch in the thermal properties of the overlay material and the substrate. When the initial LSP shot occurred, the local temperature rises significantly and causes the expansion of both the overlay and substrate. However, as the overlay is a polymer material it would naturally expand more than the substrate and this likely contributed to the localised delamination of the overlay and resulted in the ineffective confinement of the overlay for sequential shots. The surfaces of the solid confined samples were equivalent to the post LSP surface with no effective confinement.

Figure B.13 indicated the effect of the lack of confinement on the near-surface residual stress profile of a sample that had a 1 mm thick 3D printed solid overlay. The solid confinement sample had very high tensile residual stress near the surface which steadily decreased to the near-zero bulk stress of the material within the first 75 µm. This residual stress was caused by the thermal interaction between the laser pulse and the target surface. No beneficial residual stresses were introduced into the samples when a large gap developed at the confinement-sample interface.

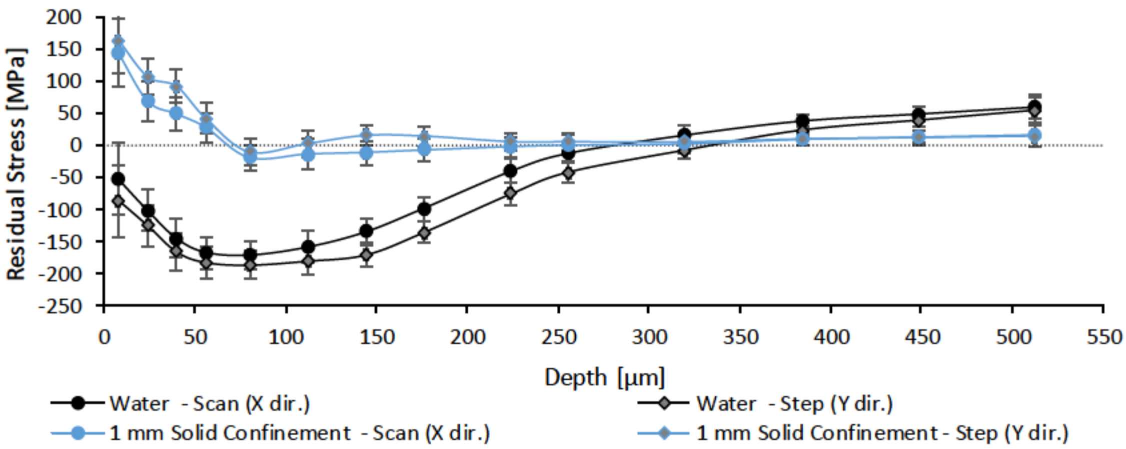

Figure B.13: Influence of inadequate confinement during patch laser peening on induced residual stress

In this study, a variety of LSP parameters were trialled with the various thicknesses of the solid confinement to identify the optimum operating LSP parameters for this strategy of confinement. These configuration and LSP outcomes are listed in Table B.3, where a single LSP layer was used with all configurations. It was clear from the outcomes of the peening trials that the vast majority of the solid confinements failed to produce a viable LSP patch in which some form of deformation and residual stress could be accurately characterised.

Table B.3: Summary of laser peening parameter configurations and outcomes

Confinement thickness [mm]	Power density [GW/cm²]	Spot overlap [%]	Outcome
1	1	0	Single viable LSP patch of 5x5 mm
2			Delamination – no confinement
3.5			Delamination – no confinement
1	1	30	Delamination – no confinement
2			Delamination – no confinement
1	2[†]	0	Delamination – no confinement

B.2.5. Induced residual stress with 3D printed solid confinement overlays

The main characterisation criterion for the 3D printed confinement LSP was the generation of compressive residual stress in the component. As detailed in Table B.3, a successful LSP patch of 5x5 mm^2 was achieved with a 1 mm thick 3D printed solid polymer-based overlay.

Figure B.14.a-c showed a successful LSP patch that had been confined by a 1 mm thick 3D printed solid confinement. The black dashed rectangle in Figure B.14.a indicated the successfully peened patch, the remaining three patches did not provide favourable results. It was clear from Figure B.14. that no significant scorching of the confinement occurred during the peening of the successful patch. Additionally, the confinement overlay only partially delaminated in the adjacent areas around the LSP patch. The larger delamination occurred due to the application of the additional three patches.

Figure B.14.b showed the overlay material with the substrate removed. It was clear that even at the lower energy the solid confinement medium suffered substantial damage during the LSP processing. As in section B.2.2, the final build layer of the outer surface of the confinement overlay (on which the laser was incident) was cracked and had begun to flake away from the lower layer. Small amounts of

[†] Increase in power density was achieved by doubling the pulse energy and maintaining the spot size at 0.4x0.4 mm.

blackening occurred in very localised areas on the interface surface. The successful patch had vastly less scorching of the interface surface than those of the unsuccessful patches. The very localised scorched areas were determined to have been caused by a small delamination gap that was caused by the previous LSP spot. The successful LSP patch presented a similar degradation mechanism to that of the characterised sample in section B.2.2 thus it was assumed that an equivalent reduction in the overlay's energy transmissibility occurred. This indicated that even upon achieving a successful patch the 3D printed overlays were a single-use confinement material.

Figure B.14.c showed the post-peened surface of solid confined samples which had approximately 40-50 µm removed from the surfaces by electro-polishing. Clear indentations caused by the LSP pulses are present in the target surface, confirming the ability of the confinement strategy to introduce surface deformations during LSP.

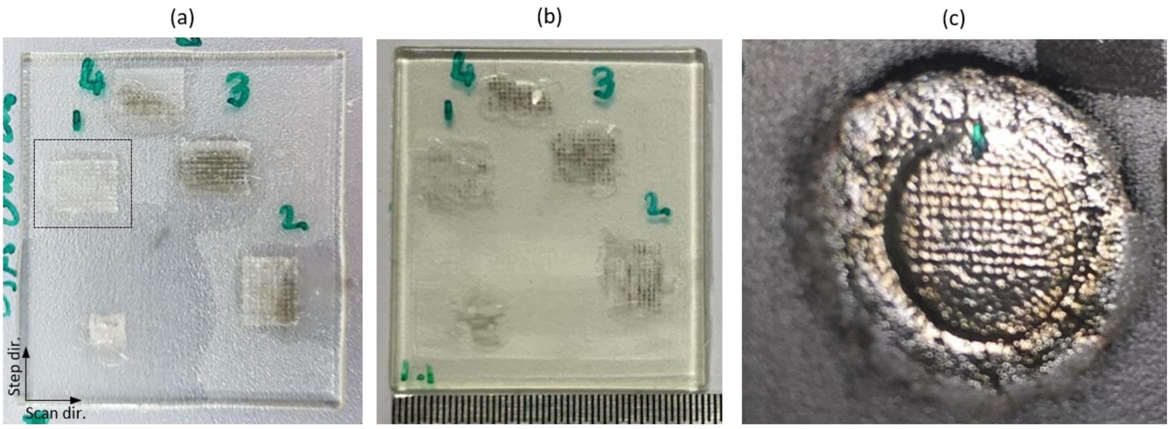

Figure B.14: Successful laser shock peening trail with 3D printed solid confinement (a) indication of post peening sample, (b) damage caused by peening on solid confinement, (c) indication of surface deformation caused by laser peening with approximately 40-50 µm removed with electro-polishing

Figure B.15 provided a comparison of the surface deformation of the water and 1 mm thick solid confinement sample with approximately 40-50 µm removed from the surface by electropolishing. Comparison of the two figures indicated that the magnitude and prominence of the LSP induced indentations of the water confined sample were greater than that of the solid confinement sample with an equivalent amount of material removed. This would suggest that a larger peening intensity occurred which would inherently result in a greater peak compressive residual stress that penetrated further into the depth of the material.

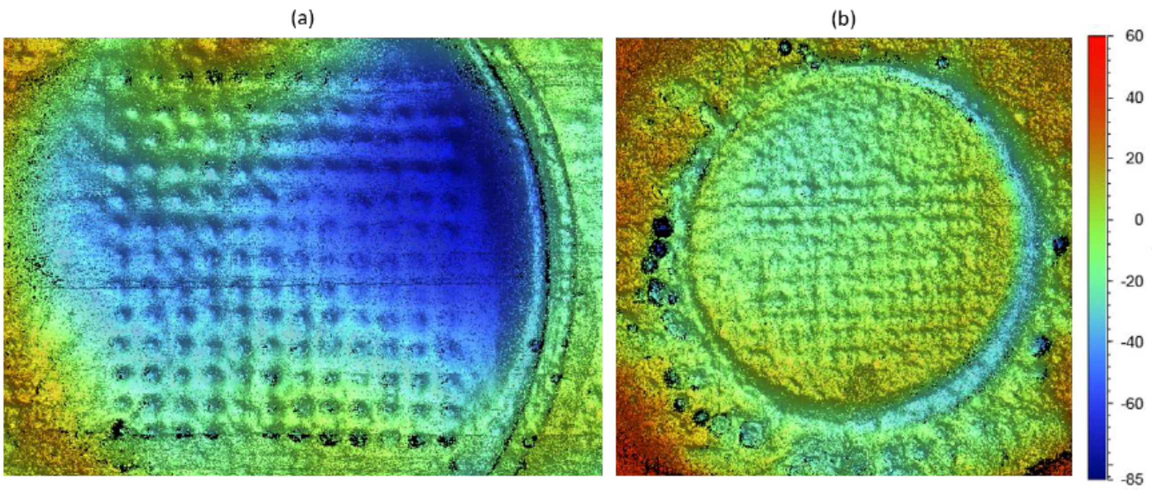

Figure B.15: Comparison of laser peening induced surface deformation with 3D printed and water confinement with 30-40 µm removed via electropolishing

Figure B.16 showed the comparison of the induced residual stress profiles of the water confinement and 1 mm thick 3D printed solid confinement, measured by XRD techniques. The residual stress at the surface of the solid confinement sample was significantly tensile compared to that of the water confinement sample.

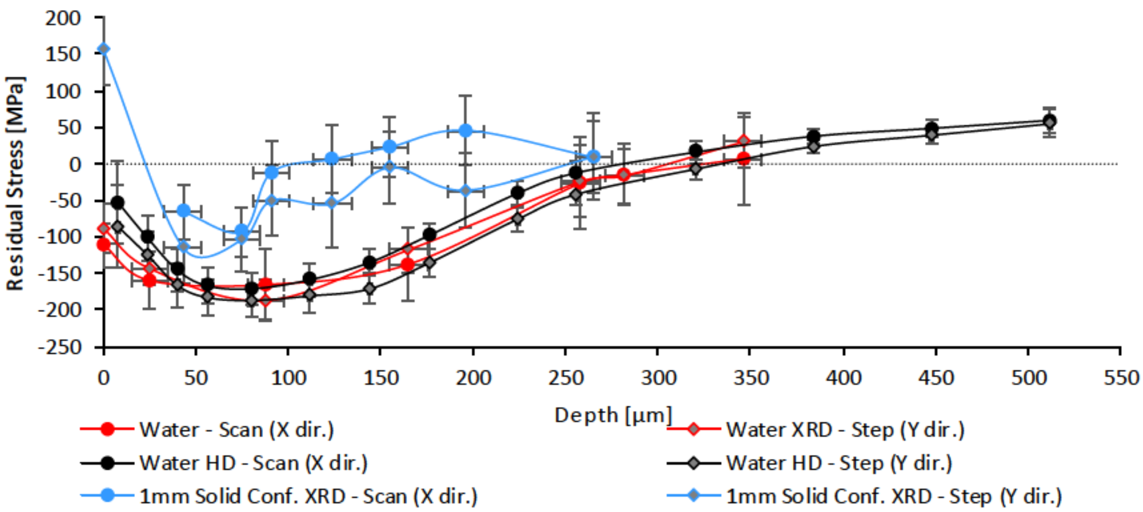

Figure B.16: Comparison of laser peening induced residual stress profiles with a 1 mm thick 3D printed solid confinement and standard water confinement

The surface stress of this solid confinement sample was equivalent to that of the sample in Figure B.13, implying that the tensile residual stresses near-surface were attributed to the thermal effects which occurred during peening. The lack of the solid confinement's ability to reduce the overall temperature of the LSP process, as in the case of the water confinement, drastically exacerbates the surface tensile stresses. However, this high tensile region was extremely shallow and was associated with the recast layer caused by the lack of an ablative coating. In addition to the higher surfaces stresses, the magnitude of the peak compressive stress with the solid confinement sample (-104 MPa) was approximately 60% of the peak compression in the water samples (-187 MPa), both occurred between 50-100 µm from the surface. The depth of compression was also reduced by as much as 100 µm in the solid confinement sample, between 150-250 µm, compared to the water sample of 250-350 µm.

Both samples displayed a large variation in the residual stress across the LSP patches. This was due to the use of no spot overlap and only a single layer of LSP being applied. This variation was seen in the reduction in the uniformity of the residual stress depth profile of the solid confinement sample. The water sample displayed similar variations but was less prominent as a larger depth increment was used in the characterisation of this sample.

The overall outcome of this chapter showed that it was possible to complete LSP with a 3D printed solid confinement. In its current form, the solid confinement sample was far more susceptible to failure than that of the water confinement. Additionally, the peak compressive stress and depth of penetration was reduced as a lower peening intensity resulted with the solid confinement.

B.3. Conclusions

The following conclusions were deduced from the results of this chapter:

- 3D printed solid confinement overlays were capable of providing suitable confinement of the plasma event to achieve a multi-shot LSP patch but require extremely tight control of the LSP parameters.
- The solid confinement mediums are only suitable for single use and need to be replaced between sequential layers of LSP processing.
- This strategy of confinement was extremely susceptible to delamination from the substrate which resulted in little to no confinement of the plasma event.
- The solid confinement medium did not provide the same level of peening intensity that was achieved through the use of a water confinement strategy.
- A higher magnitude tensile residual stress occurred at the surface of the solid confinement sample as higher temperatures occurred during the LSP process.
- The reduction in peening intensity resulted in a lower magnitude peak compressive residual stress and lower penetration of the residual stresses.
- To LSP parameters had to be significantly reduced and controlled to mitigate larger scale delamination of the confinement medium from the substrate.

- In its current form, any LSP activities with this confinement strategy will increase the processing time and cost as the overlay will need to be replaced between LSP processing layers. This would render the process almost entirely unfeasible in an industrial application and would be extremely costly to implement.

B.4. Suggested future work

The 3D printed solid confinement medium possesses a large amount of potential to be a viable replacement for the industry standard of water. Obvious drawbacks were identified in this study that should be addressed before any further implementation of this confinement strategy. The following outlines suggest future areas of development to further advance this methodology of LSP confinement:

1) Large scale delamination of the confinement medium and repeatability was the two most significant hindrances to this process. Further research should be undertaken to investigate the strength of the adhesion between the confinement and substrate.
2) Collaboration with the manufacturer of the overlays should be aimed at enhancing the damage threshold of the material. This potential would increase the ability of the overlay to confine the plasma event.
3) This overlay strategy should be integrated into the LSP processing of complex three-dimensional geometry to determine its suitability in more realistic industrial applications.

B.5. References

[1] Furfari D, Fitzpatrick M. Overlay Material For Laser Shock Peening. 16154216.2, 2016.

[2] de Visser M. 3D Printed Optical Plastics - Luximprint 2018.

[3] Fitzpatrick ME, Fry AT, Holdway P, Kandil FA, Suominen L. Determination of Residual Stresses by X-ray Diffraction - Issue 2. Natl Phys Lab - Meas Good Pract Guid No 52 2005. https://doi.org/10.1007/s00028-005-0194-y.

[4] Noyan IC, Cohen JB. Residual Stress – Measurement by Diffraction and Interpretation, Materials Research and Engineering. Springer-Verlag New York Inc.; 1987. https://doi.org/10.1007/978-1-4613-9570-6.